AD-A278 989

MENTATION PAGE

Form Approved
OMB No. 0704-0188

2

s estimated to average 1 hour per response, including the time for reviewing instructions, searching existing data sources, g and reviewing the collection of information. Send comments regarding this burden estimate or any other aspect of this g this burden to Washington Headquarters Services, Directorate for Information Operations and Reports, 1215 Jefferson to the Office of Management and Budget, Paperwork Reduction Project (0704-0188), Washington, DC 20503.

1. AGENCY USE ONLY *(Leave blank)*

2. REPORT DATE
February 1994

3. REPORT TYPE AND DATES COVERED
Final Report, Sept. 1, 1991 - Dec. 31, 1993

4. TITLE AND SUBTITLE
Expansion Effects on Supersonic Turbulent Boundary Layers

5. FUNDING NUMBERS
G-AFOSR-91-0412
2307/AS

6. AUTHOR(S)
S.A. Arnette, M. Samimy, and G.S. Elliott

7. PERFORMING ORGANIZATION NAME(S) AND ADDRESS(ES)
The Ohio State University
Department of Mechanical Engineering
Columbus, Ohio 43210

8. PERFORMING ORGANIZATION REPORT NUMBER
MEMS-94-101
AEOSR-TR- 94 0268

9. SPONSORING/MONITORING AGENCY NAME(S) AND ADDRESS(ES)
NA-
Air Force Office of Scientific Research/NA
110 Duncan Avenue, Suite B115
Bolling Air Force Base, DC 20332-0001

10. SPONSORING/MONITORING AGENCY REPORT NUMBER
AFOSR-
91-0412

11. SUPPLEMENTARY NOTES

DTIC
ELECTE
MAY 06 1994
S G D

12a. DISTRIBUTION/AVAILABILITY STATEMENT
Approved for public release;
distribution is unlimited

12b. DISTRIBUTION CODE

13. ABSTRACT *(Maximum 200 words)*

The effects of various expansion regions on the large scale structure of a Mach 3 fully-developed turbulent boundary layer are investigated. Five cases are studied: 7° and 14° centered expansions, 7° and 14° gradual expansions, and the flat plate. Multi-point surface pressure measurements, filtered Rayleigh scattering visualizations, and double-pulse visualizations were employed. Plan view images of the flat plate boundary layer reveal the presence of structures of a very large streamwise, and limited spanwise, extent. These structures were found well above the inner layer, nominally at $n/\delta = 0.5\text{-}1.0$. The structures were also found in the expanded boundary layers. Across the expansion, the large scale structures of the outer layer undergo an increase in scale and structure angle. The small scale turbulent motions of the incoming boundary layer are quenched by the expansion, while the large scale structures respond more gradually. Convection velocities from the pressure correlations are reasonable in the incoming boundary layer, but unreasonably high in the expanded boundary layers. Convection velocities from correlations of double-pulse images appear reasonable. The discrepancy between the two results suggests the relationship between the large scale structures and the convecting pressure field is severely altered by the expansions.

14. SUBJECT TERMS
Supersonic Boundary Layer, Turbulence, Expansion Effect,
Experiment, Filtered Rayleigh/Mie Scattering Diagnostics

15. NUMBER OF PAGES
185

16. PRICE CODE

17. SECURITY CLASSIFICATION OF REPORT	**18. SECURITY CLASSIFICATION OF THIS PAGE**	**19. SECURITY CLASSIFICATION OF ABSTRACT**	**20. LIMITATION OF ABSTRACT**
Unclassified	Unclassified	Unclassified	Unlimited

NSN 7540-01-280-5500

DTIC QUALITY INSPECTED 1

Standard Form 298 (Rev 2-89)
Prescribed by ANSI Std Z39-18

AFOSR-TR- 94 0268

Expansion Effects on Supersonic Turbulent Boundary Layers

Stephen A. Arnette[1], Mo Samimy[2], and Gregory S. Elliott[3]
Department of Mechanical Engineering
The Ohio State University
Columbus, OH 43210

Final Technical Report

for

The Air Force Office of Scientific Research
Grant AFOSR-91-0412 (Dr. L. Sakell)

for the Period of

September 1, 1991 - December 31, 1993

---

[1] Graduate Student, NSF Fellow
[2] Principle Investigator, Professor of Mechanical Engineering
[3] Post-Doctoral Researcher

Abstract

The effects of various expansion regions on the large scale structure of a Mach 3 fully-developed turbulent boundary layer are investigated. Five cases are studied: 7° and 14° centered expansions, 7° and 14° gradual expansions, and the flat plate. Multi-point fluctuating surface pressure measurements, instantaneous filtered Rayleigh scattering visualizations, and double-pulse visualizations were employed. Visualizations were made possible by the presence of scalar transport condensation in the freestream, and the absence of this condensation in the boundary layer due to its higher temperature. Plan view visualizations of the flat plate boundary layer reveal the well-defined presence of turbulent structures of a very large streamwise, and limited spanwise, extent. As such, these elongated longitudinal structures are somewhat similar to those found near the wall of incompressible boundary layers. However, these structures were found well above the inner layer, nominally at $n/\delta = 0.5\text{-}1.0$, and have a larger spanwise extent than the near-wall streaks of incompressible cases. Although possibly present even deeper in the boundary layer, the visualization technique precluded visualizations closer to the wall. Experiments were performed for very different upstream conditions (i.e. with and without the tunnel flow straightening assembly installed), and the elongated structures were always present. These facts suggest that the longitudinal structures are a robust feature of the compressible boundary layer. The structures were also found in the expanded boundary layers. The appearance of the elongated structures in the four expansion cases showed no noticeable differences from the flat plate case. The apparent absence of these structures in the incompressible turbulent boundary layer calls to question longstanding ideas concerning the similarity of the turbulence structure of incompressible and compressible boundary layers. The large scale structures of the outer layer increase in scale across the expansion region, probably due to dilatational effects. The structure angle increases as the structures pass through the expansion, which can be explained by basic kinematical arguments. It is not clear if this effect is long-lasting as spatial correlations show the structure angle at $s/\delta_0 \approx 10$ downstream of the 7° centered expansion to be similar to that of the flat plate boundary layer. As suggested previously, the small scale turbulent motions of the incoming boundary layer are quenched essentially immediately by the expansion, while the large scale structures respond more gradually. This point is indicated in the visualizations by the exaggerated penetration of potential fluid deep into the boundary layer between adjacent large scale structures. In the multi-point surface pressure measurements, the quenching of small scales is manifested as a concentration of the normalized power spectrum at low frequencies (frequencies associated with large scale structures). Downstream of both 14° expansion regions, a new layer of condensation in excess of that present in the incoming freestream forms above the region demarcated by the absence of condensation. Instantaneous visualizations show the source of the excess condensation to be the normal outward transport of fluid originally in the boundary layer, upon which the encountered lower temperatures lead to condensation. The excess condensation was not encountered in either of the 7° expansion cases. The convection of the boundary layer structures was investigated with surface pressure measurements and double-pulse visualizations. Convection velocities from the pressure correlations are reasonable in the incoming boundary layer, but unreasonably high in the expanded boundary layers. Convection velocities determined from correlations between the double-pulse images appear reasonable in both the flat plate and 7° centered expansion boundary layers. The discrepancy between the pressure and double-pulse results suggests the relationship between the large scale structures and the convecting pressure field is severely altered by the expansions. Downstream of the 14° centered expansion, double-pulse correlations show the large scale structures of the boundary layer to convect at a lower velocity than those in the flat plate boundary layer. This result (which is almost assuredly related to normal outward transport of boundary layer fluid in the formation of the excess condensation) shows the boundary layers downstream of the 7° and 14° centered expansions to possess fundamental differences.

Table of Contents

Nomenclature

d	Diameter of the high frequency response pressure transducers.
$I_{avg}(n)$	Average intensity as a function of the normal distance from the boundary.
$I_{avg,max}$	Maximum average intensity within an average intensity profile.
$I_j(s,n)$	Intensity at (s,n) in the jth image of the ensemble.
$I_j^*(s,n)$	Deviation from the ensemble average intensity at (s,n) in the jth image of the ensemble.
$I'(n)$	RMS intensity fluctuation as a function of the normal distance from the boundary.
n	Normal distance above the boundary.
R(ds,dn)	Spatial correlation coefficient at displacements (ds,dn) from the reference point.
$R(ds,n_{ref})$	Double-pulse correlation coefficient for the reference line at n_{ref} at a streamwise displacement ds downstream of the streamwise reference location.
Re	Reynolds number.
Re_θ	Reynolds number calculated with the boundary layer momentum thickness as the length scale.
s	Streamwise distance along the model surface measured from the beginning of the convex surface curvature.
s_{ref}	Streamwise reference location for the correlation. For spatial correlations, s_{ref} denotes a point. For double-pulse correlations, s_{ref} denotes a horizontal line of length $\delta_{vis}/2$.
q^2	Turbulent kinetic energy.
$\underline{U}$	Mean velocity vector.
U	Mean streamwise velocity.
U_c	Convection velocity of the large scale boundary layer structures.
U_∞	Streamwise velocity in the freestream.
u	Streamwise velocity fluctuations.
u_τ	Friction velocity.
V	Mean normal velocity.
v	Normal velocity fluctuations.
w	Spanwise velocity fluctuations.
x	Horizontal distance measured from (s,n) = (0,0).
y	Vertical distance measured from (s,n) = (0,0).
z	Spanwise direction.
∇	Del operator $(\nabla\cdot\underline{J} = \partial J_x/\partial x + \partial J_y/\partial y + \partial J_z/\partial z$ where $\underline{J} = J_x i + J_y j + J_z k)$.

δ_0	Boundary layer thickness of the flat plate boundary layer at s = 0 mm measured with LDV (9.2 mm).
δ_{vis}	Boundary thickness defined by 99% of the freestream intensity.
δ_{rms}	Normal distance above the boundary at which the peak in the RMS profile occurs.
ν	Kinematic viscosity.
Δs_{7G}	Streamwise distance through the 7° gradual expansion, measured along the model surface (55 mm).
Δs_{14G}	Streamwise distance through the 14° gradual expansion, measured along the model surface (110 mm).
θ	Boundary layer momentum thickness.
ρ	Density.

1. Introduction

Improved fundamental understanding of compressible turbulent boundary layers will always offer the potential for significant advances in high-speed flight applications, as boundary layers are of such central importance to issues of drag and heat transfer. While an increasingly detailed characterization of two-dimensional, flat plate, zero pressure gradient, compressible turbulent boundary layers continues to emerge [Spina et al., 1994], it is rare that such 'ideal' flows occur in applications. Instead, the compressible boundary layer encountered in an application likely experiences several 'extra rates of strain' (as defined by Bradshaw [1974]) in addition to the usual mean shear associated with the normal gradient of streamwise velocity. These strain rates are caused by effects such as pressure gradients, streamline curvature, or compression/dilatation, all of which are relevant in the current study. Although not pertinent in this study, changes in surface roughness, temperature, or heat flux can also have significant effects on the turbulent boundary layer [Smits and Wood, 1985]. Given this, the effects of extra strain rates on the compressible boundary layer must be understood if improvements in boundary layer control are to be achieved. Unfortunately, as discussed by Smits and Wood [1985], boundary layer response to such perturbations is highly nonlinear, so that the effect of multiple perturbations cannot be predicted even if the effects of the perturbations applied singularly are known.

A schematic of the passage of a two-dimensional, compressible, turbulent boundary layer through an expansion region is depicted in Fig. 1. Upon entering the expansion region, the boundary layer encounters a favorable streamwise pressure gradient ($\partial p/\partial s < 0$ where s is the streamwise coordinate), a normal pressure gradient ($\partial p/\partial n > 0$ where n is the coordinate normal to the surface and increases away from the surface), and bulk dilatation ($\nabla \bullet \underline{U} > 0$, i.e. the volume of a fluid element increases through the expansion region). This flowfield has been the subject of a surprisingly small number of investigations, the studies by Morkovin [1955], Dussauge and Gaviglio [1987], Smith and Smits [1991], and Arnette et al. [1993a] being among the few of which the authors are aware.

1.1. Large Scale Structure of Turbulent Boundary Layers

It has become increasingly clear that the turbulent boundary layer contains non-random, coherent structure. Impetus for investigating these structures comes from the discovery that they are of major importance to the dynamics of the turbulence. For example, by using the VITA technique in a nominally Mach 3 boundary layer, Spina et al. [1991] showed large-scale coherent structures to be responsible for a disproportionately large fraction of the continually-summed turbulent shear product $[(\rho u)'v']$ given the amount of time that qualifying events occupied the survey location.

As highlighted by Robinson [1991] in his review of the current state of knowledge on boundary layer structure and Spina et al. [1994] in their review of compressible turbulent boundary layers, our knowledge of coherent structures in the compressible boundary layer is limited to the δ-scale motions of the outer layer. This is in sharp contrast to the incompressible case, where several distinct categories of coherent structural elements have been investigated. These include streaks in the near-wall region (and the associated bursts resulting from the lifting and breaking-up of the streaks), horseshoe (low Reynolds number) or hairpin (higher Re) vortices, and large or δ-scale structures. A short discussion of the main features of the coherent motions of incompressible and compressible boundary layers is presented to serve as a point of departure in discussing the current results. The topics considered for the incompressible case are pursued in greater detail by Robinson [1991]. A review of coherent structures in compressible boundary layers is provided in the review by Spina et al. [1994] and in the background discussions of Spina and Smits [1987] and Spina et al. [1991].

1.1.1. Incompressible Case

Alternating streamwise streaks of low and high speed fluid, now generally accepted as a universal feature of the near-wall region of incompressible turbulent boundary layers, were first systematically investigated visually by Kline et al. [1967]. Recent numerical simulation work shows the high speed streak regions to be wider in the spanwise direction and shorter in the streamwise direction than the low speed streaks [Robinson et al., 1989]. The concept of bursting events responsible for turbulence production arose from the observation of low speed streak lift-up away from the wall and ensuing break-up. However, as discussed by Robinson [1991], the definition of bursting has evolved over the years to include several processes in which turbulence is produced via the ejection of near-wall fluid. Direct numerical simulations of turbulence [Kim, 1987, Guezennec et. al, 1989, and Robinson, 1990] have given rise to the interpretation that the ejection of near-wall fluid is dominated by the action of tilted, quasi-streamwise vortices which persist for much longer than the time associated with the ejection. As discussed by Robinson [1991], the relatively large temporal duration of the sweep and ejection regions causes the bursting process to be much more intermittent in space than in time. Experimental confirmation was found in the hot-film correlations for a channel flow by Nakagawa and Nezu [1981]. For both ejection and sweep motions, it was found that the conditionally-averaged u and v fluctuation patterns had larger temporal and spatial scales than the associated uv fluctuation pattern. This gave rise to the notion of a convecting "bursting motion" as a type of large scale eddy structure, which qualitatively agrees with the intermittent nature of bursts.

The work of Head and Bandyopadhyay [1981] demonstrated that horseshoe vortex loops, whose legs are counter-rotating vortices, are a major component of the incompressible turbulent boundary layer. Their light-sheet visualizations of smoke-filled boundary layers with $500 < Re_\theta < 17500$ showed the higher Re_θ (2000-5000) 'hairpin' structures to be thinner and more elongated than the 'horseshoe' structures found at lower Re_θ (< 800). Since these structures were seen to originate in the near-wall region and extend into the outer layer, it is thought they might be important to the exchange of momentum between the inner and outer layers.

The final broad class of coherent structures considered here are the three-dimensional δ-scale bulges seen to dominate the turbulent/non-turbulent interface of the outer layer in streamwise-normal plane visualizations. Head and Bandyopadhyay [1981] suggested that these structures are not independent entities, but instead represent a cumulative effect of agglomerated hairpin structures (several at high Re and only one or two at low Re_θ). These structures have been the subject of several investigations, and it is now widely accepted that they are significant to the dynamics of the boundary layer turbulence.

The large scale, outer layer motions are important to the entrainment of irrotational freestream fluid into the boundary layer. The fact that entrainment of irrotational fluid into the boundary layer by viscous dissipation alone could not account for the observed self-preserved development of many turbulent shear flows was first highlighted by Bevilaqua and Lykoudis [1977]. In this sense, the outer layer structures of the boundary layer are similar to those found in jets and planar mixing layers. The importance of these structures to the whole of the boundary layer was further demonstrated by Brown and Thomas [1977]. Correlations between the fluctuating wall shear stress (measured with a hot-film probe) and the fluctuating streamwise velocity at a point in the outer layer (measured with a hot-wire) were made in a boundary layer with $Re_\theta = 10160$. By conditionally sampling the signals to isolate intervals in which a large scale structure was present, it was found that the correlation levels obtained when a structure was present were much higher than those encountered in the unconditional correlation. Further, the shear stress displayed large amplitude positive fluctuations during the presence of a structure. Although the large scale structures could not be inferred the direct cause of the wall shear fluctuations, the events responsible for the fluctuations are clearly related to the passage of large scale structures.

The conditionally-sampled hot-wire measurements of Kovasznay et al. [1970] in a boundary layer with $Re_\theta \approx 2750$ did much in the way of establishing the main characteristics of the large scale structures of the outer layer. The structures were found to have a streamwise-to-spanwise aspect ratio of about 2:1, and a streamwise extent of order δ. The structures were found to convect at a velocity slightly below that of the freestream, so that the irrotational fluid of the freestream must ride up and over the structures. Indeed, the resulting shear layer formed on the upstream edge of the structures has been an often cited property of the large scale structures [Robinson, 1991]. The normal velocity component was found to be directed away from the wall within the structures and towards the wall in the potential valleys before and after the structures. However, near the upstream edge of the structure, the irrotational fluid was seen to ride up and over the structure as mentioned previously. The conditionally sampled hot-wire measurements of Hedley and Keffer [1974] at $Re_\theta = 9700$ added to this picture. Consistent with the idea that the irrotational fluid upstream of the large scale structure must navigate over the structure, intense gradients were found near the upstream edge of the structures. At the downstream edge of the structures, the higher velocity of the irrotational fluid relative to the structure gave rise to less intense gradients.

Using simultaneous smoke visualizations and hot-wire measurements in boundary layers with Re_θ of 1000 and 4000, Falco [1977] proposed the presence of 'typical eddies' in the outer layer in addition to the large scale structures. The eddies are thought to be formed on the upstream edge of the large scale structures, with the high shear region at the interface of the large scale structures presumably serving as the vorticity source. The motions identified as typical eddies were shown to be a source of significant Reynolds stress in the outer portions of the boundary layer. The scale of the typical eddies decreases significantly with increasing Reynolds number. As a result, the disparity between the typical eddy scale and the scale of the large scale structures (which universally scale with δ) would increase with Reynolds number. Thus it seems unlikely that the typical eddies would remain a strong source of Reynolds stress in the outer layer at high Reynolds number.

1.1.2. Compressible Case

The current knowledge of coherent structures in compressible turbulent boundary layers is much more limited than that for the incompressible case. While the several different types of coherent structures discussed above are known to populate the incompressible turbulent boundary layer, studies of coherent structures in high Reynolds number, compressible, turbulent boundary layers have been confined to the δ-scale motions of the outer layer. As discussed by Spina and Smits [1987], the reason for this is a lack of resolution, both spatially and temporally. For supersonic boundary layers, the region characterized by significant bursting is confined very close to the boundary. Further, the time-scale resolution required to study the bursting process, $10\upsilon/u_\tau^2$, is much smaller than that obtainable with common experimental techniques. The review of past work concerning coherent structures in compressible boundary layers presented here is drawn largely from the similar discussions of Spina and Smits [1987], Spina et al. [1991], and Spina et al. [1994].

Early visual evidence of coherent outer-layer structures in compressible turbulent boundary layers was provided by the shadowgraphs of James [1958] of the flow over axisymmetric bodies of revolution at $M_\infty = 3.1$, the shadowgraphs and Mach-Zender interferometry images of Seiff and Short of the $M_\infty = 3.5$ flow over an axisymmetric body, the schlieren photographs of Deckker and Weekes [1976] and Deckker [1980] of the subsonic boundary layer in a duct just after the passage of shock waves of different strengths (reproduced by Head and Bandyopadhyay [1981]), and the shadowgraphs presented by Van Dyke [1982] (reproduced by Spina and Smits [1987]) of the $M_\infty = 1.8$, 2.5 flows over axisymmetric bodies. In these pictures, downstream-inclined structures which span the majority of the boundary layer thickness are present at angles of approximately 45°. Visualizations of outer layer structures in two-dimensional boundary layers with the shadowgraph or schlieren technique are hampered by the inherent spanwise integration in the standard configuration where the light volume passes through the test section in spanwise direction. This is especially troublesome given the limited spanwise extent of the structures (relative to, say, the nominally two-dimensional rollers of the weakly compressible mixing layer) and the large range of scales of turbulent motions present in these high Reynolds number flows.

Despite these difficulties, Smith and Smits [1988] were able to track the convection of large outer-layer structures with the schlieren technique used in conjunction with a high-framing-rate camera in an $M_\infty = 3.0$, $Re_\theta = 15000$ boundary layer. Again, downstream-inclined structures in the visual form of 'fronts' were present. Structures having both positive and negative density gradients in the upstream direction were visualized. The positive gradient structures were found to be inclined to the wall at approximately 30°-50°, while the negative gradient structures were inclined to the wall at approximately 70°. The negative structures were found to be less coherent than the positive gradient structures, requiring a less severe knife edge setting for detection. The positive gradient structures indicate an interface with low-density boundary layer fluid downstream of high-density freestream fluid. In conjunction with the above discussion of large scale structure characteristics in incompressible boundary layers, it is likely that the positive gradient structures can be identified with the intense gradients at the upstream edge of large scale structures and negative gradient structures can be identified with the less intense gradients at the downstream edge of the large scale structures. The gradient events identified by Smith and Smits [1988] are similar to those found by Chen and Blackwelder [1978] and Cheng and Ng [1982] in heated-wall incompressible boundary layers, where the low density fluid was replaced with high temperature fluid and vice versa. Quantitative information concerning the convection of the gradient structures was obtained from the high-speed film. The convection velocities of individual structures were found to be centered around $0.9U_\infty$. This study established that the outer-layer structures of high Reynolds number compressible boundary layers are qualitatively similar to those observed in incompressible cases.

Quantitative measurements pertaining to the large outer layer structures have typically been investigated with space-time correlations of hot-wire signals. Owen and Hortsman [1972] used such measurements with streamwise wire separations in a hypersonic boundary layer ($M_\infty = 7.2$, $Re_\theta = 5800\text{-}12000$) to place the mean convection velocity at $0.8U_\infty$ in the outer layer. Evidence of structures spanning the entire boundary layer was found in the cross-correlations obtained by fixing one wire at $y/\delta = 0.06$ and traversing a second wire vertically. Robinson [1986] performed similar experiments in an $M_\infty = 2.9$, $Re_\theta = 15000$ boundary layer, fixing the lower wire at $y/\delta = 0.02$. Significant correlation levels at large vertical spacings again indicate the presence of large scale structures spanning the entire boundary layer. Isocorrelations and structure angles were similar to those obtained by Spina and Smits [1987] and Smits et al. [1991].

Spina and Smits [1987] obtained similar cross-correlations of hot-wire signals, but traversed both wires vertically through the boundary layer at a fixed separation instead of fixing one wire at the wall. Angles of inclination of the large scale structures were determined based on the average velocity at the elevation of the wires. The angles were seen to be essentially constant at approximately 45° for $y/\delta \approx 0.2$-0.9 (with smaller angles below this region, and larger values above). Instantaneous structure angles obtained by conditionally sampling the hot-wire signals compared very well to the average structure angles, with a standard deviation of approximately 20° throughout most of the boundary layer. This suggests that the VITA technique was successful in capturing the 'sloping gradient' structures. Conditionally sampled cross-correlations between the fluctuating wall pressure and fluctuating mass flux from a mobile hot-wire indicated that the large scale structures remain coherent for a streamwise distance of at least 1.5δ. Appreciable correlations between the pressure fluctuations at the wall and mass flux fluctuations in the outer layer also suggest that the passage of the outer layer structures has an effect on the inner layer. By introducing a spanwise separation between the pressure transducer and the hot-wire, it was determined that the large scale structures were of very limited spanwise extent. These results were found not to contradict the proposal by Head and Bandyopadhyay [1981] that the boundary layer is populated by a hierarchy of hairpin loop structures.

In a further study of the same boundary layer, Spina et al. [1991] utilized streamwise, spanwise, and vertical wire separations to study the convective velocities, spatial extent, and orientation of the large scale structures of the outer layer. Correlations with streamwise separations showed the convection velocity to be approximately constant and equal to $0.9U_\infty$ across most of the boundary layer. By invoking Taylor's hypothesis, the field associated with the average large scale structure was constructed by superimposing the correlation fields obtained with vertical separations at various y/δ onto the mean structure shape (obtained from the structure angle data at various y/δ). The resulting field shows the streamwise extent of the inclined structures to be on the order of δ, with characteristics similar to the isocorrelations of Robinson [1986] in compressible flow and Kovasznay et al. [1970] in incompressible flow. These findings further illustrate the similarity of the outer layer structures for compressible and incompressible boundary layers. Correlations at various spanwise separations showed the spanwise extent of the large scale structures to be slightly less than the vertical extent. Further, the isocorrelation contours constructed from the spanwise correlations showed the spanwise extent of the structures to increase with distance from the boundary.

In order to isolate the large scale events, the hot-wire signals were conditionally sampled, it having been suggested by Spina and Smits [1987] that positive VITA events could be identified with the positive gradient motions (upstream edge of a large scale structure) visualized by Smith and Smits [1988] with the schlieren technique. In a manner similar to the construction of the isocorrelations from the two-point correlations, the two-dimensional velocity field associated with a positive gradient structure in a frame of reference convecting with the structure was constructed. The streamwise velocity was calculated from the measured streamwise mass flux with the Strong Reynolds Analogy. The resulting field illustrates that there is a region of significant spanwise vorticity (with the sense of rotation expected from the mean shear) within the large scale bulges present in the outer layer of the compressible boundary layer. This suggests the outer layer bulges are active participants in the dynamics of the boundary layer (especially with regards to the entrainment of freestream fluid) and not just passive flow features that lend themselves to visualization. Again, as highlighted by Spina et al. [1991], the resulting field is very similar to those constructed for outer layer turbulent bulges in incompressible boundary layers (Kovasznay et al. [1970], Blackwelder and Kovasznay [1972], Brown and Thomas [1977], and Falco [1977]). The importance of the large scale bulges to the dynamics of the boundary layer was further demonstrated by the fact that approximately 40% of the cumulatively summed shear product $[(\rho u)'v']$ at the surveyed locations occurred in time windows containing the passage of large scale structures, although the qualifying events were present less than 25% of the time.

Despite the similarities of the outer-layer, δ-scale structures in incompressible and compressible turbulent boundary layers cited above, the direct comparison of results obtained in Mach 0.1 ($Re_\theta = 5000$) and Mach 2.9 ($Re_\theta = 80000$) turbulent boundary layers by Smits et al. [1989] suggests that significant differences do exist. Isocorrelation curves constructed from cross-correlations showed the streamwise length scale (nondimensionalized with the outer layer length scale, δ) associated with the subsonic outer layer structures to be approximately twice that found in the supersonic case. The spanwise length scales associated with the structures were found to be essentially the same for both cases. The subsonic structures were found to convect at lower velocities ($0.8U_\infty$) than their supersonic counterparts ($0.9U_\infty$). Further, the subsonic structures were found to lean forward towards the boundary more than the supersonic structures. Joint probability distributions of normal velocity fluctuations and streamwise fluctuations (velocity for the subsonic case; mass flux for the supersonic case) seem to suggest sharp differences, with the fluctuations associated with the incompressible structure being more evenly distributed through the boundary layer than those associated with the compressible structures, which are confined to lower elevations in the boundary layer. However, as discussed by Smits et al. [1989], when interpreting these results it should be kept in mind that the compared flows have a significant Reynolds number difference in addition to the Mach number difference.

Planar imaging techniques are being employed with increasing frequency for the purpose of investigating the turbulence structure of compressible boundary layers. Smith et al. [1989] utilized UV Rayleigh scattering to obtain planar visualizations which clearly demonstrate the outer layer structures. Similar Rayleigh scattering techniques are employed in this investigation. As was done in the current study [Arnette et al., 1993a], Cogne et al. [1993] and Forkey et al. [1993] have utilized a double-pulsed Nd:YAG laser to study the evolution of the large scale structures in compressible boundary layers over short time durations. Similar double-pulse visualizations were employed by Elliott et al. [1993a] to study the evolution of large scale structures in compressible mixing layers.

1.2. Effect of Convex Curvature on the Turbulent Boundary Layer

Few boundary layers found in applications are of the flat-plate, zero pressure gradient variety. As a result, knowledge of perturbed boundary layers is of prime importance. Unfortunately, boundary layer response to perturbations or 'extra rates of strain' as defined by Bradshaw [1974] is a highly nonlinear phenomenon. As such, the effect of multiple perturbations is not the simple summation of the effects of the individual perturbations. This makes the investigation of both singly-perturbed flows and flows with multiple perturbations necessary.

1.2.1. Incompressible Case

Longitudinal convex streamline curvature (convex implying that the flow is turned away from itself) has been known to be 'stabilizing' for some time. Smits et al. [1979] showed that for incompressible turbulent boundary layers, sharp differences exist for the effects of strong convex ($\delta/R \approx 0.2$) and strong concave curvature. While the boundary layer subjected to concave curvature appeared to be governed largely by the formation of longitudinal Taylor-Gortler vortices and the associated amplification of the Reynolds shear stress and turbulence intensities, the boundary layer subjected to 30° of convex curvature displayed sharp decreases in the Reynolds shear stress and turbulence intensities within the layer. Turbulent transport velocities (based on ratios of triple products of velocity fluctuations) for Reynolds shear stress ($-\overline{uv}$) and turbulent kinetic energy (q^2) were seen to decrease for the convex curvature case. Since such triple products are determined mainly by the large scale motions of the boundary layer, this gave a strong indication that the convex curvature 'virtually destroyed the large eddy structure'. As discussed by the authors, this was not altogether unexpected since the ratio of the extra strain rate to the primary strain rate, $(\partial V/\partial x)/(\partial U/\partial y)$, is greatest in the outer layer, and the effects of the extra strain rates should vary directly with this ratio. A stress 'bore' near the wall, attributed to an increase in the generation term $\overline{vv}\ \partial U/\partial y$ near the wall, appears after the curvature. The recovery of the boundary layer on the flat surface downstream of the curvature is then characterized by the diffusion of the stress bore to the outer portions of the layer. Although the Reynolds shear stress and turbulence intensities overshoot the self-preserving values in the recovery, nondimensionalized shear stress parameters recover much more quickly. Since the shear stress can be associated mainly with large scale motions (similar to the turbulent kinetic energy), a destruction of turbulence present upstream of the curvature and subsequent re-creation of similar turbulence is suggested, as opposed to an alteration of the turbulence structure by the curvature effects.

Gillis and Johnston [1980] obtained similar results for a boundary layer subjected to 90° of milder curvature ($\delta/R \sim 0.09$). Longitudinal pressure gradients associated with the curvature were eliminated by varying the cross-sectional area of the test section. The large bore near the wall was again found in the shear stress and turbulent kinetic energy profiles soon after the application of the surface curvature, with a subsequent slow diffusion of the bore to the outer portions of the layer. Also similar to Smits et al. [1979], profiles of shear stress and turbulence intensity were much slower to recover than the parameter $\overline{uv}/q^2$, which is largely a reflection of the large scale, coherent motions.

Alving et al. [1990] studied the recovery process on a flat surface for a length of $90\delta_0$ after the boundary layer had been subjected to 90° of convex curvature ($\delta/R = 0.08$). The extended distance after the curvature for which measurements were acquired resulted in a more complete picture of the incompressible boundary layer's recovery. The relaxation behavior of the skin friction and the mean velocity profile was monotonic, with rapid development toward the unperturbed state confined to about the first $10\delta_0$ downstream of the curvature. The fact that the mean velocity profile of Gillis and Johnston [1983] displayed a much more protracted evolution is attributed to differences in pressure gradient effects. The turbulence, however, was seen to recover in three stages and had not fully recovered at the last measurement station. The first stage was similar to that seen in the previously cited studies, where a bore of elevated stress levels (for all normal stresses and the shear stress) appeared near the wall and subsequently diffused to the outer portions of the boundary layer. Elevated transport velocities were found at the edge of the bore, contributing to its diffusion. The bore had filled the entire boundary layer by $30\delta_0$ downstream of the end of the curvature, but the stress levels continued to rise beyond their self-preserving levels at this point. In the final stage of recovery, the stress levels finally began to gradually decline towards their self-preserving levels. However, at the last measurement station, the stress levels were still well above the self-preserving levels and the ratios of the

Reynolds stresses were different from those found upstream of the curvature. These results suggested that the large-scale structures of the boundary layer were reorganized into a new, stable state different than that found upstream of the curvature.

At the exit of the curvature, turbulence spectra displayed lower levels at low frequencies relative to upstream of the curvature, implying the curvature has a dampening effect on the large scale structures. Space-time correlations of streamwise-separated hot-wire signals were used to infer details about the evolution of the large scale structures. Surprisingly, despite the collapse of the Reynolds stresses in the outer portions of the boundary layer after exiting the curved region, the structure angles before and after the curvature were essentially the same. However, the low Reynolds stress levels demonstrate that the structures are much weaker than those of the unperturbed boundary layer. This was further indicated by lower correlation levels downstream of the curvature than were encountered upstream, and the fact that no entrainment of freestream mass occurred for the first $12\delta_0$ of the recovery.

1.2.2. Compressible Case

Upon entering an expansion region, the compressible boundary layer encounters stabilizing convex streamline curvature, a favorable streamwise pressure gradient ($\partial p/\partial s < 0$, where s is the streamwise coordinate), a normal pressure gradient ($\partial p/\partial n > 0$, where n is the coordinate normal to the surface and increases away from the surface), and bulk dilatation ($\nabla \bullet \underline{U} > 0$, i.e. the volume of a fluid element increases through the expansion region). Extra rates of strain are introduced by the expansion, namely $\partial u/\partial x$, $\partial v/\partial y$, and $\partial v/\partial x$ in the coordinate system of Fig. 2. As mentioned previously, this flowfield has been the subject of few investigations.

Thomann [1968] isolated the effect of streamline curvature on the rate of heat transfer in a supersonic, turbulent boundary layer ($M_\infty = 2.5$) by placing appropriately shaped bodies in the freestream above convex and concave surfaces to eliminate pressure gradients. When the boundary layer was subjected to 20° of convex curvature, an approximate 20% decrease in the wall heat transfer rate was sustained. This highlights the general similarity of the effect of convex curvature on compressible boundary layers to the incompressible case. The decrease in heat transfer rate was associated with a decrease in turbulent mixing between the boundary layer and the freestream, confirming a stabilizing effect of convex curvature.

Dussauge and Gaviglio [1987] investigated the effect of a 12° centered expansion on an $M_\infty = 1.76$ boundary layer (ahead of the expansion, $\delta_0 = 10$ mm, $Re_\theta = 5000$). In addition to mean and turbulence measurements, an analysis based on Rapid Distortion Theory was performed to isolate the effect of the bulk dilatation encountered in the expansion on the evolution of the boundary layer. Mean velocity profiles downstream of the expansion region initially displayed a thick sublayer region possessing a larger normal gradient of mean streamwise velocity ($\partial U/\partial n$ in the streamwise-normal coordinate system of Fig. 2) than were found in the equilibrium profiles, with no apparent logarithmic region. After approximately $9\delta_0$, a logarithmic region reappeared. The calculations indicated that the decreases in streamwise turbulence intensity sustained through the expansion were primarily due to bulk dilatation, although near the wall the decreases in turbulence intensity were not reproduced well by the calculations based on the dilatation effects alone. After the expansion, the turbulence intensity near the wall ($n/\delta < 0.2$) is initially very low relative to the incoming levels. For $n/\delta > 0.25$, turbulence intensities decreased slightly with increasing distance from the wall and the deviation between the pre-expansion and post-expansion intensities decreases with increasing distance from the wall.

Downstream measurements showed the near-wall region to reestablish turbulence intensities comparable to the pre-expansion levels much more quickly than the outer portions of the boundary layer, where the evolution was very slow. This is intuitive; since the turbulence production is confined to the near-wall region of the boundary layer where there are significant mean gradients, the near-wall region is quicker to recover from the perturbation. In contrast, the outer portions of the boundary layer are essentially void of production and governed by diffusion and dissipative processes. Neither of the latter two processes would be expected to have significant direct effects on the large scale motions of the outer layer. Another line of reasoning arises from the relative scales which populate the near-wall and outer portions of the boundary layer. The small scale rotational motions of the near-wall region might be more susceptible to 'quenching' by bulk dilatation than the large scale motions of the outer region (i.e. if a small scale motion is idealized as a small vortex and viscous effects are neglected, conservation of angular momentum dictates that the increase in vortex size brought on by bulk dilatation will decrease the vorticity of the motion). Conversely, the larger scale motions of the outer portions of the boundary layer may be less susceptible to such an effect.

The rapid recovery of the region near the wall led Dussauge and Gaviglio [1987] to propose that a new internal layer is formed downstream of the expansion, and that the incoming boundary layer had been relaminarized. Narasimha and Sreenivasan [1973] define a relaminarized boundary layer as one in which the Reynolds stresses have become of negligible importance to the mean flow. Relaminarization can occur when a turbulent boundary layer is subjected to a large, favorable pressure gradient. For compressible turbulent boundary layers that pass through an expansion fan, Narasimha and Viswanath [1975] suggest that relaminarization occurs for $\Delta p/\tau_0$ greater than approximately 70, where Δp is the pressure difference across the expansion and τ_0 is the wall shear stress just upstream of the expansion.

Smith and Smits [1991] investigated the expansion of an $M_\infty = 2.84$ ($\delta_0 = 26$ mm, $Re_\theta = 77600$) turbulent boundary layer through a 20° centered expansion region. Mean and turbulence profiles were measured $1\delta_0$ ahead of the expansion fan and $3.5\delta_0$ downstream of the expansion corner. Similar to the results of Dussauge and Gaviglio [1987], the mean velocity profile did not possess a logarithmic region at the survey location downstream of the expansion fan. Turbulence measurements indicated that caution should be used in using the term "relaminarization" to describe these flows, as the profiles of mass flux fluctuations were essentially unchanged between the two survey locations. However, the streamwise velocity fluctuations and longitudinal normal Reynolds stress were significantly decreased across the expansion region. Thus the density fluctuations must comprise a more significant part of the mass flux fluctuations downstream of the expansion region. Calculations similar to those of Dussauge and Gaviglio [1987], based on Rapid Distortion Theory, were performed and it was again found that the dilatation was mainly responsible for the lower turbulence levels after the expansion region.

The effects of mean compression or dilatation on the turbulence of supersonic boundary layers was considered by Bradshaw [1974]. A method of incorporating corrections for such effects in standard computations was offered in light of the evidence that such effects have important ramifications for the turbulence when present. As discussed by Bradshaw, a lack of fundamental understanding of such effects remains a fundamental problem. However, as mentioned previously, such effects are intuitively connected to the principle of conservation of angular momentum in the presence of the distortion of an element of mass. When a fluid element passes through a two-dimensional expansion fan, its cross-sectional area in the X-Y, X-Z, and Y-Z planes increases due to the positive $\partial U/\partial x$ and negative $\partial V/\partial y$ (referenced to the coordinate system of Fig. 2). As a result, all three components of vorticity would be expected to be damped, resulting in an overall stabilization.

The present study represents part of an ongoing multi-faceted experimental investigation of high Reynolds number, compressible turbulent boundary layers (Mach 2 and 3) subjected to 7° and 14° centered and gradual expansions (4 cases). For the Mach 3 incoming flow, the flat plate boundary layer and four expanded boundary layers have been thoroughly interrogated with measurements of the fluctuating surface pressures, instantaneous filtered Rayleigh scattering visualizations (streamwise, spanwise, and plan views), and double-pulse visualizations (streamwise view). These results are presented in the Results and Discussion section.

2. Experimental Procedure

All of the experiments were performed at the Aeronautical and Astronautical Research Laboratory at The Ohio State University. The blow-down supersonic wind tunnel has been employed previously in a dual-stream configuration to investigate the compressible mixing layer. For the current investigation of compressible, turbulent boundary layers subjected to expansion regions, only the supersonic stream is utilized. The boundary layer develops on the flat splitter plate (which separates the two streams of the compressible mixing layer) and the expansion models are fixed to a flat plate model which replaces the interchangeable splitter plate tip. The top surface of the splitter plate is at the lateral center of the test section, so that the incoming supersonic flow occupies a passage 152.4 mm wide by 76.2 mm high. After the expansion regions, the model surfaces diverge away from the expansion corner towards the bottom of the test section, which has a total cross section of 152.4 mm wide by 152.4 mm high. Thus only half of the available test section is utilized at the onset of the expansion region. This tunnel configuration is illustrated in Fig. 1 for a centered expansion model. The coordinate system to be used is presented in Fig. 2. The streamwise coordinate, s, is measured along the surface of the expansion models. The origin (s = 0) occurs at the beginning of the expansion regions. The normal coordinate, n, is measured perpendicular to the model surface. At the model surface, n = 0.

Two four-stage compressors supply air to the system, which has a storage capacity of 42.5 m^3 at pressures up to 16.4 MPa. Supply air is introduced to the stagnation chamber through an array of radial inlet holes. The stagnation chamber pressure is maintained to within ±1% of the set point. For these experiments, the stagnation pressure was 1.14 MPa (11.2 atm), and the stagnation temperature was nominally 280 K. A flow straightening section consisting of a perforated plate, a honeycomb section 10.1 cm in length, and a stainless steel screen (with 3.8 cm gaps between consecutive sections) is present near the exit of the stagnation chamber. To investigate the effect of upstream conditions on the structure of the turbulent boundary layer, some experiments were performed with the flow straightening section removed.

Optical access to the tunnel test section is provided by a window in each bounding surface. Each side wall has an interchangeable window and blank panel which give a total possible viewing area 450 mm long by 80 mm high. The top window is 30 mm wide by 300 mm long.

Previous LDV measurements made by Samimy et al. [1992] in conjunction with the investigation of compressible mixing layers in this facility showed the freestream turbulence intensities in the Mach 3 freestream to be less than 3%. The incoming boundary layer was also characterized and shown to be a fully-developed turbulent boundary layer with $M_\infty = 3.01$, $U_\infty \approx 600$ m/s, $\delta = 9.2$ mm, $Re_\theta = 24700$, and $\theta = 0.37$ mm at the end of the splitter plate. This downstream location coincides with the start of the expansion region for the four expansion models of this study.

Photographs of the four expansion models are presented in Figs. 3 and 4. A flat section, which is connected to the centered expansion models in Figs. 3 and 4, was designed to serve as a transition between the splitter plate and the expansion models. Schematics of the two-dimensional models are given in Fig. 5. As depicted in Fig. 5b, the radius of curvature for both gradual expansion models is 450 mm, giving $R/\delta_0 \approx 50$. As far as the authors are aware, no measurements have been made in a compressible, turbulent boundary layer subjected to gradual convex curvature.

The holes present in the models (Figs, 3 and 4) were used to insert a flush-mounted transducer plug, which is depicted schematically in Fig. 6. Both of the 7° expansion models have three plug locations and both 14° expansion models have two plug locations. The transducer plug was equipped with four high-frequency Endevco transducers (Model 8514-10) mounted flush with the top surface of the transducer plug. The transducers consist of a diaphragm (diameter of approximately 1.02 mm) with an adjoined Wheatstone bridge above a cavity. Tunnel experiments indicated that the resonance frequency of the transducer diaphragm/cavity is approximately 125 kHz. Corcos [1963] demonstrated that the response of such a transducer is valid up to a dimensionless frequency of $U_c/\pi d$, where d is the transducer diameter. Taking U_c as $0.9U_\infty$ where $U_\infty \approx 600$ m/s from the previous LDV measurements for the Mach 3 flow, the maximum valid frequency for these transducers is approximately 170 kHz. Unfortunately, the resonance frequency at 125 kHz is the limiting factor.

As depicted in Fig. 6, the transducers were spaced unevenly in the transducer plug to allow coherence and space-time correlation information to be acquired for different transducer separations. The plug was made circular so that the row of four transducers could be rotated to any desired orientation. To date, only the streamwise and spanwise orientations have been employed. For streamwise correlations, the location of the first transducer is cited as the streamwise location for the measurement. The downstream transducer can be located by adding the cited transducer separation to the position of the first transducer.

The differential transducers were powered by an Ectron signal conditioner (Model 563F) which provided 10V excitation to the transducers. The signal conditioner is quoted as having a bandwidth of 200 kHz. The output of each of the four transducers was fed to a separate amplifier of the signal conditioner. The amplifier gains were set so that the output of the transducers was matched to the ±10V range of the employed A/D card, thereby maximizing the dynamic range of the measurement. The data was acquired with a Datel 12-bit A/D converter (Model PC414-A2) having five available input channels and the accompanying Datel software (PC414-SET) and stored on a 486 PC. The converter is equipped with Simultaneous Sample and Hold which allows all of the inputs to be sampled simultaneously, thereby preventing any artificial time shifts between the data of different channels. Four-channel data was acquired at a rate of 250 kHz/channel. This system has a static sensitivity of 60 Pa/bit with A/D fluctuations of approximately ±1 bit. To eliminate noise at low frequencies and any ill effects due to transducer resonance, the data were digitally filtered with a high-pass cutoff of 1.0 kHz and a low-pass cutoff of 60.0 kHz. The digital filtering and all other data processing was done with the commercially-available MATLAB software. Power spectral analysis were performed with 100 sets of 1024 data points and correlations were performed with 50 sets of 1024 data points. More details concerning transducer calibration, digital filtering, and data reduction can be found in Dawson [1993].

Inviscid calculations indicate that the expansion waves reflected downward when the primary expansion waves intersect the top wall of the test section will intersect the 7° centered expansion model near the very end of the model, intersect the 7° gradual expansion model approximately 80 mm downstream of the last plug location, and not intersect the two 14° expansion models. Thus the reflected waves should not affect the results.

In addition to the four expansion models, a flat plate model was constructed. This was done to allow detailed investigations of the non-perturbed boundary layer. With the expansion models installed, easy optical access is available for only approximately 3 cm of the incoming boundary layer. The flat plate model extends the incoming boundary layer through the length of the text section. This model was designed with a flush-mounted window (20 mm spanwise by 310 mm streamwise) on the centerline to cut down on the reflections encountered when the laser sheet intersects the boundary.

Upon the installation of any model, schlieren images were acquired to insure that no non-uniformities were present. The schlieren light source is a Xenon 437B Nanopulser which provides 5 mJ over a pulse duration of 10 ns, which is sufficient to freeze the flow field. Schlieren images were collected with an ITT intensified CCD camera and stored on S-VHS. The spanwise and streamwise distributions of the mean static pressures at the model surfaces were monitored via static pressure taps in the models and a Scanivalve 12-port switching unit. The streamwise measurements were made along a line offset 19.1 mm from tunnel center so as to not interfere with the transducer plug locations. The distance between adjacent static taps is 12.7 mm.

Upon expanding in the nozzle, small particles of condensed water are formed from the small amount of water vapor left in the supply air after being passed through the dessicant dryers. The system has two dryers; while one is in use, the other is being regenerated by heating. This condensation forms a scalar transport marker in the freestream. The higher temperature in the boundary layer resulting from frictional heating prevents this condensation from forming within the boundary layer, so that the interface between potential, free stream fluid and turbulent, boundary layer fluid may be visualized. Similar visualizations of compressible boundary layers utilizing condensation have been acquired by Smith et al. [1989].

This scalar transport condensation has been used previously to visualize an $M_c = 0.86$ mixing layer in this facility [Elliott et al., 1992a]. The high sensitivity of the collected signal to the incident polarization direction in those experiments and in the present work suggests that the scattering falls near the Rayleigh regime. For the employed 532 nm illumination, this places the effective particle diameter on the order of 50 nm, suggesting that the particles are sufficiently small to accurately represent the features of the flow field.

The majority of the visualizations obtained in this study were acquired with the filtered Rayleigh scattering (FRS) technique, originally proposed by Miles et al. [1991]. The technique has been successfully applied in supersonic jets [Arnette et al., 1993b], compressible mixing layers [Elliott et al., 1992a], and supersonic turbulent boundary layers [Smith et al., 1989], and has been discussed in detail by Miles et al. [1991, 1992] and Elliott et al. [1992b, 1993b]. As a result, only a cursory treatment is given here. In the technique, an optical cell containing diatomic iodine vapor is used as a frequency-discriminating device. Miles et al. [1991] showed that diatomic iodine possesses electronic transitions that absorb the frequency-doubled 532 nm radiation of the Nd:YAG laser. The cumulative absorption of the iodine molecules forms a notch or band-reject filter in the transmission versus light frequency domain. The absorption profile of the filter can be modified by changing the thermodynamic state of the iodine vapor [Miles et al., 1991] or the composition of the gases in the cell [Elliott et al., 1993b].

Scattering from particles or molecules in the flow will possess a positive Doppler shift for appropriate laser sheet/camera arrangements. By using an injection-seeded, frequency-doubled Nd:YAG laser, the linewidth of the laser is narrow enough so that if the laser frequency is properly tuned, the absorption profile of the iodine vapor will absorb unwanted background reflections (which will be at the illuminating frequency), while passing Doppler shifted scattering from the flow onto the camera. For molecular Rayleigh scattering, large Doppler shifts are required to obtain sufficient frequency separation between the unshifted and shifted light to totally pass the shifted light (while suppressing unshifted background light) because of the large linewidths associated with molecular Rayleigh scattering. This is discussed in detail by Elliott et al. [1992b]. For the case of particle scattering, however, the linewidth of the scattered light is simply that of the illuminating laser. As a result, background elimination with no signal attenuation is more easily accomplished. This situation is depicted in Fig. 7. It should be mentioned that although the technique is used only for visualizations in this study, we have successfully extended FRS to the FPV technique capable of two-dimensional instantaneous velocity measurements and obtained measurements in the compressible mixing layer that are accurate to within ±8% [Elliott et al., 1994]. In addition, modifications to improve the FPV technique's accuracy to ±3% have been presented.

Several sheet orientations were employed for the instantaneous filtered Rayleigh scattering visualizations of this study. The optical arrangement for the streamwise and spanwise views are shown in Figs. 8a and 8b, respectively. For the plan view images, the rather unorthodox configuration shown in Fig. 9 was required. For the plan views, obtaining a frequency shift that sufficiently separated the scattering from the condensed particles from the background reflections required that the filter/camera be rotated forward approximately 45° from the spanwise-aligned axis of the laser sheet. In order to view the laser sheet, the cameral/filter obviously had to be elevated. For the flat plate, the camera was elevated approximately 35° above the plane of the laser sheet. For the expansion models, this angle was increased by approximately the expansion angle for that model as the width of the sheet was kept parallel to the surface and the camera was placed in nominally the same position (in the laboratory reference frame) for all of the experiments. The pulse duration of the employed Nd:YAG laser is 9 ns, which effectively freezes the flow field. In frequency-doubled mode, the Nd:YAG laser is capable of 660 mJ/pulse.

In addition to the single-pulsed filtered Rayleigh scattering images, double-pulsed images were acquired for streamwise views of the flat plate model and the centered expansion models. Our Nd:YAG laser has been equipped with the capability to provide two pulses for each lamp excitation by multiple Q switching, so that two light pulses with a controllable delay from approximately 15.0 μs to 200.0 μs can be obtained.

Correlations in two spatial dimensions were made between the initial and delayed images to obtain information about the large scale, outer layer structures. Because of both the strong reflections associated with solid model surfaces and the fact that the laser energy per pulse is much lower in double-pulse mode than in single pulse mode, it would be desirable to utilize the filtered Rayleigh scattering technique to acquire the double-pulse images. Unfortunately, when operated in double-pulse mode, the laser is not injection seeded. As a result, the linewidth of the laser is significantly greater than that obtained in single-pulse mode. This renders the molecular iodine filter useless. To overcome this obstacle, the two centered expansion models were equipped with centered, flush-mounted surface windows approximately 20 mm wide. The windows reduced the surface reflections enough to allow the acquisition of double-pulse images.

Images are collected with computer-controlled Princeton Instruments 14-bit ICCD cameras. The cameras are thermoelectrically cooled so as to allow sensitivities on the order of 10 to 100 counts/photon. The laser provides a TTL output for each pulse, which is fed to the pulse generator of the ICCD camera for synchronization. The 14-bit images are stored in digital format on the controlling 486 PC. The next image is not acquired until the previous image is stored in memory. This results in an imaging rate of approximately 0.5 Hz for full array images. Parts of the array can be disabled to improve the framing rate. However, all of the available framing rates result in consecutively acquired instantaneous images being totally uncorrelated to each other. Two such camera systems are available and were used in the double-pulse experiments. When operated in double-pulse mode, the Nd:YAG laser provides two outputs for camera synchronization. The camera controllers possess circuitry which allows the cameras to be wired such that each will wait until the other is ready to acquire an image (finished storing the previous image), and then the two cameras will acquire images at the next double-pulse from the laser.

3. Results and Discussion

3.1. Mean Static Pressures and Schlieren Visualizations

Instantaneous schlieren images of the flat plate, 7° centered expansion, and 14° centered expansion given in Figs. 10a, 10b, and 10c , respectively, show the general development of the flow fields (all obtained with a horizontal knife edge). The images show the freestream to be free of any strong, undesired waves. The flat plate images display the presence of forward-inclined large scale structures which span the entire boundary layer thickness, similar to those found by Smith and Smits [1988]. The boundary layer thickness is seen to increase across the expansion, more for the 14° case than the 7° case, which is associated with the decrease in density sustained across the expansion. A second more significant observation is the brightness of the boundary layers downstream of the expansion for the 7° and 14° cases relative to the incoming boundary layer ($s < 0$ mm). The density gradients associated with the expanded 7° boundary layer are clearly smaller than those found upstream of the expansion. To image the boundary layer downstream of the 14° expansion, a less severe knife edge setting was required. This is indicated by the relative brightness of the expansion fans for the 7° and 14° cases. The expansion fans would have similar brightness for similar knife edge settings. The smaller gradients downstream of the expansions is not an unexpected result. Thinking of the density gradient associated with the edge of a large scale structure as being proportional to $\Delta\rho_1 = \rho_f - \rho_s$, where ρ_f is the density of the freestream fluid adjacent to the structure and ρ_s is the density of the structure, $\Delta\rho_2 \approx (\rho_{\infty,2}/\rho_{\infty,1})\,\Delta\rho_1$ if the structure responds immediately to the change in density across the expansion region, resulting in a weaker gradient downstream of the expansion. In the other extreme, if the structure is slow to respond to the density change across the expansion and maintains its upstream density for at least some distance downstream of the expansion, $\Delta\rho_2 \approx (\rho_{\infty,2}/\rho_{\infty,1})\rho_f - \rho_s$, which would also result in a decreased gradient.

The mean static pressures at the wall are monitored via pressure taps in the model surfaces. The streamwise variation of the mean static pressure at the model surfaces is presented in Fig. 11. Spanwise measurements in the incoming boundary layer and downstream of each of the four expansion regions are presented in Fig. 12. A standard inviscid analysis based on an incoming Mach 3.0 free stream gives pressure ratios (p_2/p_1) of 0.56 for the 7° expansions and 0.30 for the 14° expansions. The same ratios based on the hypersonic similarity parameter, $K = M_\infty \alpha$ (where α is the turning angle in radians), in the limit of infinite Mach number gives values of 0.33 for the 14° expansion and 0.59 for the 7° expansions [Lu and Chung, 1992]. The measured pressure ratios were 0.53 for the 7° centered case, 0.60 for the 7° gradual case, 0.36 for the 14° centered case, and 0.41 for the 14° gradual case.

The correlation of Tetervin [1967] (as presented by Narasimha and Viswanath [1975]) was used to estimate the skin friction coefficient for the incoming boundary layer from incoming M_∞ and Re_θ, and the criterion of Narasimha and Viswanath [1975] that relaminarization occurs for $\Delta p/\tau_0 > 75$ was used to examine the possibility of relaminarization. For the 7° and 14° centered expansion cases, this method gives $\Delta p/\tau_0$ estimates of 48 and 76, respectively. Thus it appears that the only flow which falls near possible relaminarization is the 14° centered expansion. Although $\Delta p/\tau_0$ is the same for the two 14° expansion cases, relaminarization is sensitive to the magnitude of the favorable pressure gradient, not the pressure difference across the expansion region. As a result, the 14° gradual case is not considered to be close to relaminarization. Despite satisfying the published criterion for relaminarization, Smith and Smits [1991] caution against the use of the term "relaminarization" based on their measurements of mass flux fluctuations in an expanded boundary layer.

The streamwise development of the RMS surface pressure fluctuations normalized by the local mean static pressure is presented in Fig. 13. Downstream of the four expansion regions, the ratio never drops below the level encountered in the incoming flat plate boundary layer. For the two centered expansions, the ratio increases substantially just across the expansion region. This effect is more pronounced for the 14° case. With these exceptions, the ratio generally remains very similar to that encountered in the incoming boundary layer. This demonstrates that there are significant turbulent fluctuations downstream of the expansion region. This would seem to support the idea that the boundary layers downstream of the expansion regions are not relaminarized. However, within the context of the strict definition of relaminarization offered by Narisimha and Viswanath [1973] in which a relaminarized boundary layer is simply one in which the Reynolds stresses have ceased to be important to the mean flow, it is more difficult to comment on relaminarization. Nevertheless, all indications are that the four expanded boundary layers do not experience relaminarization.

3.2. Qualitative Filtered Rayleigh Scattering Visualizations

Streamwise and spanwise instantaneous filtered Rayleigh scattering visualizations were used to investigate the effect of the various expansion regions on the structural features of the incoming compressible turbulent boundary layer. Plan view visualizations showed elongated longitudinal structures to be a fairly robust feature of both the flat plate boundary layer and the boundary layers downstream of the various expansion regions. The main results of these visualizations have been presented previously by Arnette et al. [1993a].

3.2.1. Flat Plate Boundary Layer

Instantaneous schlieren images of the flat plate boundary layer obtained with a tighter view than that presented previously are given in Fig. 14. The images were obtained with a horizontal knife edge. Similar to other investigators, downstream-inclined fronts which can be associated with the large scale structures of the outer layer are clearly present.

Instantaneous streamwise FRS visualizations of the flat plate boundary layer are presented in Fig. 15. The flow direction in the images is right to left. In these and all other presented streamwise and spanwise visualizations, the added white lines indicate the position of the solid surface. The outer portions of the boundary layer are clearly dominated by the presence of large scale structures. Similar to the observations by Falco [1977] in the incompressible case, the large scale structures display the presence of smaller scale motions at their outer edges. However, these smaller motions are much too large to be identified with Falco's 'typical eddies' at the current Reynolds number ($Re_\theta \sim 25000$). As discussed by Smits et al. [1989], motions of this scale in compressible boundary layers must be considered to scale on outer layer variables.

Spanwise visualizations of the incoming boundary layer at a streamwise distance of 25 mm upstream of the location which corresponds to the beginning of the expansion regions (s = -25 mm) are presented in Fig. 16. In these and all other spanwise visualizations, the 0 mm mark corresponds to the tunnel centerline. The large δ-scale structures of the outer layer are clearly present, giving the top edge of the boundary layer a highly intermittent appearance. The structures are of limited spanwise extent.

3.2.2. Boundary Layer Downstream of the 7° Centered Expansion

Streamwise views of the 7° centered expansion region are presented in Fig. 17. Again, white lines have been superimposed on the images to indicate the position of the model surface. The large scale structures of the outer layer are seen to maintain their identity across the expansion region. Further, most of the large scale structures are of larger scale than those encountered in the incoming boundary layer. This is not surprising when the strong dilatation encountered across the expansion region is considered. Recognizing a large scale structure as a correlated mass of fluid, the decrease in density across the expansion would necessitate an increase in scale. Another observation from images such as those of Fig. 17 is that the structure angle (relative to the boundary downstream of the structure) appears to increase across the expansion region. A simple consideration of the kinematics associated with a large scale structure passing through the expansion region gives a possible explanation. Previous studies of compressible boundary layers [Spina et , 1987, Robinson, 1986, Smits et al., 1991] have shown that the large scale structures are inclined to the wall at an angle of approximately 45° across most of the boundary layer thickness. The forward boundary of an expansion region is inclined at 19.5° for a Mach 3.0 incoming flow. Although the forward boundary of the expansion region is inclined at larger angles closer to the surface because of the Mach number gradient across the boundary layer, Mach angles close to 45° (which corresponds to a Mach number of approximately 1.41) are confined very close to the surface. Therefore, the expansion region is inclined more to the wall than the large scale structures. As a result, the bottom of the large scale structure will encounter the expansion region before the top of the structure. In addition, the expansion fan diverges away from the corner, so that the bottom of the structure will be accelerated through the expansion region before the top of the structure. The net result of these two effects would be to displace the bottom of the structure further downstream relative to the top of the structure, which would be observed as an increase in the structure angle across the expansion region.

Streamwise images acquired further downstream of the 7° centered expansion are presented in Fig. 18. At this location, the boundary layer has taken on a fuller appearance than that encountered just downstream of the expansion corner. This trend is more apparent in the spanwise visualizations presented below. Although large scale structures are seen to corrugate the top interface of the boundary layer, the presence of smaller scale motions makes their presence less obvious.

Spanwise views which illustrate the development of the boundary layer downstream of the 7° centered expansion are presented in Figs. 19-21. At $s/\delta_0 = 4.2$ downstream of the expansion corner (Fig. 19), the boundary layer displays two major differences with the spanwise views obtained in the flat plate boundary layer (Fig. 16). First, the large scale structures at this location have increased in vertical scale relative to the flat plate case. Secondly, the wells of potential fluid from the freestream (which is marked by condensation) are seen to penetrate deeper into the boundary layer than upstream of the expansion corner. This appearance is due in part to the increase in scale of the large scale structures of the outer layer. However, it also appears that the smaller scale motions have been quenched by the expansion region. At $s/\delta_0 = 13.9$ (Fig. 20) and 24.3 (Fig. 21), the boundary layer is seen to recover its fullness. At the last location, it appears that the boundary layer is less intermittent in appearance than even the flat plate boundary layer. The cited quenching of the small scales is why the presence of the large scale structures in the streamwise visualizations is more obvious just downstream of the expansion than further downstream. Although the small scale motions are quenched by the expansion region, they recover and 'fill out' the boundary layer further downstream.

3.2.3. Boundary Layer Downstream of the 7° Gradual Expansion

Streamwise views of the 7° gradual expansion region are presented in Fig. 22. Again, white lines have been superimposed on the images to indicate the contour of the gradual convex surface curvature. Similar images obtained further downstream of the expansion are presented in Fig. 23. Observations are similar to those put forth in conjunction with the streamwise views of the 7° centered expansion. In the expansion region, an increase in scale of the large scale structures combined with the quenching of the small scale motions gives rise to an increased visual dominance of the outer-layer structures relative to that encountered in the flat plate boundary layer. Further downstream, the reestablishment of small scale motions makes the large scale structure presence less obvious.

Spanwise views of the boundary layer downstream of the 7° gradual expansion are presented in Figs. 24-26. At $s/\delta_0 = 4.1$ (Fig. 23), which is still within the gradual expansion region, the boundary layer has assumed a more intermittent appearance, as discussed above. Further downstream at $s/\delta_0 = 14.1$ (Fig. 24) and 24.2 (Fig. 25), the boundary layer is seen to recover its fullness. The images at the latter two streamwise positions appear very similar to the spanwise visualizations of the flat plate boundary layer.

3.2.4. Boundary Layer Downstream of the 14° Centered Expansion

Streamwise views of the 14° centered expansion region are presented in Fig. 27. Clearly, the structures sustain a large increase in scale through the expansion. Further, several structures are seen to be essentially perpendicular to the surface downstream of the expansion corner. This dramatic increase in structure angle was quite common for this expansion case. The increases in scale and structure angle were most significant for this expansion case. If the increase in scale of the large scale structures is a dilatational effect and the increase in structure angle is a kinematical effect as discussed previously, both would be expected to be most significant for the 14° centered expansion. The increased clarity of the large scale structures due to the quenching of the small scale motions, which was discussed above in conjunction with other models, appears to be short-lived for the boundary layer downstream of the 14° centered expansion.

Another significant observation arises in conjunction with Fig. 27. Near the downstream edge of the images, occurrences of condensation brighter than that encountered in the freestream are seen just above the edge of the layer demarcated by the lack of condensation. This condensation, which is in excess of the scalar transport condensation present in the freestream, is thought to result from the transport of fluid originally present in the flat plate boundary layer away from the surface downstream of the expansion corner. As this fluid (which contains uncondensed water vapor) moves away from the wall and encounters colder temperatures, excess condensation is formed. Similar streamwise views obtained just downstream of the 14° centered expansion taken at another date are presented in Fig. 28. In Fig. 28, the appearance of the excess condensation appears to occur 10-20 mm further upstream than in Fig. 27. This is almost certainly a result of the varying water vapor content of the tunnel supply air, with moister supply air resulting in the onset of the condensation further upstream. Several images like those of Figs. 28a and 28b capture the transport of boundary layer fluid away from the wall, which presumably gives rise to the excess condensation. It should be noted that the excess condensation was never encountered for either of the 7° expansions.

Streamwise views further downstream of the 14° centered expansion are presented in Fig. 29. In these images the excess condensation has filled the imaged region above the boundary layer. The boundary layer has a very full, non-intermittent appearance. Several images, like those of Figs. 29c and 29d, capture the loss of boundary layer fluid to the excess condensation.

Spanwise views at three locations are presented in Figs. 30-32. At $s/\delta_0 = 2.1$ (Fig. 30), the spanwise views show the boundary layer to have evolved similar to the other cases just downstream of the expansion corner. The large scale structures have increased in vertical extent and the wells of potential fluid between the structures are seen to penetrate deep into the boundary layer. At $s/\delta_0 = 14.6$ (Fig. 31), the boundary layer appears very full. The excess condensation has filled approximately 30 mm above the boundary layer and the fueling of the condensation formation by the outward transport of boundary layer fluid is captured in the instantaneous images. At $s/\delta_0 = 22.1$ (Fig. 32), the boundary layer appears even less intermittent with little indication of large scale structures. The sidewall boundary layer is evident on the left edge of the images.

3.2.5. Boundary Layer Downstream of the 14° Gradual Expansion

Streamwise images of the 14° gradual expansion region are presented in Fig. 33. The gradual surface curvature begins at s = 0 mm and ends at s = 110 mm. Similar to the other models, the large scale structures are seen to increase in scale as they travel through the expansion region and the small scale motions are quenched by the expansion, leaving the large scale structures more visually accessible. The structure angle increases, although less dramatically than for the 14° centered expansion. It seems almost as if the large scale structures convect with no change in orientation, and it is the convex curvature of the surface alone that gives rise to the increase in structure angle.

Streamwise images acquired further downstream are presented in Fig. 34. The excess condensation is seen to form for this case as well as the 14° centered expansion. However, the new condensation appears further downstream of the end of the expansion region for this case than in the 14° centered expansion case. Again, the boundary layer appears very full and the excess condensation appears to be fueled by the transport of fluid originally in the boundary layer away from the wall.

Spanwise views at three locations are presented in Figs. 35-37. At $s/\delta_0 = 4.8$ (Fig. 35), which is approximately halfway through the gradual expansion region, the spanwise views appear similar to other cases with very large outer layer structures and a high degree of intermittency. At $s/\delta_0 = 14.8$ (Fig. 36), the excess condensation has filled a thin region above the boundary layer. The top interface of the boundary layer indicates the presence of large scale structures. At $s/\delta_0 = 27.6$ (Fig. 37), the boundary layer appears very full and the excess condensation has filled the imaged region above the boundary layer. The interaction of the boundary layer with those on the side wall has led to a spanwise nonuniform boundary layer thickness in some of the images.

The analysis of the FRS instantaneous images highlights several general trends. It seems that soon after the onset of the expansion region, and the associated dilatation effect, the small scale motions are quenched. Qualitatively, one can think in terms of the usual association of the small scale motions with fluctuating vorticity. It seems the conservation of angular momentum coupled with the increase in the volume of fluid elements due to the dilatation is enough to quench the small scale motions. This result seems to agree with the measurements of Dussauge and Gaviglio [1987] and Smith and Smits [1991], where the turbulent fluctuations near the wall (associated mainly with small scale motions) were found to be suppressed significantly relative to the incoming boundary layer. The result of the small scale quenching is an increased visual prominence of the large scale structures of the outer layer. The large scale structures both increase in scale and sustain an increase in structure angle across the expansion region. The former effect is thought to be caused by dilatation brought on by the expansion region. The latter is thought to result from the kinematics associated with the passage of a large scale structure through the expansion region.

The formation of the excess condensation is an interesting result in and of itself. This may cast light on the results of Thomann [1968], where a significant decrease in the heat transfer to the wall was measured for a Mach 2.5 boundary layer passed through 20° of convex curvature (although the streamwise pressure gradient was eliminated in Thomann's experiment, which is not done here). If some of the boundary layer fluid is transported away from the wall and forms a "buffer" layer between the boundary layer and the free stream, it is clear from simple proximity arguments that the ability of the boundary layer to transport low temperature free stream fluid to the wall will be decreased, which will result in decreased heat transfer. The decreased turbulence intensities known to exist in the expanded boundary layer would also account for a decrease in heat transfer rate at the wall.

3.2.6. Elongated Longitudinal Structures

This study is designed to investigate the effects of various expansion regions on compressible turbulent boundary layers, a flow field about which very little is known. However, when embarking upon a study of perturbed boundary layers, it must be kept in mind that our knowledge of equilibrium, compressible turbulent boundary layers is far from complete. Given this fact, and the fact that our incoming flat plate boundary layers will be probed extensively so that the effects of the various expansion regions can be identified, it is not at all surprising that new knowledge concerning flat plate compressible turbulent boundary layers will emerge from the current study.

A previously unreported structural feature was identified with the plan view FRS visualizations. The optical configuration is presented in Fig. 9. For all of the plan views, the laser sheet is parallel to the model surface. Figure 38 presents three instantaneous plan views obtained in the flat plate boundary layer with the laser sheet at an elevation of 4.5 mm ($n/\delta_0 = 0.50$). The flow direction is from upper right to lower left. The spanwise extent of the test section is indicated by the lines aligned in the streamwise direction. Two lines aligned in the spanwise direction have been superimposed and labeled with the appropriate positions to give a sense of scale. Similar to the streamwise and spanwise visualizations, the bright regions in the image indicate positions where the water condensation is present. Given the well-documented strong, negative correlation between temperature and streamwise velocity fluctuations in compressible turbulent boundary layers [Spina et al., 1994], these regions may be nominally thought of as high-velocity fluid. In Fig. 38, it is apparent that the regions containing condensation appear as elongated "streaks" nominally aligned in the streamwise direction. The term "streak" is used only to infer the large aspect ratio (streamwise to spanwise extent) associated with the structures. The term "elongated longitudinal structures" is used instead of "streak" because of the universal association of "streak" with the structures found near the wall in incompressible boundary layers. Further discussion of these structural features is given by Samimy et al. [1994].

Referring to Fig. 38 at $n/\delta_0 = 0.50$, the spanwise extent of the longitudinal structures is on the order of millimeters. This highlights a fundamental difference between these structures and the low speed streaks found in the inner-layer of incompressible boundary layers. The longitudinal structures visualized here are much larger than the inner-layer streaks of incompressible boundary layers. Although it is now known that the high speed streaks found adjacent to the low-speed streaks of incompressible boundary layers are wider and of a shorter streamwise extent than the low speed streaks [Robinson, 1991], the structures visualized here are of much larger scale. Secondly, the streaks in incompressible boundary layers exist only in the inner-layer very close to the surface. The structures visualized here are shown to exist for $0.5 < n/\delta_0 < 1.0$. Because of a lack of condensation particles closer to the wall, no comment can be made on the existence of the elongated longitudinal structures below $n/\delta_0 = 0.5$.

Figure 39 presents similar plan views in the flat plate boundary layer at n = 6.0 mm ($n/\delta_0 = 0.65$). At this elevation, the elongated longitudinal structures are again present. It appears that the spanwise scale of the structures is greater than that encountered at $n/\delta_0 = 0.50$. Figure 40 presents plan views at $n/\delta_0 = 0.87$. As the top of the boundary layer is approached, more of the image is filled with fluid containing the scalar transport condensation. The presence of the elongated structures is not as clear at this elevation, although some images do give indications of their presence.

Figure 41 presents plan views of the boundary layer at n = 5.0 mm ($n/\delta_0 = 0.54$) downstream of the 7° centered expansion. Unfortunately, strong reflections from the model surface were not eliminated by the molecular iodine filter. These bright reflections have been blacked out in the images to allow the observer to concentrate on the scattering from the flow. The elongated longitudinal structures were clearly present at this elevation. The images of Fig. 42 were acquired at an elevation of n = 6.5 mm ($n/\delta_0 = 0.71$). Again, a strong presence of the longitudinal structures is indicated. Figure 43 presents similar plan views at n = 8.0 mm ($n/\delta_0 = 0.87$). Even at this elevation, there is a well-defined presence of the elongated longitudinal structures.

Figures 44-46 present instantaneous plan views of the boundary layer downstream of the 14° centered expansion at elevations of n = 12.0 mm, 15.0 mm, and 17.0 mm. The appearance of the structures at greater distances above the wall for this case is a consequence of the large increase in the boundary layer thickness across the expansion. At the lower two elevations, the elongated longitudinal structures are clearly present. At the highest elevation, there presence is less prominent.

Figures 47-49 present instantaneous plan views of the boundary layer downstream of the 14° gradual expansion at elevations of n = 10.0 mm, 13.5 mm, and 17.0 mm. The elongated longitudinal structures are most evident at the lowest elevation. At the middle elevation, indications of the structures are still present in most of the acquired images. At the highest elevation, their presence is less prominent.

In order to get a reading on the robustness of these structural features, experiments were performed with the flow straightening assembly removed from the exit of the wind tunnel stagnation chamber. For the flat plate boundary layer, plan views are presented in Figs. 50-52 at n = 4.5, 6.0, and 8.0 mm ($n/\delta_0 = 0.50$, 0.65, and 0.87). Unfortunately, significant reflections from the surface were not totally eliminated for the two lower sheet elevations by the iodine filter. When necessary, these regions were blacked out in the images. The elongated structures are still clearly present in all of the plan views, suggesting they are a fairly robust feature of the compressible turbulent boundary layer. Again the structures appear more clearly at the lower two sheet elevations, although evidence is present in many of the visualizations at the largest sheet elevation. The elongated longitudinal structures appear similar to those obtained without the flow straightening assembly removed.

Instantaneous plan views downstream of the 7° centered expansion obtained with the flow straightening assembly removed are presented in Figs. 53-56 at n = 4.5 mm, 6.5 mm, 8.5 mm, and 10.5 mm ($n/\delta_0 = 0.50$, 0.71, 0.92, and 1.14), respectively. Again the elongated longitudinal structures are most clearly present at the lowest two elevations. No noticeable differences exist between the structures in these figures and those visualized without the flow straightening assembly removed, although these visualizations are located further downstream of the expansion corner.

Instantaneous plan views downstream of the 7° gradual expansion with the flow straightening assembly removed are presented in Figs. 57-59 at n = 6.5 mm, 9.0 mm, and 11.5 mm ($n/\delta_0 = 0.71$, 0.98, and 1.25), respectively. Strong reflections from the model surface that were not totally absorbed by the molecular iodine filter have been blacked out in Fig. 57b to differentiate between the reflections and the scattering from the flow for the observer. Again the elongated longitudinal structures are most clearly present at the lowest two elevations.

In comparing the elongated longitudinal structures with and without the flow straightening assembly, no significant differences can be identified from the qualitative analysis of the visualizations. The fact that the elongated longitudinal structures are seen to populate the upper half of the flat plate and expanded boundary layers suggests the elongated structures are a significant structural feature of these flows. The clear presence of the structures for such varied upstream conditions further suggests they are a robust feature of the compressible, turbulent boundary layer. However, no statement can be made about their importance to the dynamics of the turbulent boundary layer based on these instantaneous visualizations.

Before leaving the subject of the elongated longitudinal structures, a comment should be made on our good fortune in visualizing these structural features. Because of the low levels of water vapor content in our tunnel supply air, the scalar transport condensation used to differentiate the boundary layer from the freestream in the visualizations is not formed at Mach 2. As a result, we will have to develop a suitable seeding technique to investigate the presence of these structures in the Mach 2 case. Further, we were not able to acquire a global plan view of the elongated longitudinal structures without employing the filtered Rayleigh scattering technique. The signal levels scattered by the condensation (which is obviously diluted as it penetrates deeper into the boundary layer) simply are not strong enough relative to the intense background reflections that will always be present when imaging a flow in the proximity of a solid boundary. Given that the filtered Rayleigh scattering technique has been available only for the past several years [Miles et al., 1991], it is not surprising that these structural features have, until now, gone unvisualized.

Although not presented here, the ensembles of plan views displaying the elongated longitudinal structures were averaged together to check if they tended to occur at specific spanwise locations, which might suggest a facility disturbance was responsible for the formation of the streaks. However, all of the averaged images ensembles displayed uniform intensity across the span, indicating that there was no preferred spanwise distribution for any of the cases investigated.

Another interesting observation came from plan views acquired at the top of the boundary layer downstream of the 14° centered expansion within the previously mentioned 'excess' condensation. The instantaneous plan views revealed that the interface between the dark boundary layer fluid and the fluid containing the "excess" condensation was characterized by very dramatic streamwise 'streaks'. Images obtained downstream of the 14° centered expansion at n = 20.0 and 23.0 mm are presented in Figs. 60 and

61, respectively. The streaks are seen to be of significantly larger streamwise and spanwise scales than the elongated longitudinal structures visualized within the boundary layer, suggesting that these streaks are fundamentally different from those found closer to the wall. However, the mere presence of streaks in the interface between the boundary layer fluid and the fluid containing "excess" condensation raises the possibility that the elongated longitudinal structures within the boundary layer may be of importance to the fluid transport process which leads to the excess condensation.

3.3. Statistics of Single-Pulse Visualizations

Large ensembles of instantaneous streamwise views were obtained of the flat plate boundary layer (250 images) and the boundary layers downstream of both the 7° centered expansion (250 images) and 14° centered expansion (200 images). The filtered Rayleigh scattering technique was used for the visualizations of the first two flows. Because of the presence of the excess condensation downstream of the 14° centered expansion region, the filtered Rayleigh scattering technique was not required for this case. Four of the images of the flat plate boundary layer were presented in Fig. 15. Four of the images of the boundary layer downstream of the 7° centered expansion are presented in Fig. 62, and four of the images of the boundary layer downstream of the 14° centered expansion are presented in Fig. 63 (note that the surface in Fig. 63 appears horizontal only because the camera has been rotated away from the horizontal). For the images of Fig. 63, the entire imaged region above the boundary layer is occupied by the excess condensation discussed above.

3.3.1. Average and RMS Profiles

Average intensity and RMS intensity fluctuation (normalized by the local average intensity) images for ensembles of instantaneous streamwise views of the flat plate boundary layer, the boundary layer downstream of the 7° centered expansion, and the boundary layer downstream of the 14° centered expansion are presented in Figs. 64, 65, and 66, respectively. It should be noted that the Gaussian distribution present in the raw average images due to the Gaussian intensity distribution in the illuminating laser sheet has been removed by normalizing each column in the average images by the maximum intensity in that column. For the RMS images, normalization of the RMS by the local raw average removes the Gaussian sheet distribution.

Growth of the flat plate boundary layer is evident in the average image of Fig. 64a. In addition to the growth of the boundary layer thickness, the normalized RMS image of Fig. 64b shows the region possessing significant RMS fluctuations to increase in normal extent with increasing downstream distance. The localized discontinuities present in the RMS image of Fig. 64b are the result of the occurences of particles at these locations in selected instantaneous images. The growth of the significant-RMS region occurs mainly near the top of the boundary layer, and the bottom of the significant-RMS region remains at essentially the same normal elevation for the streamwise extent of the image.

The average image of the boundary layer downstream of the 7° centered expansion (Fig. 65a) shows the growth rate of the boundary layer thickness to be less than that encountered in the flat plate boundary layer. In addition, the significant-RMS region appears to decrease in normal extent with increasing downstream distance beyond s = 75 mm. For this case, the top of the significant-RMS region appears to remain at essentially the same normal elevation for the streamwise extent of the view and the bottom of the region appears to move further from the boundary with increasing downstream distance. Since the RMS intensity fluctuations are undoubtedly related to the passage of the large scale structures of the outer layer, this trend seems to suggest that the structures of the boundary layer downstream of the 7° centered expansion are becoming less prominent. To at least some extent, this effect is related to the recovery of the small scale turbulence which causes the penetrations of potential fluid (and associated high intensities) between the structures to become less significant.

The average and RMS images of the boundary layer downstream of the 14° centered expansion are presented in Figs. 66a and 66b, respectively. Recall from the discussion presented in conjunction with Fig. 63 that the 'excess' condensation is present at this streamwise location. The average image shows little, if any, growth in the boundary layer thickness occurs in this region. The decreasing peak RMS level and decreasing thickness of the significant-RMS region in Fig. 66b both suggest that the formation of the excess condensation is becoming less significant with increasing downstream distance. The thickness of the significant-RMS region as a fraction of the boundary layer thickness is much less for this case than the flat plate boundary layer or the boundary layer downstream of the 7° centered expansion, suggesting that fundamental differences exist for this case. Despite an ensemble of 200 images, the RMS image does not display smooth gradients.

The average intensity profiles and RMS fluctuation profiles (normalized by the corresponding average profiles) drawn from Figs. 64 and 65 for the flat plate boundary layer and the boundary layer downstream of the 7° centered expansion are presented in Fig. 67. Although the profiles are reported as being for $s/\delta_0 = 11.4$, all of the profiles represent the average of 11 profiles centered about $s/\delta_0 = 11.4$. The 11 profiles were evenly spaced between $s/\delta_0 = 4.50$ and $s/\delta_0 = 18.3$. The boundary layer profiles were found to be very stationary at all of these streamwise locations. The profiles for the 7° centered expansion case displayed significant evolution between the two extreme locations. This is not surprising given the images of Fig. 65. Clearly the strongly perturbed boundary layer is far from equilibrium at this streamwise location. As a result, the transition from boundary layer to freestream at the top of the combined average profile downstream of the 7° expansion is not as well defined as for the combined average profile for the flat plate boundary layer. This made the identification of $I_{avg,max}$ difficult for the 7° expansion profile. A representative freestream intensity has been chosen for the normalization.

The elevation at which the peak in the RMS profile occurs, denoted by δ_{RMS}, has been identified as an effective parameter for collapsing the two average profiles onto one another. The average profiles of Fig. 67 suggest that the actual boundary layer thickness for the intensity profiles is approximately 3.5 δ_{RMS}. One can develop a line of reasoning that suggests a length scale derived from the intensity fluctuations due to the turbulence is appropriate. If, as is suggested in the streamwise visualizations, the outer layer of the turbulent boundary layer is dominated by the large scale structures, then the average profile is determined largely by the scale, orientation, and frequency of occurrence of the large scale structures. There is no disputing the fact that the intensity fluctuations associated with the passage of large scale structures (large masses of low intensity in the images), which are led and trailed by fluid containing condensation, are the main contributors to the RMS intensity fluctuations. Thus the elevation of the peak in the RMS profile is largely a function of the scale, orientation, and frequency of occurrence of the large scale structures as well. In this sense, the length scale provided by the RMS profile is relevant to the average profile. Although certainly not the firmest of arguments, the collapse of the mean profiles is fairly good. Further, the length scale derived from the RMS profiles provides a locally pertinent, obtainable parameter on which to base comparisons of the various cases.

Looking at the RMS profiles of Fig. 67, the peak in the RMS downstream of the 7° centered expansion is only approximately 2/3 of the peak in the flat plate boundary layer RMS profile. The freestream RMS, due mainly to fluctuations in laser intensity, is approximately 0.12 for both cases. This suggests that a direct comparison of the two profiles is valid. The reason for the large reduction in the peak RMS downstream of the 7° centered expansion is not altogether clear. It is almost certainly related to the previously cited loss of 'visual' intermittency caused by the recovery of the small scale turbulent fluctuations downstream of the expansion region, an occurrence which was documented in the spanwise and streamwise visualizations presented earlier. If one considers a boundary layer where the outer layer is occupied only by large scale structures, the bright regions of potential fluid upstream and downstream of the structures would give rise to large fluctuations above the mean when a structure was not present, and vice versa. Thus it seems that the presence of smaller scale turbulent motions may be more prominent at this location in the boundary layer downstream of the 7° centered expansion than in the flat plate boundary layer.

Similar normalized average and RMS profiles are presented for the boundary layer downstream of the 14° centered expansion at $s/\delta_0 = 11.4$ in Fig. 68. Unlike those of Fig. 67, these profiles are for this single location. Again, the normal distance from the wall has been normalized by δ_{RMS} and the RMS profile has been normalized by the average profile. Looking at the average profile of Fig. 68, a sharp drop off occurs just after the maximum is reached. This is due to the presence of the excess condensation above the region that possesses no condensation. The drop off at normal distances above the maximum shows the excess condensation to be most intense near the region that does not possess condensation. This further supports the idea that the excess condensation is formed by the transport of fluid originally in the boundary layer towards the freestream. For this case, the boundary layer thickness that would be defined from the average profile is only $1.4\delta_{RMS}$. This represents a significant departure from the flat plate and 7° centered expansion profiles of Fig. 67. The full or nonintermittent appearance of the boundary layer in Fig. 63 has resulted in the region characterized by significant RMS levels to be confined close to the condensation/no condensation interface. In this region, the alternating occurrences of extremely high and extremely low intensities has resulted in an RMS peak significantly higher than is encountered for the flat plate or 7° centered expansion cases. Since this appears to be an artifice of the excess condensation, comparisons between the profiles of the boundary layer downstream 14° centered expansion are not considered valid.

3.3.1. Spatial Correlations

Spatial correlations were calculated for the ensembles of instantaneous, streamwise visualizations. These correlations are unconditional in the sense that a reference location is defined in the image space and then the correlation field surrounding that point in each of the ensemble images is calculated and the resulting correlation fields are then averaged over the ensemble. If an effective means of locating the correlation reference point in a similar position relative to, or within, large scale structures in many images were derived, averaging the correlations would yield information that is a direct reflection of the large scale structure geometry and orientation. From this perspective, defining a single reference location for an ensemble of images and averaging the correlations for each image together is undesirable since the reference point does not always occur at the same position relative to large scale structures. When this occurs, the high correlation region about the reference point is not necessarily a direct result of large scale structures (for example, if a reference point near the edge of a boundary layer fell between the outer excursions of adjacent large scale structures). For this reason, care was taken to define the reference points for the spatial correlations within the boundary layer thickness defined by the average intensity profile.

The formulae for the spatial correlation are given by

$$I_j^{*}(s,n) = I_j(s,n) - \frac{1}{p}\sum_{j=1}^{p} I_j(s,n) \tag{1}$$

$$I'(s,n) = \left[\frac{1}{p}\sum_{j=1}^{p}\left(I_j^{*}(s,n)\right)^2\right]^{\frac{1}{2}} \tag{2}$$

$$R(ds,dn) = \frac{\frac{1}{p}\sum_{j=1}^{p}\left[I_j^{*}(s_{ref},n_{ref})\; I_j^{*}(s_{ref}+ds,n_{ref}+dn)\right]}{I'(s_{ref},n_{ref})\; I'(s_{ref}+ds,n_{ref}+dn)} \tag{3}$$

where $I_j(s,n)$ is the instantaneous intensity at a given (streamwise, normal) location (s,n) in the jth image of the ensemble containing p images, $I'(s,n)$ is the RMS fluctuation at that location, (s_{ref},n_{ref}) is the reference point location, and R(ds,dn) is the correlation coefficient at a given displacement from the reference point. With this standard formulation, the correlation coefficient at the reference location is 1.00 by definition.

In order to draw relevant comparisons between the different cases, the normal length scale derived from the RMS profiles of Figs. 67 and 68 was used to locate the reference point in the spatial correlations. For all of the presented spatial correlations, the streamwise direction is horizontal right to left. A spatial correlation field calculated for the 250 image ensemble of streamwise views acquired in the flat plate boundary layer is presented in Fig. 66. The reference point is located at $(s_{ref},n_{ref}) = (13.0\delta_0, 1.0\delta_{RMS})$ where $\delta_0 = 9.2$ mm and $\delta_{RMS} = 4.2$ mm, and the normal and streamwise displacements from the reference point have been normalized by δ_{RMS}. Thus, $(n-n_{ref})/\delta_{RMS} = -1.0$ corresponds to the model surface. Recall from the average profile of Fig. 67 that the average intensity profile has a thickness of approximately $3.5\delta_{RMS}$. Accordingly, this reference point location is located well within the region that does not contain any condensation. As a result, correlations at higher elevations would be expected to occur only when large scale motions are in the vicinity. The correlation contours are seen to slope downstream with increasing normal distance at an angle of approximately 45°. This is a result of the forward inclination of the large scale structures. Similar forward-inclined correlation contours were obtained by Smith et al. [1989].

Another spatial correlation field calculated from the ensemble of flat plate boundary layer visualizations is presented in Fig. 70. For this correlation field, the reference point is located further from the wall at the same streamwise location $[(s_{ref},n_{ref}) = (13.0\delta_0, 2.0\delta_{RMS})]$. The model surface is at $(n-n_{ref})/\delta_{RMS} = -2.0$. Contours of significant correlation are seen to extend out to $n/\delta_{RMS} = 3.0$ and beyond, essentially to the top of the boundary layer as defined by the average intensity profile. In general, this correlation field is more well defined than the field derived for the lower reference point. The region characterized by significant correlation is of much greater streamwise and normal extent. This is not altogether unexpected when one considers the typical scales of turbulent motions present at different normal elevations in the boundary layer. One would expect to encounter a much stronger presence of smaller scale motions closer to the wall than in the outer reaches of the boundary layer, where the large scale structures appear to be the dominant motions. Given this, it is likely that the correlation centered further from the wall is better reflection of the large scale structures than the one centered neared the wall. The contours appear to be forward-inclined at an angle close to 45°. It should be noted that spatial correlation fields calculated at $s_{ref}/\delta_0 = 9.2$ (with the reference point located at $n_{ref}/\delta_{RMS} = 1.0$ and 2.0 as was done above) were essentially identical to those presented in Figs. 69 and 70, as would be expected in this equilibrium boundary layer.

Spatial correlation fields calculated from the ensemble of 250 streamwise visualizations obtained downstream of the 7° centered expansion, centered at $(s_{ref},n_{ref}) = (9.2\delta_0, 1.0\delta_{RMS})$ and $(s_{ref},n_{ref}) = (9.2\delta_0, 2.0\delta_{RMS})$ where $\delta_{RMS} = 6.4$ mm, are presented in Figs. 71 and 72, respectively. Compared to the flat plate spatial correlation field centered at $n_{ref}/\delta_{RMS} = 1.0$ (Fig. 69), the region of significant correlation in Fig. 71 has a greater dimensionless spatial extent. Given the discussion presented in conjunction with the RMS profiles concerning the recovery of the boundary layer from the small scale quenching effect at this streamwise location, the proper interpretation of the increased dimensionless spatial extent of the correlation at this elevation is not clear. The correlation fields centered at $n_{ref}/\delta_{RMS} = 2.0$ for the flat plate case (Fig. 70) and the 7° expansion case are very similar, with the regions of significant correlation having approximately the same dimensionless spatial extent. Similar to the flat plate case, the correlation contours appear to be inclined at angles of approximately 45° in both Figs. 71 and 72. Thus no increase in structure angle due to the expansion is apparent in the spatial correlations at this downstream location. However, as discussed above, the structure angle is larger than that found in the flat plate boundary layer just downstream of the expansion regions. Although this effect was not as prominent for the 7° expansions as for the 14° expansions, these spatial correlation results suggest that the increase in structure angle may be a short-lived effect. It is also be noted that spatial correlations calculated at $s_{ref}/\delta_0 = 11.4$ (centered at the same dimensionless normal distances) downstream of the 7° centered expansion appeared very similar to those presented in Figs. 71 and 72. Although a difference in streamwise location of only $2.2\delta_0$ was achieved, the fact that the correlation fields are not evolving very rapidly is demonstrated.

A spatial correlation field centered at $(s_{ref},n_{ref}) = (13.9\delta_0, 1.0\delta_{RMS})$ [$\delta_{RMS} = 16.7$ mm] downstream of the 14° centered expansion calculated from the ensemble of 200 images is presented in Fig. 73. Recall that excess condensation is present above the boundary layer in these images (see Fig. 63). The spatial correlation field bears no resemblance to those calculated in the flat plate and 7° expansion cases. The dimensionless extent of the region possessing significant correlation is much smaller than in the other cases. Further, the contours do not exhibit any downstream inclination. It appears that the structure of the boundary layer at this location is drastically different from that encountered in the incoming boundary layer. The spatial correlation filed centered at $(s_{ref},n_{ref}) = (17.6\delta_0, 1.0\delta_{RMS})$ appeared very similar to Fig. 73, again indicating that the spatial correlation field does not evolve rapidly in the streamwise direction. Since the boundary layer thickness defined by the average intensity profile of Fig. 68 is approximately $1.4\delta_{RMS}$, no correlations were calculated for $n_{ref} = 2.0\delta_{RMS}$.

3.4. Double-Pulse Visualizations

Double-pulse streamwise visualizations were acquired in order to gain some insight into the evolution of the large scale structures in the time domain. Because of the inability to employ the filtered Rayleigh scattering technique for background suppression when operating the Nd:YAG laser in double-pulse mode, a method to reduce the strong reflections caused by the intersection of the laser sheet and the solid model surface had to be devised. Similar to that originally designed into the flat plate model, the 7° centered expansion and 14° centered expansion models were modified to include a flush-mounted glass window 20 mm in width at the model centerline. Bringing the sheet into a glass surface reduced the reflections enough to allow the acquisition of double-pulse visualizations. In the presented double-pulse images, the streamwise direction is from right to left, per usual. However, for all of the double-pulse correlation fields, the streamwise direction is from left to right.

Double-pulse visualizations of the flat plate boundary layer acquired with a time delay of 25.0 μs are presented in Figs. 74 and 75. The flow is again from right to left. Assuming a large scale structure convection velocity of $0.9U_\infty$, the large scale structures would be expected to travel 13.5 mm based on the freestream velocity measurement of 600 m/s acquired with LDV in this wind tunnel previously [Samimy et al., 1992]. Looking at the image pairs of Figs. 74 and 75, the large scale structures can be easily tracked from the initial to the delayed images. In addition to the convection of the large scale structures, if one studies the most prominent structures of Figs. 74a, 74b, and 75a, the process of fluid entrainment by the large scale structures appears to be captured. In these, and many other of the acquired image pairs, the entrainment process appears to occur when the tops of the large scale structures rotate forward, capture some of the leading potential fluid, and isolate it from the freestream. The entrainment of the potential fluid is indicated in many of the image pairs by the destruction of the condensation originally present in the potential fluid when the higher temperatures of the boundary layer are encountered. In as much as the large scale structures are responsible for the entrainment of fresh potential fluid into the boundary layer, it is clear that they are of central importance to the maintenance of the boundary layer turbulence.

Another observation is that the large scale structures tend to display the presence of smaller scale motions along their perimeter. This is especially true at the back edges of the structures, and it is possible that these motions are a product of the strong shear imposed on the back of the structure by potential fluid just upstream of the structure that possesses a higher streamwise velocity than the structure. As was discussed previously, although their visual appearance is reminiscent of the typical eddies proposed by Falco [1977], the scale of these eddies precludes their identification as typical eddies at this Reynolds number. Head and Bandyopadhyay [1981] suggested that the small scale indentations along the structures' perimeter might be an indication that the large scale structures are composed of several hairpin vortex structures.

In addition to qualitative observations such as these, quantitative information concerning the convection of the large scale structures can be gained from the double-pulse data. As a first attempt, one might try to identify the "centroids" of large scale structures, measure the centroid translation between the initial and delayed images, and calculate the structure convection velocity from the known time delay between the initial and delayed images. This was the general approach adopted by Cogne et al. [1993] and Forkey et al. [1993]. However, there are problems with this approach. For the small time delays employed in these visualizations, the difficulty that would be encountered in identifying the "centroid" of the large scale structures would give rise to very high uncertainties in the individual structure velocities. Further, if a structure possesses spanwise vorticity with the sense of rotation expected from the normal gradient of streamwise velocity, the upper portion of the structure will appear to convect further downstream than the approximate center of the structure, i.e. it is difficult to delineate rotation and convection with this analysis.

A second approach to obtaining quantitative information concerning the convection of the large scale structures is to perform space-time correlations on ensembles of image pairs obtained at a specific time delay. Such correlations have been calculated by Elliott et al. [1993a] for double-pulse images of $M_c = 0.51$ and 0.86 mixing layers in order to study the large scale turbulent structures. As discussed by Elliott et al. [1993a], these correlations are somewhat different from the typical correlation of two signals giving the temporal variation of a measured quantity at two points. For this case, one has spatially two-dimensional information at only two instants in time. The presented correlations are based on 150 pairs of initial and delayed images. Before the correlations were calculated, average images were generated for both the 150 initial images and the 150 delayed images. The appropriate average image was then subtracted from each of the initial and delayed images, so that the correlations are of the fluctuations from the local mean.

In the initial fluctuation image, a two-dimensional region is defined. The region defined in the initial image is denoted by (s_{ref},n_{ref}). The signal at each pixel in this region is then correlated with the corresponding signal in the delayed image at various streamwise displacements $(s_{ref}+ds,n_{ref})$. The correlations for each pixel in the defined region is then averaged with the correlations of pixels falling on the same horizontal line of the defined region, so that the resulting correlation at a point (ds,n_{ref}) reflects the cumulative correlation of a horizontal line at vertical position n_{ref} shifted a streamwise distance ds in the delayed image. This process is repeated for each horizontal line in the defined region. The resulting correlation is then averaged over the 150 image pairs in the ensemble. The resulting expressions for the space-time correlation are given by

$$I^{*}_{j,(i/d)}(s,n) = I_{j,(i/d)}(s,n) - \frac{1}{p}\sum_{j=1}^{p} I_{j,(i/d)}(s,n) \tag{4}$$

$$R(ds,n_{ref}) = \frac{1}{p}\sum_{j=1}^{p}\left[\sum_{s_{ref}} I^{*}_{j,i}(s_{ref},n_{ref})\, I^{*}_{j,d}(s_{ref}+ds,n_{ref})\right] \tag{5}$$

where $I_{j,(i/d)}(s,n)$ is the instantaneous intensity in the initial or delayed image, p is the number of image pairs in the ensemble acquired at the given time delay, $I^{*}_{j,(i/d)}(s,n)$ is the instantaneous intensity fluctuation from the local mean in the initial or delayed image, and R(ds,n) is the spatial correlation. The correlation coefficients obtained with Eqn. 5 are normalized by the maximum encountered correlation coefficient for convenience. As a result, a correlation coefficient of 1.0 does not imply perfect correlation as in the usual two-point correlation formula.

Although functional dependence of $R(ds,n_{ref})$ on the choice of the spatial region to be correlated in the initial images is implied, this dependence would disappear for a sufficiently large ensemble. This is because (1) the same spatial region (same pixel coordinates) are correlated for each pair of delayed images, i.e. the correlated region is defined unconditionally, (2) each of the collected image pairs are unrelated to one another in time (framing rate of approximately 2 Hz for the double-pulse visualizations), and (3) the boundary layer is a statistically stationery flow.

The correlation described reflects the level of correspondence of a two-dimensional region shifted in one direction. Since the region that is correlated is not specified to include large scale structures, the spatial shift at which the maximum correlation occurs does not correspond strictly to the large scale structures. However, the large, distinct spatial patterns associated with large scale structural features would undoubtedly represent the events of highest correlation. Although correlations are typically nondimensionalized by RMS fluctuations, this was not done here. The main reason is that the appropriate way to calculate the RMS for two-dimensional spatial regions that continually change is not altogether clear. We are currently investigating alternative formulations for the correlation between double-pulse images.

The correlation contours calculated for an ensemble of 150 images pairs obtained in the flat plate boundary layer with a time delay of 25.0 μs is presented in Fig. 76. In performing the correlations, a normal length scale was defined by examining the average intensity profile at the center of the mean initial image. The thickness of the average profile as defined by the transition to the freestream intensity at the top of the average profile (99% thickness) is denoted as δ_{vis}. For the flat plate boundary layer at this location, $\delta_{vis} = 11.8$ mm. The two-dimensional region was then defined with a streamwise width of $\delta_{vis}/2$. This width was chosen as greater widths produced no noticeable differences in the resulting correlation field despite the added computer run time. The point corresponding to maximum correlation in Fig. 76 occurs at $n/\delta_{vis} = 0.58$ and corresponds to a velocity of 610 m/s. For the given spatial magnification and time delay, a streamwise displacement corresponding to a single pixel element corresponds to a velocity difference of 9.4 m/s. As a result, reported velocities are cited only to the nearest 10 m/s. The velocity corresponding to the streamwise extremes of the R = 0.92 profile are 570 m/s and 650 m/s.

The presence of significant correlation levels at streamwise displacements corresponding to velocities greater than the freestream is not surprising when one considers the streamwise extent of the large scale structures. If one were correlating a convecting thin vertical line, the correlation would quickly peak when the optimal streamwise displacement had been achieved in the delayed image and then quickly return to negligible correlation levels. However, for the case of the large scale structures, which possess a significant streamwise extent, the transition from negligible correlation levels to the peak and back to negligible levels would be much more gradual. Although the peak should occur at the streamwise displacement corresponding to the structure's convection, significant correlation levels would be achieved at displacements even larger than this because of the still significant overlap between the pattern of the structure from the initial image and the structure in the delayed image. Another possible reason comes from the cited entrainment of freestream fluid by the large scale structures. If potential fluid is entrained at the front of the structure, the apparent increase in scale of the structure caused by the condensation destruction may be interpreted by the correlation program as an additional streamwise displacement. It is also important to remember that the correlation is unconditional, so that if potential fluid occupies the region to be correlated in the initial image, the optimal streamwise shift at that normal location will correspond to the freestream velocity.

Double-pulse images acquired in the flat plate boundary layer with a time delay of 50.0 μs are presented in Fig. 77. Unfortunately, the initial camera was collecting a significant reflection. For this time delay, the structures would travel 30.0 mm if they convected at 600 m/s. This distance corresponds to approximately half of the width of the images in Fig. 77. Spina and Smits [1987] showed that the large scale structures maintain their identity for at least 1.5δ by analyzing streamwise-separated patterns of conditionally-sampled mass flux fluctuations and wall pressure fluctuations. In Fig. 77 the structures are convecting approximately $3\delta_{vis}$, and most are easily tracked between the initial and delayed images. This speaks to the robustness of the large scale structures. The correlation field calculated from an ensemble of 150 images like those of Fig. 77 is presented in Fig. 78. For the given spatial magnification and time delay, the resulting velocity resolution of the correlation is 4.7 m/s/pixel, and the cited velocities are reported only to the nearest 5 m/s. The velocity obtained from the streamwise displacement corresponding to maximum correlation, which occurs at n/δ_{vis} = 0.59, is 595 m/s. The velocities corresponding to the streamwise extremes of the R = 0.92 contour are 570 m/s and 630 m/s.

Double-pulse images obtained downstream of the 7° centered expansion with a time delay of 23.9 μs are presented in Fig. 79. The cameras have been rotated so as to make the surface of the sloping model horizontal. An inviscid analysis gives a streamwise velocity of 630 m/s downstream of the 7° centered expansion. Structures convecting at this velocity would travel 15.1 mm between the initial and delayed images. Examination of the average intensity profile at the center of the mean initial image resulted in δ_{vis} = 14.0 mm. The correlation field calculated from an ensemble of 150 images obtained with a time delay of 16.0 μs is presented in Fig. 80. For the given parameters, the velocity resolution of the correlation is 13.2 m/s/pixel, and the cited velocities are reported only to the nearest 10 m/s. The point of maximum correlation occurs at n/δ_{vis} = 0.73 and corresponds to a velocity of 590 m/s. The velocities corresponding to the streamwise extremes of the R = 0.85 contour are 550 m/s and 700 m/s.

In order to draw relevant comparisons between the correlations in the flat plate boundary layer and those downstream of the centered expansions, the delays for the expansion cases were chosen such that the structures would convect a similar distance in all of the boundary layers. Accordingly, the 25.0 μs delay for the flat plate boundary layer was scaled to 23.9 μs for the boundary layer downstream of the 7° centered expansion based on the ratio of the freestream velocities across the expansion region, which was obtained from a standard inviscid analysis. Similarly, the 50.0 μs delay for the flat plat case was scaled to 47.9 μs for the boundary layer downstream of the 7° centered expansion.

The correlation field calculated from an ensemble of 150 images obtained with a delay of 23.9 μs is presented in Fig. 81. For the given parameters, the velocity resolution of the correlation is 8.9 m/s/pixel, and the cited velocities are reported only to the nearest 10 m/s. The point of maximum correlation occurs at n/δ_{vis} = 0.71 and corresponds to a velocity of 620 m/s. The velocities corresponding to the streamwise extremes of the R = 0.92 contour are 600 m/s and 660 m/s.

The correlation field calculated from an ensemble of 150 images obtained with a delay of 47.9 μs is presented in Fig. 82. For the given parameters, the velocity resolution of the correlation is 4.4 m/s/pixel, and the cited velocities are reported only to the nearest 5 m/s. The point of maximum correlation occurs at n/δ_{vis} = 0.71 and corresponds to a velocity of 615 m/s. The velocities corresponding to the streamwise extremes of the R = 0.92 contour are 595 m/s and 645 m/s.

The fact that point of maximum correlation occurred at essentially the same dimensionless normal elevation for the correlations for all of the employed time delays for both the flat plate and 7° centered expansion boundary layers suggests that the same structural features were responsible for the correlations for all employed time delays. The fact that this location is a significant fraction of the boundary layer thickness from the wall, but still well within the boundary layer suggests that the main contributors to the correlation are the large scale structures of the outer layer. All of the velocities corresponding to the streamwise displacement at maximum correlation appear reasonable for the flat plate and the 7° centered expansion. The scatter in the velocities could very well be due to the modest sample sizes. This is especially true considering the limited velocity resolutions. It is also worth noting that variations in stagnation temperature, which are encountered on a seasonal and daily basis could cause slight variations in the Mach 3 freestream velocity. For example, if the stagnation temperature rose 10 °K above the value of 280 K recorded when the freestream velocity of 600 m/s was measured with LDV [Samimy et al., 1992], a simple inviscid analysis shows that the freestream velocity would increase to 610 m/s.

Double-pulse images obtained downstream of the 14° centered expansion with a time delay of 23.0 μs are presented in Fig. 83. The 23.0 μs was scaled from the 25.0 μs delay for the flat plate case based on the freestream velocity ratio across the expansion. The cameras have again been rotated so as to make the surface of the sloping model appear horizontal. An inviscid analysis gives a streamwise velocity of 650 m/s downstream of the 14° centered expansion. Structures convecting at this velocity would travel 14.9 mm between the initial and delayed images. Examination of the average intensity profile resulted in δ_{vis} = 22.3

mm. The correlation field calculated from an ensemble of 150 images obtained with a time delay of 23.0 μs is presented in Fig. 84. For the given parameters, the velocity resolution of the correlation is 9.1 m/s/pixel, and the cited velocities are reported only to the nearest 10 m/s. The point of maximum correlation occurs at $n/\delta_{vis} = 0.94$ and corresponds to a velocity of 500 m/s. The velocities corresponding to the streamwise extremes of the R = 0.92 contour are 420 m/s and 570 m/s.

The fact that the large scale structures appear to decelerate across the 14° centered expansion again suggests that the boundary layer has undergone a very complex distortion. This again points out that the large scale structure of the boundary layer downstream of the 14° centered expansion region is vastly different from that found in the flat plate boundary layer or the boundary layer downstream of the 7° centered expansion. Further, the low convection velocities call to question whether the region containing the excess condensation is simply part of the freestream. It seems entirely possible that there is a mean streamwise velocity gradient associated with this layer, and that it serves as a "buffer" of sorts between the layer demarcated by the absence of condensation and the freestream. Another observation is that the point of maximum correlation falls very near the top of the boundary layer ($n/\delta_{vis} = 0.94$). This is a quantitative illustration of the lack of identifiable large scale structures in the outer portions of the boundary layer.

3.5. Fluctuating Surface Pressure Measurements

The transducer plug shown in Fig. 6 was used to obtain measurements of the fluctuating surface pressures at various locations in the flat plate and expanded boundary layers. After filtering, fluctuating pressure data is available for $1 \text{ kHz} \leq f \leq 60 \text{ kHz}$. The circular plug design allows the transducers to be aligned in any direction. To date, only the streamwise and spanwise orientations have been used. One plug hole was located just upstream of the beginning of the expansion regions in the flat transitional model that connects to the splitter plate. Two plug holes are available downstream of the 14° expansion regions. Three plug holes are available downstream of the 7° expansion regions. In each of the expansion models, the first plug hole is located as close as possible to the end of the expansion region. Subsequent plug holes are located further downstream. A complete accounting of the surface pressure measurements can be found in Dawson [1993] and further discussion of the results can be found in Dawson and Samimy [1994].

3.5.1. Normalized Power Spectra

The normalized power spectra obtained in the incoming flat plate boundary layer with the transducers aligned in the streamwise direction and their average are presented in Fig. 85. Although slight variations exist, which are probably due to varying transducer sensitivities, the spectra appear quite uniform. This is as would be expected in the equilibrium flat plate boundary layer. The normalized power spectra obtained just downstream of the 7° centered expansion with the plugs aligned in the streamwise direction are presented in Fig. 86 along with the spectrum obtained in the incoming boundary layer. The streamwise locations at which measurements are made span only $0.58 \leq s/\delta_0 \leq 2.21$ ($\delta_0 = 9.2$ mm). Clearly, there is a rapid distortion of the incoming spectrum through the expansion and a rapid development of the spectrum in this short distance. At the first location, $s/\delta_0 = 0.58$, a much higher percentage of the fluctuation "energy" is seen to be confined to lower frequencies ($f < 20$ kHz) than in the incoming boundary layer. Concomitantly, a much smaller fraction of the fluctuation energy is located at higher frequencies ($f > 25$ kHz). The spectra at $s/\delta_0 = 0.91$ are essentially identical to those at $s/\delta_0 = 0.58$. At $s/\delta_0 = 1.40$, the low frequency levels have begun to drop and the high frequency levels have begun to rise. At $s/\delta_0 = 2.21$, the spectra has moved much closer to that of the incoming boundary layer, although are still higher levels at very low frequencies ($f < 10$ kHz) and slightly lower levels for higher frequencies ($f > 25$ kHz).

The concentration of the fluctuation energy in the lower frequency fluctuations just after the expansion fits quite well with the idea of a small scale damping process being caused by the expansion region. Larger scale structures are associated with low frequencies, and vice versa. If smaller scale turbulent motions were to suddenly be quenched by the expansion process, one would obviously expect to see a larger fraction of the fluctuation energy concentrated at low frequencies. This is not to say that the larger scale motions are strengthened by the expansion process. Indeed, previous work [Dussauge and Gaviglio, 1987 and Smith and Smits, 1991] suggests that all scales of turbulent fluctuations are weakened by the dilatational effect associated with the expansion region. Recall that the presented power spectra are normalized, which is to say they do not give an indication of the amount of fluctuation energy present at a given frequency (or in a total spectrum). Instead, the spectra indicate how the existing fluctuation energy is distributed in the frequency domain.

The normalized spectra for a single transducer at various plug locations in the 7° centered expansion model are presented in Fig. 87. The first location downstream of the expansion corner, which is carried over from Fig. 86, illustrates the energy concentration at the lowest frequencies. Although the normalized power spectrum at the last transducer in the first plug location appears to be on the verge of reassuming the shape found in the incoming boundary layer (Fig. 86), the spectra of Fig. 87 show that the streamwise evolution of the normalized power spectrum is not a simple monotonic recovery. At $s/\delta_0 = 8.87$, the spectrum is indeed very similar to that found in the incoming boundary layer. However, at $s/\delta_0 = 28.2$, the spectrum again displays a slightly elevated concentration of the fluctuation energy at low frequencies ($f < 10$ kHz) relative to both the incoming boundary layer and the previous station downstream of the expansion.

Similar to Fig. 86 for the 7° centered expansion case, Fig. 88 presents the streamwise evolution of the normalized power spectrum at the first plug location downstream of the 7° gradual expansion. All of the spectra are very similar to the spectrum of the flat plate boundary layer and even more similar to each other. Consistent with the trend found for the 7° centered expansion, the small deviation between the spectra before and after the expansion takes the form of a larger percentage of the fluctuation energy being concentrated at low frequencies ($f < 10$ kHz) and a smaller percentage at higher frequencies ($f > 30$ kHz). The extent of the surface curvature for the 7° gradual expansion measured along the model surface (s-direction; see Fig. 2) is $\Delta s_{7G} = 55$ mm ($5.98\ \delta_0$). The essentially stationary spectrum shape at all four transducers in the first plug shows that all, if any, rapid changes in the spectrum shape have occurred and dissipated within the confines of the expansion region.

Although Fig. 88 certainly gives the impression that the streamwise evolution of the normalized power spectrum downstream of the first plug location in the 7° gradual expansion will produce nothing of interest, this is not the case. Fig. 89 presents the downstream evolution of the normalized power spectra at the three plug locations. Although the spectrum at $s/\delta_0 = 14.9$ is essentially identical to that obtained at $s/\delta_0 = 6.58$, the spectrum at $s/\delta_0 = 34.2$ displays a marked difference. At this location, the lower frequency levels ($f < 20$ kHz) are identical to those found in the incoming boundary layer, the high frequency levels ($f > 30$ kHz) are slightly lower than those found in the incoming boundary layer, and a plateau of significant energy concentration has emerged in the 20 kHz-30 kHz frequency range. This concentration of energy is not encountered anywhere upstream of the last plug location. This same plateau is found in the spectra of all four transducers at the third plug location.

The streamwise evolution of the normalized power spectrum at the first plug location downstream of the 14° centered expansion is presented in Fig. 90. The four spectra at this plug location show the same trend as that encountered for the first plug location downstream of the 7° centered expansion, only more exaggerated. At the first location, there is a concentration of the fluctuation energy at the lower frequencies ($f < 15$ kHz) and very little of the energy is present at higher frequencies ($f > 30$ kHz). Also similar to the 7° centered expansion, the spectrum of the second transducer is identical to that of the first. At the third and fourth transducers, the low frequencies' levels become progressively lower, moving towards the levels encountered in the incoming boundary layer (although they are still elevated relative to the incoming boundary layer at the last transducer). As the low frequency levels decrease, the high frequency levels begin to recover towards the spectrum of the incoming boundary layer, although they are still lower at the last transducer. If one looks closely at the spectra for the first plug location downstream of the 7° and 14° centered expansion (Figs. 86 and 90, respectively) it is almost as if there is a "pivot frequency" above which the energy concentration is decreased and below which the energy concentration is increased. For the 7° centered expansion, the pivot frequency is approximately 20 kHz. For the 14° centered expansion, the pivot frequency appears to be closer to 15 kHz. This agrees with the idea that the observed distortion of the spectrum shape is due to the quenching of turbulent scales by dilatation. Since the dilatational effect across the 14° centered expansion is greater than that across the 7° centered expansion, it would be expected that the 14° centered expansion would be able to quench lower-frequency (larger scale) motions than the 7° centered expansion could. This would result in a lower pivot frequency for the 14° centered expansion.

The downstream evolution of the normalized power spectrum for the same transducer in the various plug holes downstream of the 14° centered expansion is presented in Fig. 91. At the first location, the energy is concentrated at low frequencies, as previously discussed. At the next plug location ($s/\delta_0 = 8.87$), the spectrum is essentially identical to that obtained in the incoming flat plate boundary layer.

The streamwise evolution of the normalized power spectrum at the first plug location downstream of the 14° gradual expansion is presented in Fig. 92. The extent of the expansion region at the model surface is $\Delta s_{14G} = 110$ mm ($11.96\ \delta_0$). The four spectra at this plug location display similar characteristics to the spectra obtained at the first plug locations downstream of the 7° and 14° centered expansions, only much less exaggerated. The spectrum levels are elevated at low frequencies ($f < 10$ kHz) and depressed at high frequencies ($f > 25$ kHz) relative to those found in the incoming boundary layer. The distortion of the spectrum shape is more pronounced than that encountered at the first plug location downstream of the 7° gradual expansion (Fig. 86). Although one cannot identify a "pivot frequency" for the first plug location downstream of the two gradual expansions as was done for the centered expansions, both 1) the frequencies which experience an increase in spectrum level are confined to lower frequencies and 2) the frequencies which experience a decrease in spectrum level extends to lower frequencies for the 14° gradual expansion relative to the 7° gradual expansion. These observations are again consistent with the concept of small scale quenching due to dilatation.

The downstream evolution of the normalized power spectrum for the same transducer at the two plug locations downstream of the 14° gradual expansion is presented in Fig. 93. At the first location, the energy is concentrated at low frequencies, as has been the case to at least some degree for all of the expansion models. At the next plug location ($s/\delta_0 = 20.82$), the spectrum is essentially identical to that obtained in the flat plate boundary layer.

3.5.2. Streamwise Transducer Separations

Coherence and space-time correlations were calculated from the simultaneous measurements at different transducer separations. The transducers placed in the plug, which is shown schematically in Fig. 6, were spaced unevenly to afford measurements at transducer separations of 3.0 mm ($\Delta s/\delta_0 = 0.33$), 7.5 mm ($\Delta s/\delta_0 = 0.82$), and 15.0 mm ($\Delta s/\delta_0 = 1.63$). In order to present the observed trends in the most succinct manner possible, the results presented here are almost exclusively for a transducer separation of 7.5 mm.

The streamwise coherence for the incoming flat plate boundary layer at the three transducer spacings are presented in Fig. 94. As expected, the coherence levels for a given frequency decrease with increasing transducer separation. At the largest separation, only low frequencies ($f < 20$ kHz) exhibit appreciable coherence. This is because the low frequency fluctuations are associated with larger scale structures, which maintain their identity for greater streamwise distances than smaller scale motions. The space-time correlations for these three transducer separations are presented in Fig. 95. The temporal resolution is limited to 4.0 μs increments due to the employed sampling frequency of 250 kHz/channel. If one takes the time delay corresponding to the peak of the correlation curve for $\Delta s/\delta_0 = 0.33$ to be 6.0 μs (half way between the points at 4.0 and 8.0 μs), the resulting velocity is 500 m/s. Taking the time delay at maximum correlation for $\Delta s/\delta_0 = 0.82$ to be 14.0 μs, the resulting velocity is 535 m/s. Taking the time delay at maximum correlation for $\Delta s/\delta_0 = 1.63$ as 32.0 μs, the resulting velocity is 470 m/s. These velocities represent 80%-90% of the Mach 3 freestream velocity of 600 m/s measured previously with LDV [Samimy et al., 1992], which compares well to the convection velocity results of other investigators.

The downstream evolution of the 7° centered expansion streamwise coherence for $\Delta s/\delta_0 = 0.82$ is presented in Fig. 96. The coherence profile is very similar at the three surveyed locations for this transducer separation. In fact, the shape and levels of the profile are very close to those obtained in the incoming boundary layer for this transducer separation. The space-time correlations at the three plug locations for this transducer separation are presented in Fig. 97. Taking the time delays corresponding to the peaks of the correlation curves for $s/\delta_0 = 0.58$, $s/\delta_0 = 8.87$, and $s/\delta_0 = 28.2$ as 6.0 μs, 8.0 μs, and 10.0 μs, the resulting velocities are 1250 m/s, 940 m/s, and 750 m/s. These velocities are obviously too high to represent the convection of the large scale structures, which were found to convect at velocities on the order of 600 m/s in the double-pulse correlations. It is not at all clear what causes the space-time correlation to give time delays which result in unrealistically high convection velocities. This is especially puzzling given the cited favorable comparison of the coherence spectrum at this location and in the incoming boundary layer for this transducer separation (Fig. 94).

The downstream evolution of the 7° gradual expansion streamwise coherence for $\Delta s/\delta_0 = 0.82$ is presented in Fig. 98. Again, these coherence spectra are very similar in shape and level to the coherence spectrum obtained in the incoming boundary layer. One deviation is the coherence at low frequencies ($f <$ 10 kHz) which is higher than that found in the incoming boundary layer at $s/\delta_0 = 6.58$, and then lower at $s/\delta_0 = 14.9$ and $s/\delta_0 = 34.2$. It is also noted that the coherence in the 20-30 kHz frequency range has risen above the levels encountered anywhere further upstream, although not dramatically. The space-time correlations at the three plug locations for this transducer separation are presented in Fig. 99. The time delays corresponding to the maximum correlation coefficients are 8.0 μs at $s/\delta_0 = 6.58$, $s/\delta_0 = 14.9$, and $s/\delta_0 = 34.2$. These correspond to a velocity of 940 m/s, again unrealistically high for a structure convection velocity.

The downstream evolution of the 14° centered expansion streamwise coherence for $\Delta s/\delta_0 = 0.82$ is presented in Fig. 100. The coherence spectrum at $s/\delta_0 = 0.58$ is identical to that obtained in the flat plate boundary layer upstream of the expansion in both level and shape. Further downstream at $s/\delta_0 = 8.87$, the coherence spectrum possesses the same shape as those further upstream, but there is a broadband increase of 0.2 in the correlation level. The space-time correlations at the three plug locations for this transducer separation are presented in Fig. 101. The time delays corresponding to the maximum correlation coefficients are 8.0 μs and 10.0 μs at $s/\delta_0 = 0.58$ and $s/\delta_0 = 8.87$, respectively. These time delays correspond to velocities of 940 m/s and 750 m/s.

The downstream evolution of the 14° gradual expansion streamwise coherence for $\Delta s/\delta_0 = 0.82$ is presented in Fig. 102. The three spectra are similar for frequencies greater than 20 kHz. At $s/\delta_0 = 12.6$, the only deviation from the coherence of the incoming boundary layer is a lower coherence level for frequencies below 5 kHz. At $s/\delta_0 = 20.8$, the coherence levels for frequencies less than 15 kHz are higher than at any position further upstream. The space-time correlations at the three plug locations for this transducer separation are presented in Fig. 103. The time delays corresponding to the maximum correlation coefficients are 8.0 μs and 10.0 μs at $s/\delta_0 = 12.6$ and $s/\delta_0 = 20.8$, respectively. These time delays correspond to velocities of 940 m/s and 750 m/s.

The convection velocities derived from the streamwise space-time correlations are unrealistically high downstream of the expansion regions for all of the models. A few comments are in order. First, one should not loose sight of the fact that the space-time correlations from the double-pulse visualizations have given entirely reasonable convection velocities for the large scale structures of the flat plate boundary layer and the boundary layer downstream of the 7° centered expansion. For the 14° centered expansion, the double-pulse correlations showed the large scale features of the boundary layer to be travelling at a velocity significantly less than the freestream velocity expected from a standard inviscid analysis. This leads to the conclusion that the large scale structures that give rise to the double-pulse correlations are **not** the same features that give rise to the space-time correlations of the surface pressure fluctuations. Secondly, the fact that the streamwise pressure space-time correlations yield reasonable velocities in the boundary layer upstream of the expansion regions suggests that the structure of the boundary layer is changed dramatically across the expansion regions.

In closing, the fact that the correlations are based on pressure fluctuations may be significant. Lee et al. [1992] used two-point space-time correlations in a spatially-simulated, turbulent, supersonic flow to test the applicability of Taylor's hypothesis in compressible turbulence. Convection velocities derived from streamwise correlations of velocity and vorticity fluctuations corresponded well to the streamwise velocity of the flow. However, convection velocities derived from streamwise correlations of dilatation fluctuations

($\partial u/\partial x + \partial v/\partial y + \partial w/\partial z$) did **not** correspond to the flow velocity. Further, the derived convection velocities were greater than the mean flow velocity. This is related to the wave propagation of acoustic disturbances relative to the flow velocity. As pressure fluctuations are clearly related to dilatation fluctuations, it is entirely possible that the unrealistically high convection velocities derived from the streamwise correlations of pressure fluctuations are caused by similar effects.

3.5.3. Spanwise Transducer Separations

Multi-point surface pressure fluctuation data were acquired with the transducers aligned in the spanwise direction. The spanwise coherence obtained in the flat plate boundary layer upstream of the expansion region are presented in Fig. 104. As expected, the spanwise coherence levels are much lower than the levels obtained for streamwise transducer orientations. Negligible coherence levels exist for the largest two separations. The spanwise space-time correlations obtained at these locations are presented in Fig. 105. For the smallest transducer separation ($\Delta z/\delta_0 = 0.33$), the correlation peak is seen to be centered near a time delay of 0.0 μs as would be expected for the two-dimensional boundary layer. For the larger two transducer separations, the correlation levels are negligible.

The spanwise coherence spectra ($\Delta z/\delta_0 = 0.82$) at the different plug locations on the 7° centered expansion are presented in Fig. 106. At the first location after the expansion corner ($s/\delta_0 = 1.24$) the coherence levels are negligible, similar to those of the flat plate boundary layer. Although the second location downstream of the expansion corner ($s/\delta_0 = 9.52$) displays increased levels for lower frequencies ($f < 30$ kHz), the levels are still minimal. The third location downstream of the expansion ($s/\delta_0 = 28.8$), however, displays significant coherence levels in the frequency range of 10-30 kHz. This implies that there are turbulent motions associated with these frequencies that exhibit significant correlation for the spanwise separation of $\Delta z/\delta_0 = 0.82$. The spanwise space-time correlations obtained at these locations for this transducer separation are presented in Fig. 107. At $s/\delta_0 = 1.24$, the correlation level is negligible, similar to those of the flat plate boundary layer. At $s/\delta_0 = 9.52$, the correlation level is not negligible. Further, the correlation exhibits a non-zero time shift of magnitude 12.0 μs at the peak correlation. At $s/\delta_0 = 28.8$, the correlation levels have increased even further and display a time shift of magnitude 8.0 μs at the peak correlation level.

The streamwise evolution of the spanwise coherence spectra ($\Delta z/\delta_0 = 0.82$) for the 7° gradual expansion are presented in Fig. 108. At the first location downstream of the expansion region ($s/\delta_0 = 7.22$) the coherence levels are significant for low frequencies ($f < 30$ kHz). At the second location ($s/\delta_0 = 15.5$) the coherence spectrum is similar to that encountered as $s/\delta_0 = 7.22$. At the final location ($s/\delta_0 = 34.9$), the portion of the spectrum displaying significant coherence level appears to have concentrated into the frequency range of 15-25 kHz. The spanwise space-time correlations obtained at these locations for this transducer separation are presented in Fig. 109. For all three locations, the peak correlation level is significant. At $s/\delta_0 = 7.22$, 15.5, and 34.9 the correlation peak occurs at a time delay of magnitude 16.0 μs, 12.0 μs, and 10.0 μs.

The streamwise evolution of the spanwise coherence spectra ($\Delta z/\delta_0 = 0.82$) for the 14° centered expansion are presented in Fig. 110. At the first location downstream of the expansion corner ($s/\delta_0 = 1.24$) the coherence levels are negligible, similar to those found in the flat plate boundary layer for this transducer separation. At the second location ($s/\delta_0 = 9.52$) the coherence levels are negligible at all frequencies except for $f < 10$ kHz. The spanwise space-time correlations obtained at these locations for this transducer separation are presented in Fig. 111. At $s/\delta_0 = 1.24$ the correlation levels are negligible. At $s/\delta_0 = 9.52$ the modest correlation peak occurs at a time delay of magnitude 12.0 μs.

The streamwise evolution of the spanwise coherence spectra ($\Delta z/\delta_0 = 0.82$) for the 14° gradual expansion are presented in Fig. 112. At the first location downstream of the expansion corner ($s/\delta_0 = 13.2$) the coherence levels are elevated above those of the flat plate boundary layer, especially for $f < 30$ kHz.. At the second location ($s/\delta_0 = 21.5$) the coherence levels are even more significant than at the previous station for $f < 30$ kHz. The spanwise space-time correlations obtained at these locations for this transducer separation are presented in Fig. 113. At $s/\delta_0 = 13.2$ a significant correlation peak occurs at a time delay of magnitude 12.0 μs. At $s/\delta_0 = 21.5$ the peak correlation level is even higher, and occurs at a time delay of magnitude 8.0 μs.

The non-zero time delays at maximum correlation for the spanwise transducer separations are not understood at this point. The appreciable correlation levels might possibly be the result of several of the previously discussed elongated longitudinal structures being distributed across the span. However, since the spanwise correlations in the flat plate boundary layer did not display significant peaks at non-zero time delays, a more prominent presence of the elongated longitudinal structures relative to the large scale structures of the outer layer is implied. The fact that the correlations for the spanwise transducer separations are not symmetric about zero time delay is not understood. This would seem to suggest that the (spanwise separated) events giving rise to the correlations at large transducer separations are staggered in the streamwise direction. Even if this were the case, though, it is not clear why events at one spanwise location would tend to lead (or follow) the corresponding event at a different spanwise location.

For the longer 7° expansion cases, the last measurement station was $30\delta_0$ downstream of the expansion corner. The surface pressure fluctuations at this location still displayed significant differences from those encountered in the incoming boundary layer, suggesting that the changes brought on by the expansion region are long-lasting.

4. Conclusion

This report presents the results of an extended investigation of the effects of four expansion regions on an incoming Mach 3 fully-developed, compressible turbulent boundary layer. The four expansion regions consist of 7° and 14° centered expansions and 7° and 14° gradual expansions ($R/\delta_0 = 50$). The flat plate boundary layer is studied as well. Multi-point fluctuating surface pressure measurements, instantaneous filtered Rayleigh scattering visualizations, and double-pulse visualizations were employed. The visualizations were made possible by the condensation of the small amount of water vapor left in the tunnel supply air after drying, which was present in the freestream, and the absence of this condensation in the boundary layer due to the higher temperatures resulting from frictional heating. All of the measurements indicate that the expansion regions cause profound and lasting changes in the boundary layers.

In addition to the previously visualized large scale structures of the outer layer, visualizations of the fully-developed flat plate boundary layer reveal the well-defined presence of turbulent structures of a very large streamwise, and limited spanwise, extent. As such, these 'streaky' structures appear nominally similar to those found near the wall of incompressible boundary layers. However, the elongated structures were found well above the inner layer, nominally at $y/\delta = 0.5$-1.0. Although they may be present even closer to the wall, the current visualization technique was not capable of visualizations below $y/\delta \approx 0.5$ due to the lack of condensation particles at these elevations within the boundary layer. The elongated structures were also seen to have a larger spanwise extent than the near-wall streaks of incompressible cases. Experiments were performed for very different upstream conditions (i.e. with and without the flow straightening assembly at the exit of the stagnation chamber), and the elongated structures were always present. These facts suggest that the elongated longitudinal structures are a robust feature of the compressible turbulent boundary layer. The apparent absence of these structures in the incompressible turbulent boundary layer calls to question the longstanding notion that the turbulence structure of compressible turbulent boundary layers should be similar to those of their incompressible counterparts for freestream Mach numbers up to approximately 5.

The elongated longitudinal structures were also present in the boundary layers downstream of all four expansion regions, again both with and without the flow straightening assembly installed in the wind tunnel. The appearance of the structures in the four expanded boundary layers were not noticeably different from that found in the flat plate boundary layer. No comment can be made on the importance of the elongated longitudinal structures to the dynamics of the turbulent boundary layer based on these visualizations. However, the predominant visual presence of the structures in the flows studied here leads the authors to wonder if this is a common feature of compressible boundary layers that has, until now, gone unvisualized. The fact that these structural features have not been previously witnessed is not surprising when one considers that attempts to image the low signal levels associated with these structures without the filtered Rayleigh scattering technique were met with little success, and the filtered Rayleigh scattering technique has been available only for the past few years.

In addition to the surprising finding of the elongated longitudinal structures, the effect of the expansion regions on the large-scale ('δ-scale') bulges known previously to exist in the compressible, turbulent boundary layer was studied. Spatial correlations show the angle of inclination of the large scale structures to be approximately 45° in the flat plate boundary layer. The structures increase in scale across the expansion region, which seems reasonable given the strong dilatation encountered across the expansion region. Also, the angle between the structures and the downstream wall was seen to increase. A possible explanation for this effect is provided by a consideration of the kinematics associated with the passage of a large scale structure through an expansion region. It seems the increase in structure angle is a short-lived effect, though, as spatial correlations at $s/\delta_0 \approx 10$ downstream of the 7° centered expansion give a structure angle of approximately 45° (same as that found in the flat plate boundary layer).

Downstream of both 14° expansion regions, a new layer of condensation in excess of that present in the incoming freestream was found to form above the region demarcated by the absence of condensation. Instantaneous visualizations show the source of the excess condensation to be the transport of fluid originally in the boundary layer (which contains uncondensed water vapor) away from the wall, where lower temperatures which lead to condensation are encountered. Repetition of experiments showed the distance downstream of the expansion regions at which the excess condensation appeared to vary slightly. It is believed that this is a result of the varying water vapor content of the tunnel supply air. The excess condensation was not encountered in either of the 7° expansion cases. Spatial correlations in the boundary layer downstream of the onset of the excess condensation for the 14° centered expansion bear no resemblance to those of the flat plate boundary layer and the boundary layer downstream of the 7° centered expansion. This suggests that the large scale structure of the boundary layer is drastically altered across the 14° centered expansion.

As previously suggested, the small scale motions in the incoming boundary layer appear to respond essentially immediately to the expansion region, while the large scale motions appear to respond more gradually. This point is indicated in the visualizations by the apparent quenching of the small scale motions in the expansion region (presumably due mainly to dilatation, as suggested previously), while the large scale motions retain their identity as they convect through the expansion. This results in an increased 'visual dominance' of the large scale motions relative to the smaller scale motions after the expansion region. (i.e. after the quenching of the small scale motions, large regions of potential fluid containing condensation are seen to penetrate deep into the boundary layer between adjacent large scale structures). Confirmation of this small scale quenching effect is provided by the multi-point surface pressure measurements. The normalized power spectra of the surface pressure fluctuations immediately downstream of the expansion regions show the fluctuations to be much more concentrated at low frequencies (associated with large scale structures) than in the flat plate boundary layer. The high frequency portion of the spectra display levels much lower than those found in the flat plate boundary layer.

The convection of the boundary layer structural features was investigated with the multi-point fluctuating surface pressure measurements and double-pulse visualizations. Convection velocities determined from the fluctuating pressure measurements appear entirely reasonable in the incoming boundary layer, but unreasonably high in the expanded boundary layers. Convection velocities were also determined from two-dimensional space-time correlations between the ensembles of initial and delayed double-pulse images. For the flat plate boundary layer, double-pulse ensembles acquired at time delays of 25.0 μs and 50.0 μs gave convection velocities of approximately 610 m/s and 595 m/s, respectively. For the boundary layer downstream of the 7° centered expansion, double-pulse ensembles acquired at time delays of 16.0 μs, 23.9 μs, and 47.9 μs gave convection velocities of approximately 590 m/s, 620 m/s, and 615 m/s, respectively. The discrepancy between the pressure results and the double-pulse results downstream of the expansion regions suggests that the relationship between the large scale structures and the convected pressure field is severely altered by the expansion regions. Clearly, the large scale structures of the outer layer, which are shown to convect at the expected velocities in the double-pulse correlations, are not responsible for the pressure correlations (or at least not predominately).

Downstream of the 14° centered expansion, the double-pulse correlations show the large scale structures of the boundary layer to be convecting at a lower velocity than in the flat plate boundary layer, which is very surprising given the freestream acceleration through the expansion region. This is almost assuredly related to the formation of the excess condensation layer and suggests that a normal gradient of streamwise velocity may exist across the region containing excess condensation. This further confirms strong differences to exist in the structure of the boundary layers downstream of the 14° expansions and those downstream of the 7° expansions.

5. References

Alving, A.E., Smits, A.J., and Watmuff, J.H., 1990, "Turbulent Boundary Layer Relaxation from Convex Curvature," Journal of Fluid Mechanics, 211: 529-556.

Arnette, S.A., Samimy, M., and Elliott, G.S., 1993a, "The Effect of Expansion on the Large Scale Structure of a Compressible Turbulent Boundary Layer," AIAA 24th Fluid Dynamics Conference, AIAA-93-2991.

Arnette, S.A., Samimy, M., and Elliott, G.S., 1993b, "On Streamwise Vortices in High Reynolds Number Supersonic Axisymmetric Jets," Physics of Fluids A, 5: 187-202.

Bevilaqua and Lykoudis, 1977, "Some Observations on the Mechanism of Entrainment," AIAA Journal, 15: 1194-1196.

Blackwelder, R.F. and Kovasznay, L.S.G., 1972, "Time Scales and Correlations in a Turbulent Boundary Layer," Physics of Fluids, 15: 1545-1554..

Bradshaw, P., 1974, "The Effect of Mean Compression or Dilatation on the Turbulence Structure of Supersonic Boundary Layers," Journal of Fluid Mechanics, 63: 449-464.

Brown, G.L. and Thomas, A.S.W., 1977, "Large Structure in a Turbulent Boundary Layer," Physics of Fluids, 20: S243-S251.

Chen, C.P. and Blackwelder, R.F., 1978, "Large-Scale Motion in a Turbulent Boundary Layer: a Study Using Temperature Contamination," Journal of Fluid Mechanics, 89: 1-31.

Cheng, R.K. and Ng, T.T., 1982, "Some Aspects of Strongly Heated Turbulent Boundary Layer Flow," Physics of Fluids, 25: 1333-1341.

Cogne, S., Forkey, J., Lempert, W., Miles, R.B., and Smits, A.J., 1993, "The Evolution of Large-Scale Structures in a Supersonic Turbulent Boundary Layer," Proceedings of the Symposium on Transitional and Turbulent Compressible Flows, ASME Fluids Engineering Conference.

Corcos, G.M., 1963, "Resolution of Pressure in Turbulence," The Journal of the Acoustical Society of America, 35: 192-199.

Dawson, J.D., 1993, "An Experimental Investigation of Supersonic Turbulent Boundary Layers After an Expansion via Wall Pressure Measurements", MS Thesis, Ohio State University.

Dawson, J.D. and Samimy, M., 1994, "The Effects of Expansion on a Supersonic Boundary Layer: Surface Pressure Measurements ", 32nd Aerospace Sciences Meeting & Exhibit, AIAA-94-0648 (submitted to AIAA Journal).

Deckker, B.E.L. and Weekes, M.E., 1976, "The Unsteady Boundary Layer in a Shock Tube," Proceedings Inst. Mechanical Engineering, 190: 287.

Deckker, B.E.L., 1980, "Boundary Layer on a Shock Tube Wall and at a Leading Edge Using Schlieren," Second International Symposium on Flow Visualization, Ruhr-Universitat Bochum, West Germany. Edited by W. Merzkirch, Hemisphere, 413.

Dussauge, J.P. and Gaviglio, J., 1987, "The Rapid Expansion of a Supersonic Turbulent Flow: Role of Bulk Dilatation," Journal of Fluid Mechanics, 174: 81-112.

Elliott, G.S., Samimy, M., and Arnette, S.A., 1992a, "Study of Compressible Mixing Layers Using Filtered Rayleigh Scattering Based Visualizations," AIAA Journal, 30: 2567-2569.

Elliott, G.S., Samimy, M., and Arnette, S.A., 1992b, "Filtered Rayleigh Scattering Based Measurements in Compressible Mixing Layers," 28th Joint Propulsion Conference, AIAA Paper 92-3543.

Elliott, G.S., Samimy, M., and Arnette, S.A., 1993a, "The Evolution of Large Scale Structures in Compressible Mixing Layers," Ninth Turbulent Shear Flow Conference, Kyoto, Japan.

Elliott, G.S., Samimy, M., and Arnette, S.A., 1993b, "Molecular Filter-Based Diagnostics in High Speed Flows ," 31st Aerospace Sciences Meeting & Exhibit, AIAA-93-0512.

Elliott, G.S., Samimy, M., and Arnette, S.A., 1994, "Details of a Molecular Filter-Based Velocimetry Technique," 32nd Aerospace Sciences Meeting & Exhibit, AIAA-94-0490.

Falco, R.E., 1977, "Coherent Motions in the Outer Region of Turbulent Boundary Layers," Physics of Fluids, 20: S124-S132.

Forkey, J., Cogne, S., Smits, A., Bogdonoff, S., Lempert, W.R., and Miles, R.B., 1993, "Time-Sequenced and Spectrally Filtered Rayleigh Imaging of Shock Wave and Boundary Layer Structure for Inlet Characterization," 29th Joint Propulsion Conference and Exhibit, AIAA Paper 93-2300.

Gillis, J.C. and Johnston, J.P., 1980, "Experiments on the Turbulent Boundary Layer Over Convex Walls and Its Recovery to Flat-Wall Conditions," In Turbulent Shear Flows 2, ed. Bradbury, L.J.S., Durst, F., Launder, B.E., Schmidt, F.W., and Whitelaw, J.H., Springer Verlag.

Guezennec, Y.G., Piomelli, N., and Kim, J., 1989, "On the Shape and Dynamics of Wall Structures in Turbulent Channel Flow," Physics of Fluids A, 1: 764-766.

Head, M.R. and Bandyopadhyay, P., 1981, "New Aspects of Turbulent Boundary-Layer Structure," Journal of Fluid Mechanics, 107: 297-338.

Hedley, T.B. and Keffer, J.F., 1974, "Some Turbulent/Non-Turbulent Properties of the Outer Intermittent Region of a Boundary Layer," Journal of Fluid Mechanics, 64: 645-678.

James, C.S., 1958, "Observations of Turbulent-Burst Geometry and Growth in Supersonic Flow," NASA TN 4235.

Kline, S.J., Reynolds, W.C., Schraub, F.A., and Runstadler, P.W., 1967, "The Structure of [illegible]ent Boundary Layers," Journal of Fluid Mechanics, 30: 741-773.

Kovasznay, L.S.G., Kibens, V., and Blackwelder, R.F., 1970, "Large-Scale Motion in the Intermittent Region of a Turbulent Boundary Layer," Journal of Fluid Mechanics, 41: 283-325.

Kim, J., 1987, "Overview of Research by the Turbulence Structure Group," Proceedings 1987 Summer Program Center for Turbulence Research , Center for Turbulence Research, Stanford CA, 231-235.

Lee, S., Lele, S.K., and Moin, P., 1992, "Simulation of Spatially Evolving Turbulence and the Applicability of Taylor's Hypothesis in Compressible Flow," Physics of Fluids A, 4: 1521-1530.

Lu, F.K. and Chung, K., 1992, "Downstream Influence Scaling of Turbulent Flow Past Expansion Corners," AIAA Journal, 30: 2976-2977.

Miles, R.B., Lempert, W.R., and Forkey, J., 1991, "Instantaneous Velocity Fields and Background Suppression by Filtered Rayleigh Scattering," 29th Aerospace Sciences Meeting, AIAA- 91-0357.

Miles, R.B., Forkey, J.,and Lempert, W.R., 1992, "Filtered Rayleigh Scattering Measurements in Supersonic/Hypersonic Facilities," AIAA 17th Aeropace Ground Testing Meeting, AIAA-92-3894.

Morkovin, M.V., 1955, "Effects of High Acceleration on a Turbulent Supersonic Shear Layer," Heat Transfer and Fluid Mechanics Institute, Stanford University.

Nakagawa, H. and Nezu, I., 1981, "Structure of Space-Time Correlations of Bursting Phenomena in an Open-Channel Flow," Journal of Fluid Mechanics, 104: 1-43.

Narisimha, R. and Sreenivasan, K.R., 1973, "Relaminarization in Highly Accelerated Turbulent Boundary Layers," Journal of Fluid Mechanics, 61: 417-447.

Narasimha, R. and Viswanath, P.R., 1975, "Reverse Transition a ansion Corner in Supersonic Flow," AIAA Journal, 13: 693-695.

Owen, F.K. and Hortsman, C.C., 1972, "On the Structure of Hypersonic Turbulent Boundary Layers," Journal of Fluid Mechanics, 53: 611-636.

Robinson, S.K., Kline, S.J., and Spalart, P.R., 1989, "A Review of Quasi-Coherent Structures in a Numerically-Simulated Turbulent Boundary Layer," NASA TM 102191.

Robinson, S.K., 1991, "The Kinematics of Turbulent Boundary Layer Structure," NASA TM 103859.

Robinson, S.K., 1986, "Space-Time Correlation Measurements in a Compressible Turbulent Boundary Layer," AIAA Paper 86-1130.

Robinson, S.K., 1991, "Coherent Motions in the Turbulent Boundary Layer," Annual Review of Fluid Mechanics, 23: 601-639.

Samimy, M., Arnette, S.A., and Elliott, G.S., 1994, "Streamwise Structures in a High Reynolds Number Supersonic Boundary Layer," to appear in March, 1994 issue of Physics of Fluids.

Seiff, A. and Short, B.J., 1958, "An Investigation of Supersonic Turbulent Boundary Layers on Slender Bodies of Revolution in Freeflight by use of a Mach-Zehnder Interferometer and Shadowgraph," NASA TN4364.

Smith, M.W. and Smits, A.J., 1988, "Cinematic Visualization of Coherent Density Structures in a Supersonic Turbulent Boundary Layer," AIAA 26th Aerospace Sciences Meeting, AIAA-88-0500.

Smith, M. Smits, A., and Miles, R., 1989, "Compressible Boundary-Layer Density Cross Sections by UV Rayleigh Scattering," Optics Letters, 14: 916-918.

Smith, D.R. and Smits, A.J., 1991, "The Rapid Expansion of a Turbulent Boundary Layer in a Supersonic Flow," Theoret. Comput. Fl. Dyn., 2:319-328.

Smits, A.J., Young, S.T.B., and Bradshaw, P., 1979, "The Effect of Short Regions of High Surface Curvature on Turbulent Boundary Layers," Journal of Fluid Mechanics, 94: 209-242.

Smits, A.J., Spina, E.F., Alving, A.E., Smith, R.W., Fernando, E.M. and Donovan, J.F., 1989, "A Comparison of the Turbulence Structure of Subsonic and Supersonic Boundary Layers," Physics of Fluids A, 1: 1865-1875.

Smits, A.J. and Wood, D.H., 1985, "The Response of Turbulent Boundary Layers to Sudden Perturbations," Annual Review of Fluid Mechanics, 17: 321-358.

Spina, E.F., Smits, A.J., and Robinson, S.K., 1994, "The Physics of Supersonic Turbulent Boundary Layers," to appear in Annual Review of Fluid Mechanics.

Spina, E.F., Donovan, J.F., and Smits, A.J., 1991, "On the Structure of High-Reynolds-Number Supersonic Turbulent Boundary Layers," Journal of Fluid Mechanics, 222: 293-327.

Spina, E.F. and Smits, A.J., 1987, "Organized Structures in a Compressible, Turbulent Boundary Layer," Journal of Fluid Mechanics, 182: 85-109.

Tetervin, N., 1967, "An Analytical Investigation of the Flat Plate Turbulent Boundary Layer in Compressible Flow," NOLTR 67-39, Aerodynamics Research Report 286, Naval Ordnance Lab, Silver Springs, MD.

Thomann, H., 1968, "Effect of Streamwise Wall Curvature on Heat Transfer in a Turbulent Boundary Layer," Journal of Fluid Mechanics, 33: 283-292.

Van Dyke, M., 1982, An Album of Fluid Motion, The Parabolic Press, Stanford, CA.

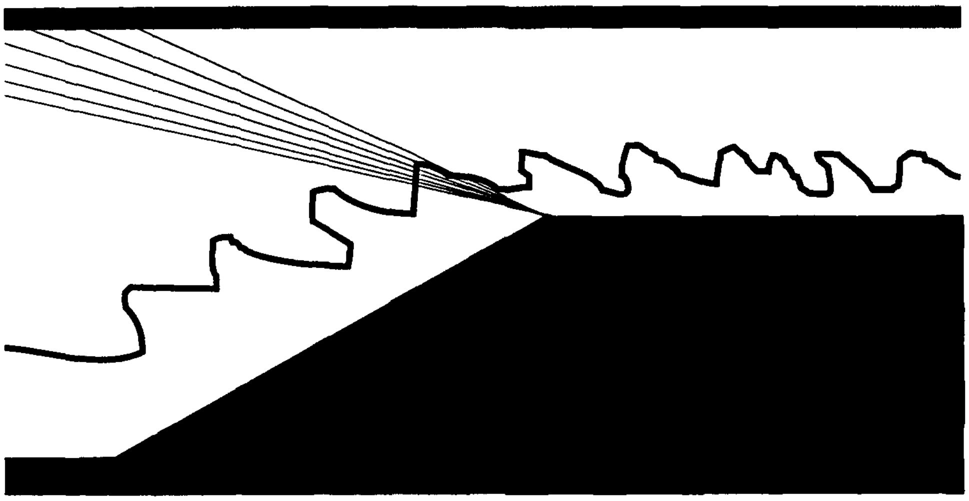

Figure 1. Schematic depiciting the tunnel configuration for the passage of compressible turbulent boundary layers through expansion regions.

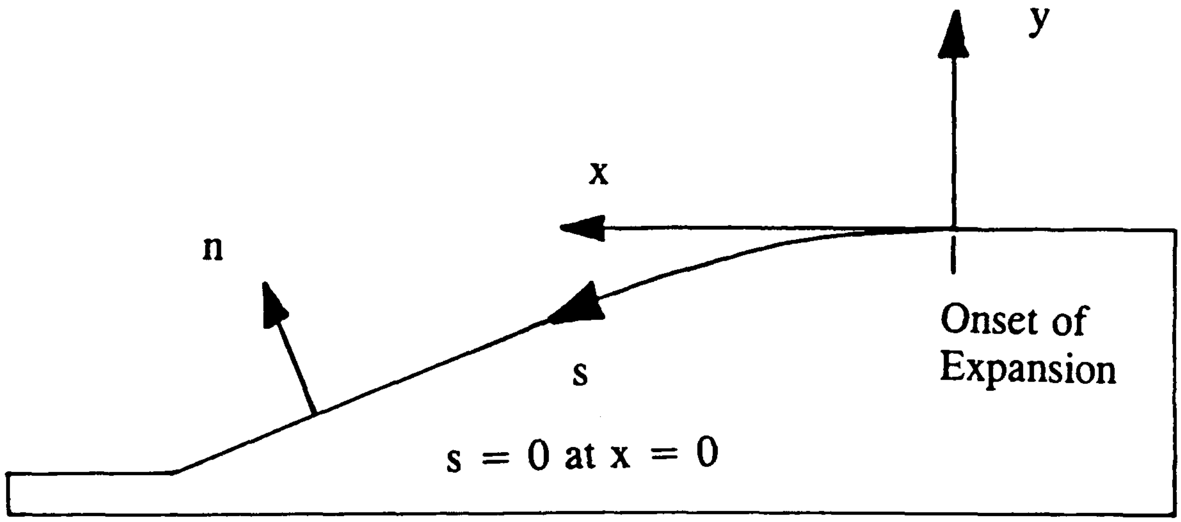

Figure 2. Schematic illustrating the coordinate system used to specify measurement locations.

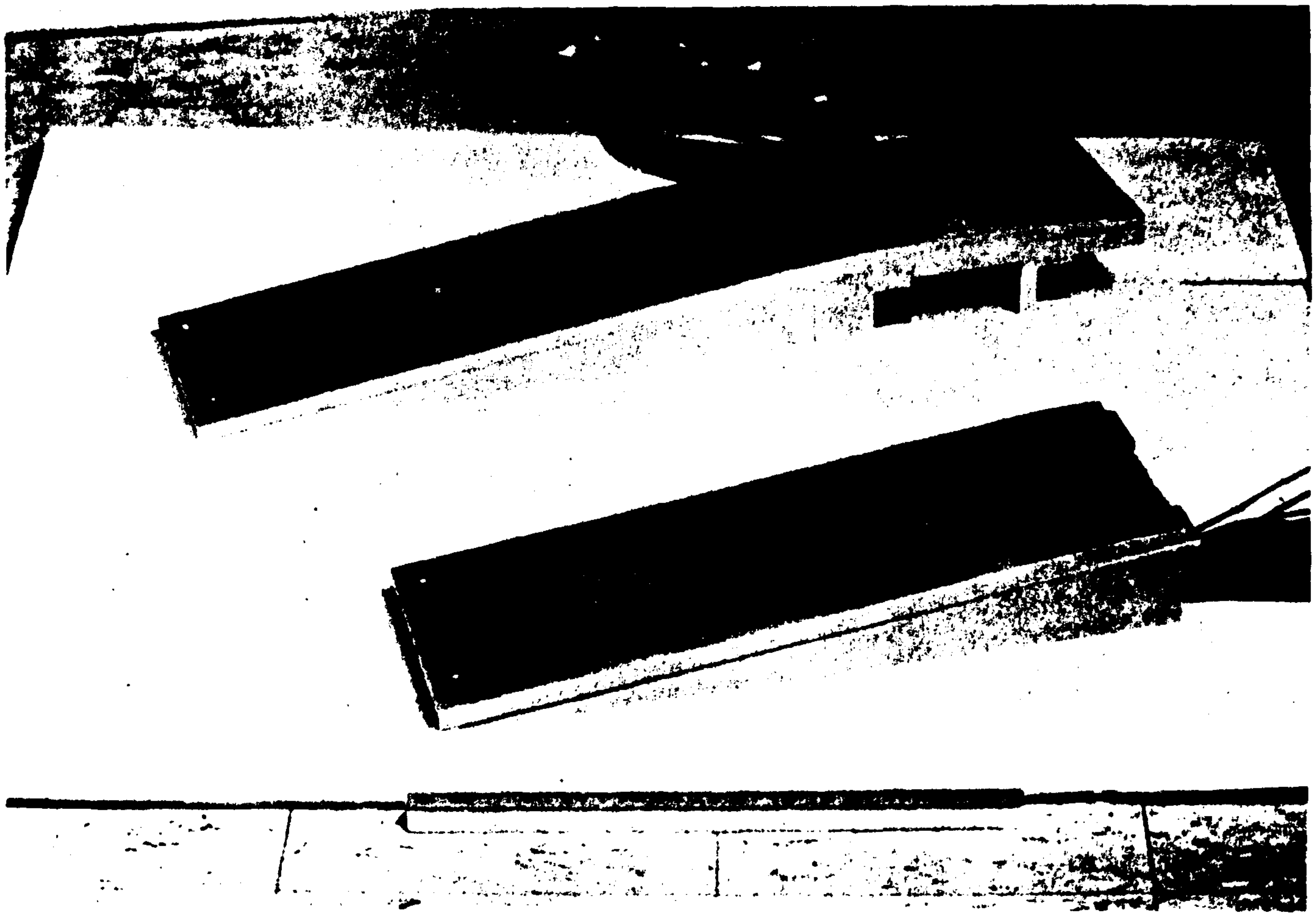

Figure 3. Photographs of the 7° centered and gradual expansion models. The centered expansion model is attached to the transitional model that connects to the splitter plate. The holes in the models are for the insertion of a transducer plug.

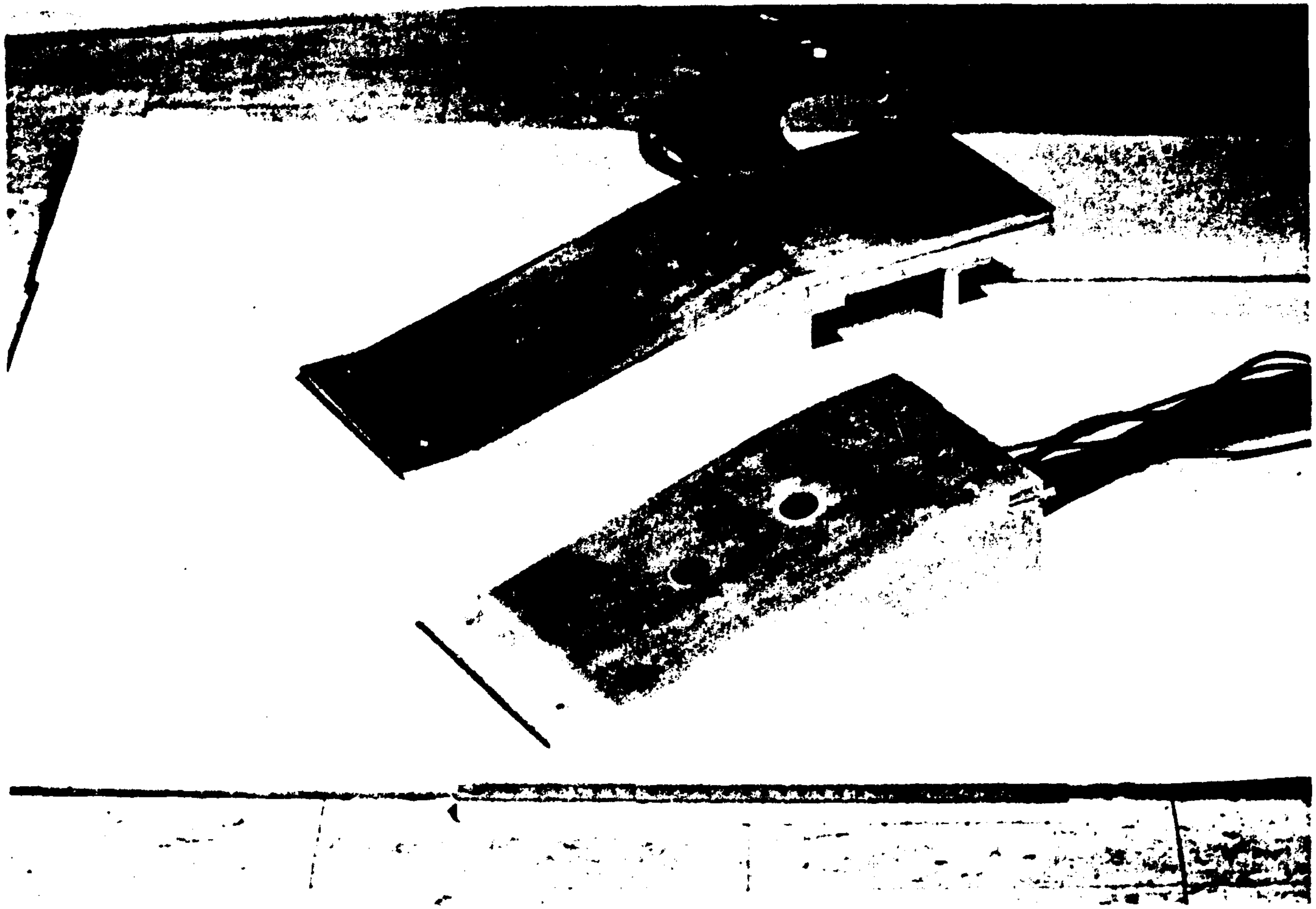

Figure 4. Photographs of the 14° centered and gradual expansion models. The centered expansion model is attached to the transitional model that connects to the splitter plate. The holes in the models are for the insertion of a transducer plug.

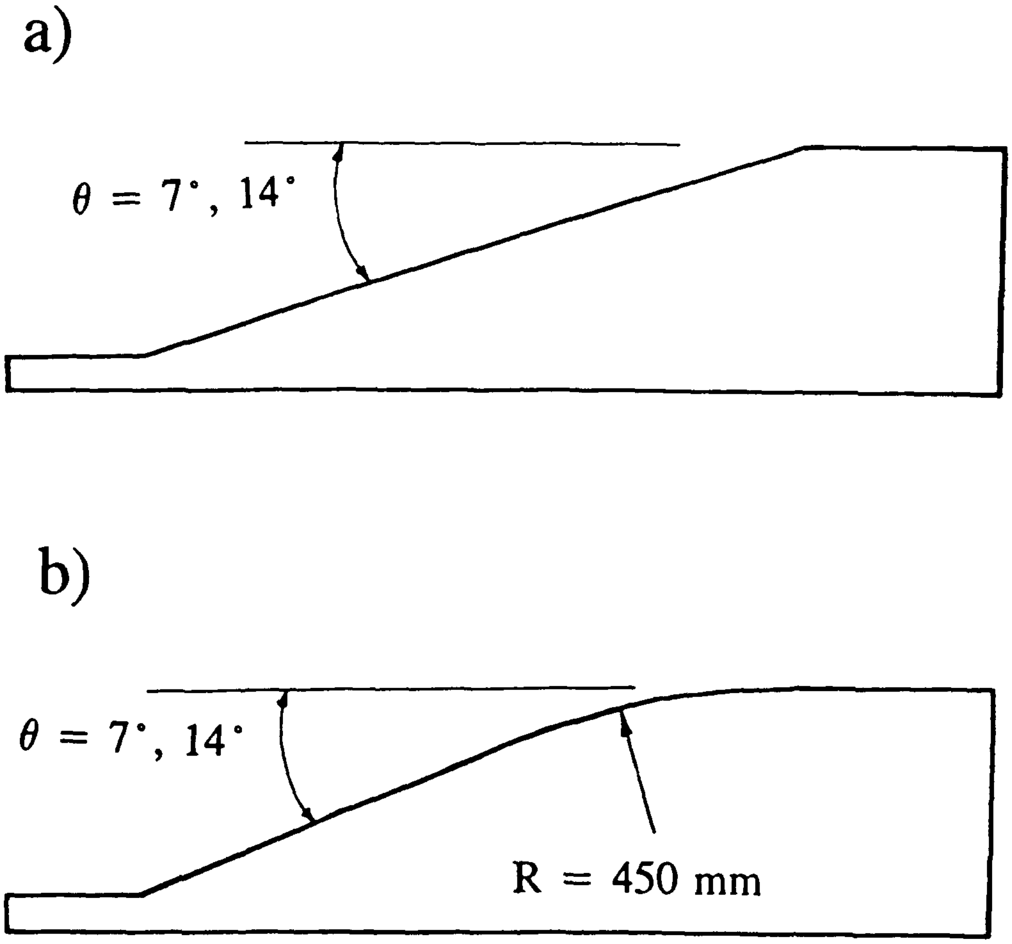

Figure 5. Schematics of the two-dimensional a) centered and b) gradual expansion models.

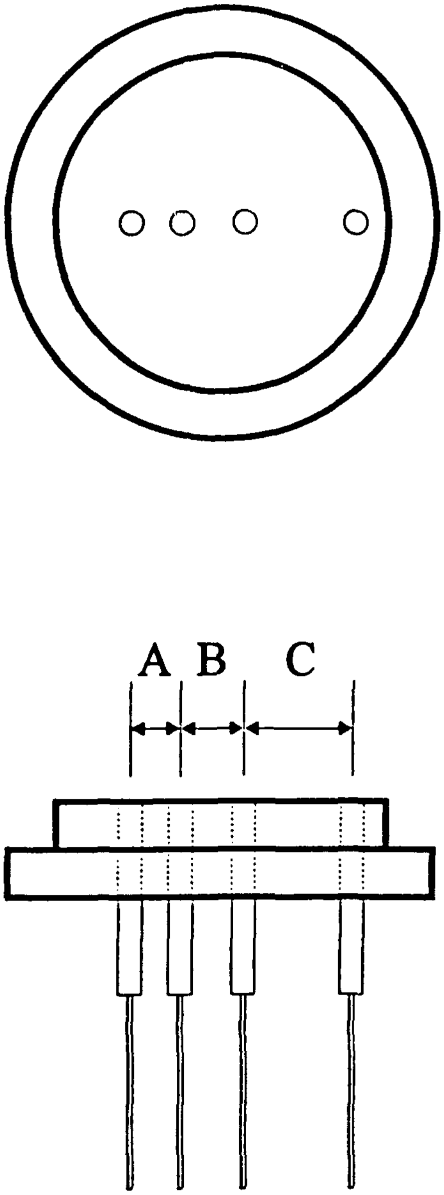

Figure 6. Top and side view schematics of the transducer plug, which contains four high frequency response pressure transducers mounted flush with the top surface. The separations between adjacent transducers are A = 3.0 mm, B = 4.5 mm, and C = 7.5 mm.

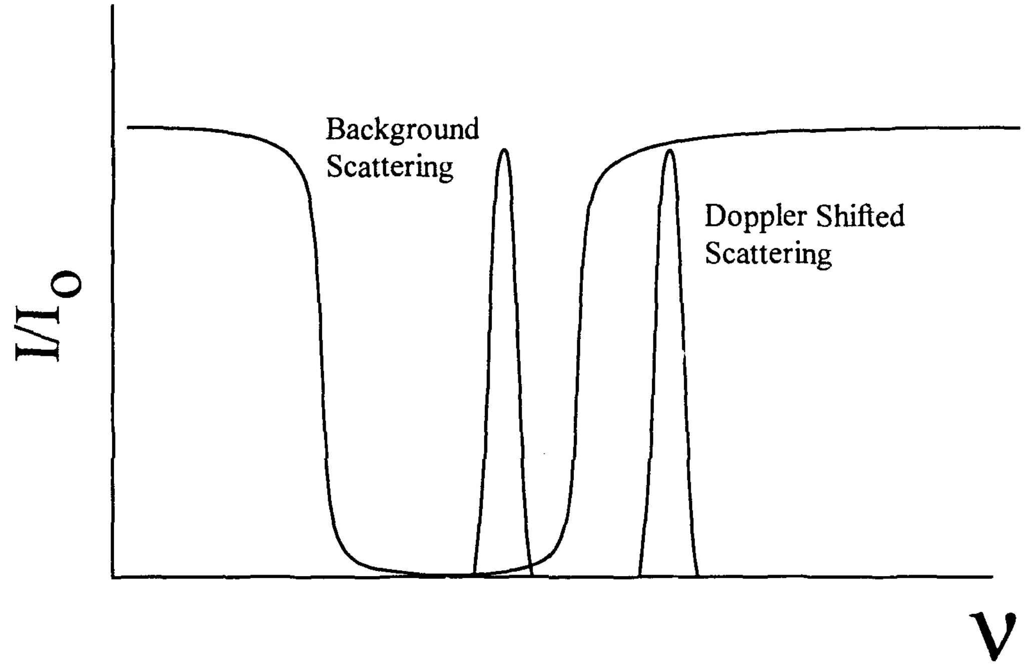

Figure 7. Schematic of the background suppression process employed in Filtered Rayleigh Scattering visualizations.

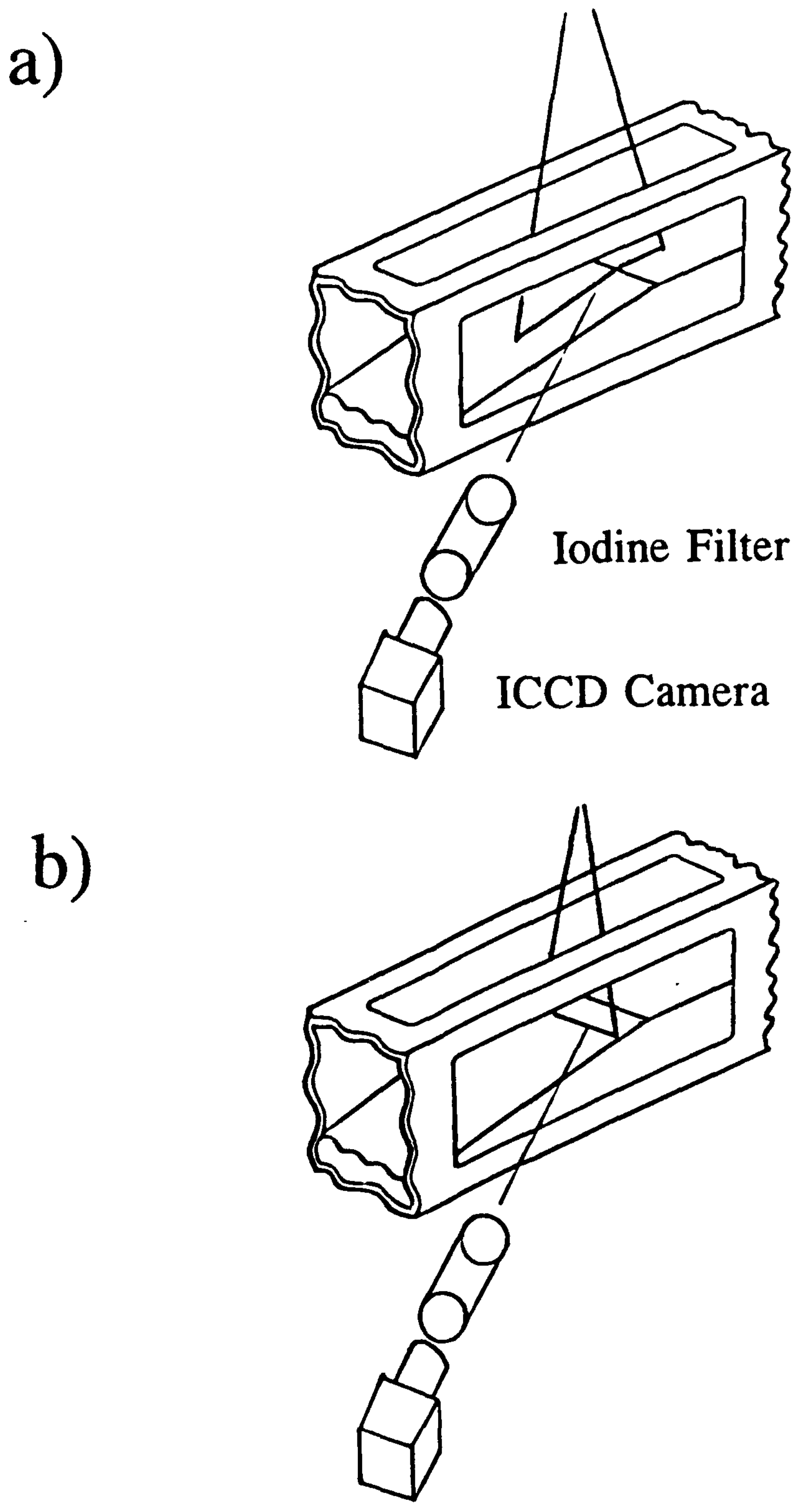

Figure 8. Schematics of the laser sheet and camera/filter configuration for a) streamwise and b) spanwise filtered Rayleigh scattering visualizations.

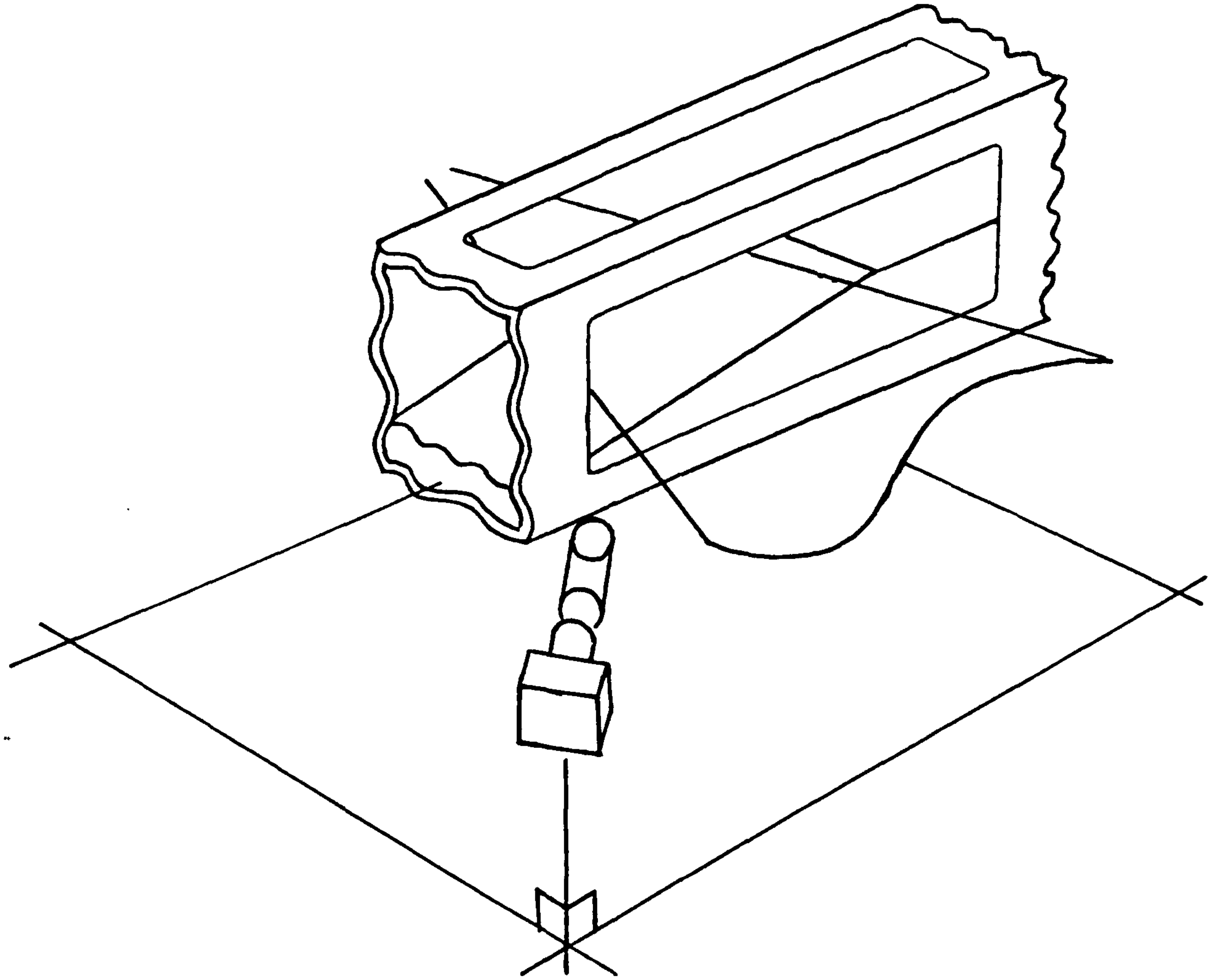

Figure 9. Schematic of the laser sheet and camera/filter configuration for plan view filtered Rayleigh scattering visualizations. The width of the laser sheet runs parallel to the model surface. The cameral is approximately 45° downstream of the spanwise-aligned axis of the laser sheet. The camera is approximately 35° above the plane of the laser sheet.

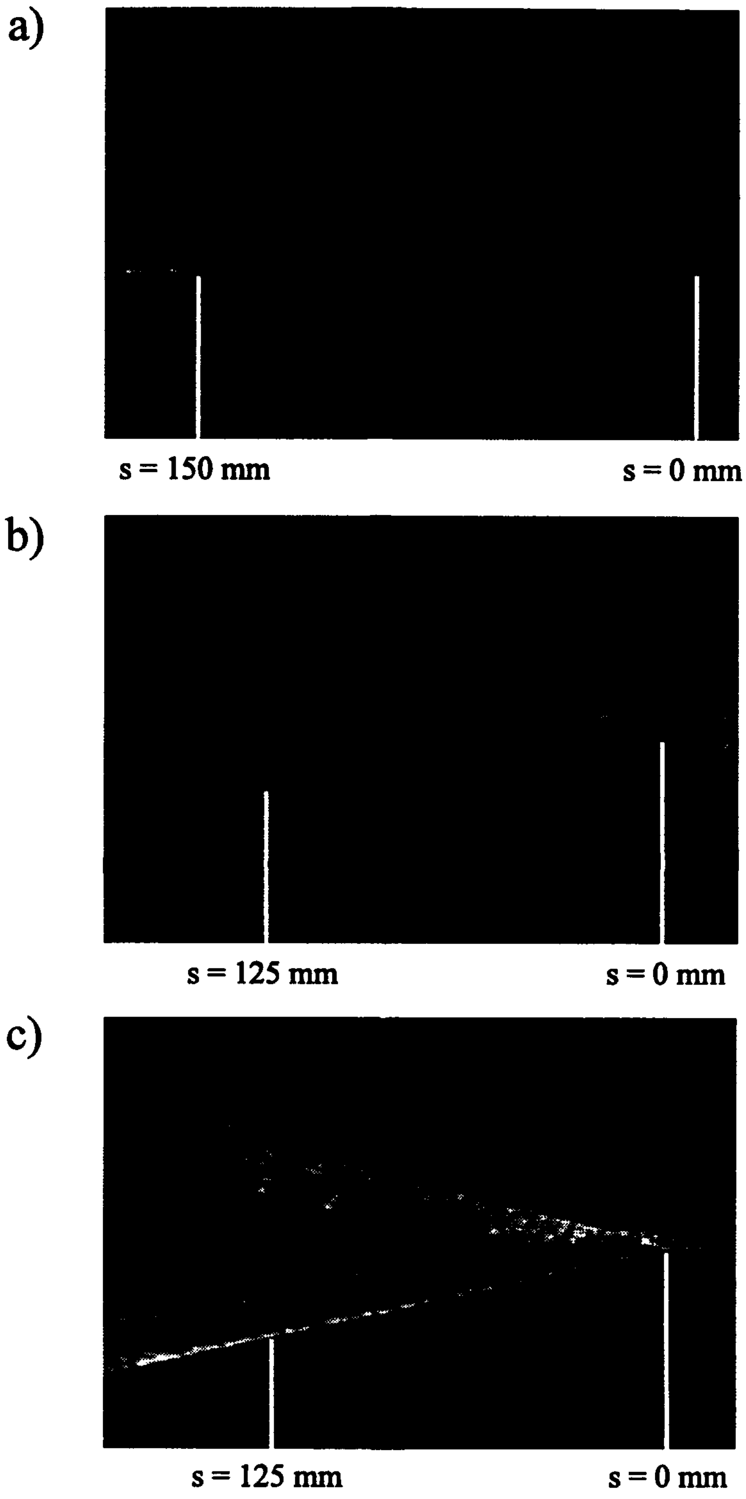

Figure 10. Instantaneous schlieren views of the (a) flat plate, (b) 7° centered expansion, and (c) 14° centered expansion boundary layers.

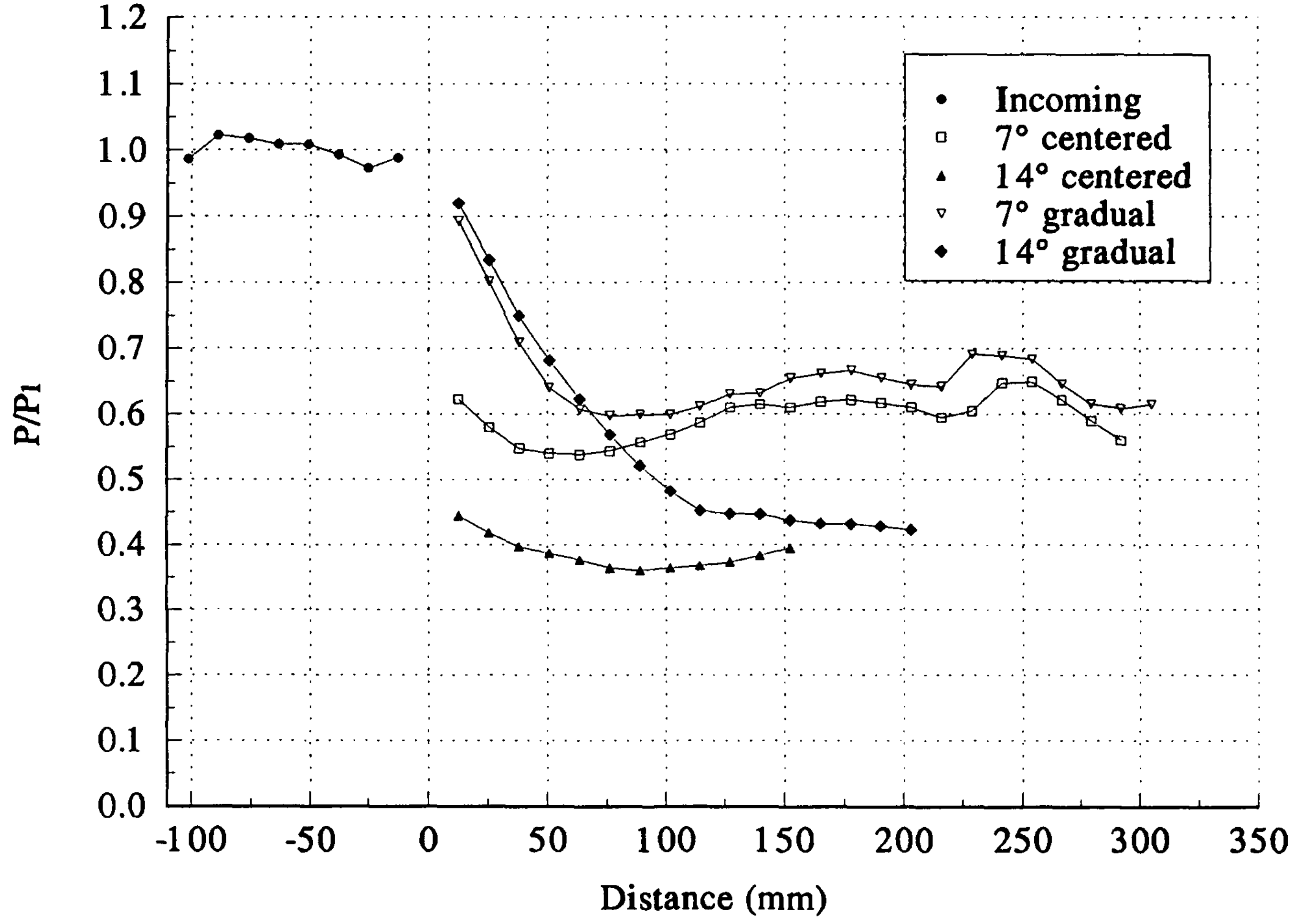

Figure 11. Streamwise mean static pressure distribution at the model surfaces for the incoming and expanded boundary layers (P_1 = 21.94 kPa).

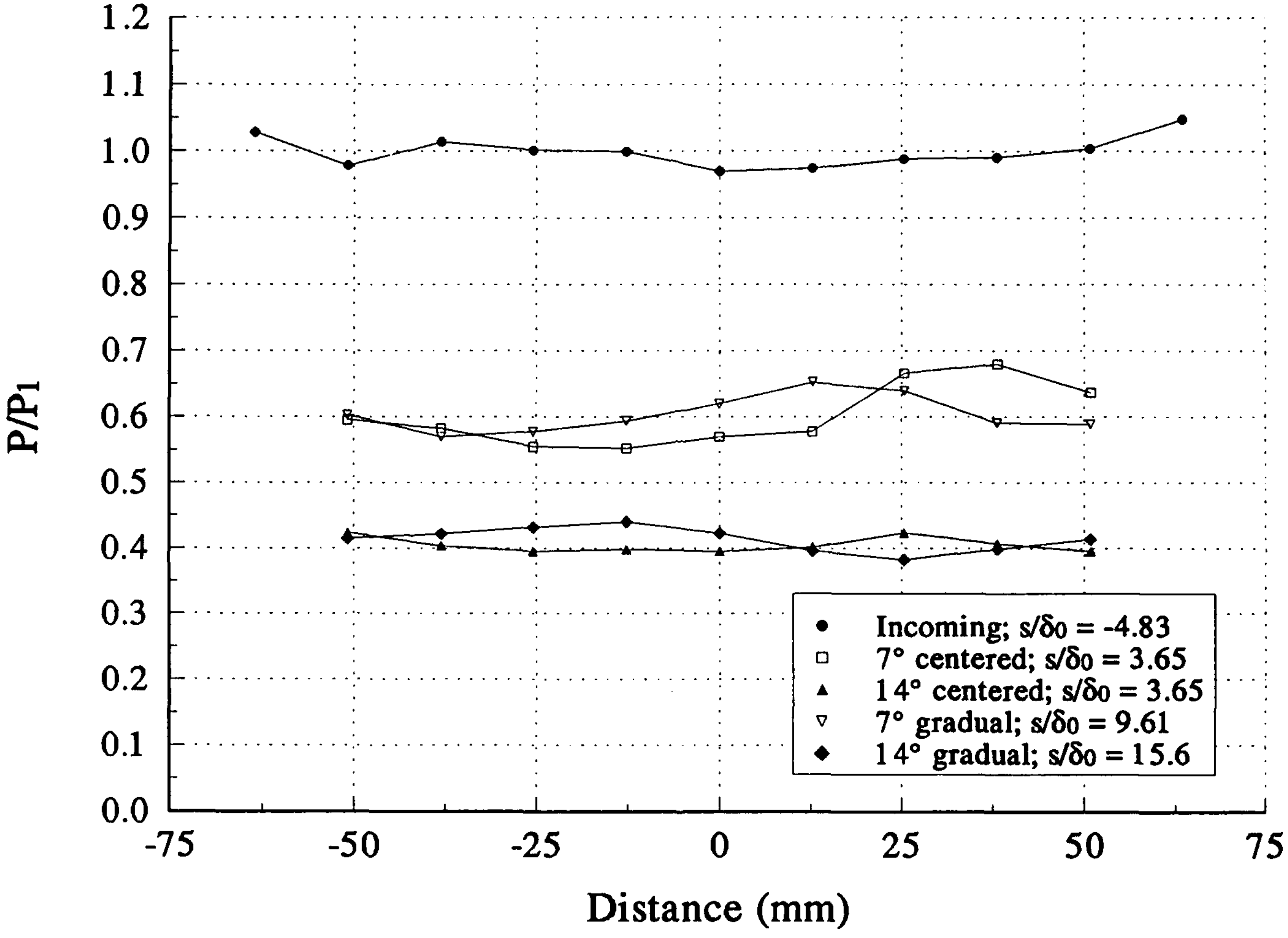

Figure 12. Spanwise mean static pressure distribution at the model surfaces for the incoming and expanded boundary layers (P_1 = 22.31 kPa).

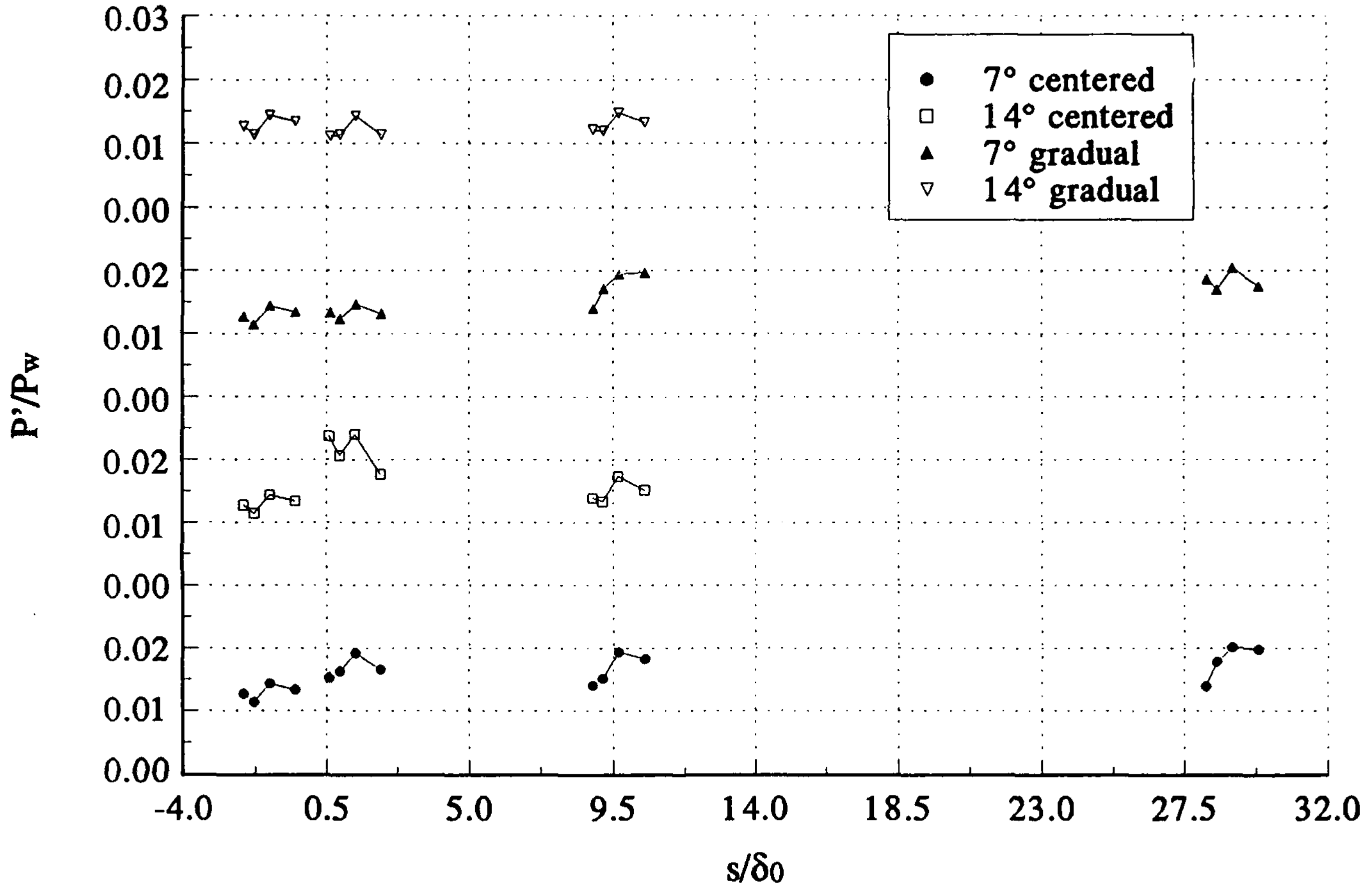

Figure 13. RMS surface pressure fluctuation normalized by the local mean static pressure along the expansion models. The plots for the different models have been staggered vertically.

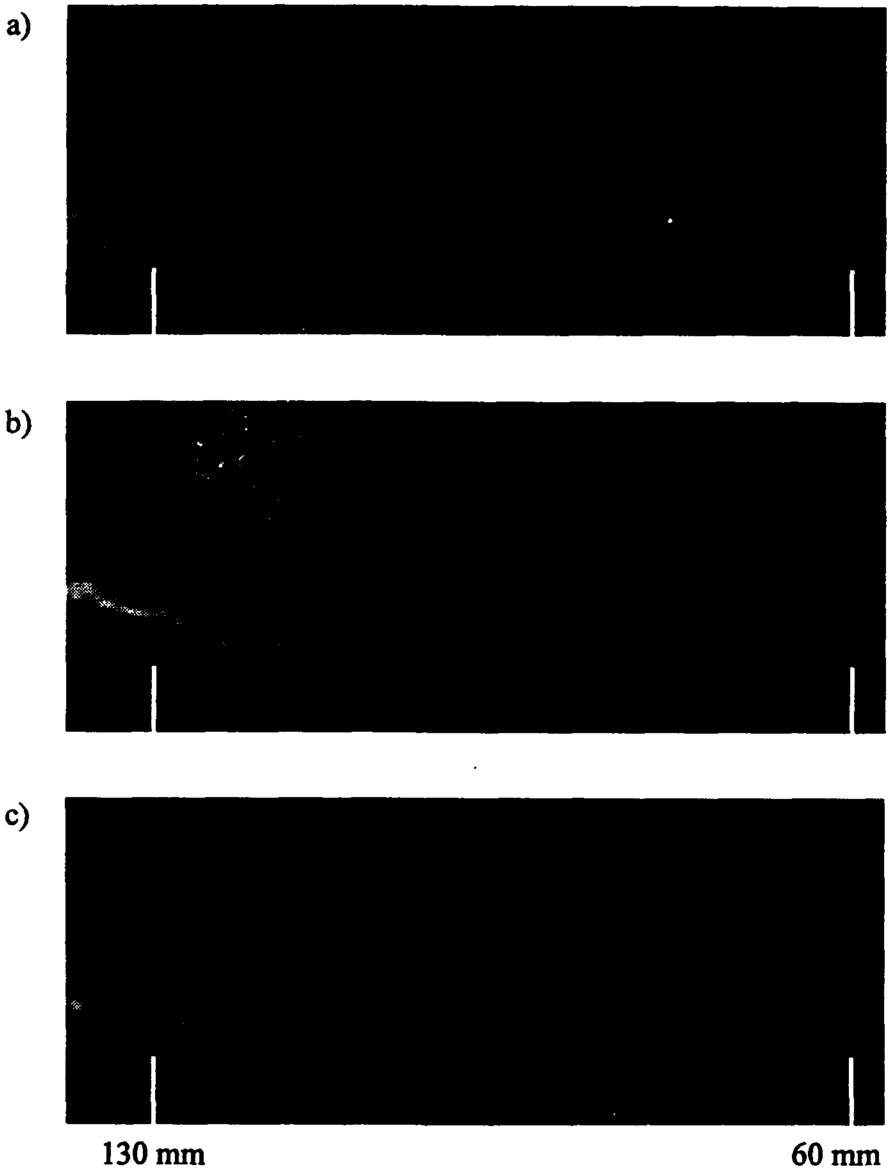

Figure 14. Instantaneous schlieren images of the flat plate boundary layer.

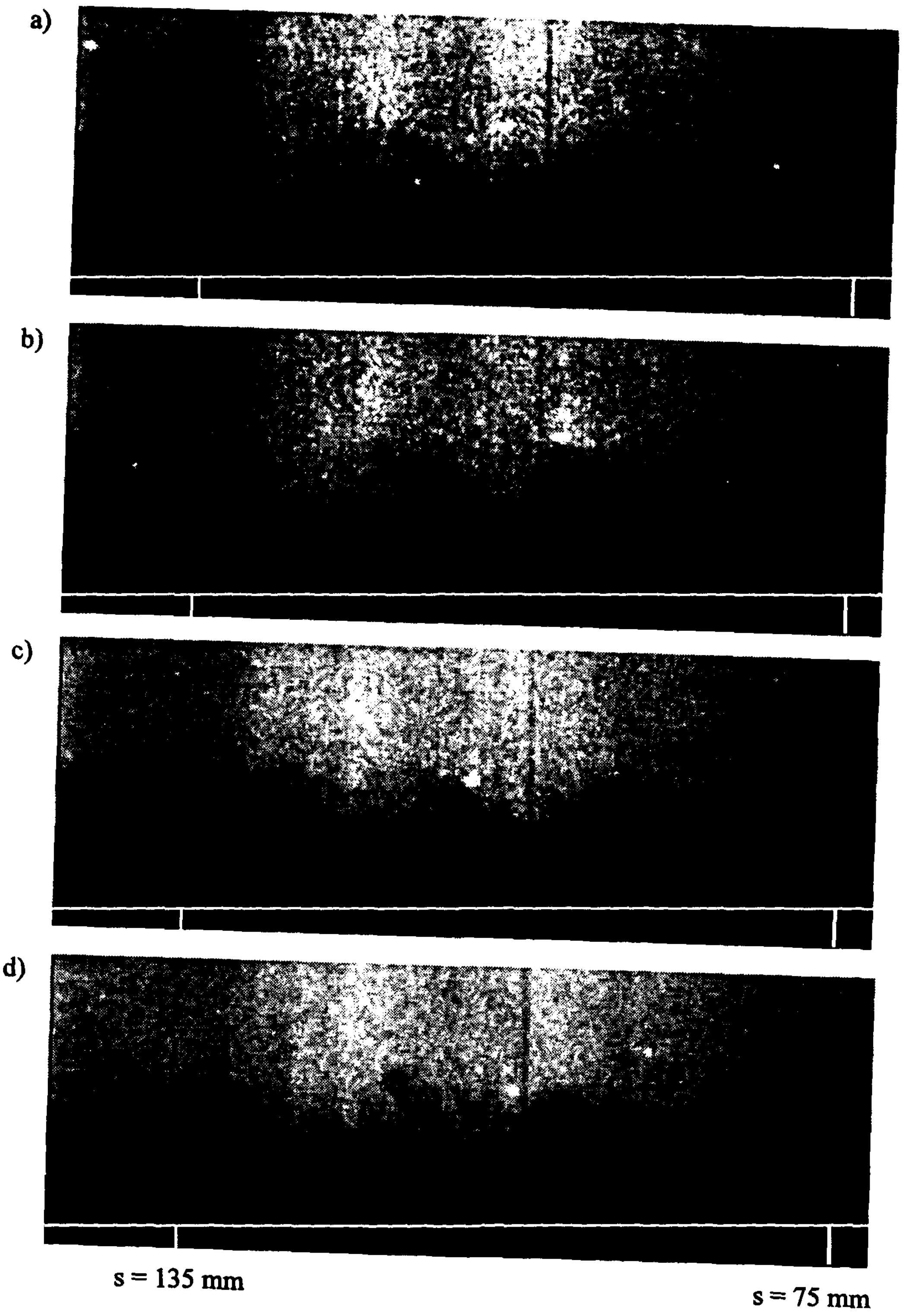

Figure 15. Instantaneous FRS streamwise views of the flat plate boundary layer. The added white lines indicate the position of the model surface. Indicated distances are relative to s = 0 mm at the position where the expansion regions begin when an expansion model is installed.

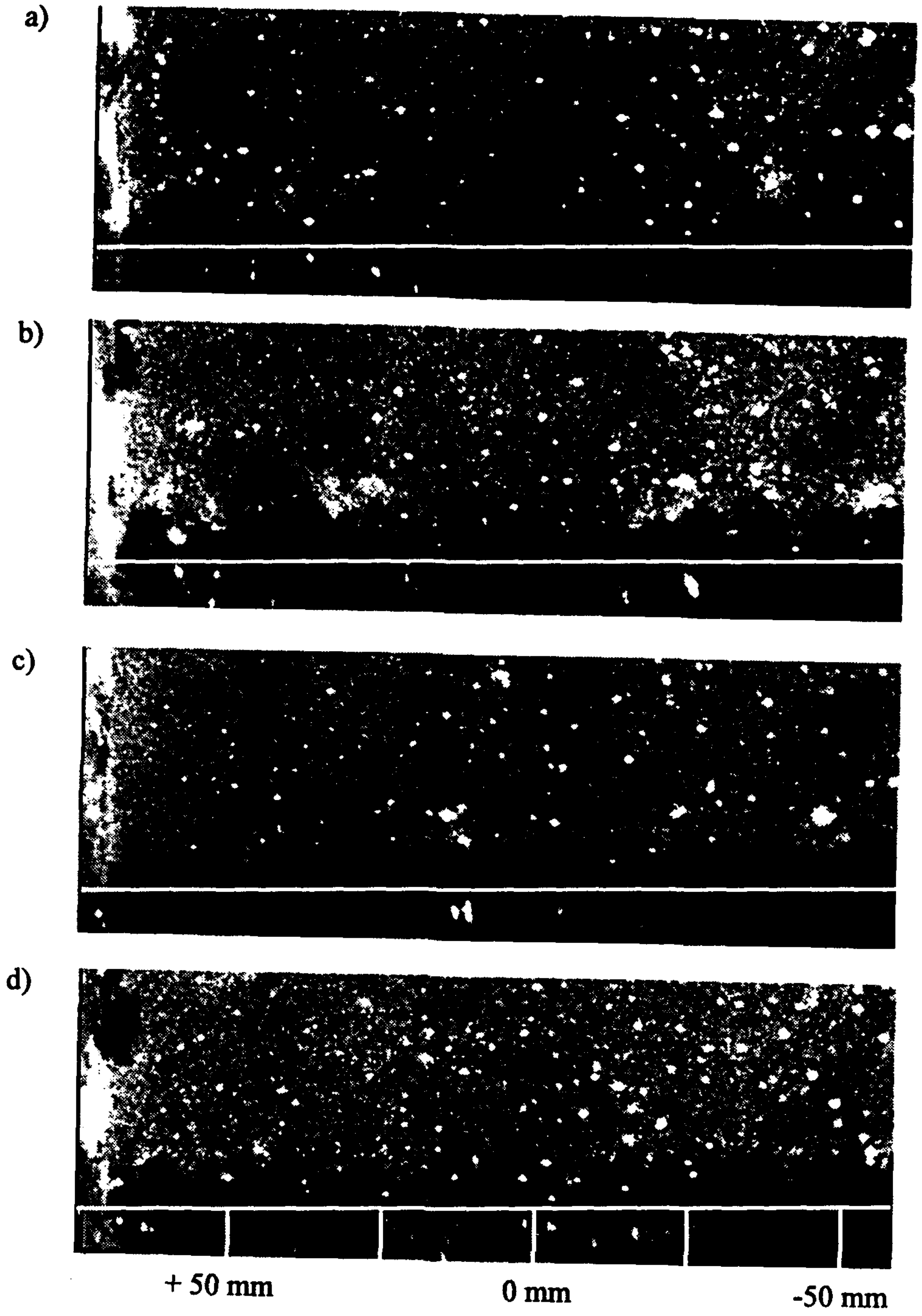

Figure 16. Instantaneous FRS spanwise views of the flat plate boundary layer 25 mm upstream of the position corresponding to the beginning of the expansion regions. The white lines indicate the model surface.

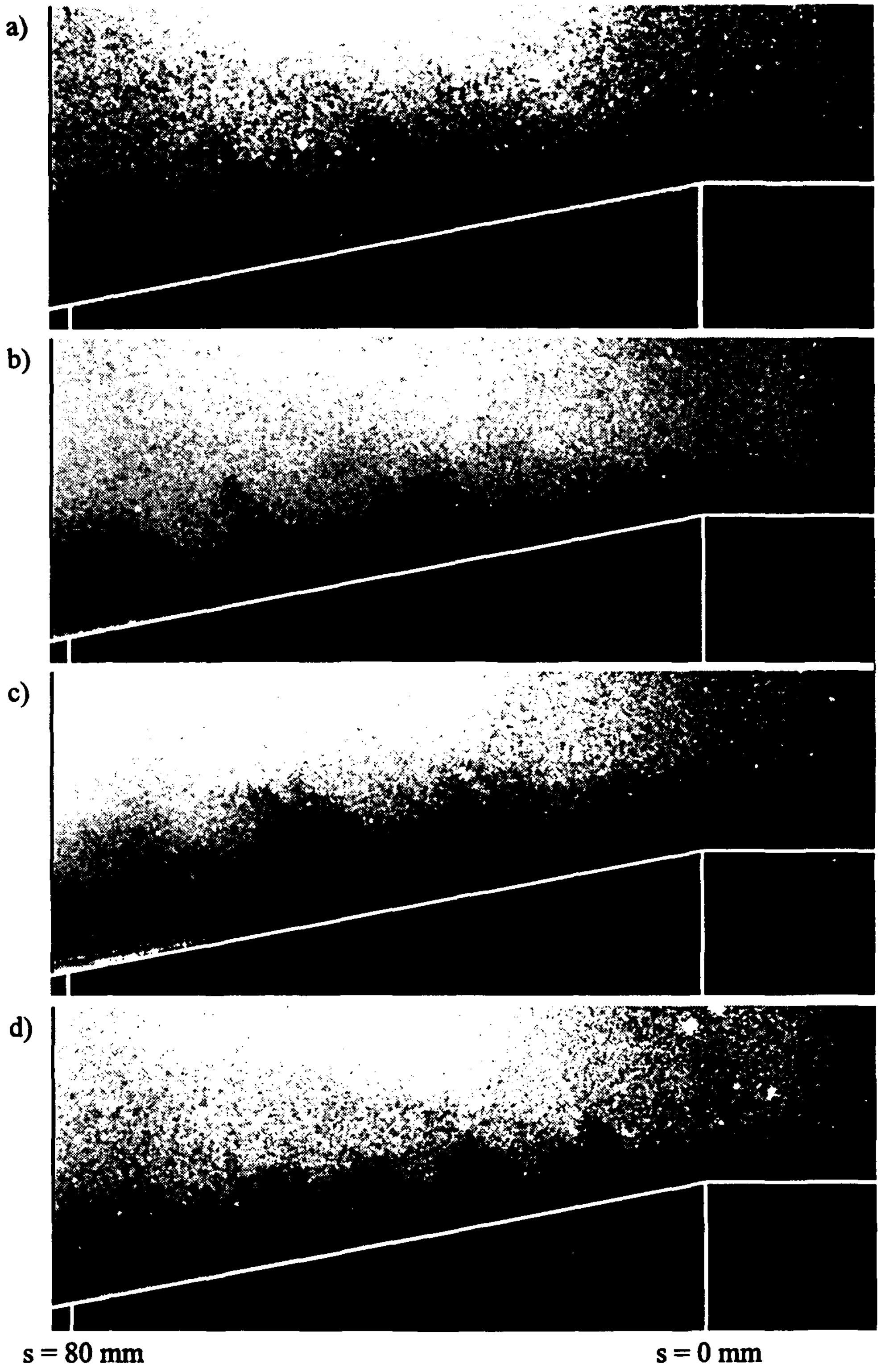

Figure 17. Instantaneous FRS streamwise views of the 7°centered expansion region. The added white lines indicate the position of the model surface.

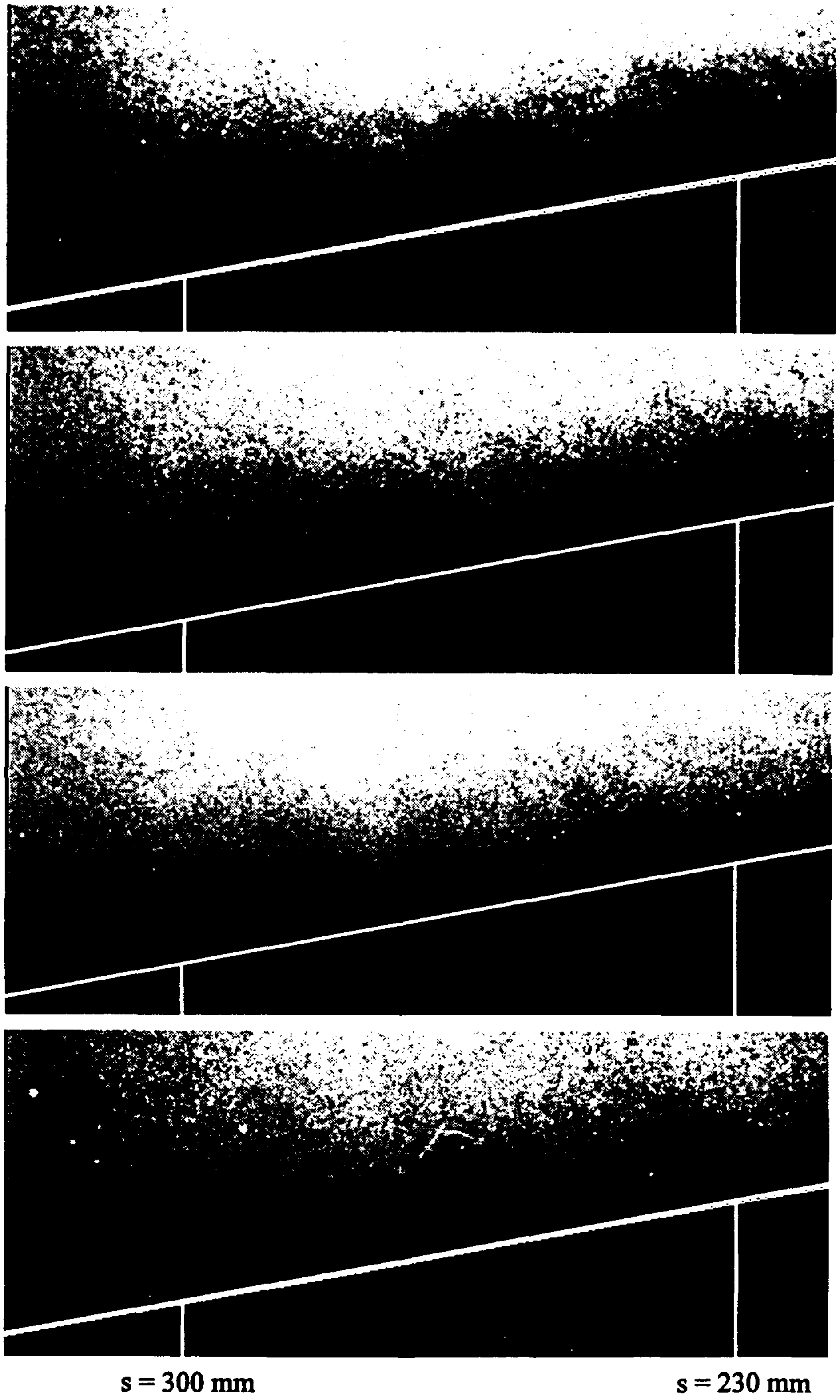

Figure 18. Instantaneous FRS streamwise views downstream of the 7°centered expansion region. The added white lines indicate the model surface.

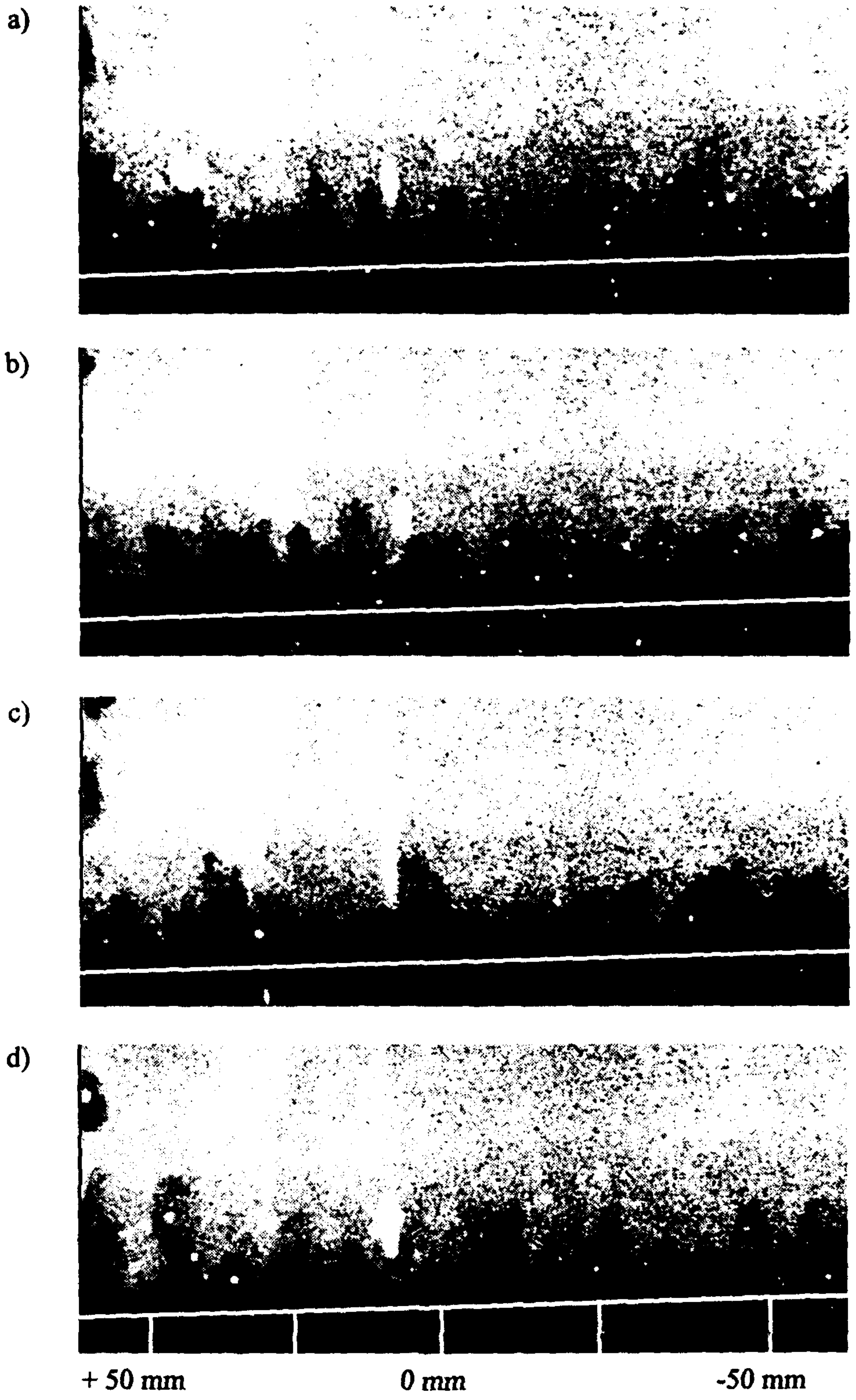

Figure 19. Instantaneous FRS spanwise views of the boundary layer 4.2 δ_o downstream of the beginning of the 7°centered expansion (δ_o= 9.2 mm).

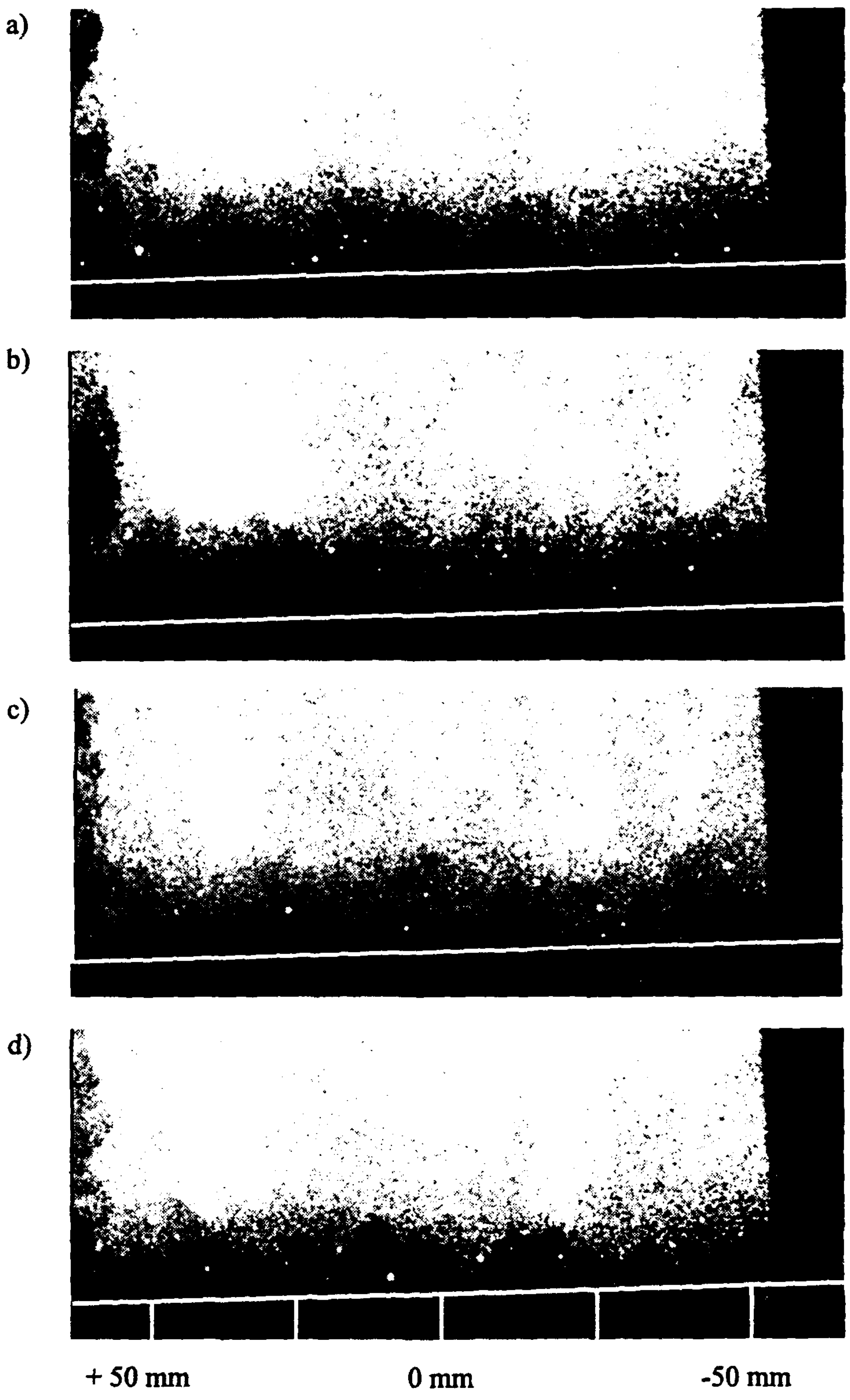

Figure 20. Instantaneous FRS spanwise views of the boundary layer 13.9 δ_o downstream of the beginning of the 7°centered expansion (δ_o= 9.2 mm).

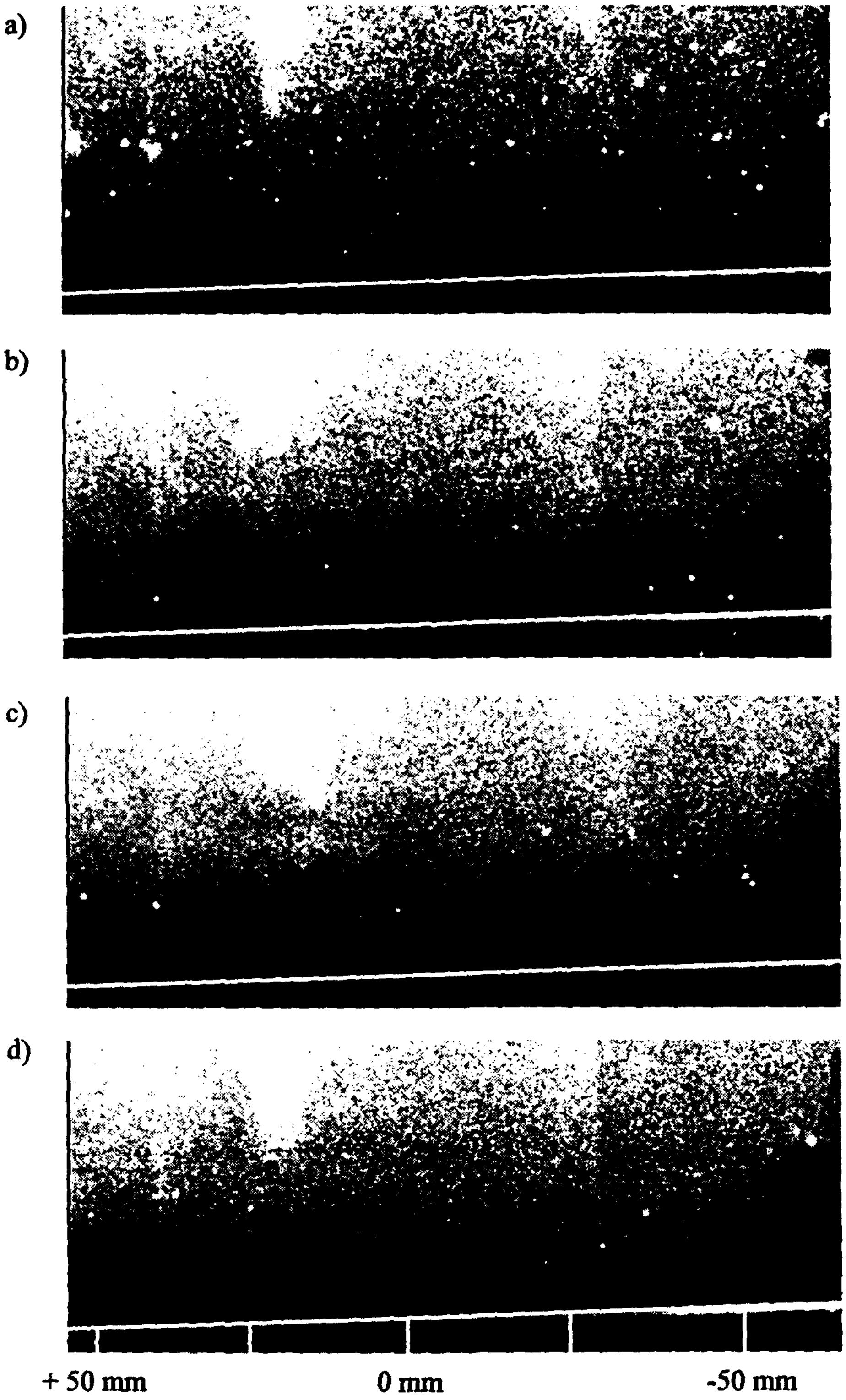

Figure 21. Instantaneous FRS spanwise views of the boundary layer 24.3 δ_o downstream of the beginning of the 7°centered expansion (δ_o= 9.2 mm).

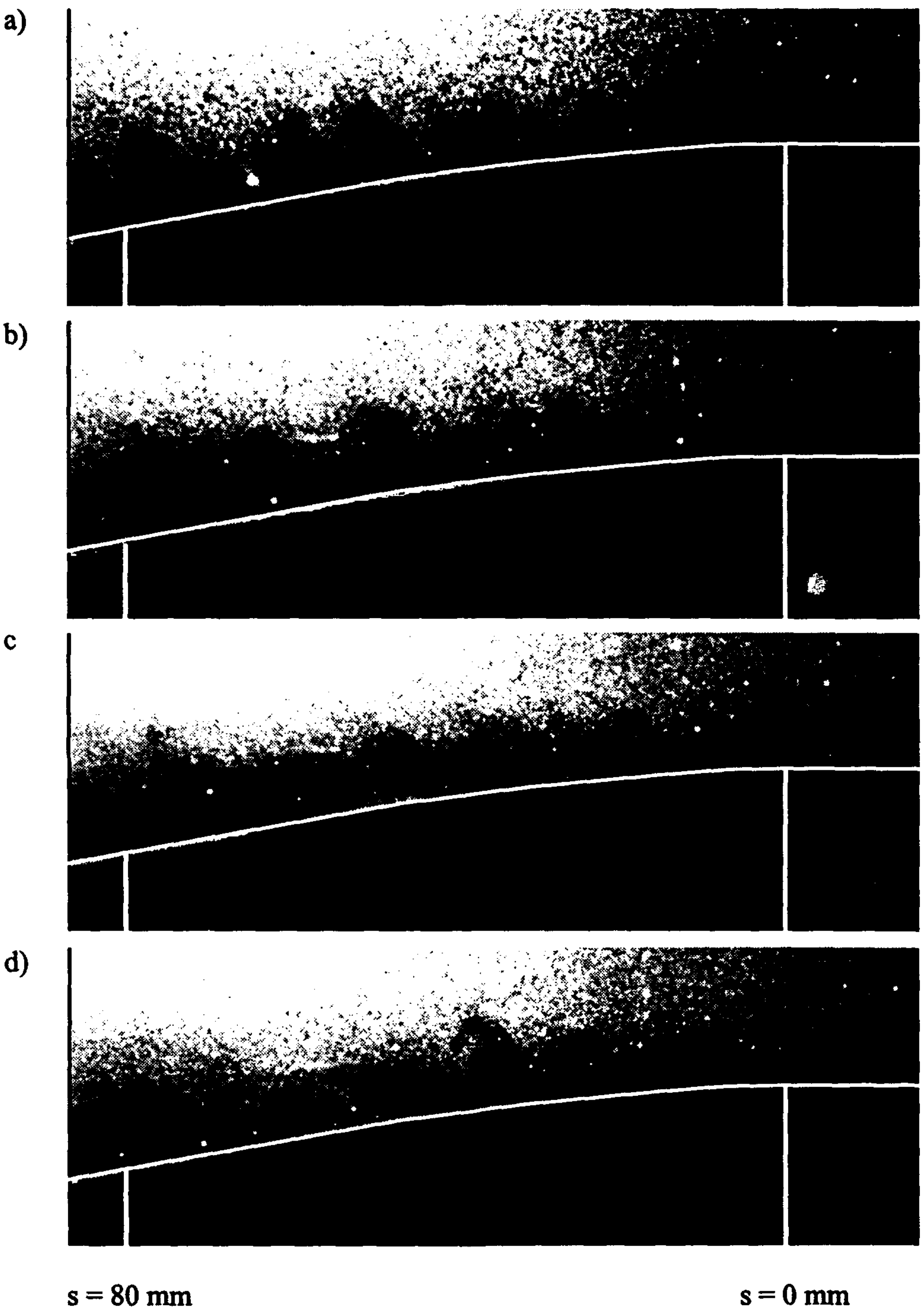

Figure 22. Instantaneous FRS streamwise views of the 7° gradual expansion region. The added white lines indicate the position of the model surface.

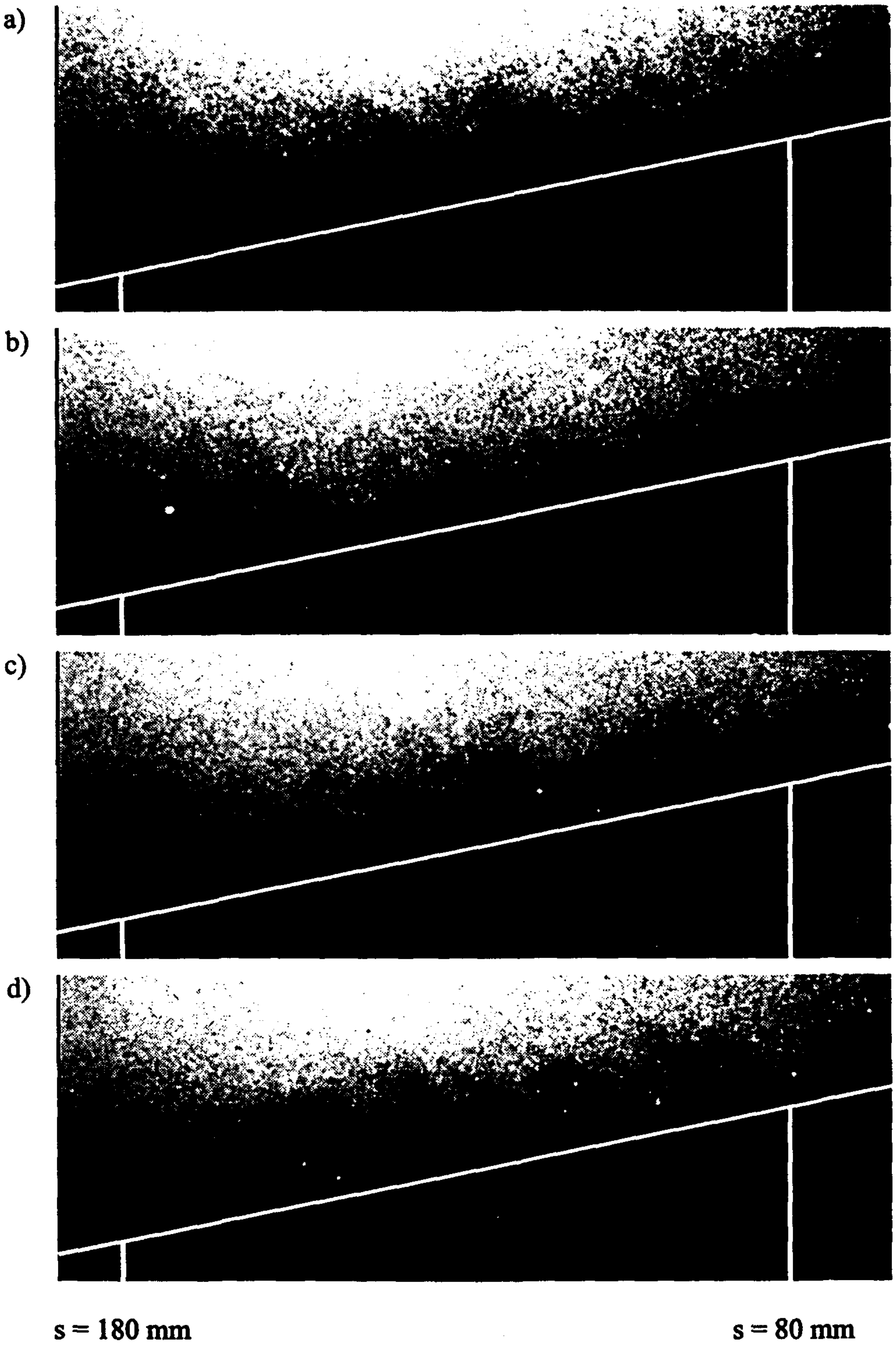

Figure 23. Instantaneous FRS streamwise views of the boundary layer downstream of the 7° gradual expansion. The added white lines indicate the position of the model surface.

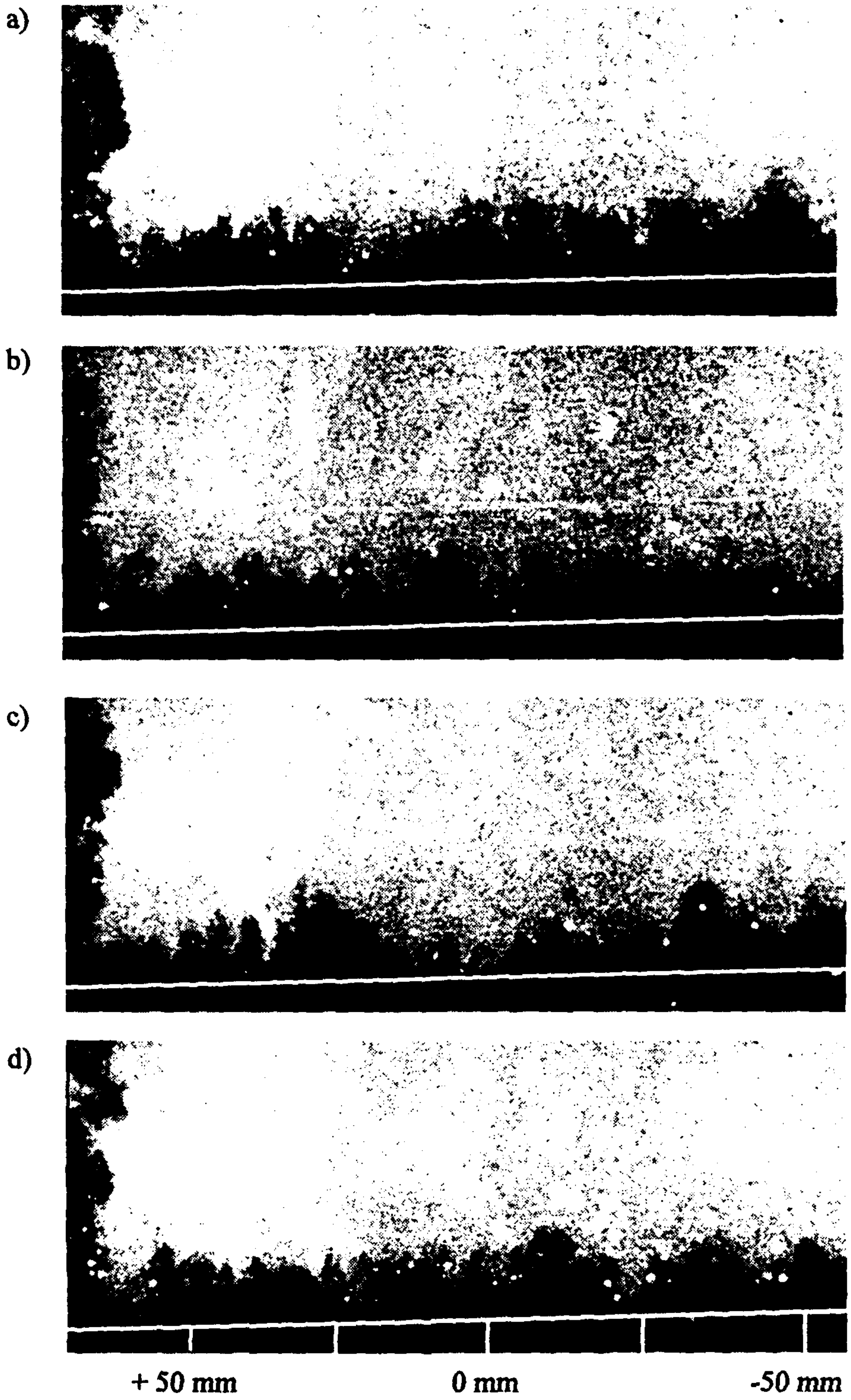

Figure 24. Instantaneous FRS spanwise views of the boundary layer 4.1 δ_o downstream of the beginning of the 7° gradual expansion (δ_o= 9.2 mm).

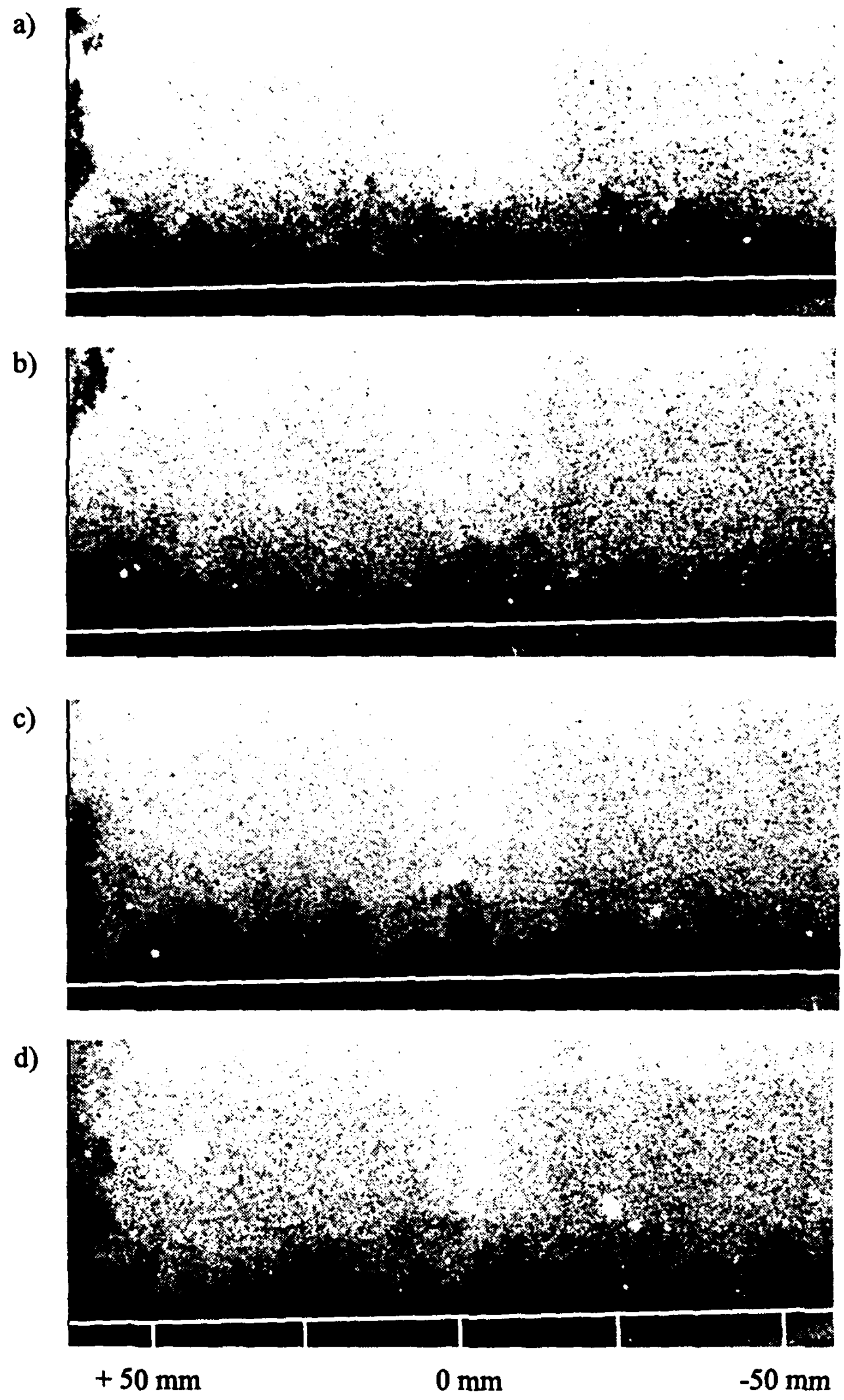

Figure 25. Instantaneous FRS spanwise views of the boundary layer 14.1 δ_o downstream of the beginning of the 7° gradual expansion (δ_o= 9.2 mm).

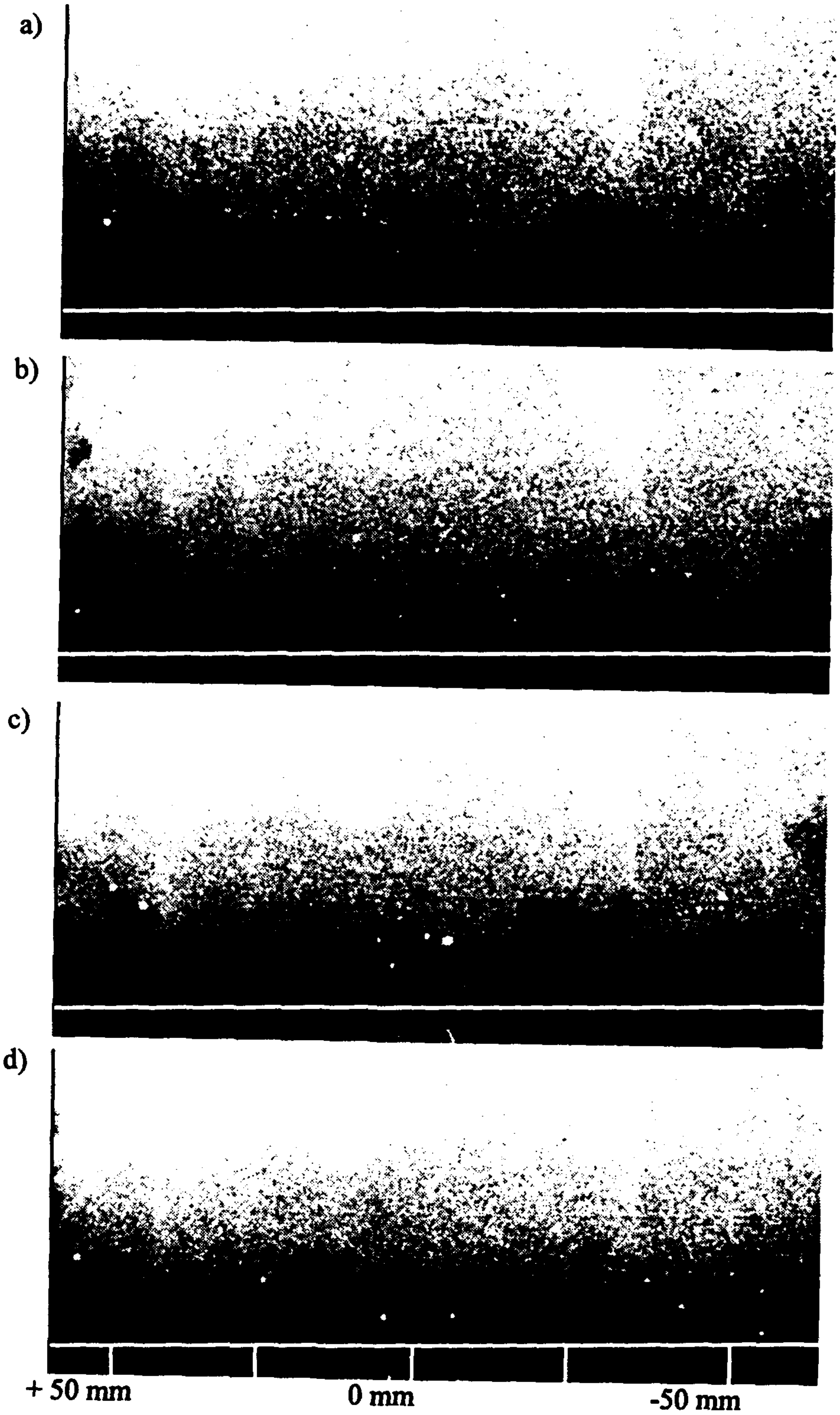

Figure 26. Instantaneous FRS spanwise views of the boundary layer 24.2 δ_o downstream of the beginning of the 7° gradual expansion ($\delta_o = 9.2$ mm).

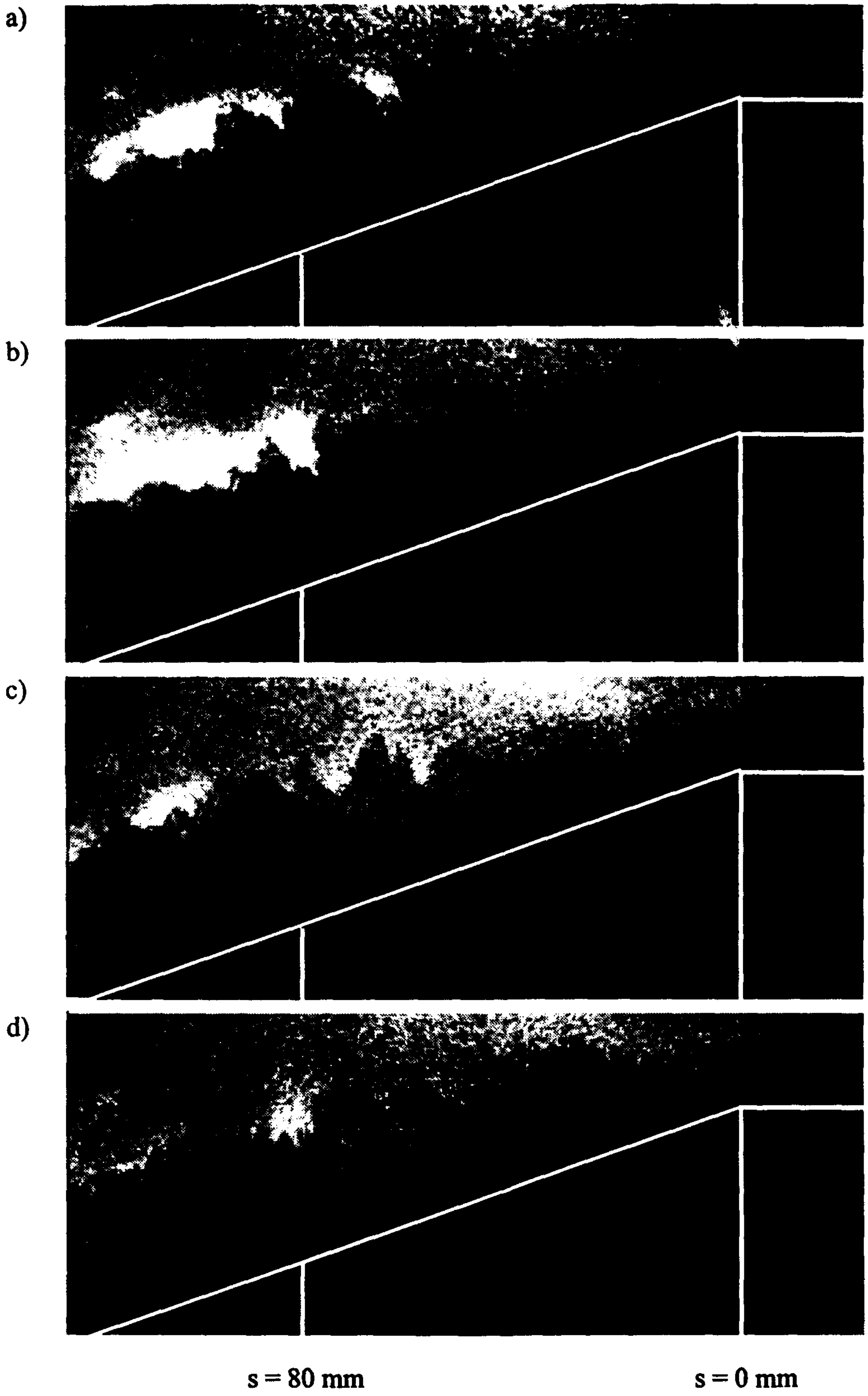

Figure 27. Instantaneous FRS streamwise views of the 14° centered expansion region. The added white lines indicate the position of the model surface.

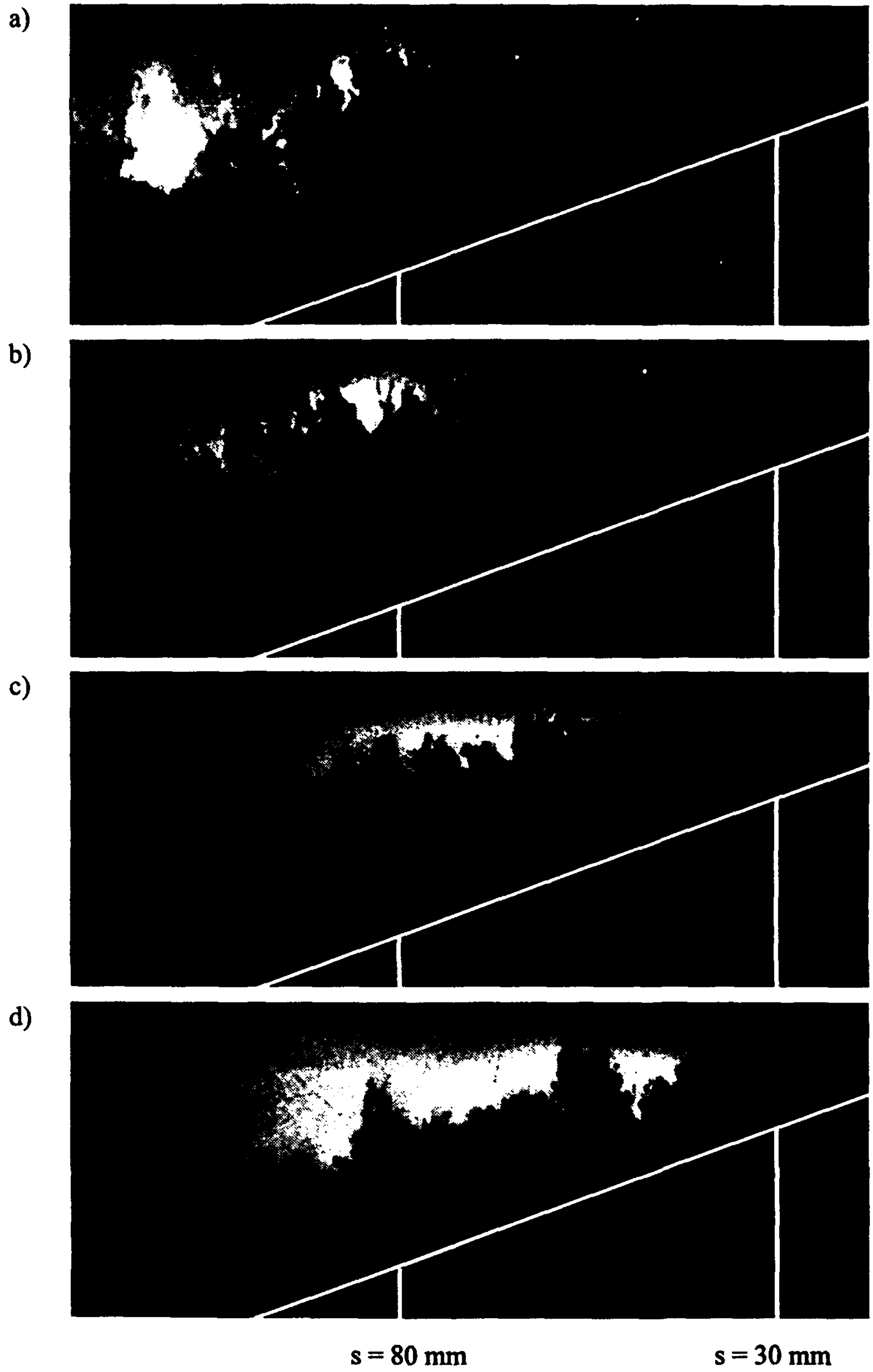

Figure 28. Instantaneous FRS streamwise views of the 14° centered expansion region. The added white lines indicate the position of the model surface.

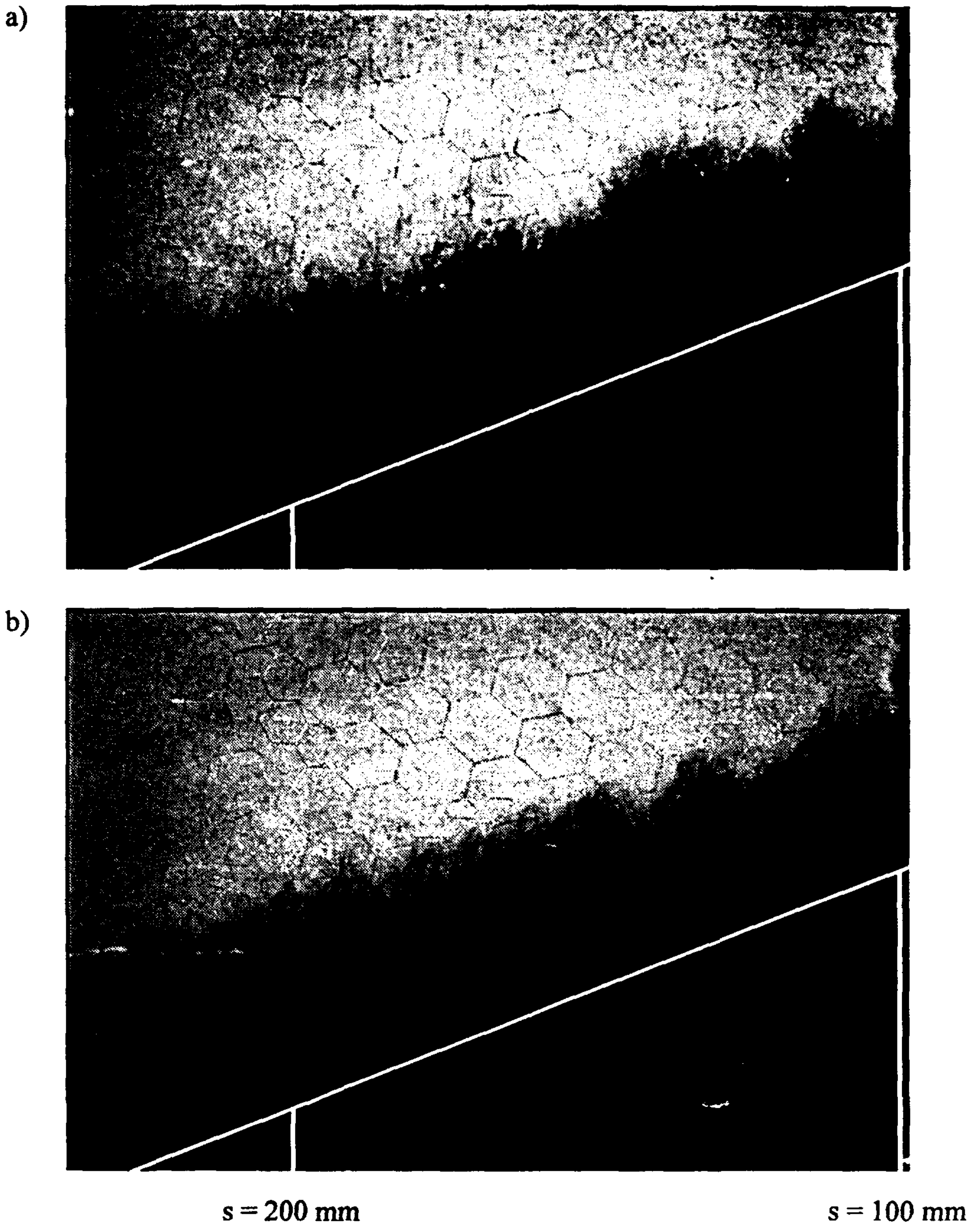

Figure 29. Instantaneous FRS streamwise views of the 14° centered expansion region. The added white lines indicate the position of the model surface. The figure is continued on the next page.

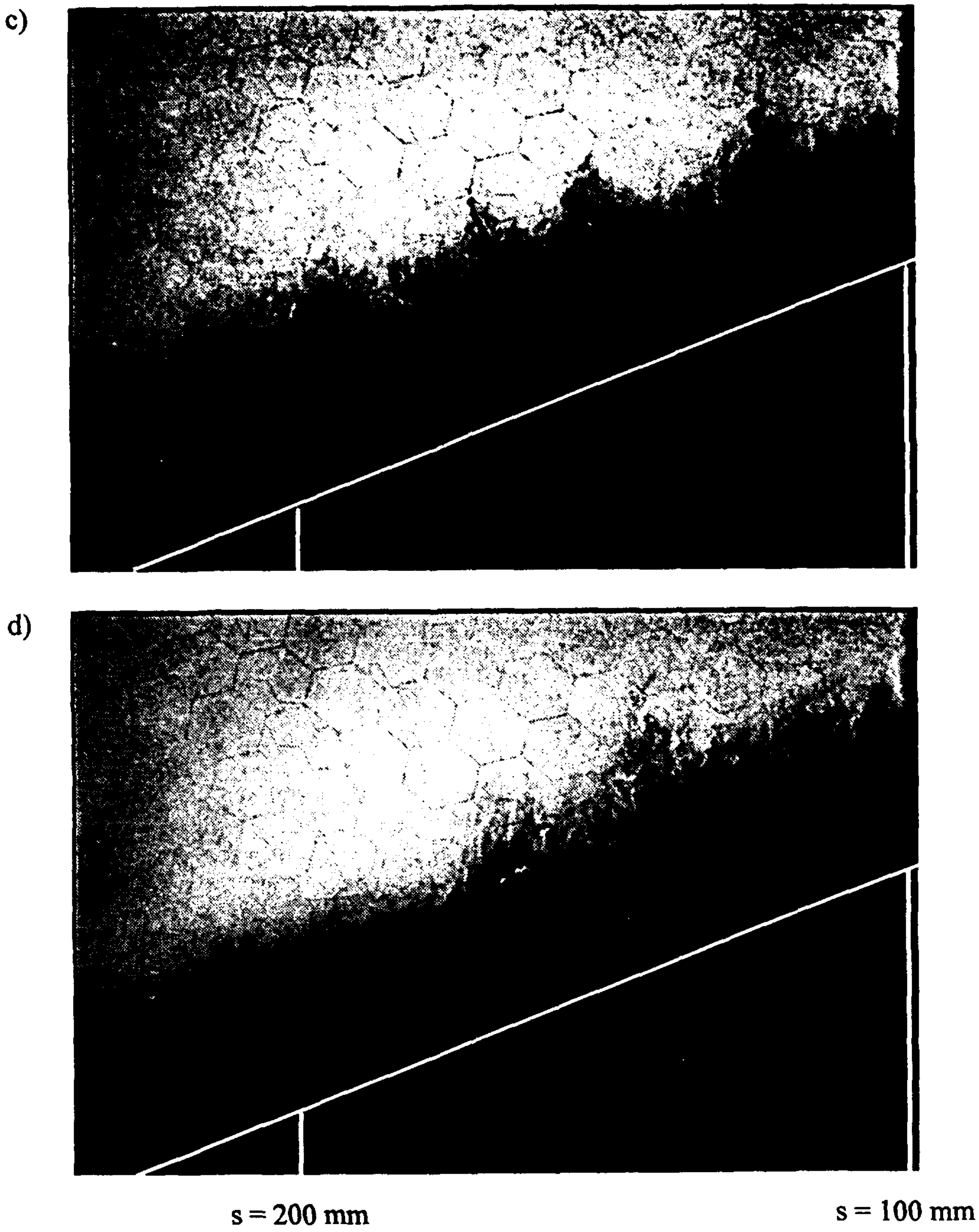

Figure 29. Instantaneous FRS streamwise views of the 14° centered expansion region. The added white lines indicate the position of the model surface. Continued from the previous page.

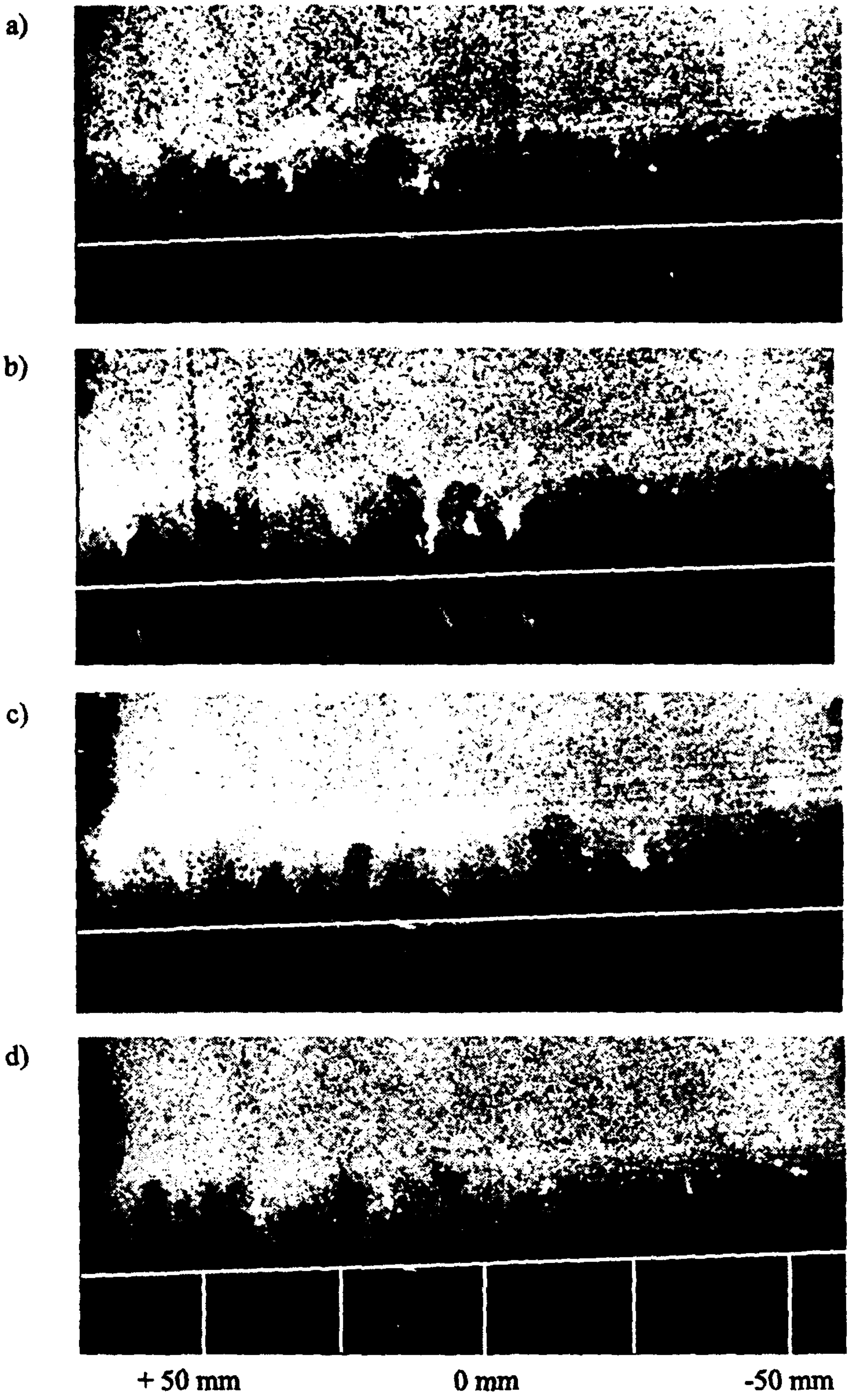

Figure 30. Instantaneous FRS spanwise views of the boundary layer 2.1 δ_o downstream of the beginning of the 14° centered expansion (δ_o= 9.2 mm).

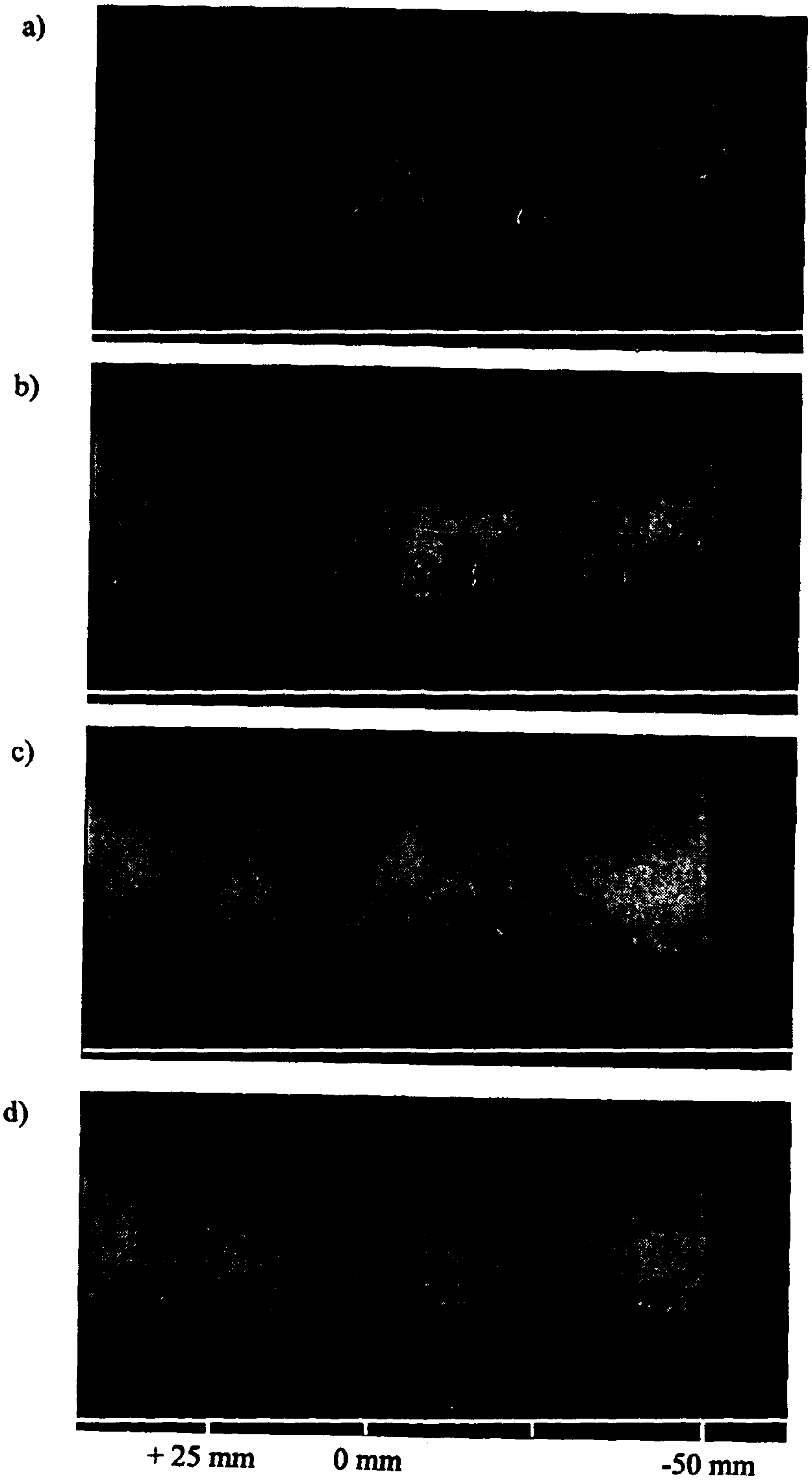

Figure 31. Instantaneous FRS spanwise views of the boundary layer 14.6 δ_o downstream of the beginning of the 14° centered expansion (δ_o= 9.2 mm).

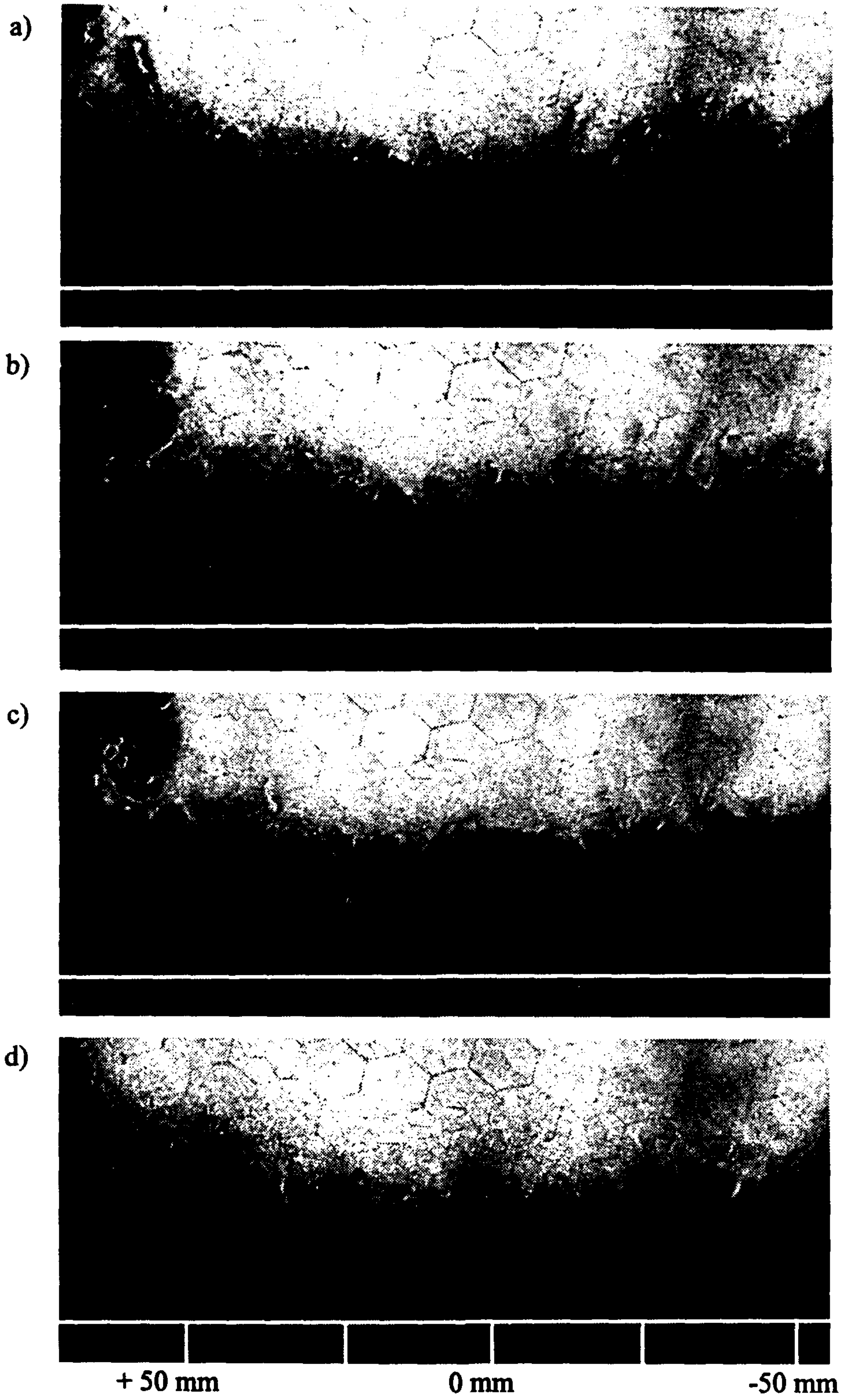

Figure 32. Instantaneous FRS spanwise views of the boundary layer 22.1 δ_o downstream of the beginning of the 14° centered expansion (δ_o= 9.2 mm).

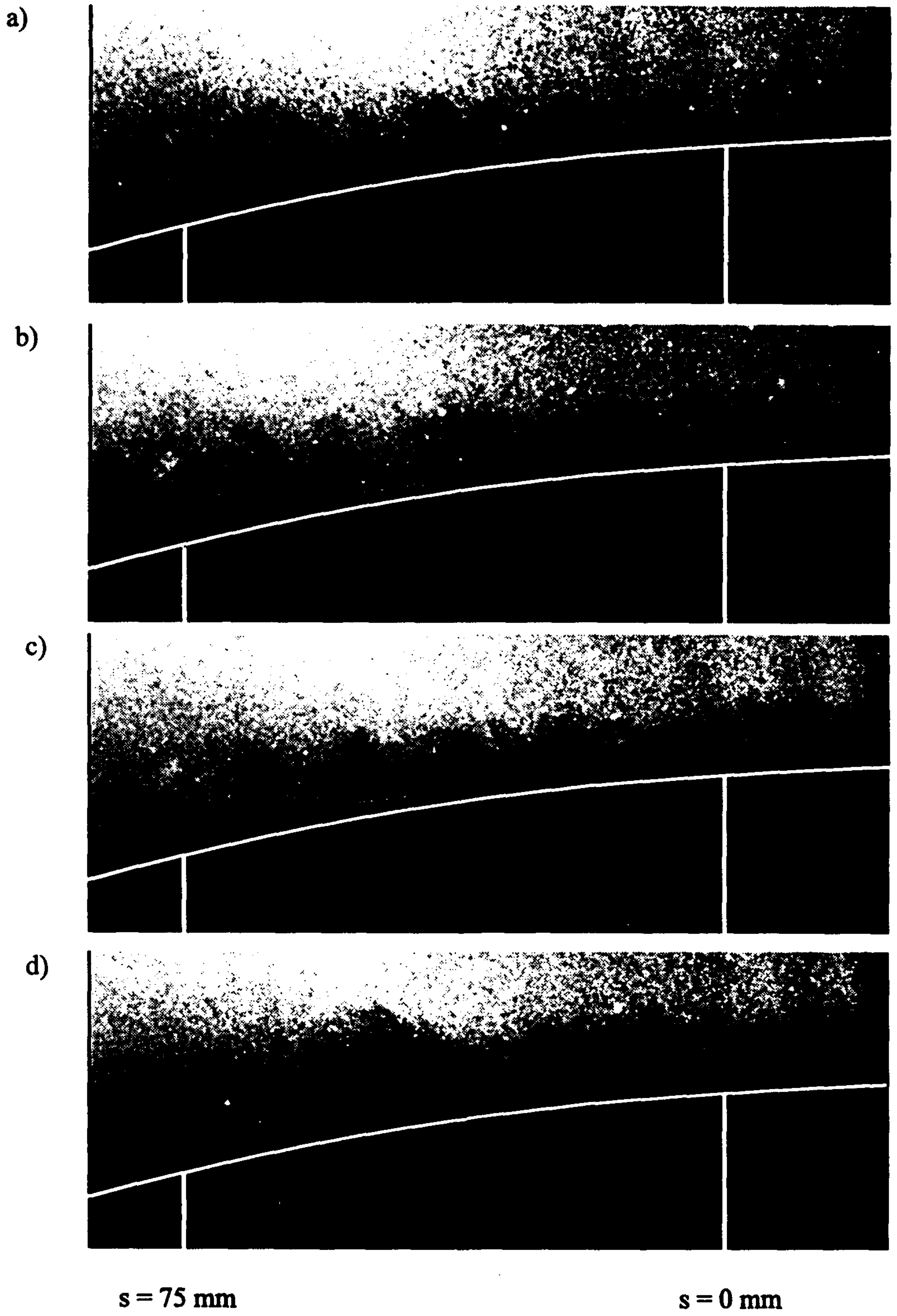

Figure 33. Instantaneous FRS streamwise views of the 14° gradual expansion region. The added white lines indicate the position of the model surface.

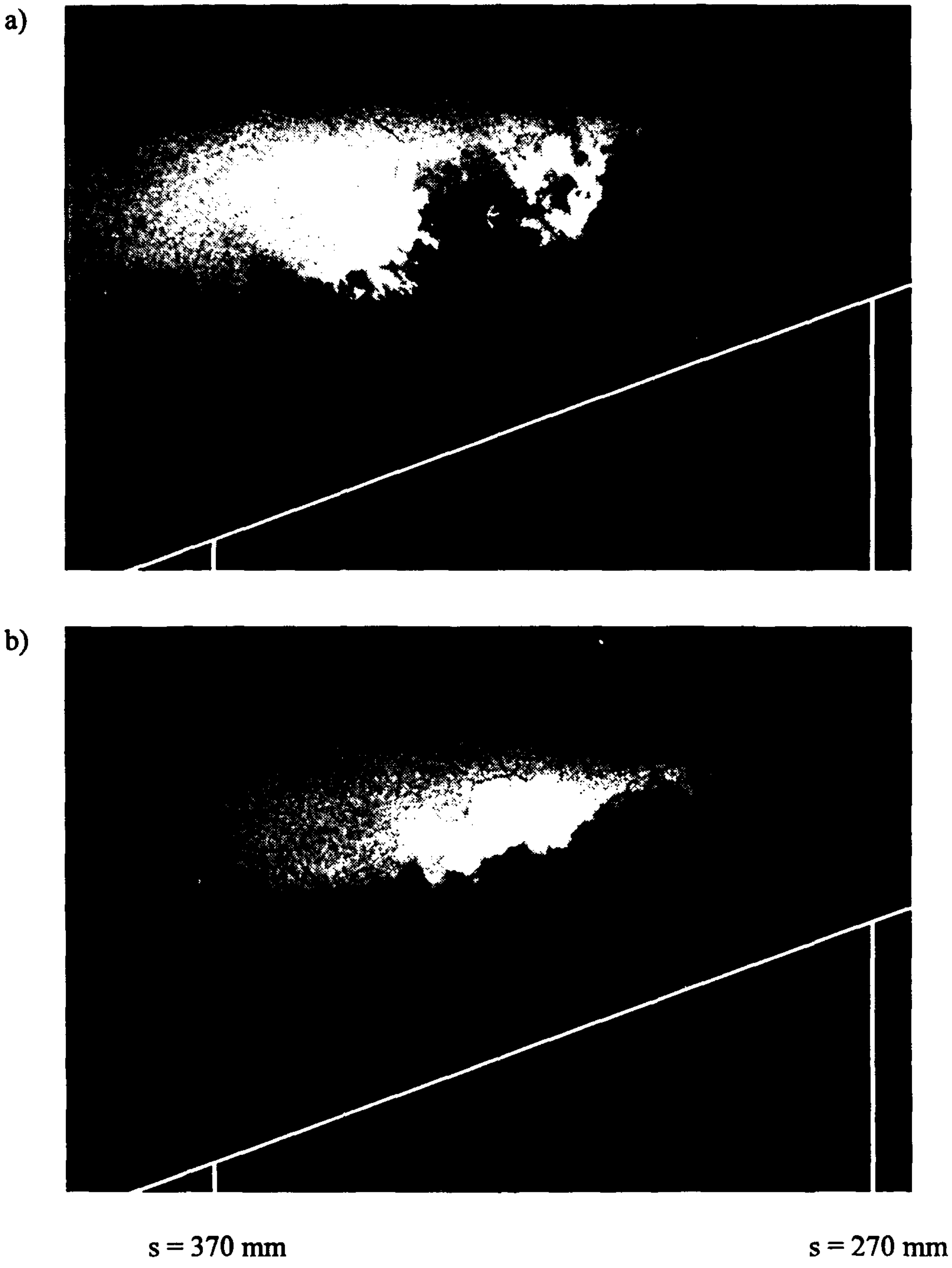

Figure 34. Instantaneous FRS streamwise views of the boundary layer downstream of the 14°gradual expansion region. Figure is continued on the next page.

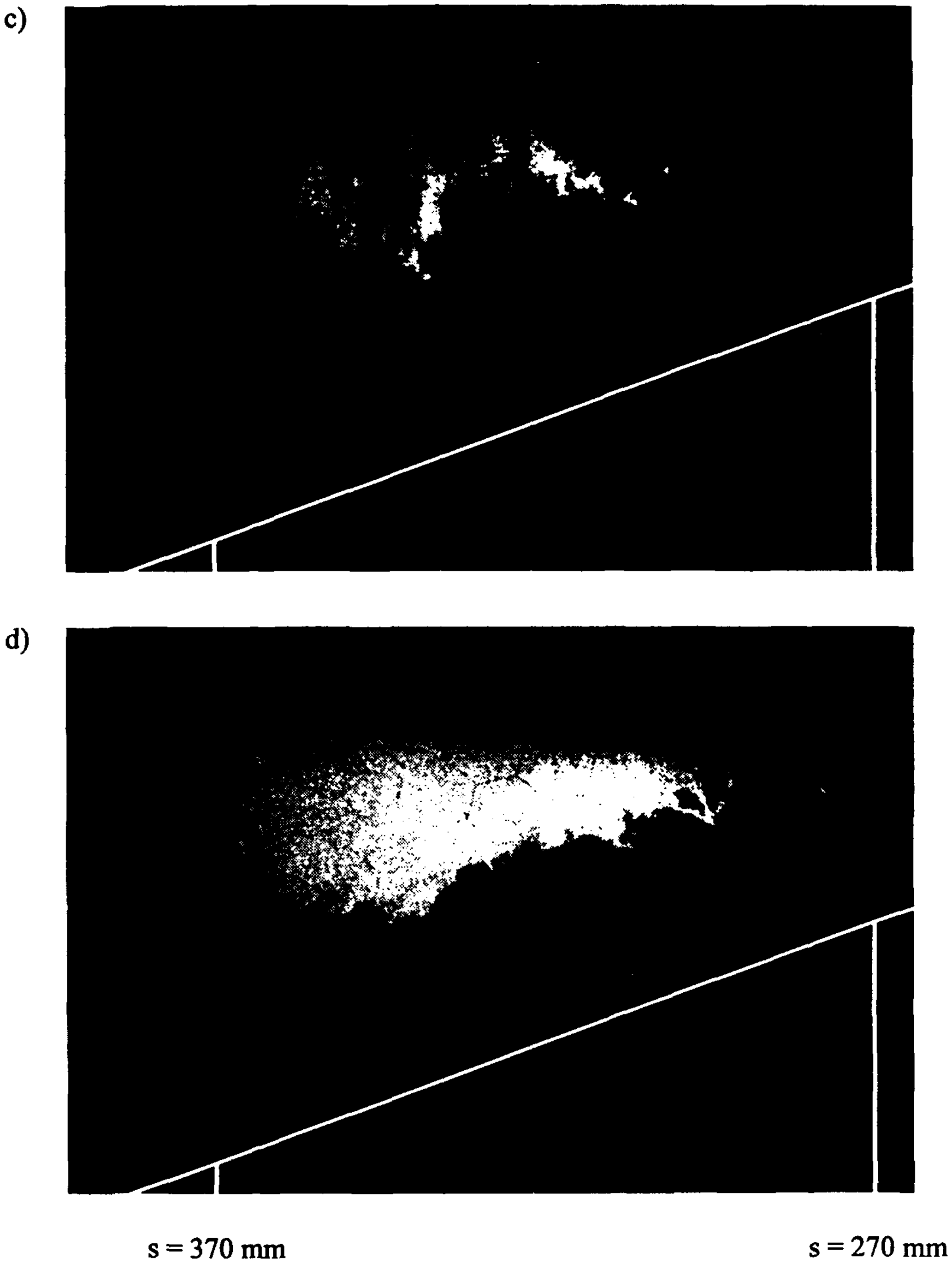

Figure 34. Instantaneous FRS streamwise views of the boundary layer downstream of the 14° gradual expansion region. Continued from previous page.

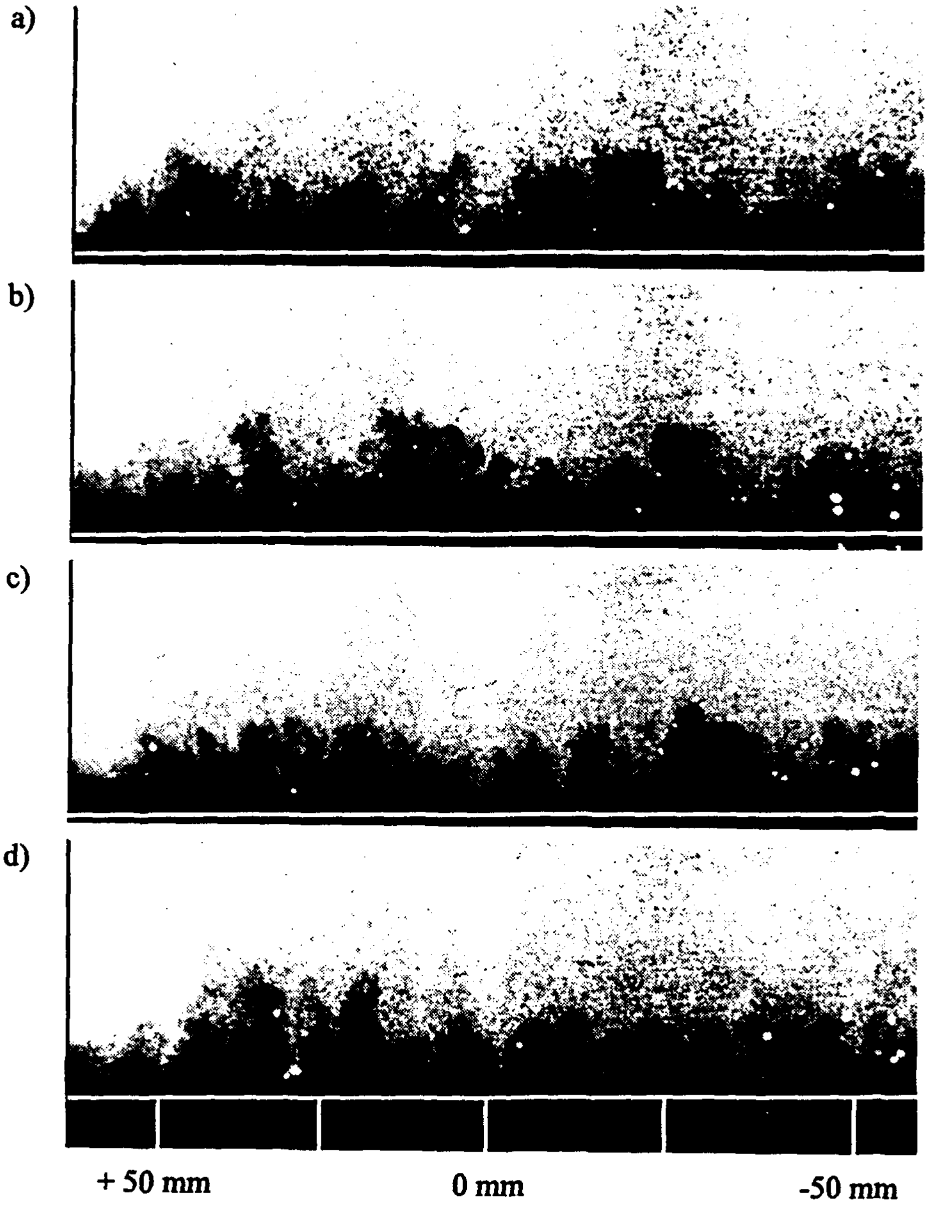

Figure 35. Instantaneous FRS spanwise views of the boundary layer 4.8 δ_o downstream of the beginning of the 14° gradual expansion (δ_o= 9.2 mm).

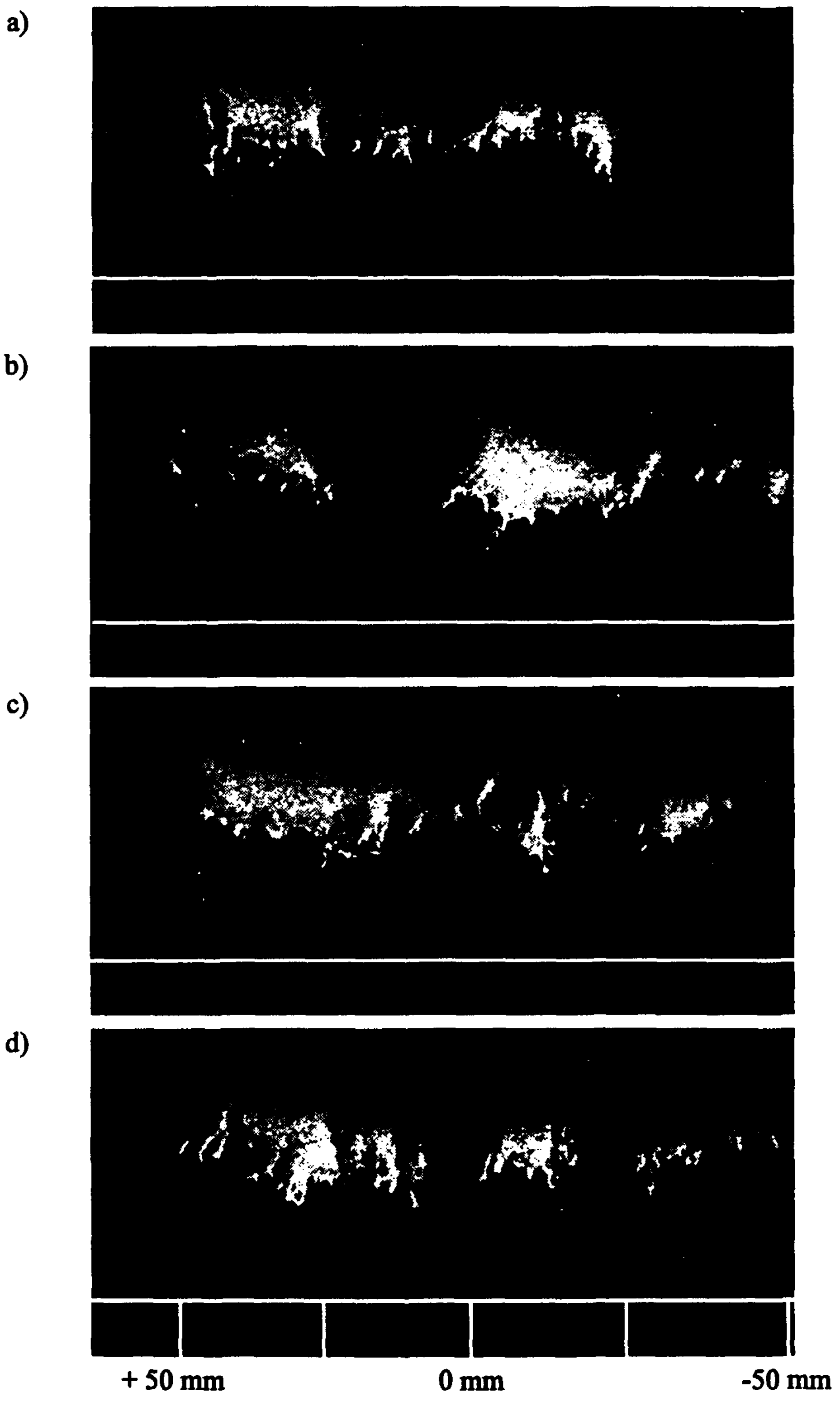

Figure 36. Instantaneous FRS spanwise views of the boundary layer 14.8 δ_o downstream of the beginning the 14° gradual expansion (δ_o= 9.2 mm).

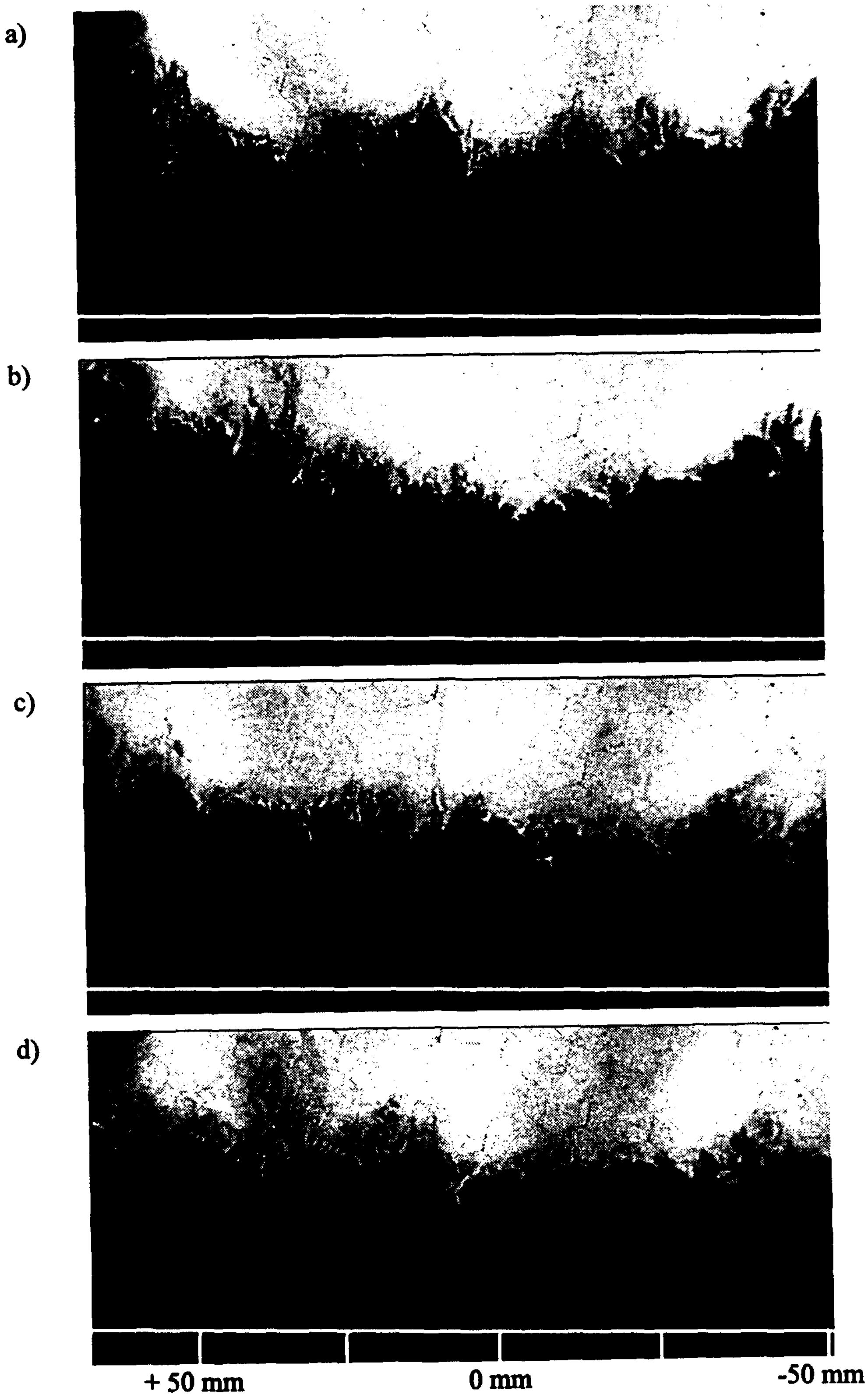

Figure 37. Instantaneous FRS spanwise views of the boundary layer 27.6 δ_o downstream of the beginning of the 14° gradual expansion (δ_o= 9.2 mm).

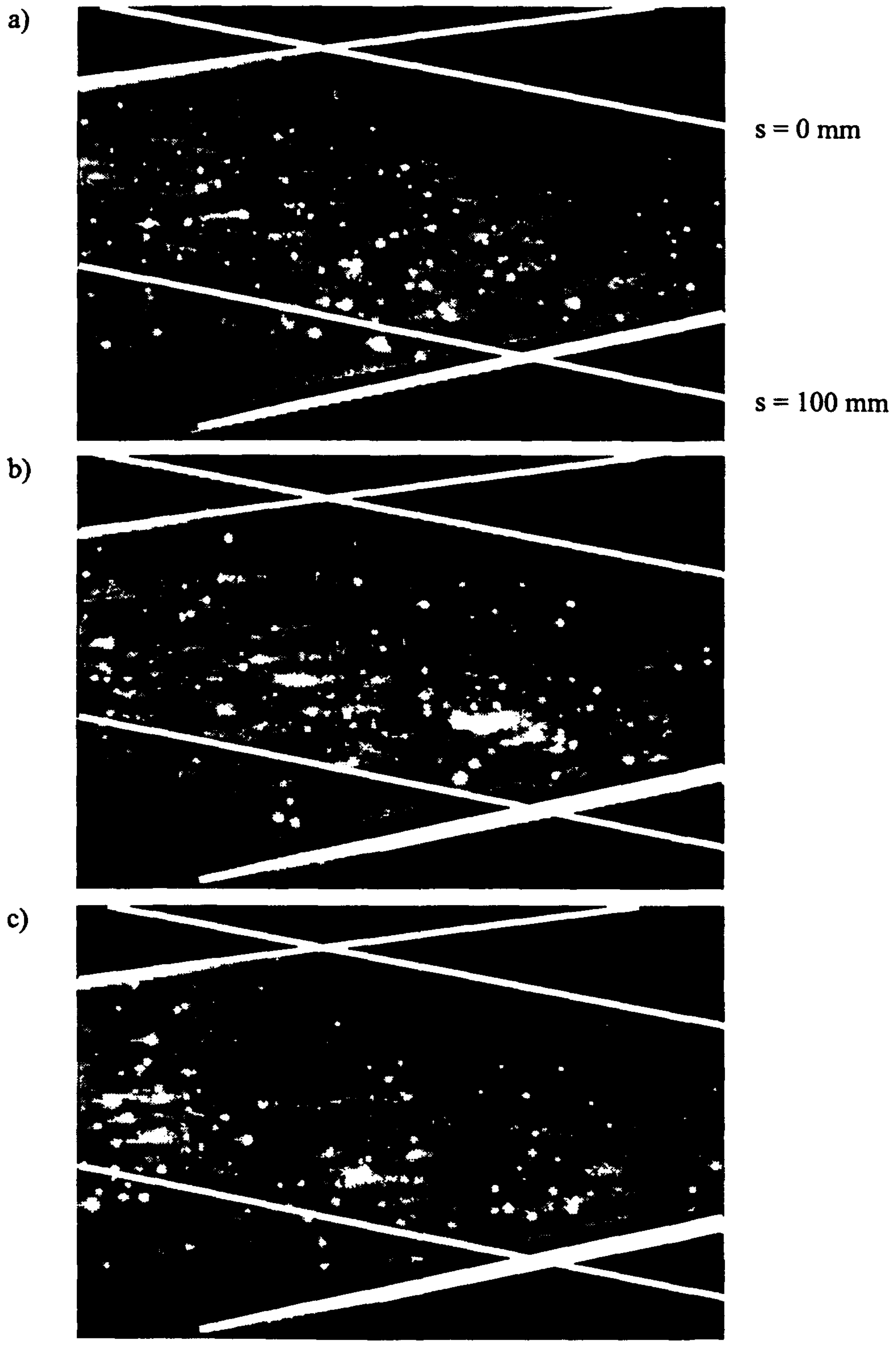

Figure 38. Instantaneous FRS plan views of the flat plate boundary layer. The sheet is parallel to the surface at an elevation of 4.5 mm.

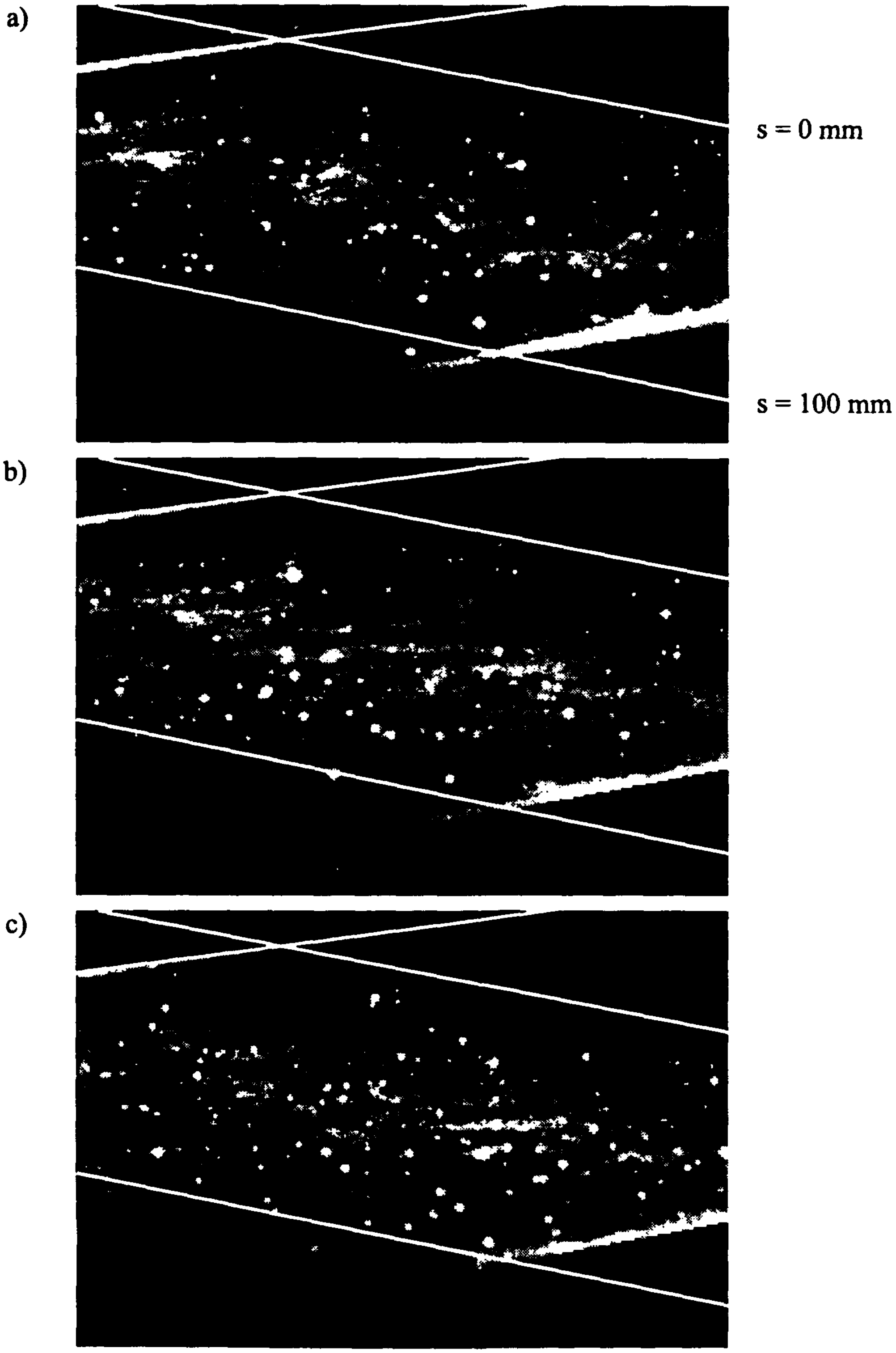

Figure 39. Instantaneous FRS plan views of the flat plate boundary layer. The sheet is parallel to the surface at an elevation of 6.0 mm.

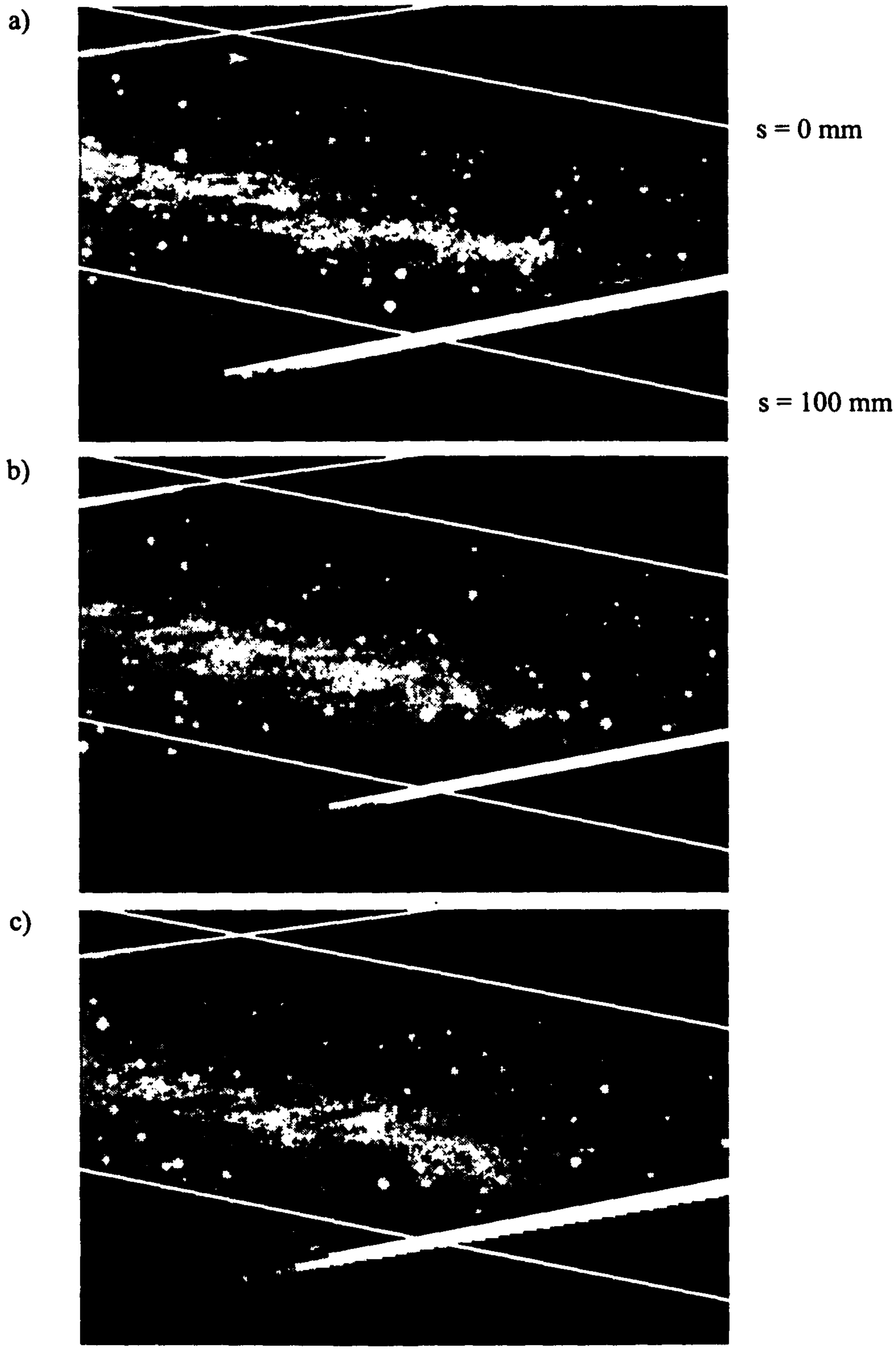

Figure 40. Instantaneous FRS plan views of the flat plate boundary layer. The sheet is parallel to the surface at an elevation of 8.0 mm.

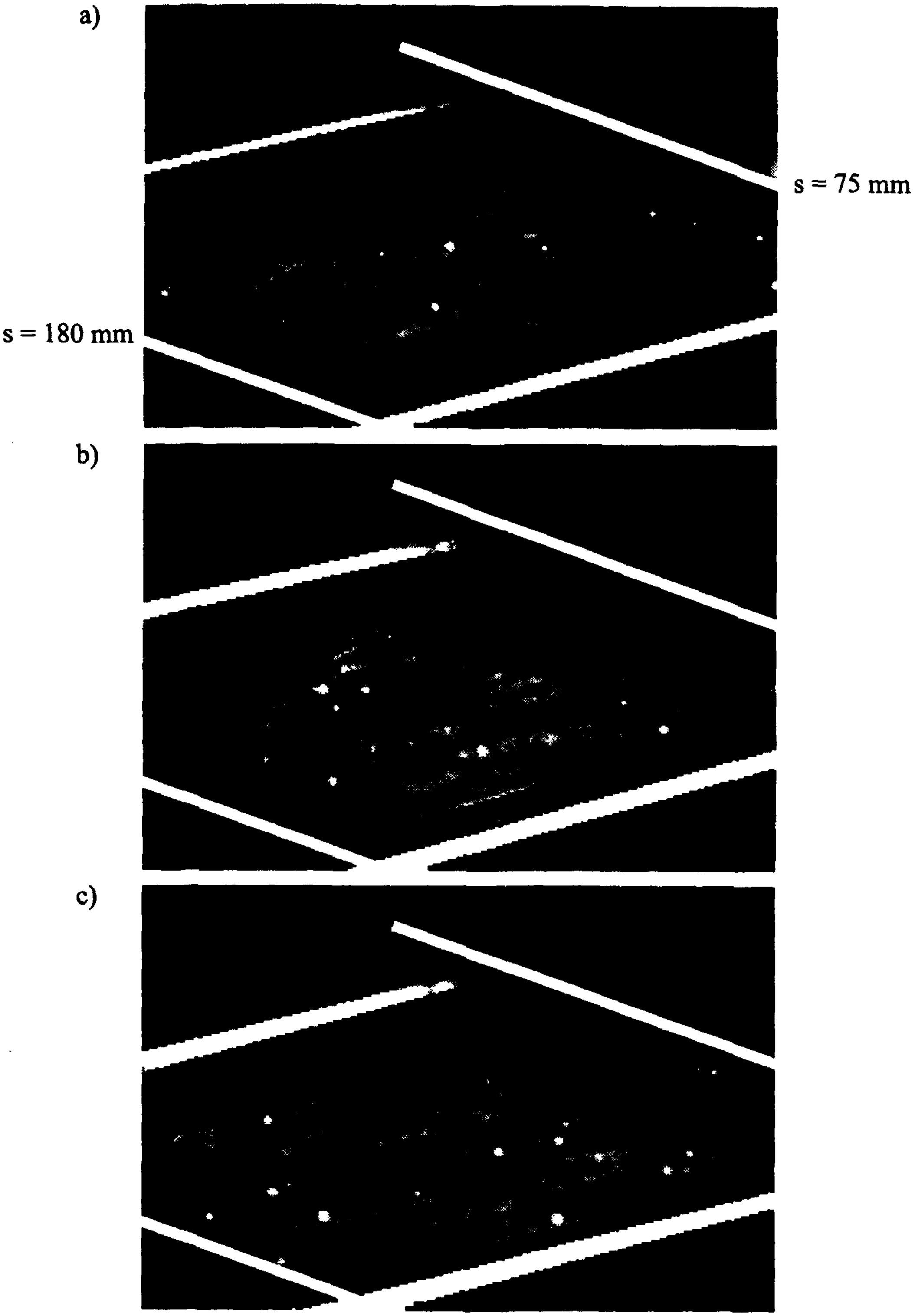

Figure 41. Instantaneous FRS plan views of the boundary layer downstream of the 7° centered expansion. The laser sheet is parallel to the surface at an elevation of 5.0 mm. Strong reflections from the model surface have been blacked out near the left side of the image.

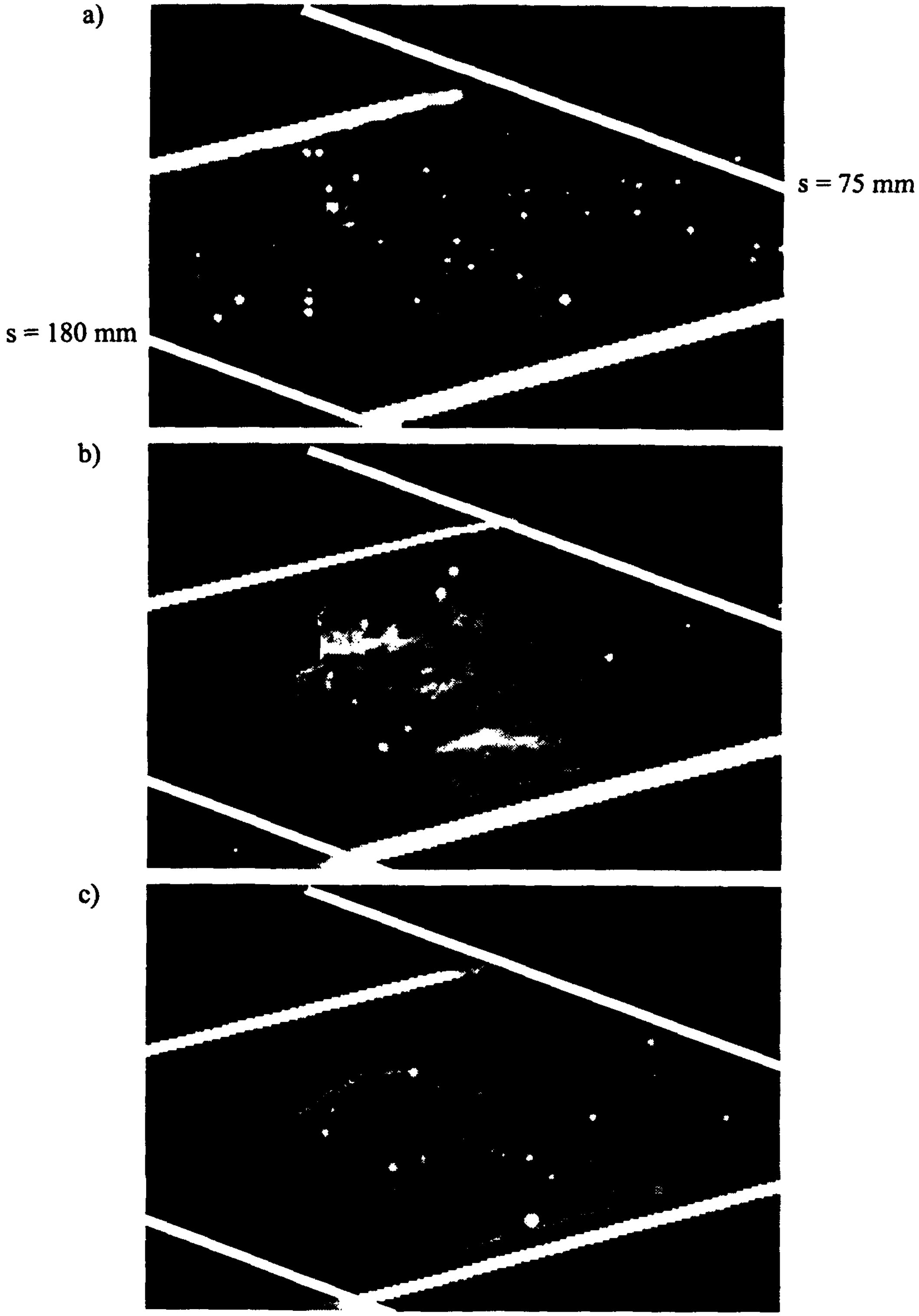

Figure 42. Instantaneous FRS plan views of the boundary layer downstream of the 7°centered expansion. The laser sheet is parallel to the surface at an elevation of 6.5 mm. Strong reflections from the model surface have been blacked out near the left side of the image.

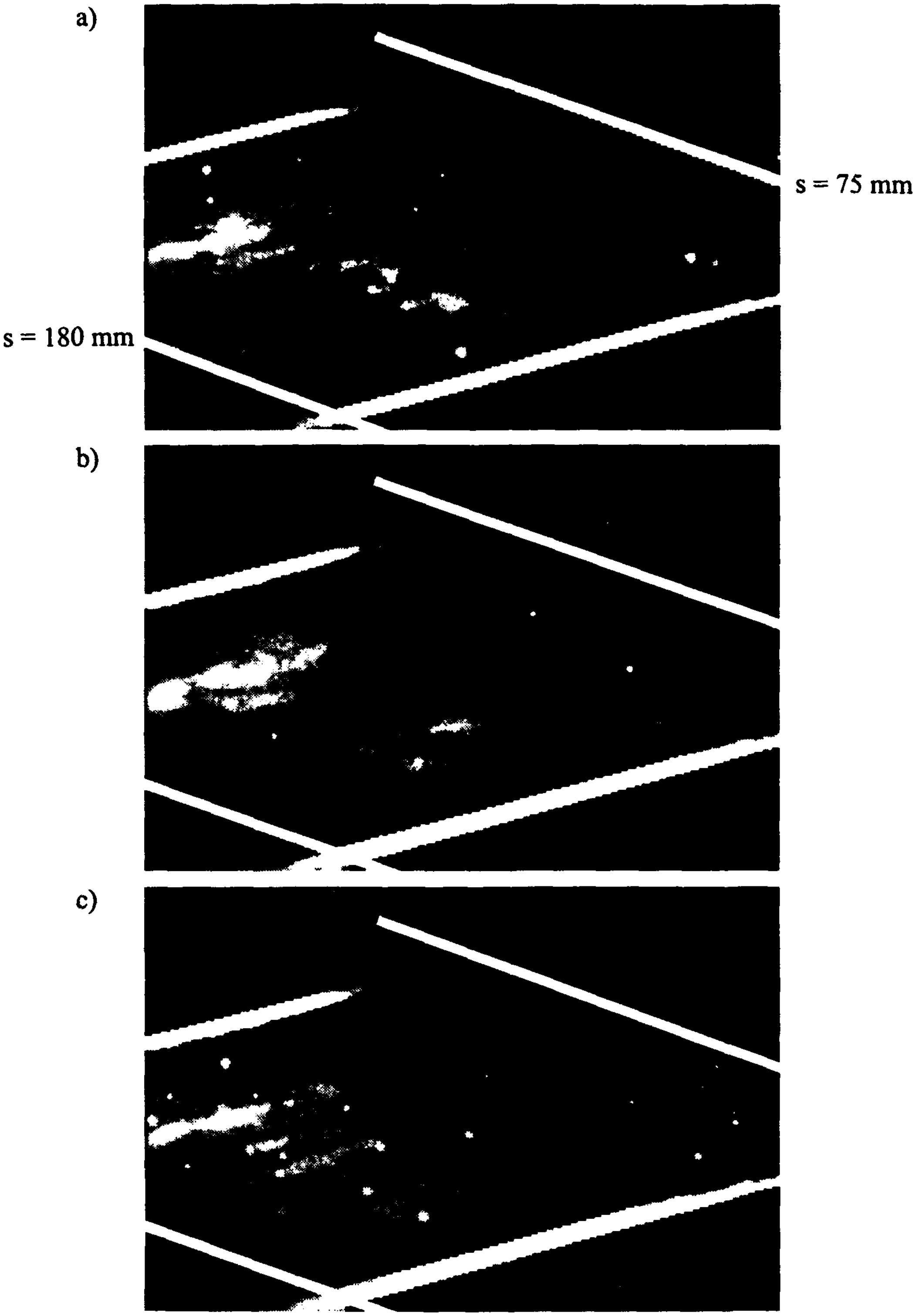

Figure 43. Instantaneous FRS plan views of the boundary layer downstream of the 7° centered expansion. The laser sheet is parallel to the surface at an elevation of 8.0 mm.

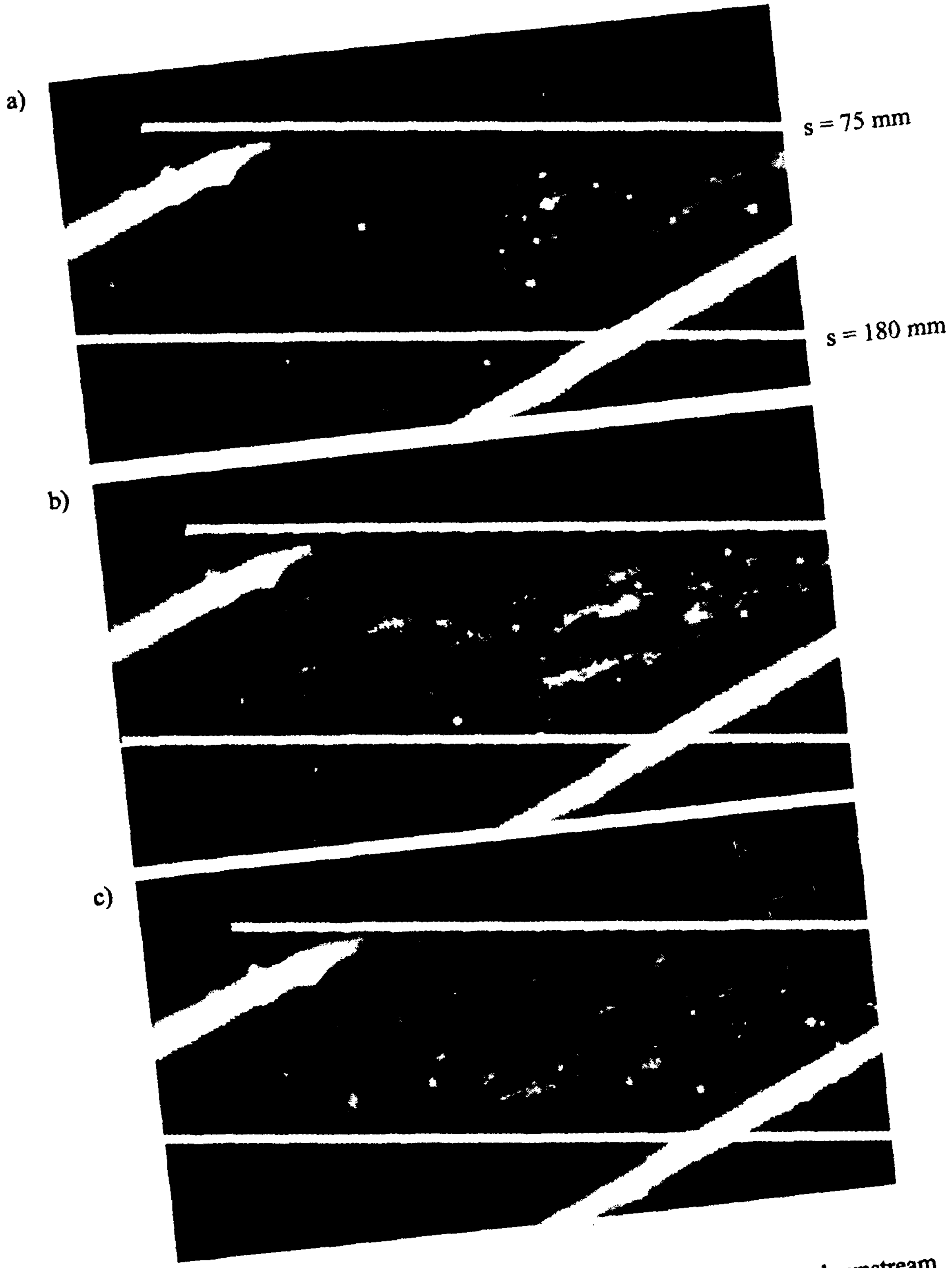

Figure 44. Instantaneous FRS plan views of the boundary layer downstream of the 14° centered expansion with flow straightening assembly removed. The laser sheet is parallel to the surface at an elevation of 12.0 mm.

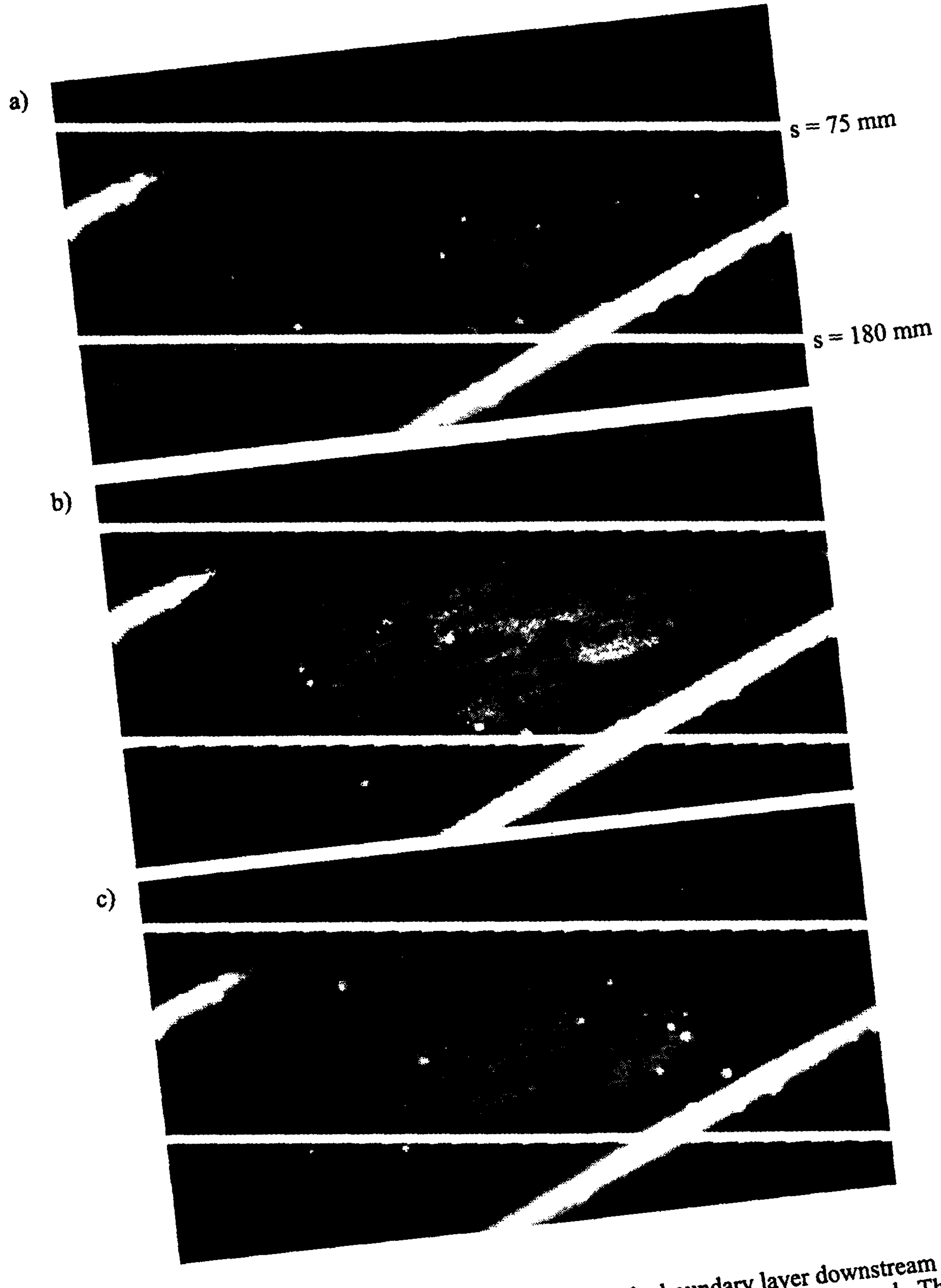

Figure 45. Instantaneous FRS plan views of the boundary layer downstream of the 14° centered expansion with flow straightening assembly removed. The laser sheet is parallel to the surface at an elevation of 15.0 mm.

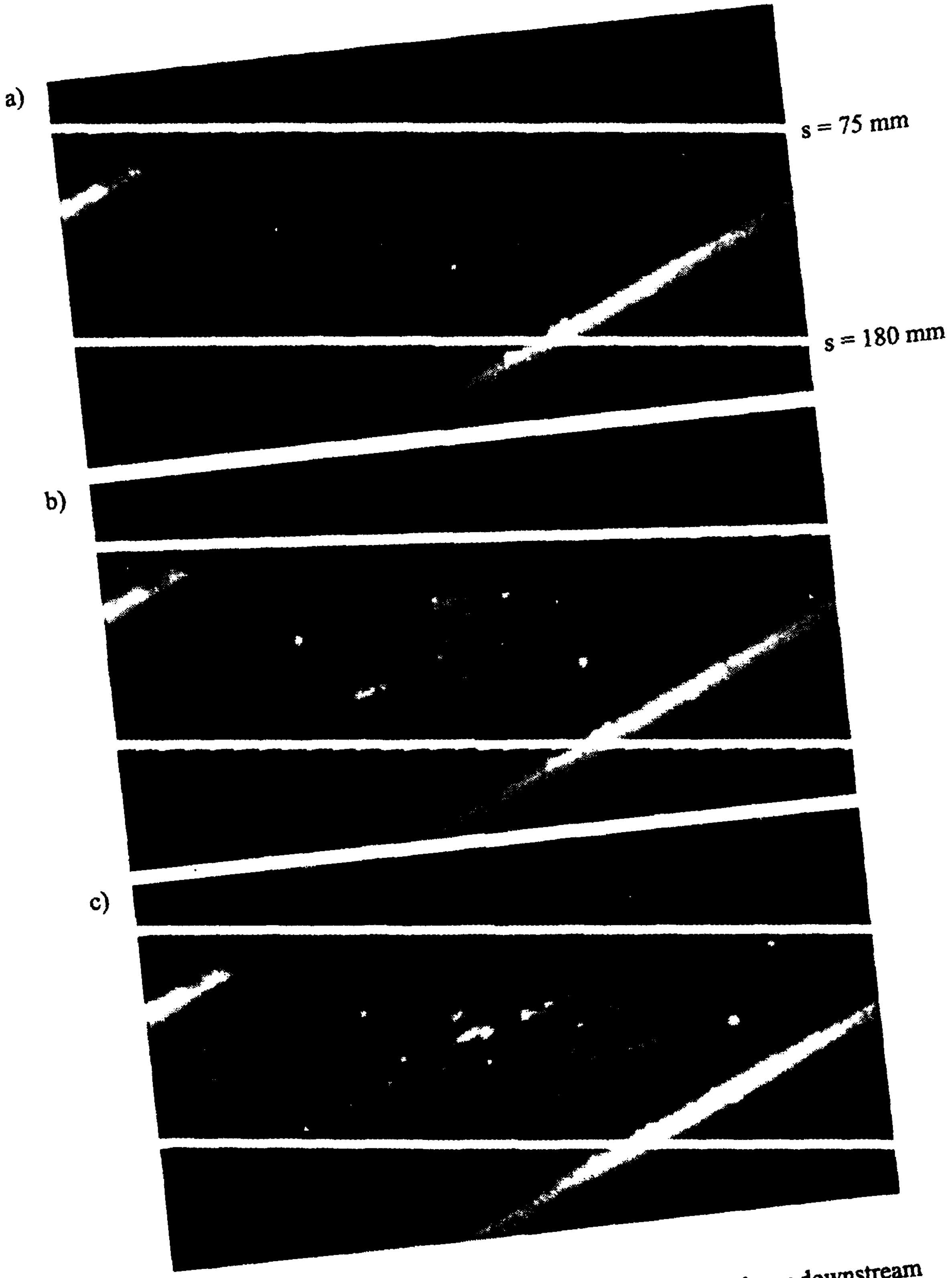

Figure 46. Instantaneous FRS plan views of the boundary layer downstream of the 14° centered expansion with flow straightening assembly removed. The laser sheet is parallel to the surface at an elevation of 17.0 mm.

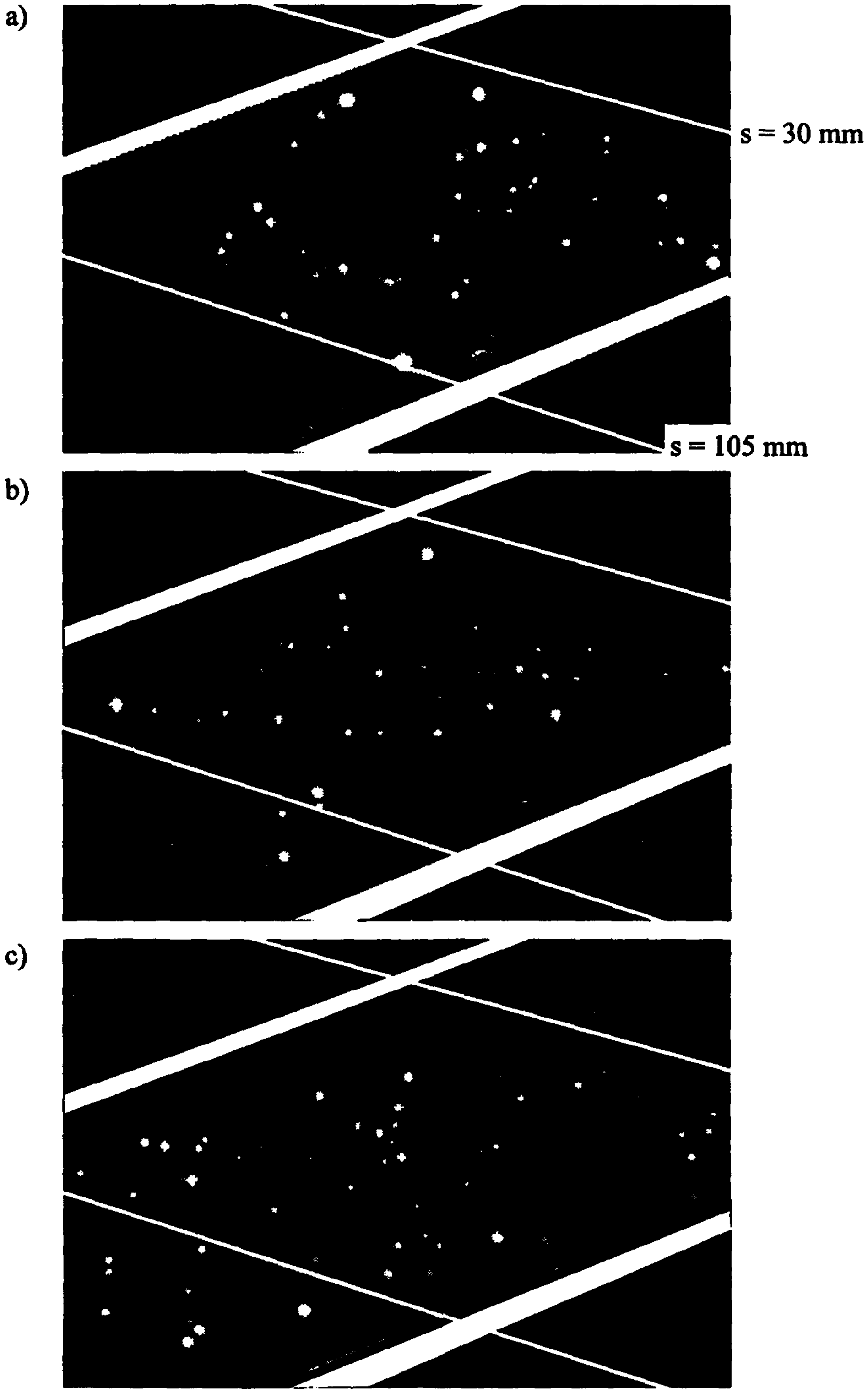

Figure 47. Plan views of the boundary layer downstream of the 14° gradual expansion. The sheet is parallel to the surface at an elevation of 10.0 mm.

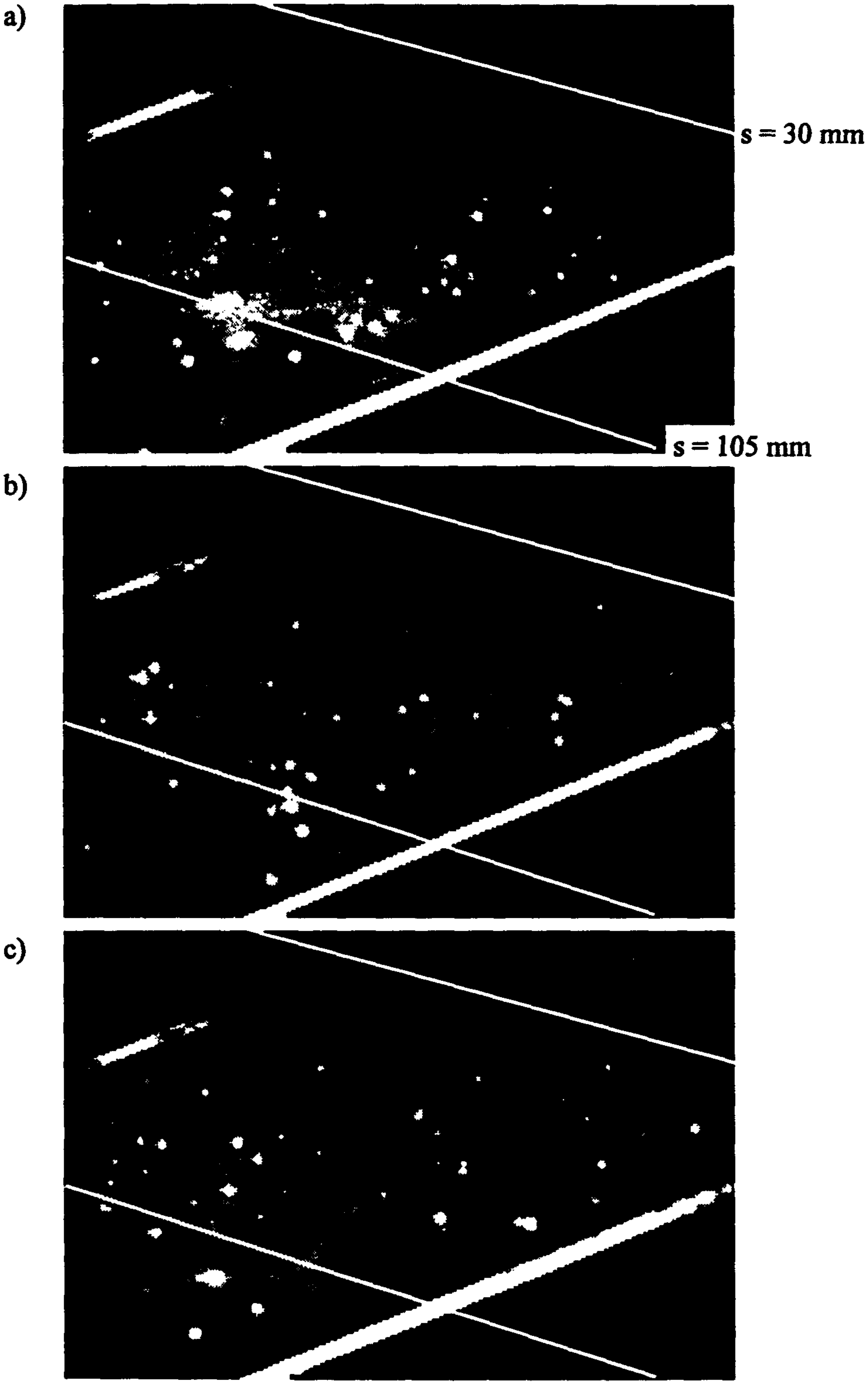

Figure 48. Plan views of the boundary layer downstream of the 14° gradual expansion. The sheet is parallel to the surface at an elevation of 13.5 mm.

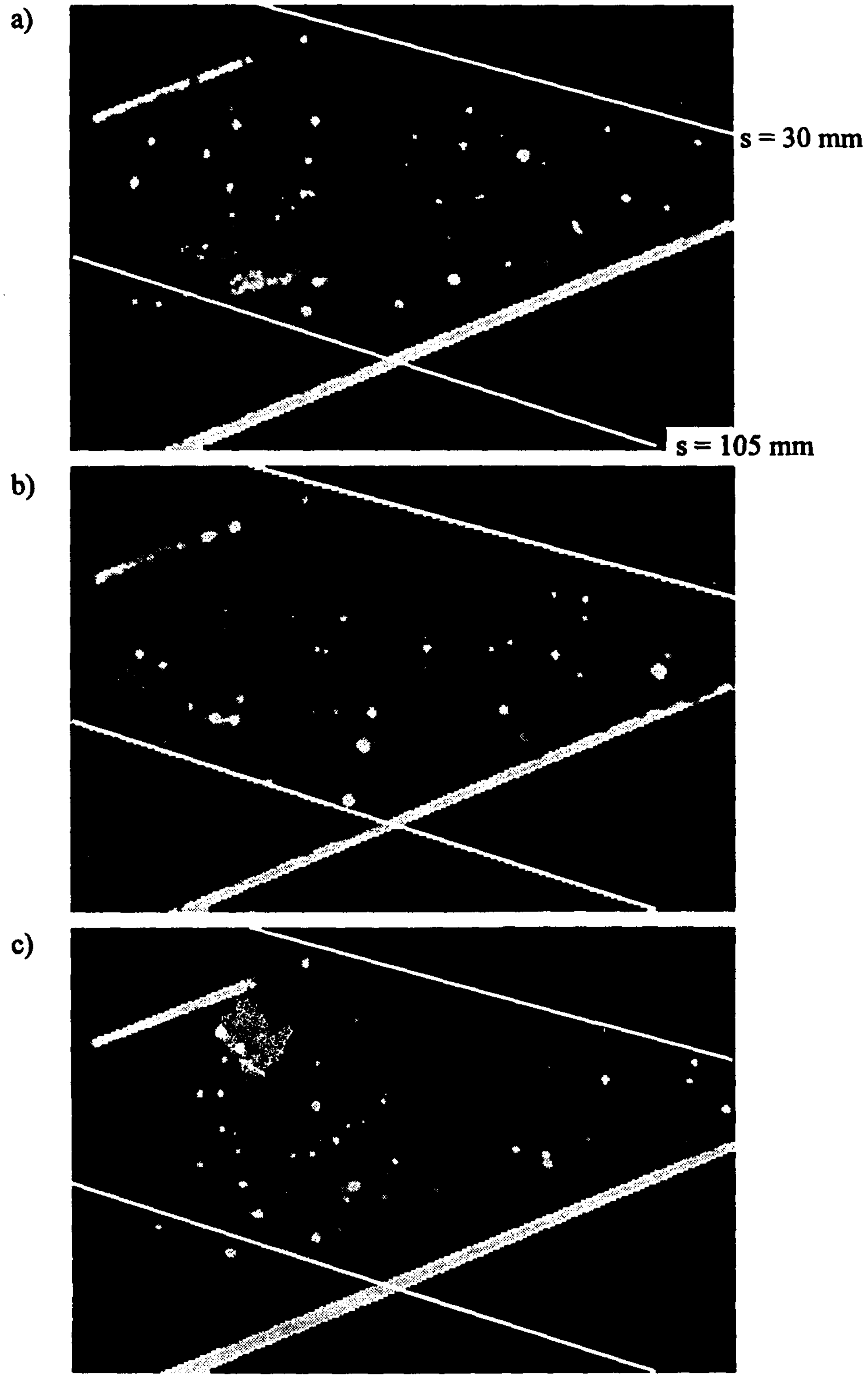

Figure 49. Plan views of the boundary layer downstream of the 14° gradual expansion. The sheet is parallel to the surface at an elevation of 17.0 mm.

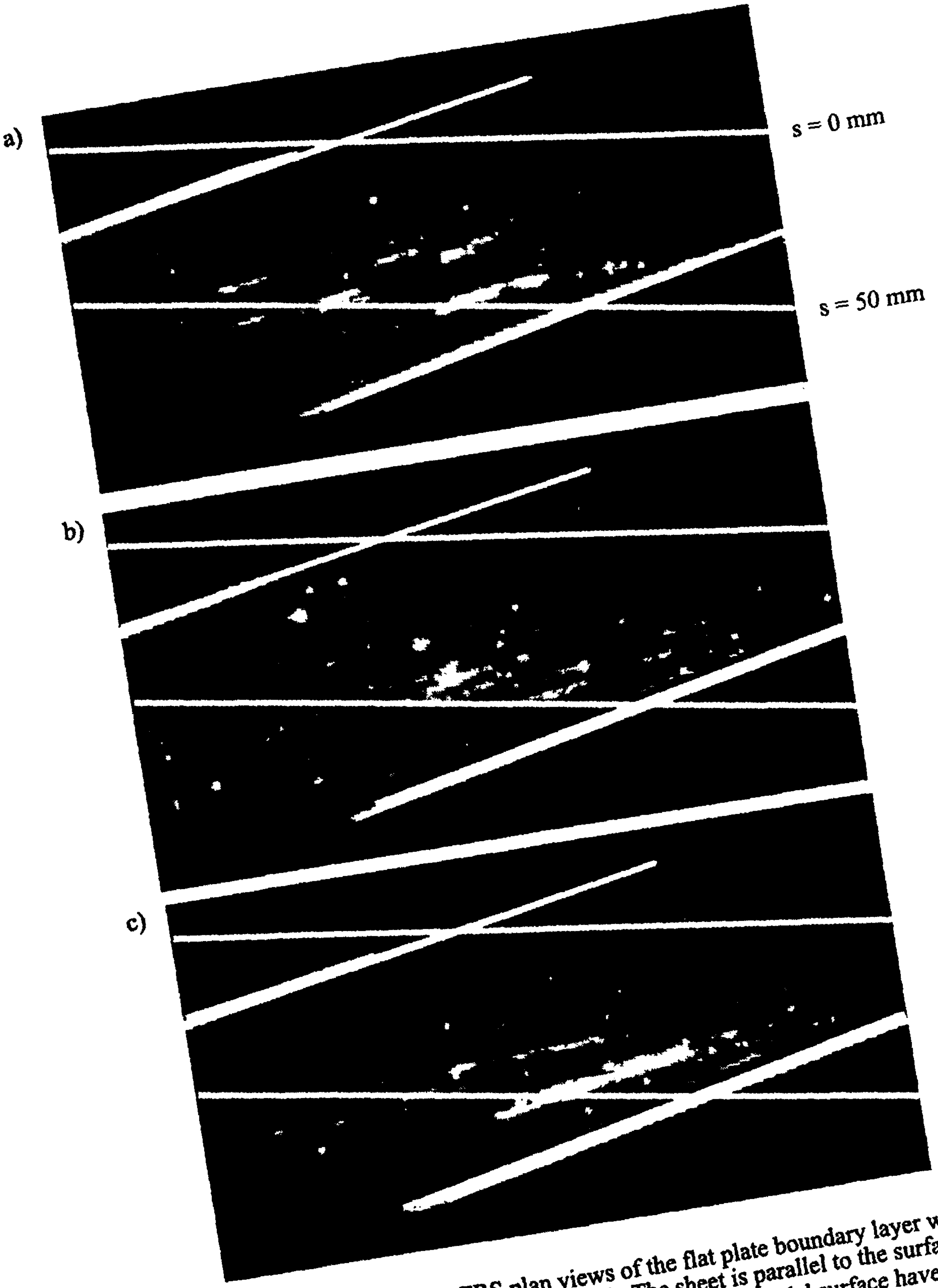

Figure 50. Instantaneous FRS plan views of the flat plate boundary layer with the flow straightening assembly removed. The sheet is parallel to the surface at an elevation of 4.5 mm. Strong reflections from the model surface have been blacked out.

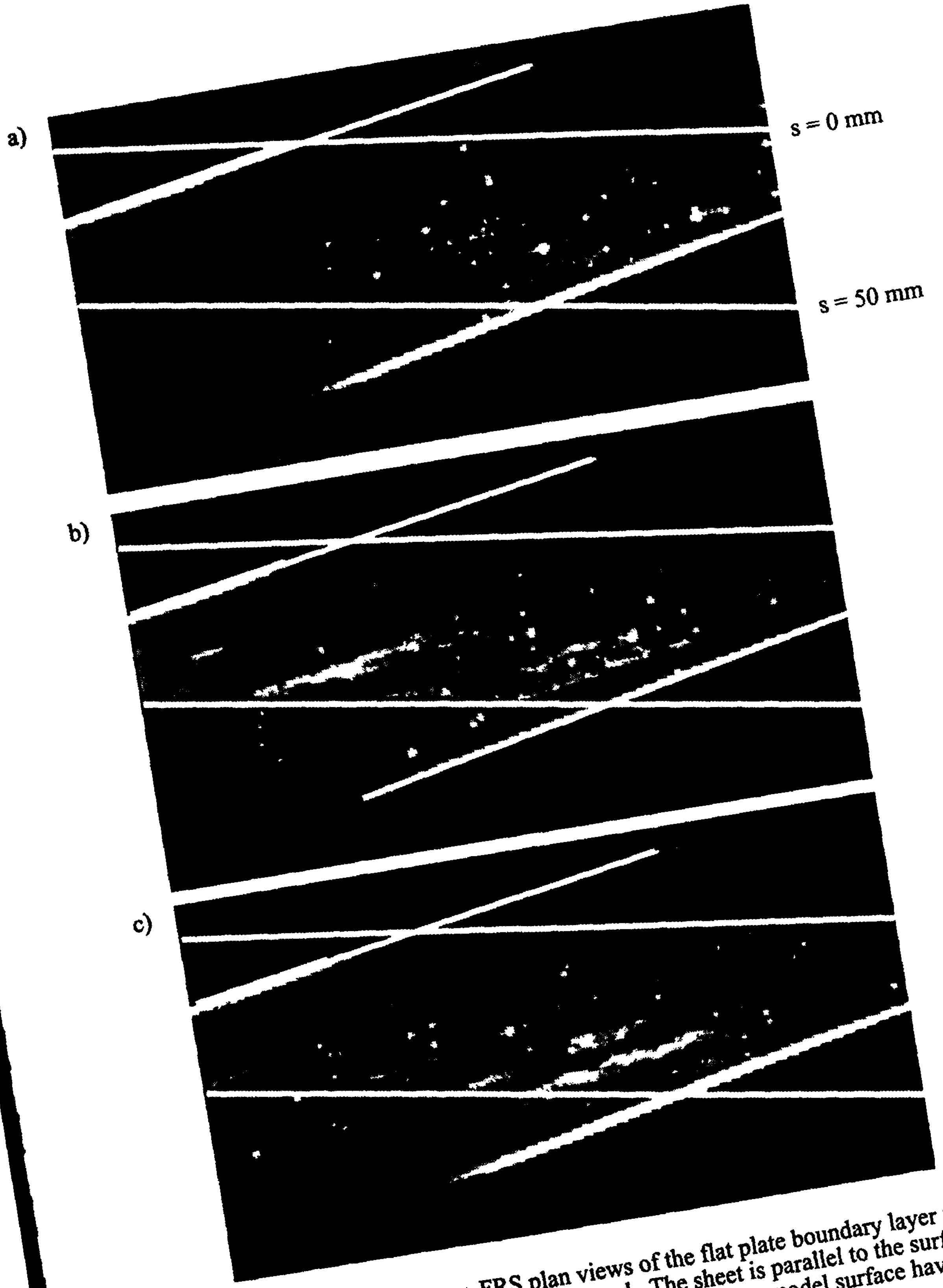

Figure 51. Instantaneous FRS plan views of the flat plate boundary layer with the flow straightening assembly removed. The sheet is parallel to the surface at an elevation of 6.0 mm. Strong reflections from the model surface have been blacked out in Image (a).

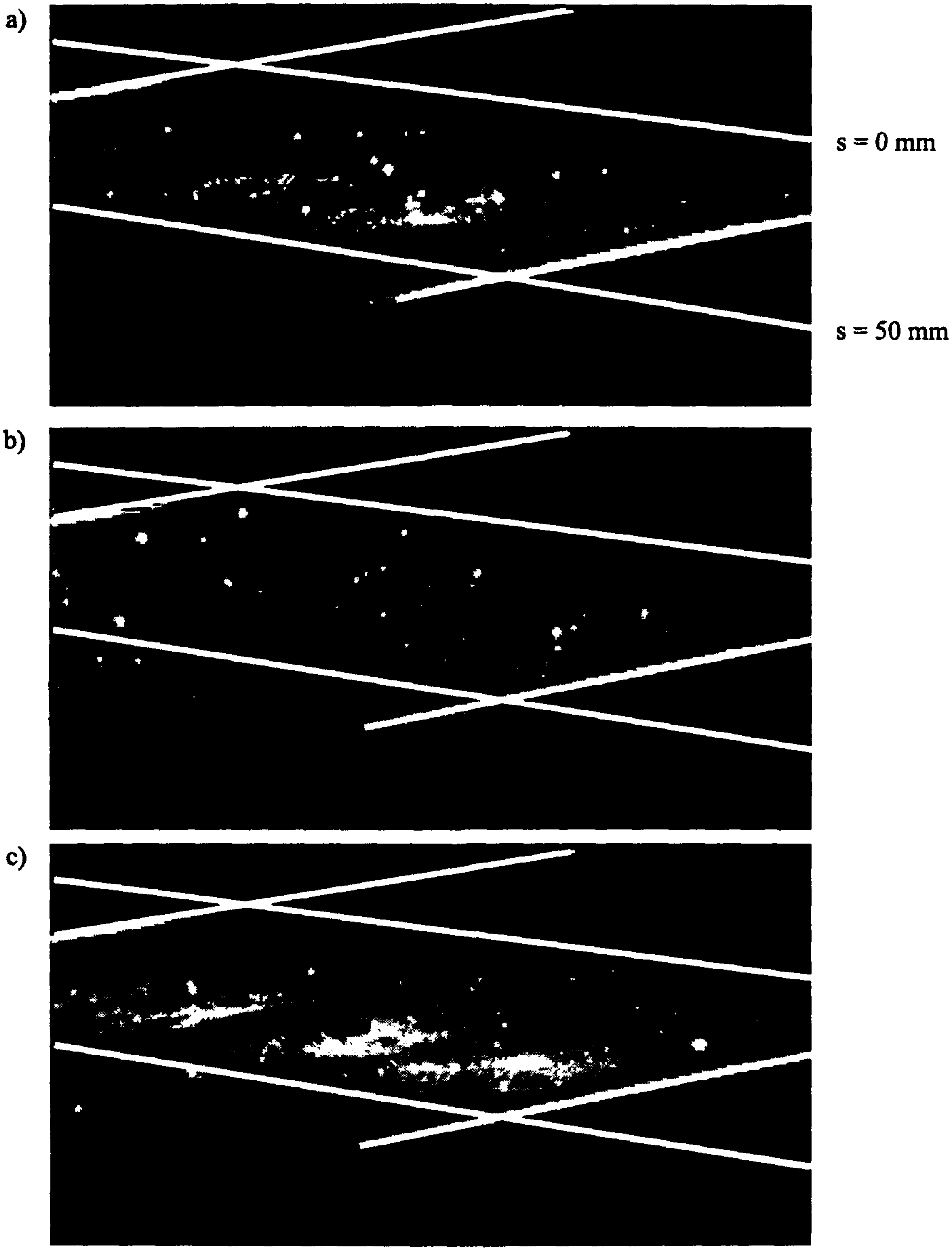

Figure 52. Instantaneous FRS plan views of the flat plate boundary layer with the flow straightening assembly removed. The sheet is parallel to the surface at an elevation of 8.0 mm.

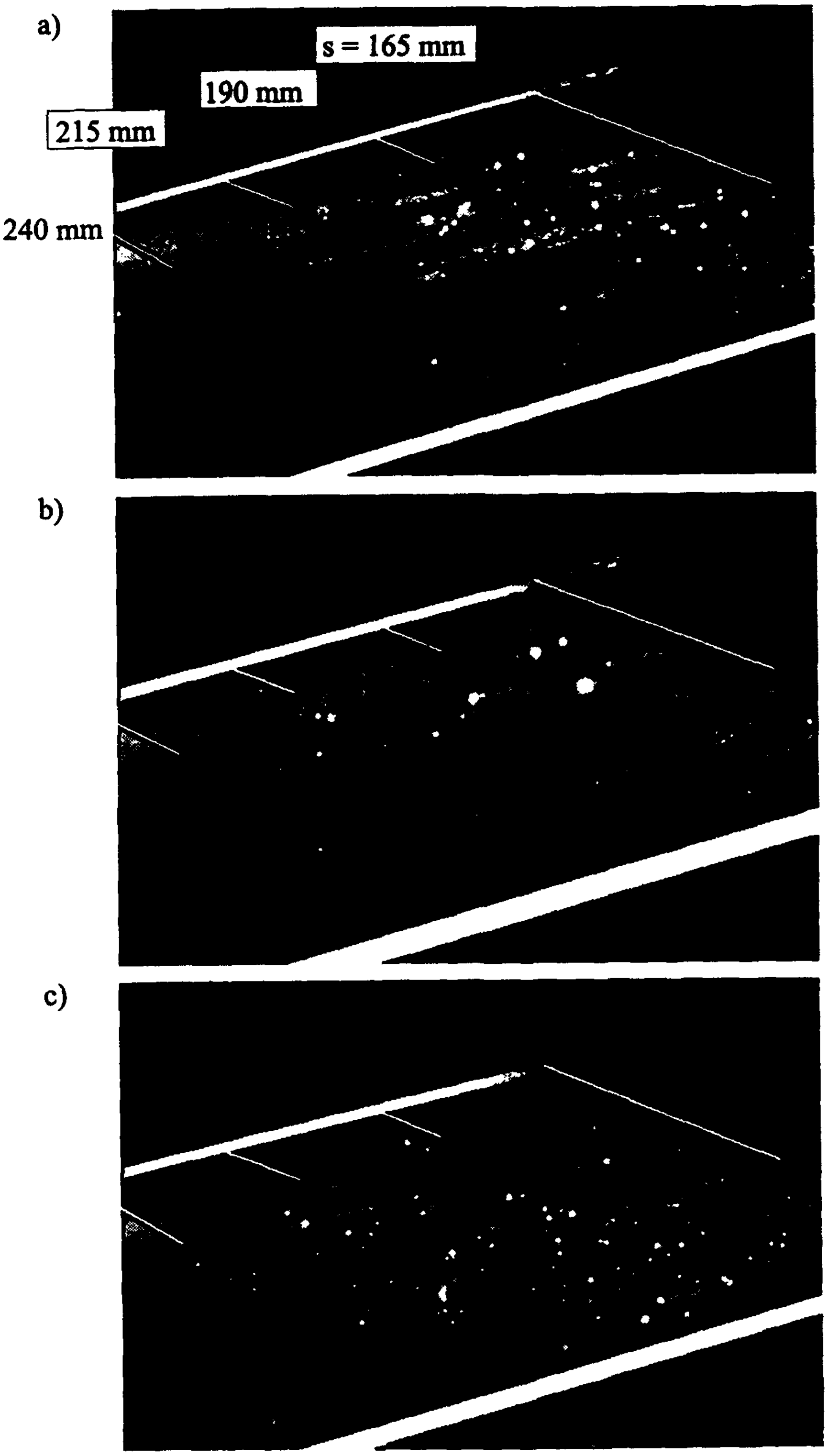

Figure 53. Instantaneous FRS plan views of the boundary layer downstream of the 7° centered expansion with flow straightening assembly removed. The laser sheet is parallel to the surface at an elevation of 4.5 mm.

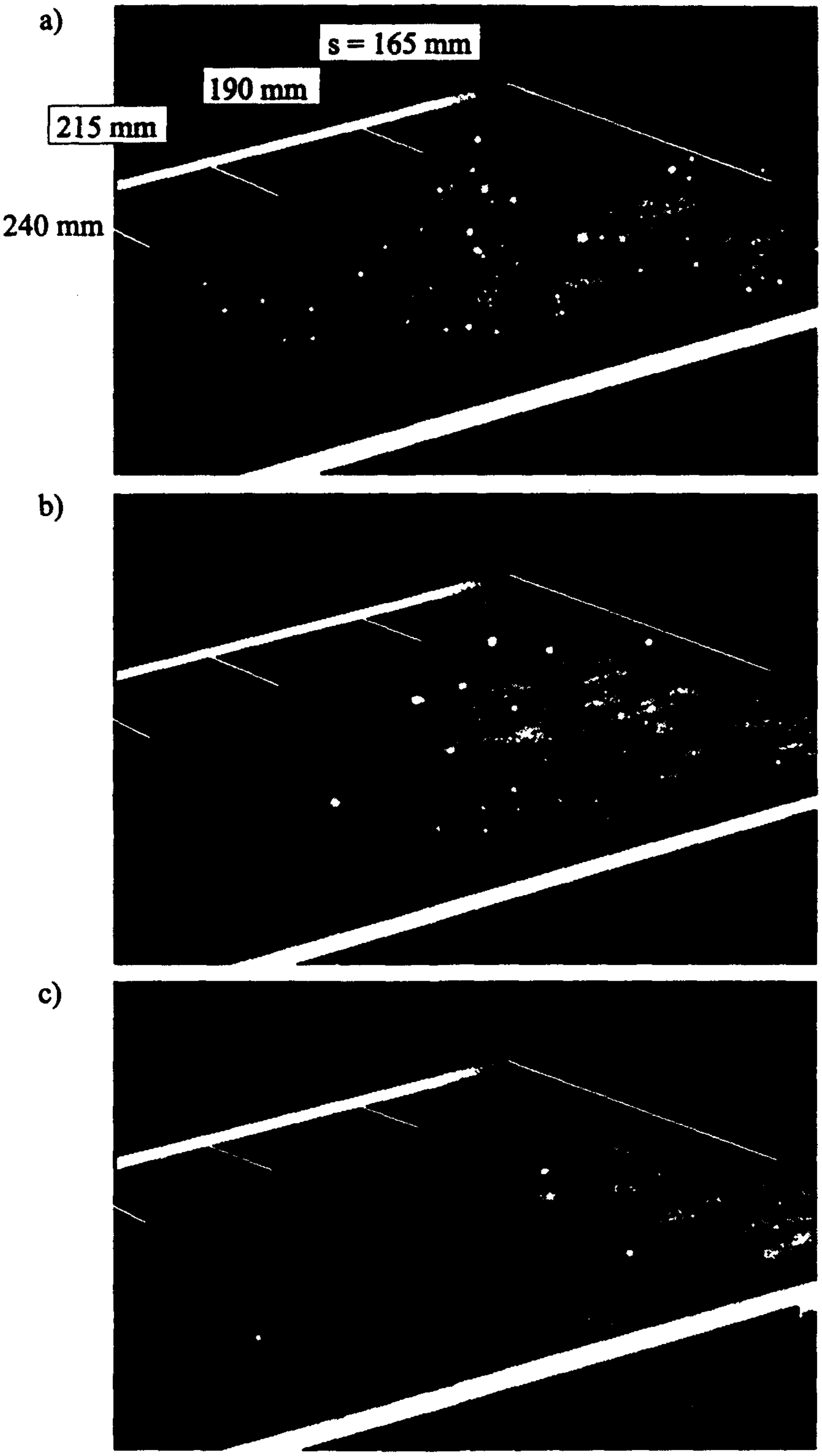

Figure 54. Instantaneous FRS plan views of the boundary layer downstream of the 7° centered expansion with flow straightening assembly removed. The laser sheet is parallel to the surface at an elevation of 6.5 mm.

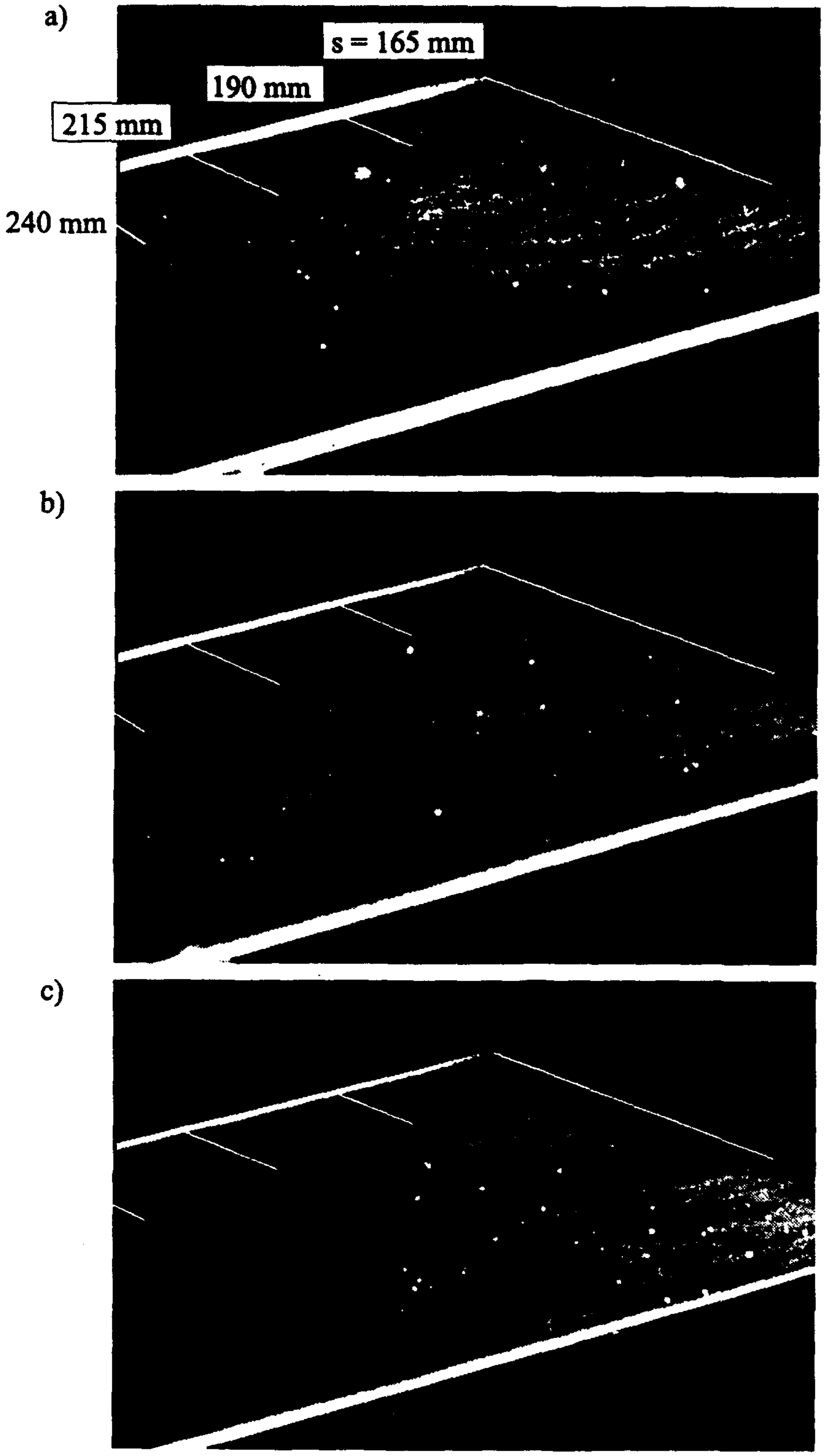

Figure 55. Instantaneous FRS plan views of the boundary layer downstream of the 7° centered expansion with flow straightening assembly removed. The laser sheet is parallel to the surface at an elevation of 8.5 mm.

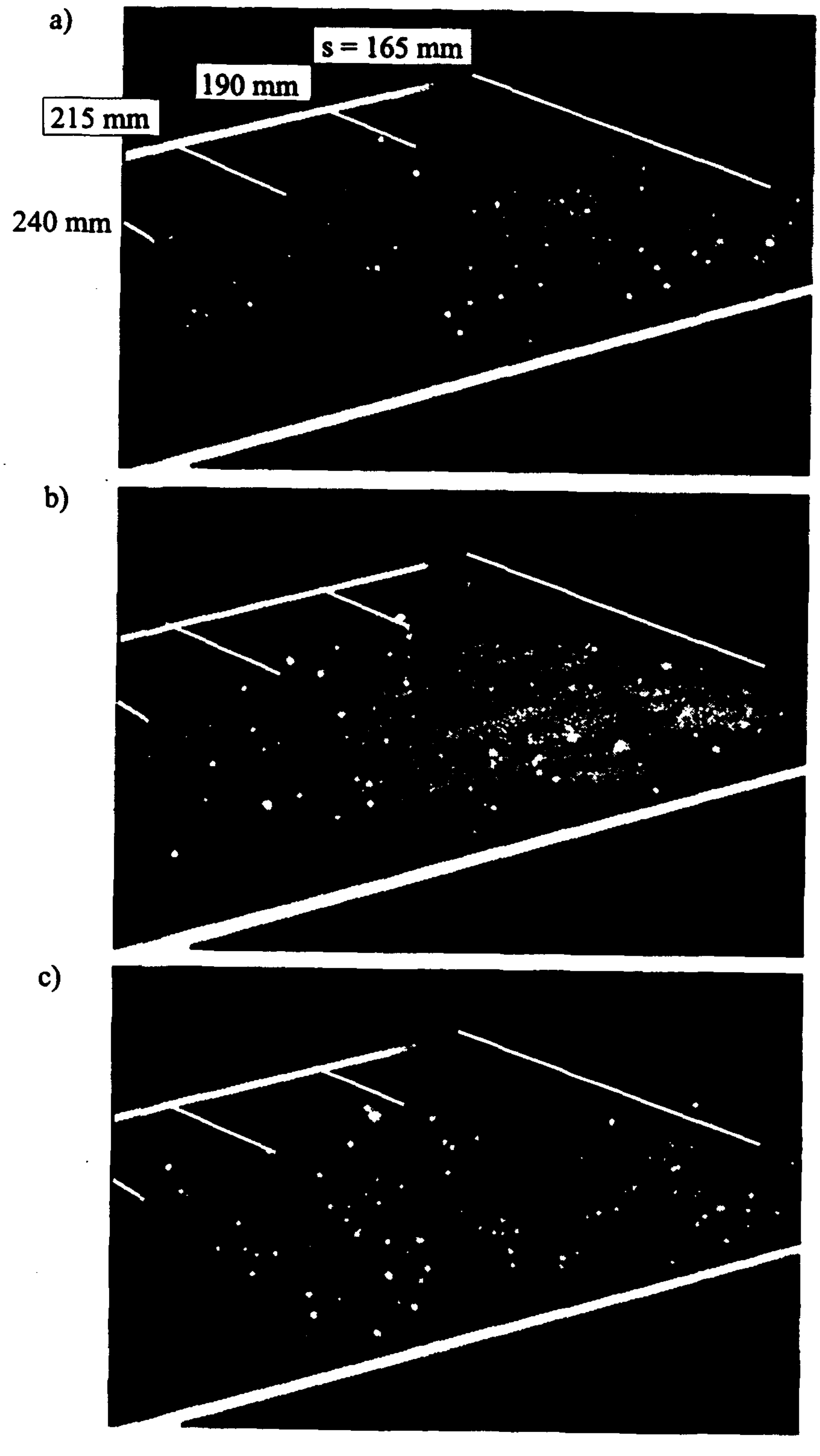

Figure 56. Instantaneous FRS plan views of the boundary layer downstream of the 7° centered expansion with flow straightening assembly removed. The laser sheet is parallel to the surface at an elevation of 10.5 mm.

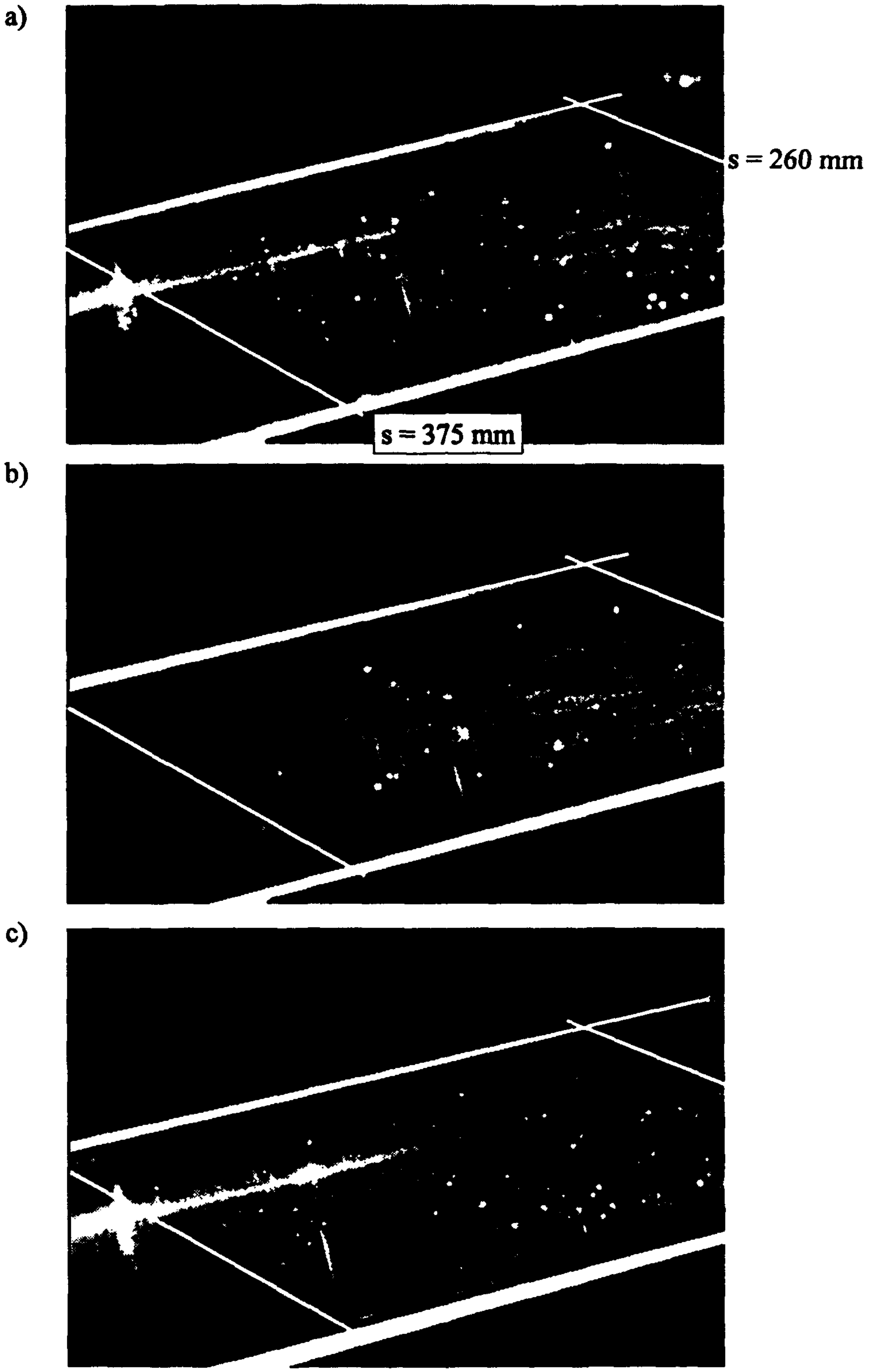

Figure 57. Instantaneous FRS plan views of the boundary layer downstream of the 7° gradual expansion with flow straightening assembly removed. The laser sheet is parallel to the surface at an elevation of 6.5 mm. The strong reflections from the model surface just left of tunnel center that are apparent in Images (a) and (c) have been blacked out in Image (b).

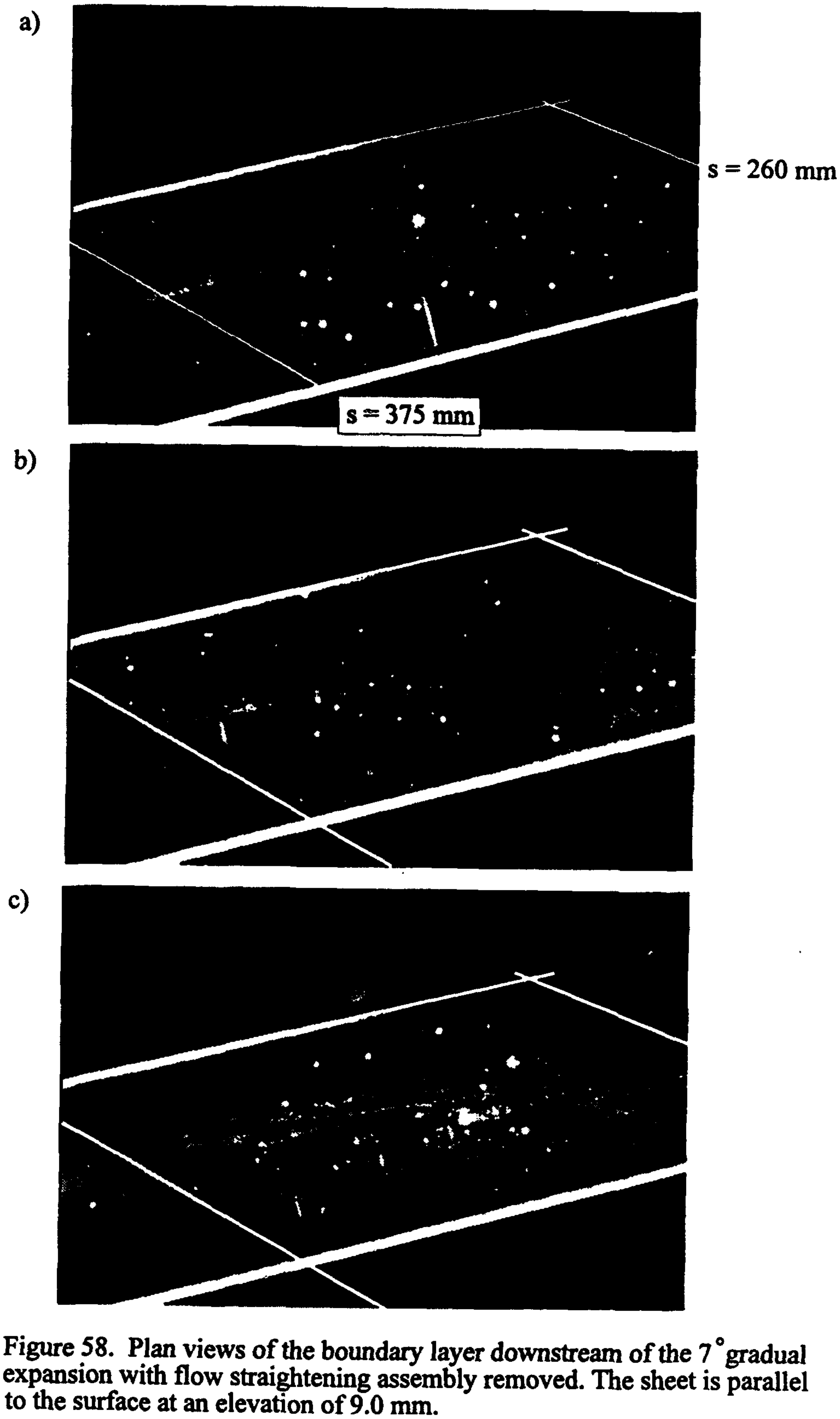

Figure 58. Plan views of the boundary layer downstream of the 7° gradual expansion with flow straightening assembly removed. The sheet is parallel to the surface at an elevation of 9.0 mm.

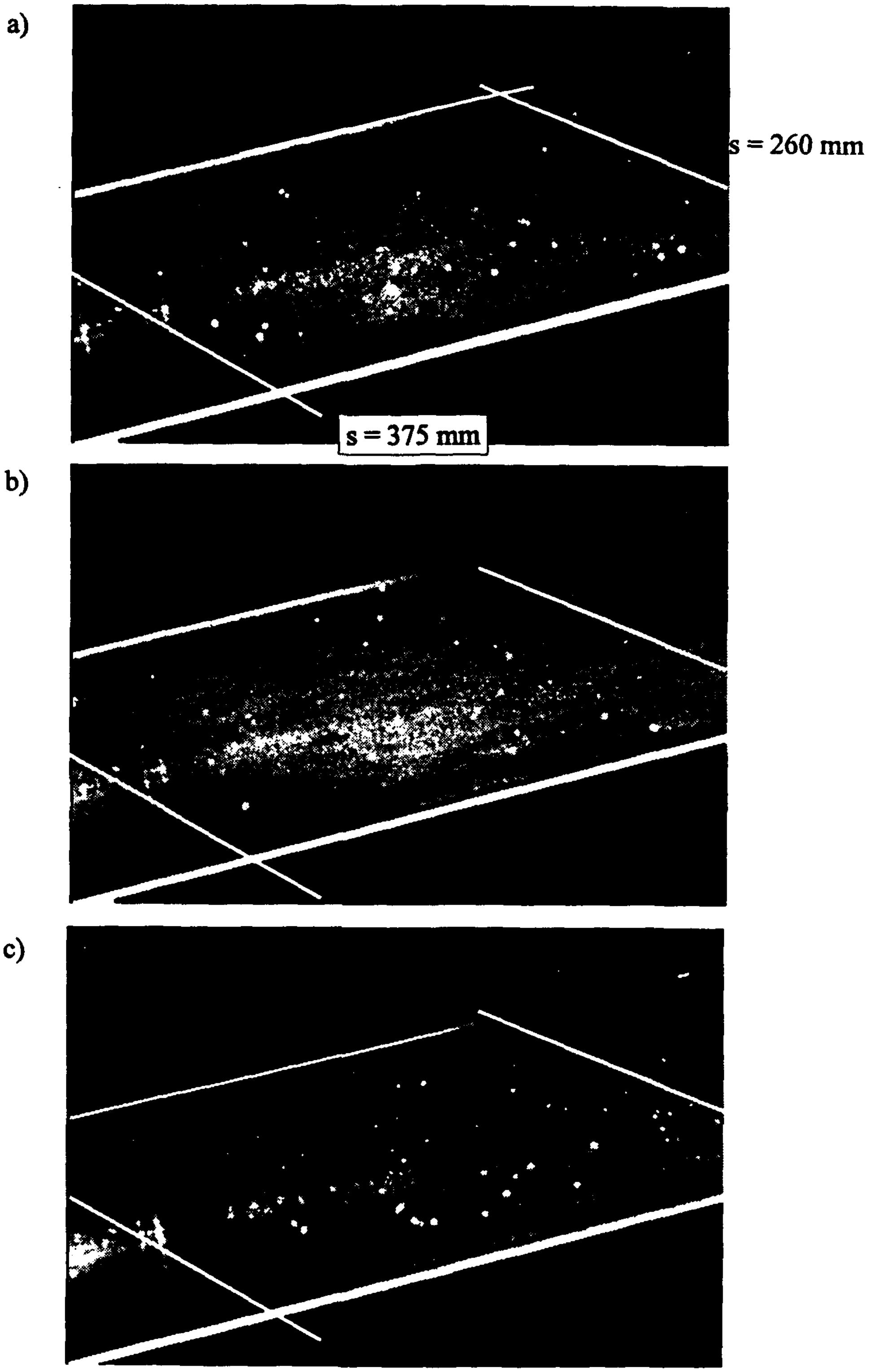

Figure 59. Instantaneous FRS plan views of the boundary layer downstream of the 7° gradual expansion with flow straightening assembly removed. The laser sheet is parallel to the surface at an elevation of 11.5 mm.

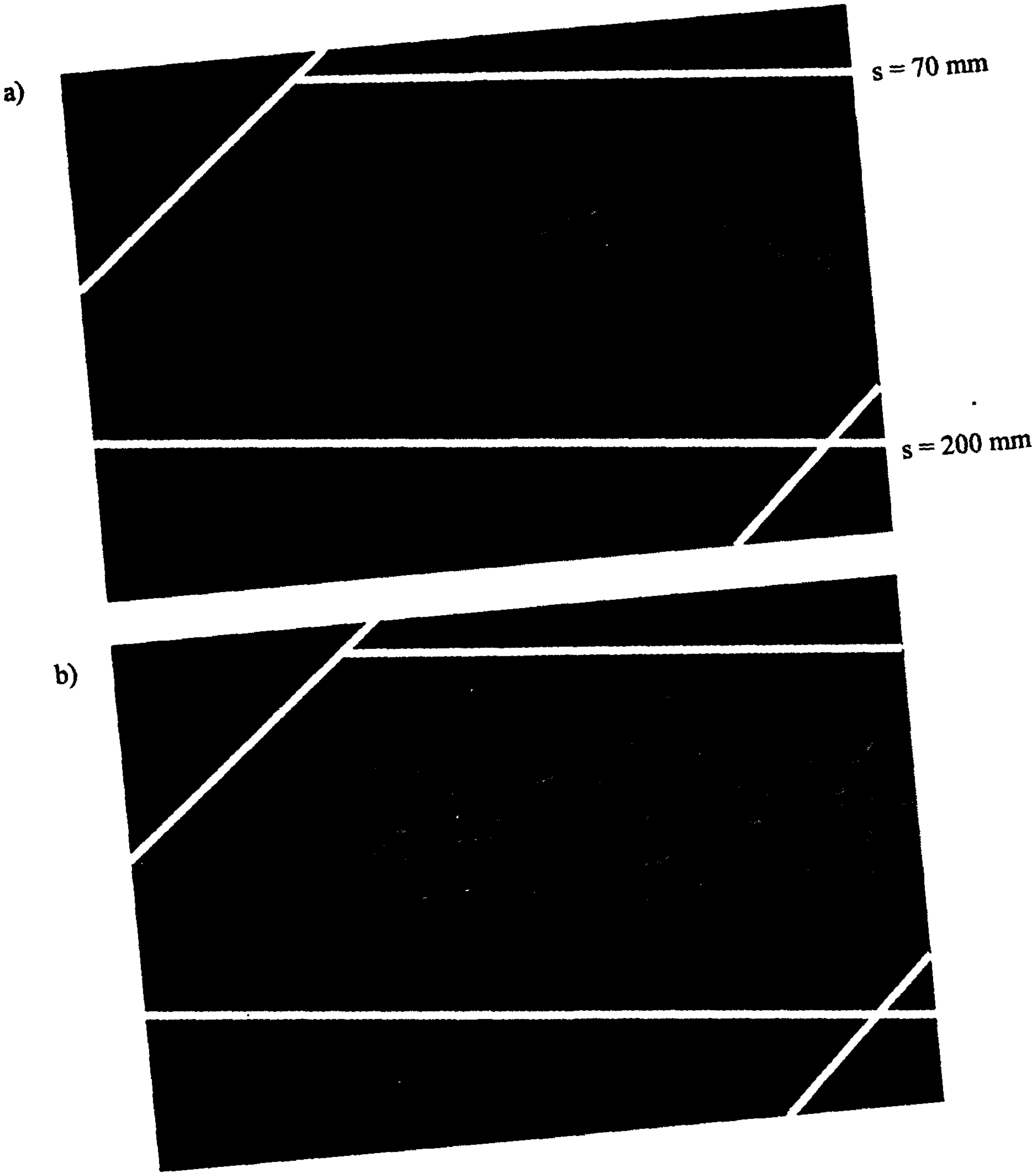

Figure 60. Instantaneous FRS plan views of the boundary layer downstream of the 14° centered expansion with flow straightening assembly removed. The laser sheet is parallel to the surface at an elevation of 20.0 mm.

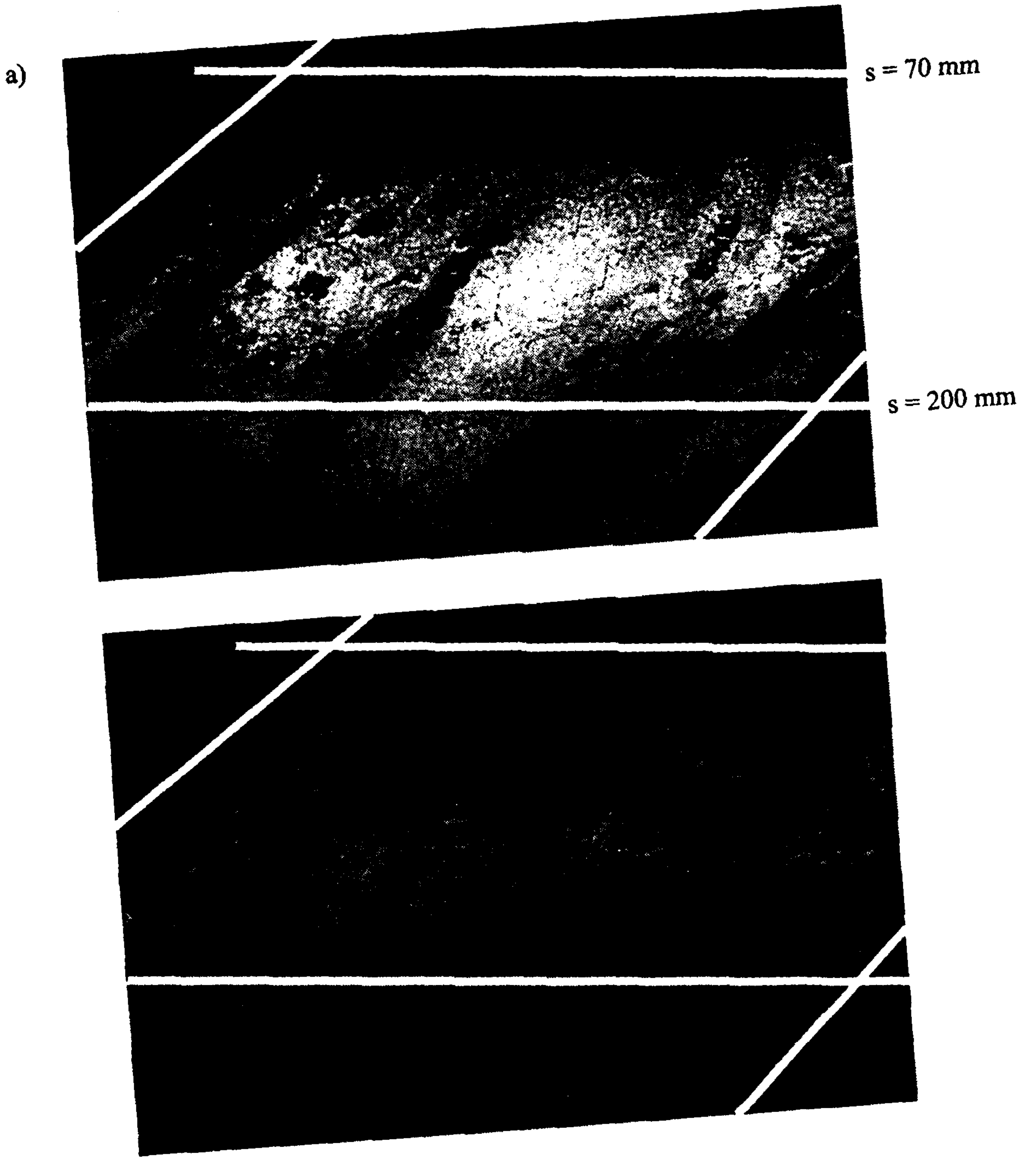

Figure 61. Instantaneous FRS plan views of the boundary layer downstream of the 14° centered expansion with flow straightening assembly removed. The laser sheet is parallel to the surface at an elevation of 23.0 mm.

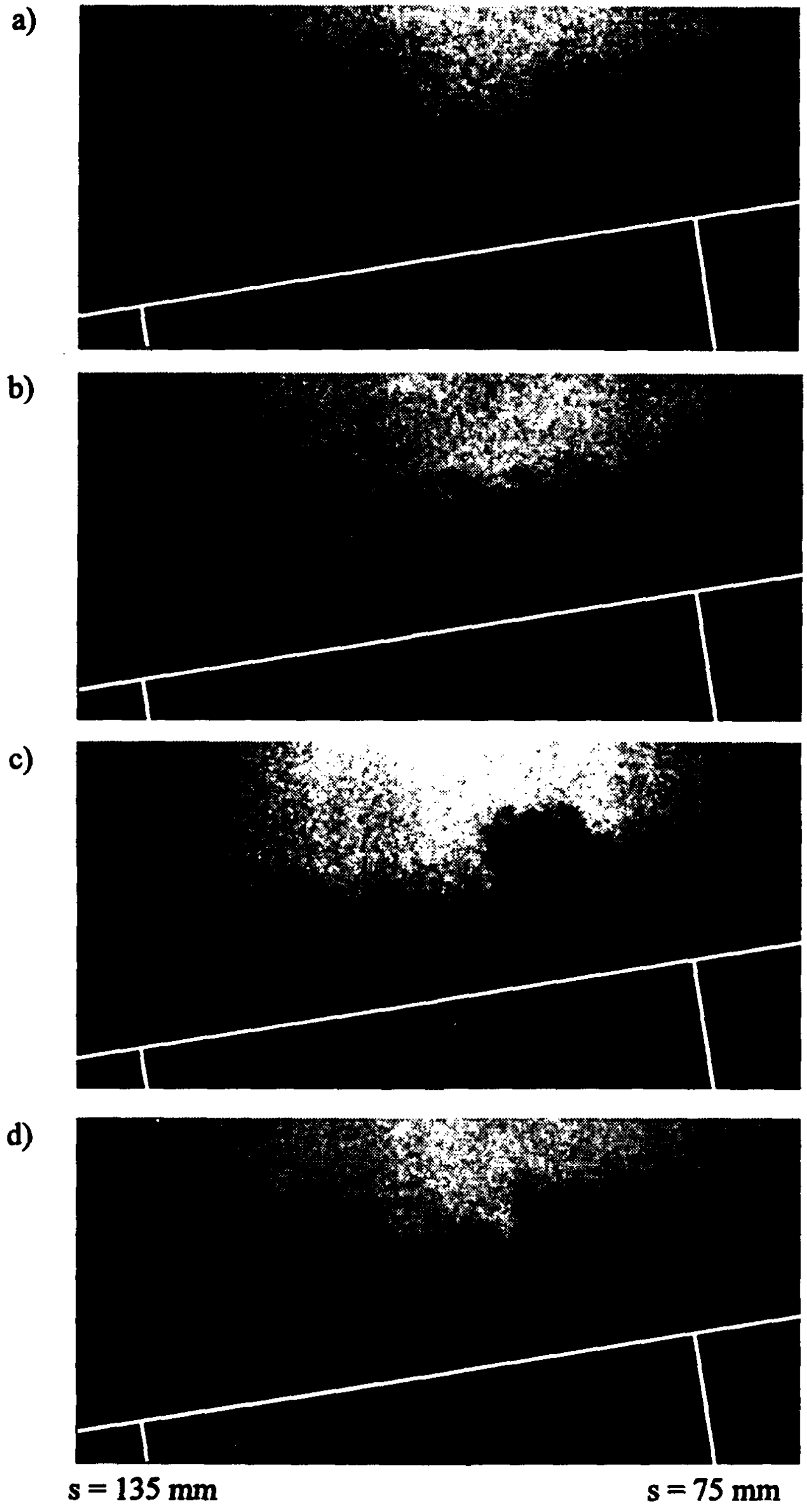

Figure 62. Instantaneous FRS streamwise views of the boundary layer downstream of the 7° centered expansion.

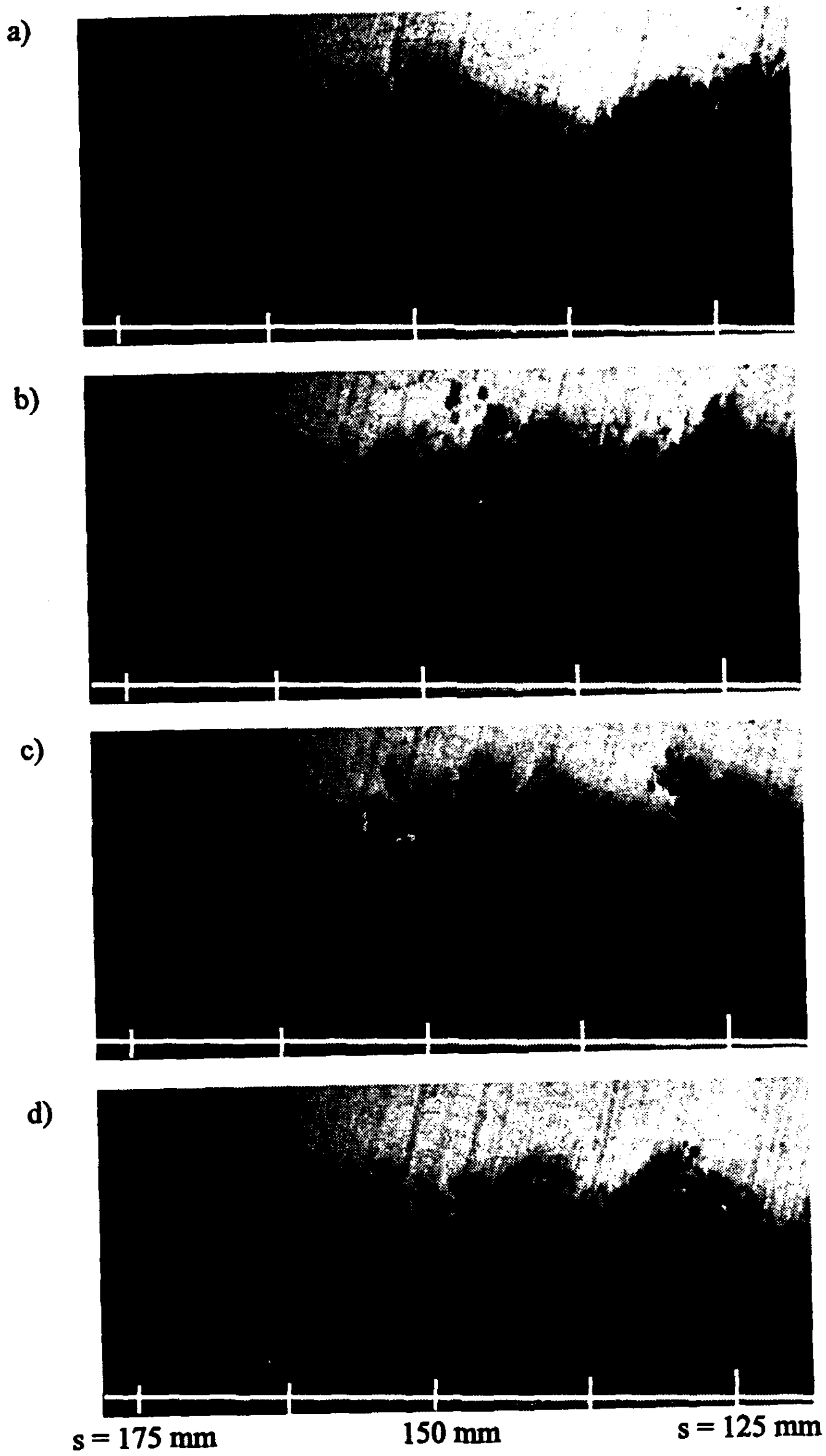

Figure 63. Instantaneous streamwise views of the boundary layer downstream of the 14° centered expansion.

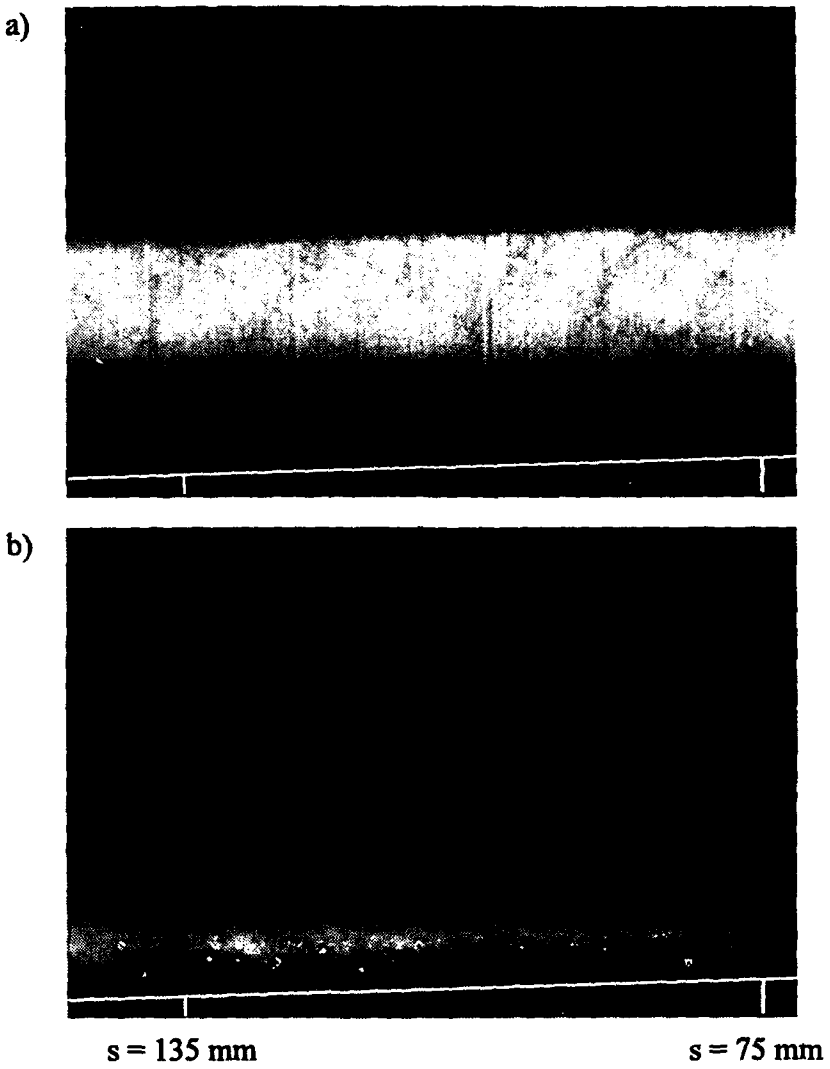

Figure 64. Average (a) and RMS normalized by average (b) images for the ensemble of FRS streamwise views of the flat plate boundary layer.

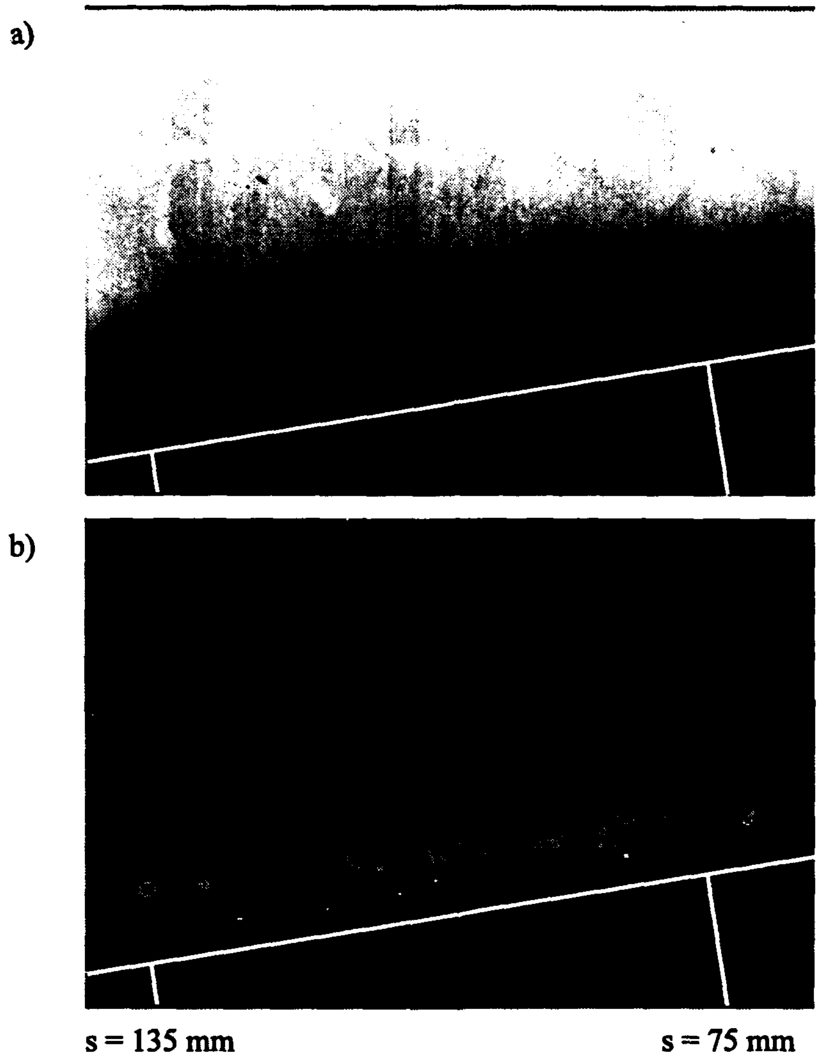

Figure 65. Average (a) and RMS normalized by average (b) images for the ensemble of FRS streamwise views acquired downstream of the 7° centered expansion.

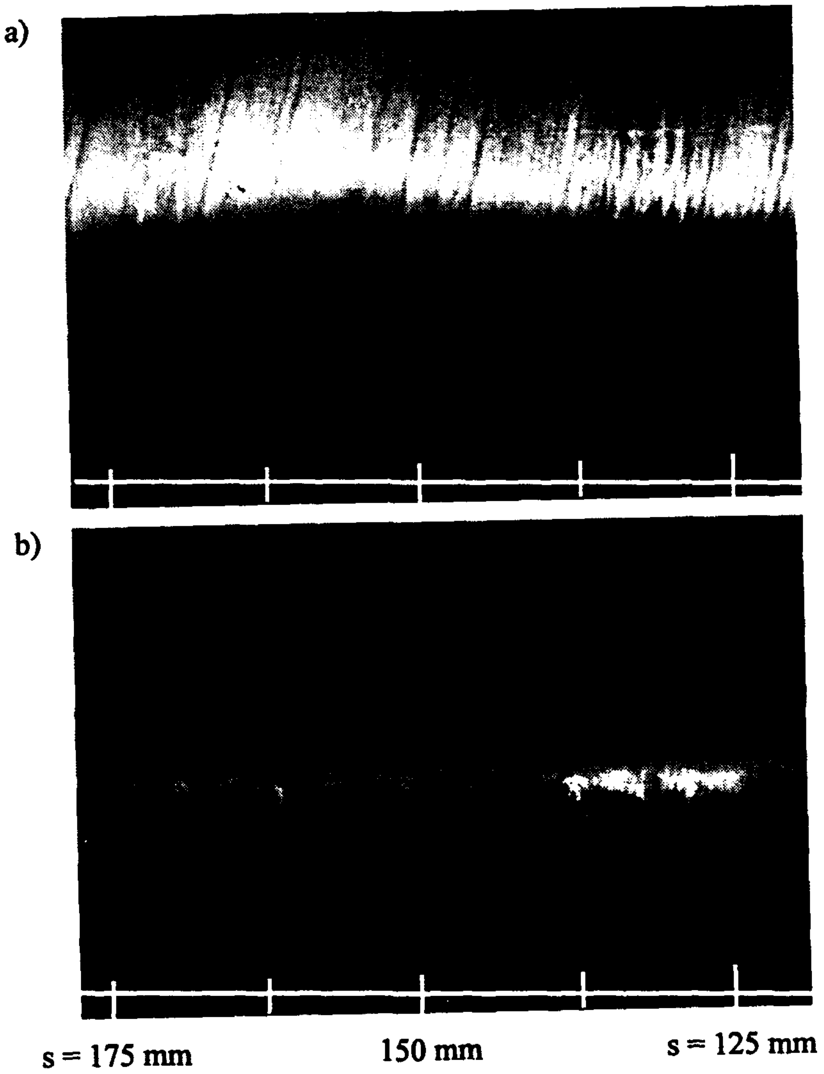

Figure 66. Average (a) and RMS normalized by average (b) images for the ensemble of FRS streamwise views acquired downstream of the 14° centered expansion.

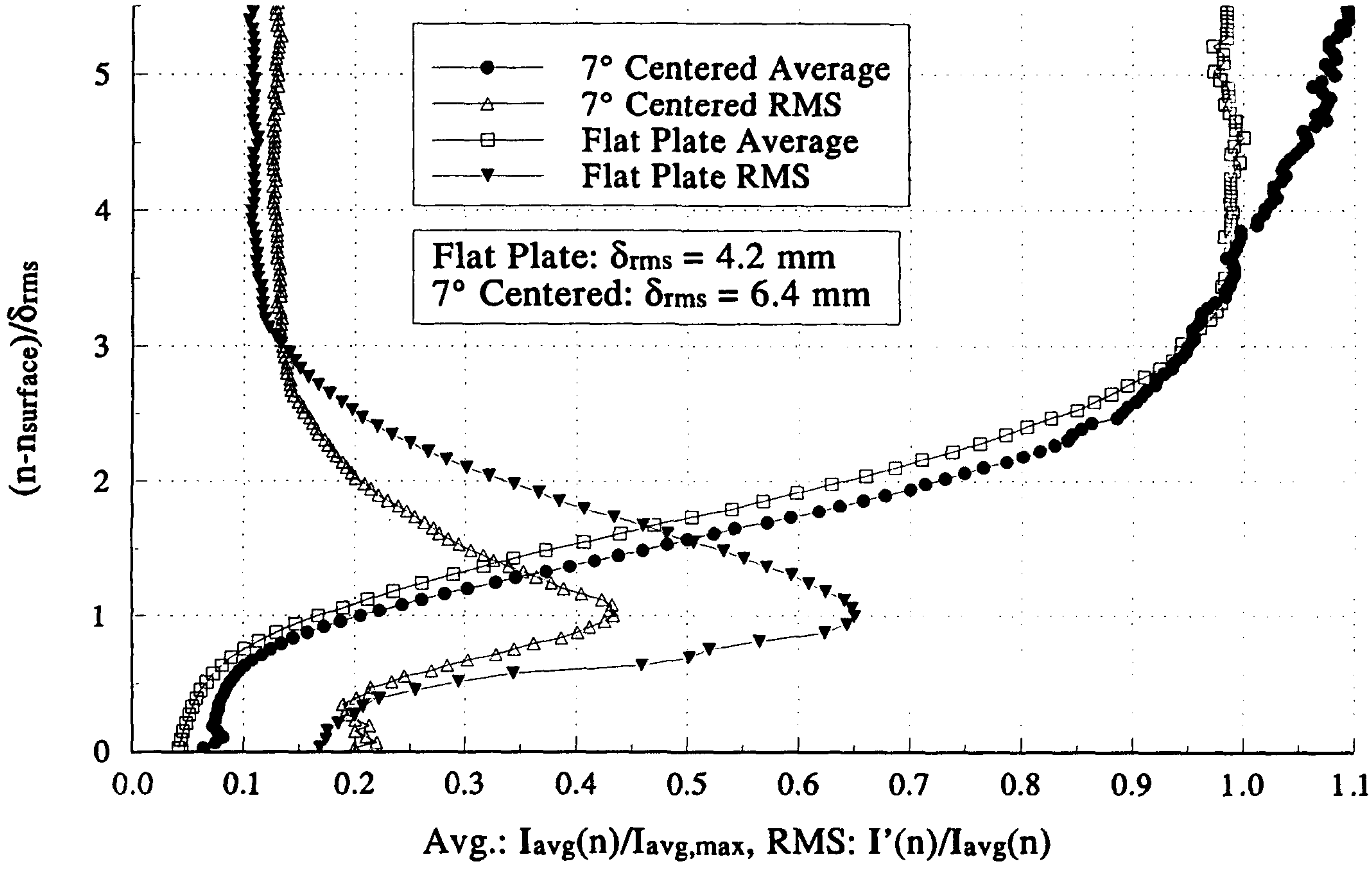

Figure 67. Average and RMS profiles for the flat plate boundary layer ($s/\delta_0 = 11.4$; $\delta_0 = 9.2$ mm) and the boundary layer downstream of the 7° centered expansion ($s/\delta_0 = 11.4$). For both the flat plate and the 7° expansion cases, the normal distance from the surface has been nondimensionalized by the distance above the surface at which the peak in the RMS profile occurs.

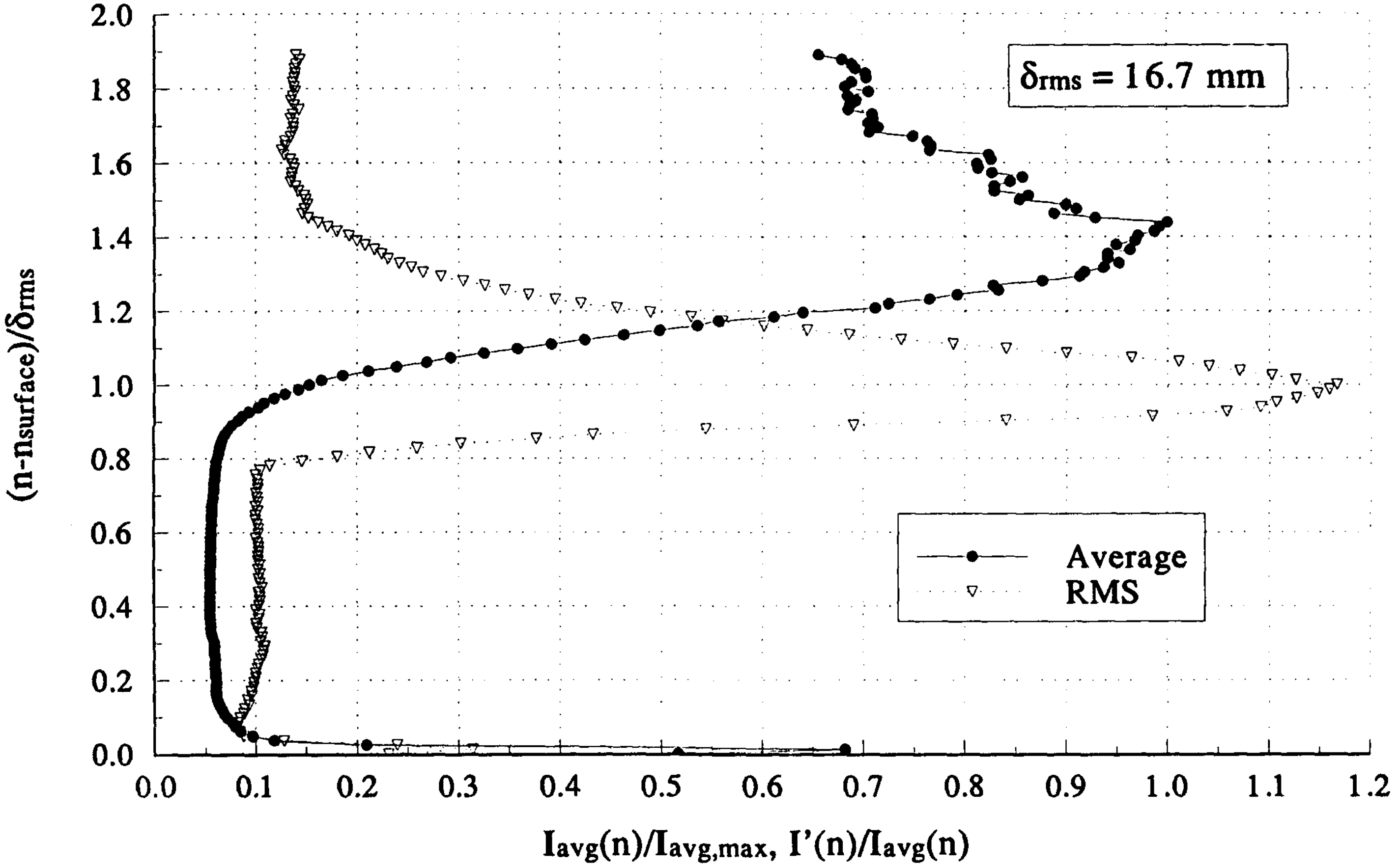

Figure 68. Average and RMS profiles at $s/\delta_0 = 14.7$ downstream of the 14° centered expansion. The normal distance from the surface has been nondimensionalized by the distance above the surface at which the peak in the RMS profile occurs.

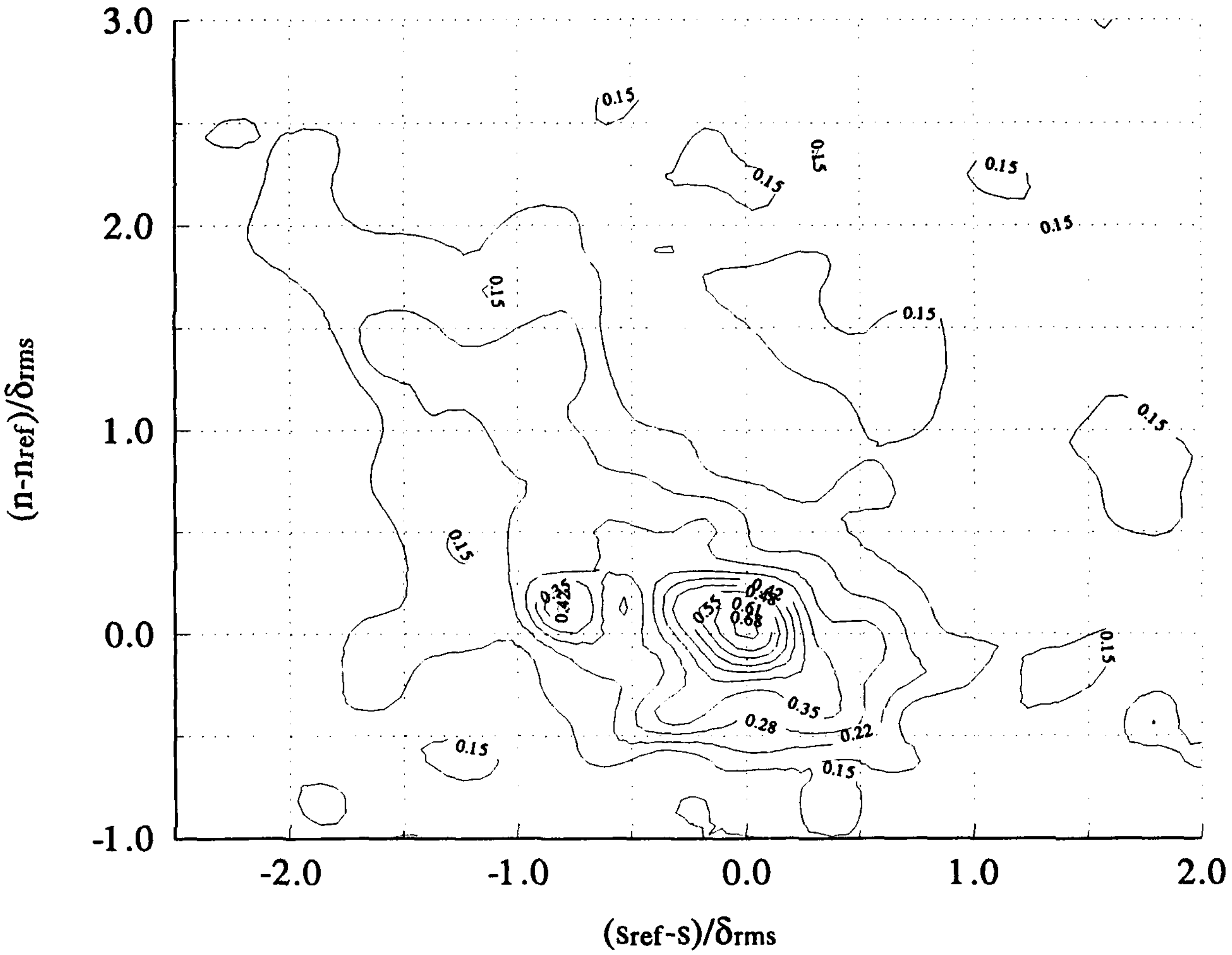

Figure 69. Spatial correlation contours for the ensemble of streamwise visualizations of the flat plate boundary layer. The reference point for the correlation is at a normal distance of $n/\delta_{rms} = 1.0$ above the surface.

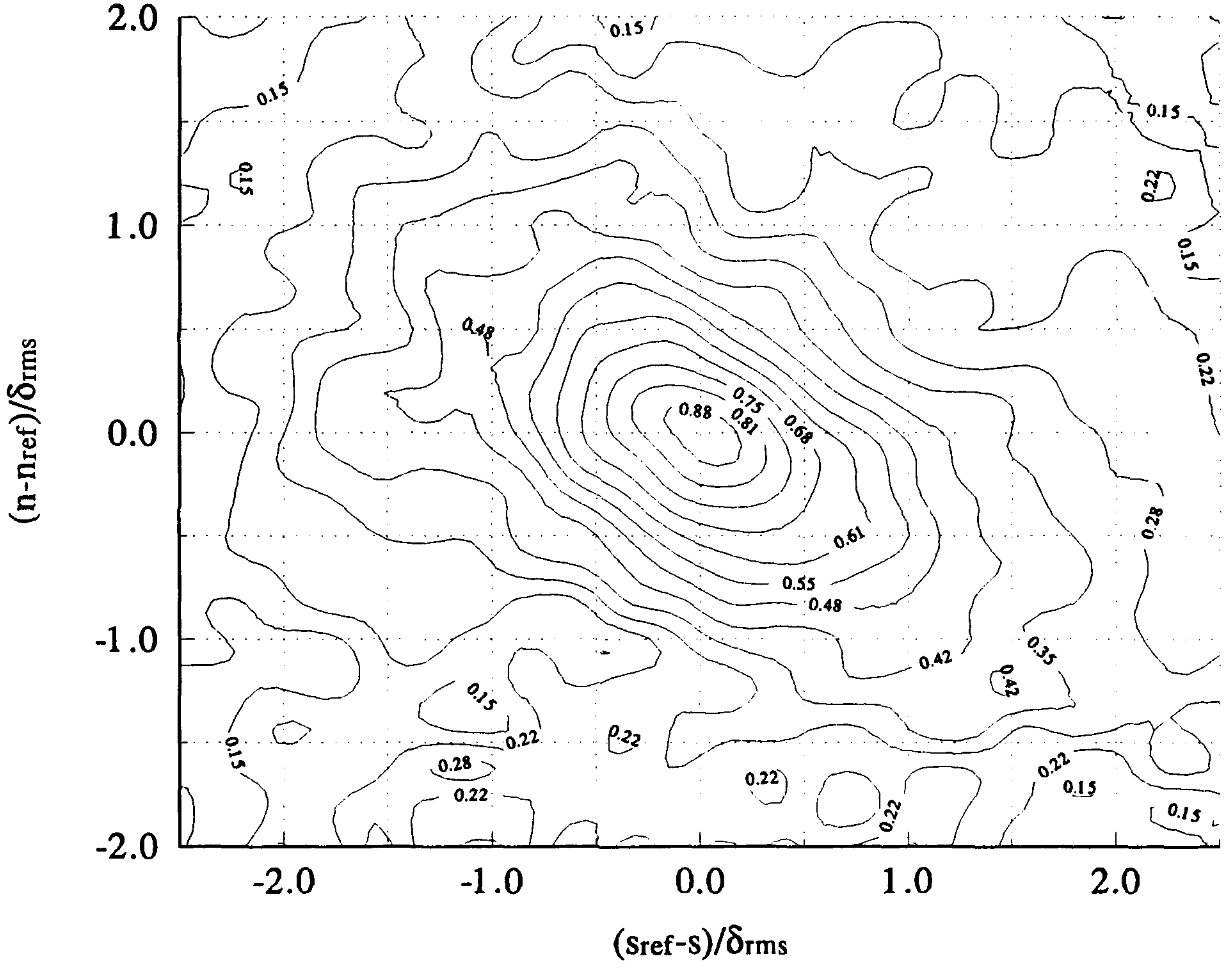

Figure 70. Spatial correlation contours for the ensemble of streamwise visualizations of the flat plate boundary layer. The reference point for the correlation is at a normal distance of $n/\delta_{rms} = 2.0$ above the surface.

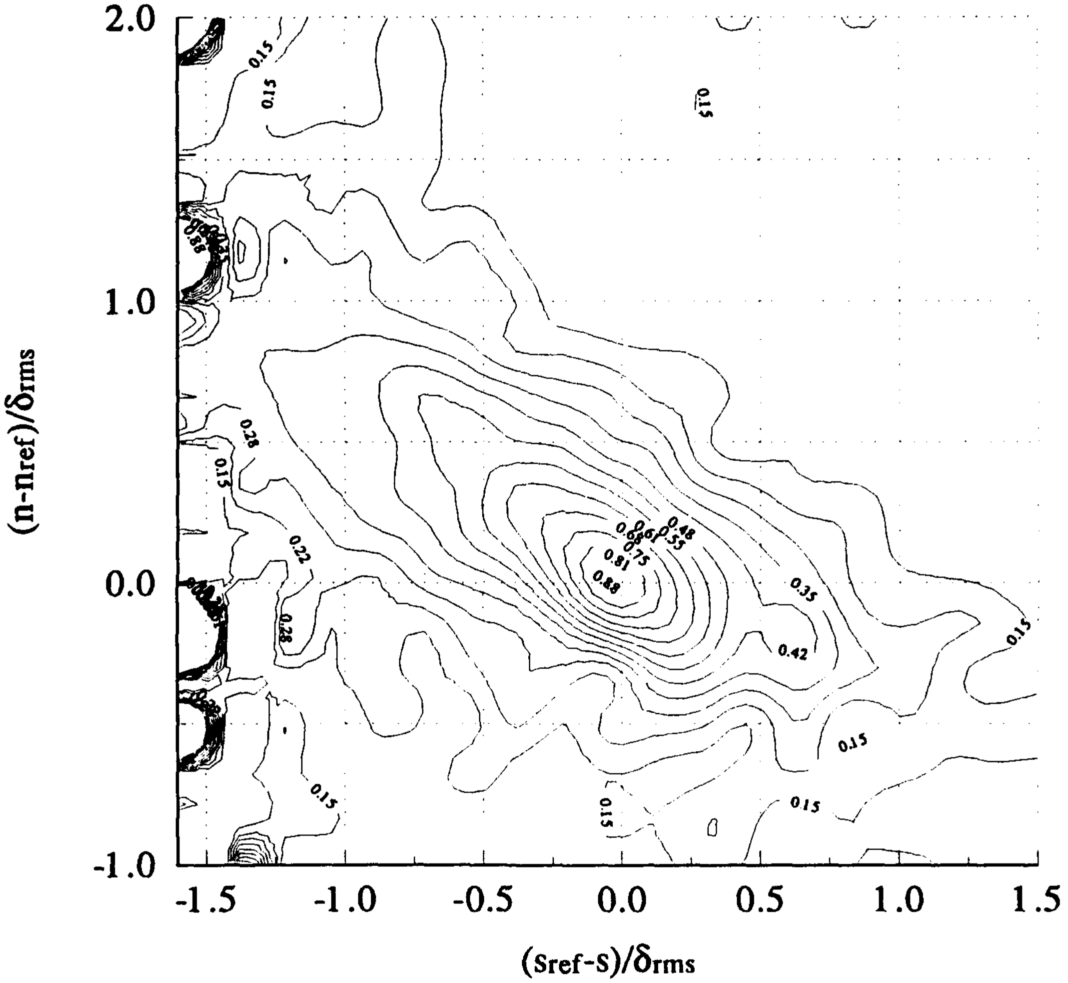

Figure 71. Spatial correlation contours for the ensemble of streamwise visualizations of the boundary layer downstream of the 7° centered expansion. The reference point for the correlation is at a normal distance of $n/\delta_0 = 1.0$ above the surface.

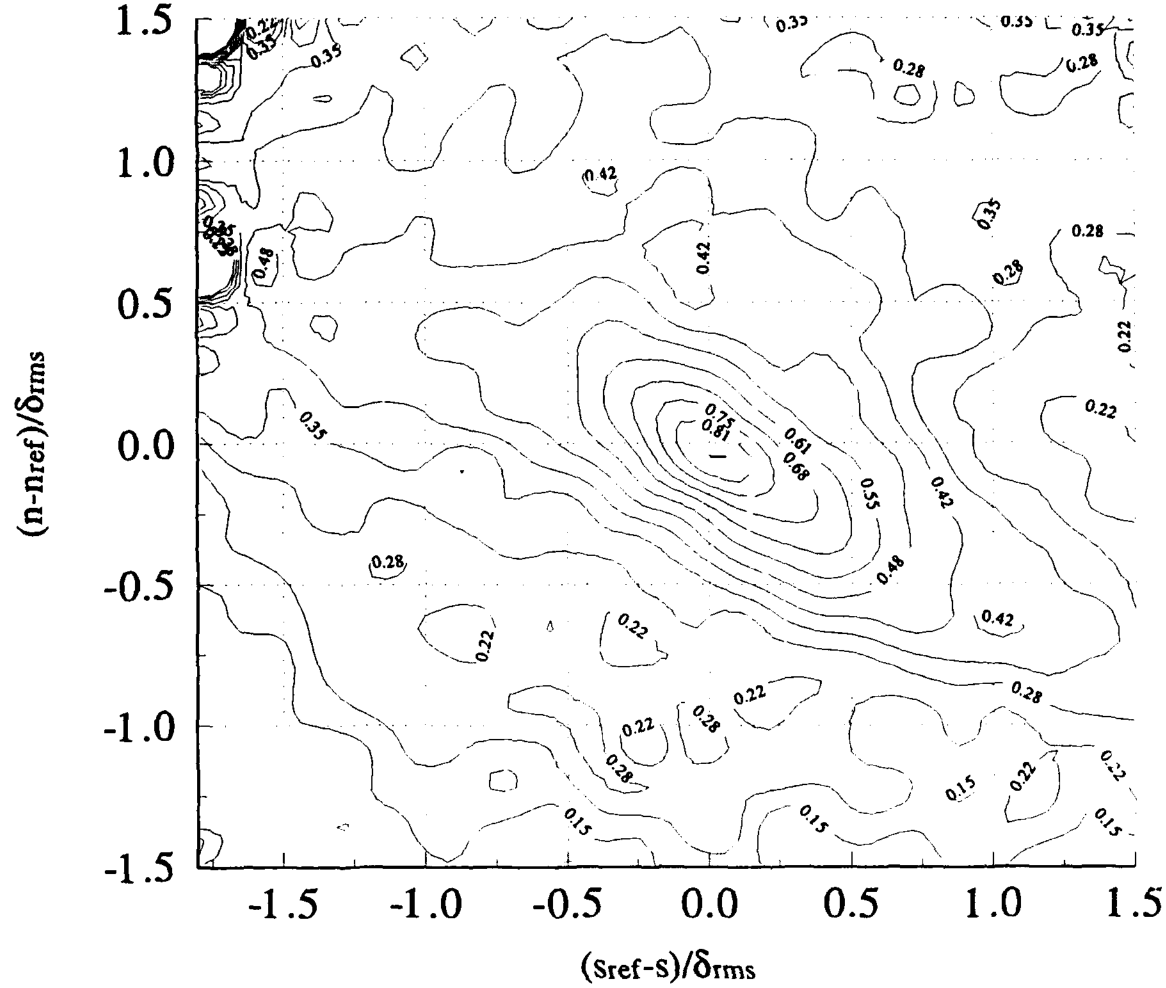

Figure 72. Spatial correlation contours for the ensemble of streamwise visualizations of the boundary layer downstream of the 7° centered expansion. The reference point for the correlation is at a normal distance of $n/\delta_0 = 2.0$ above the surface.

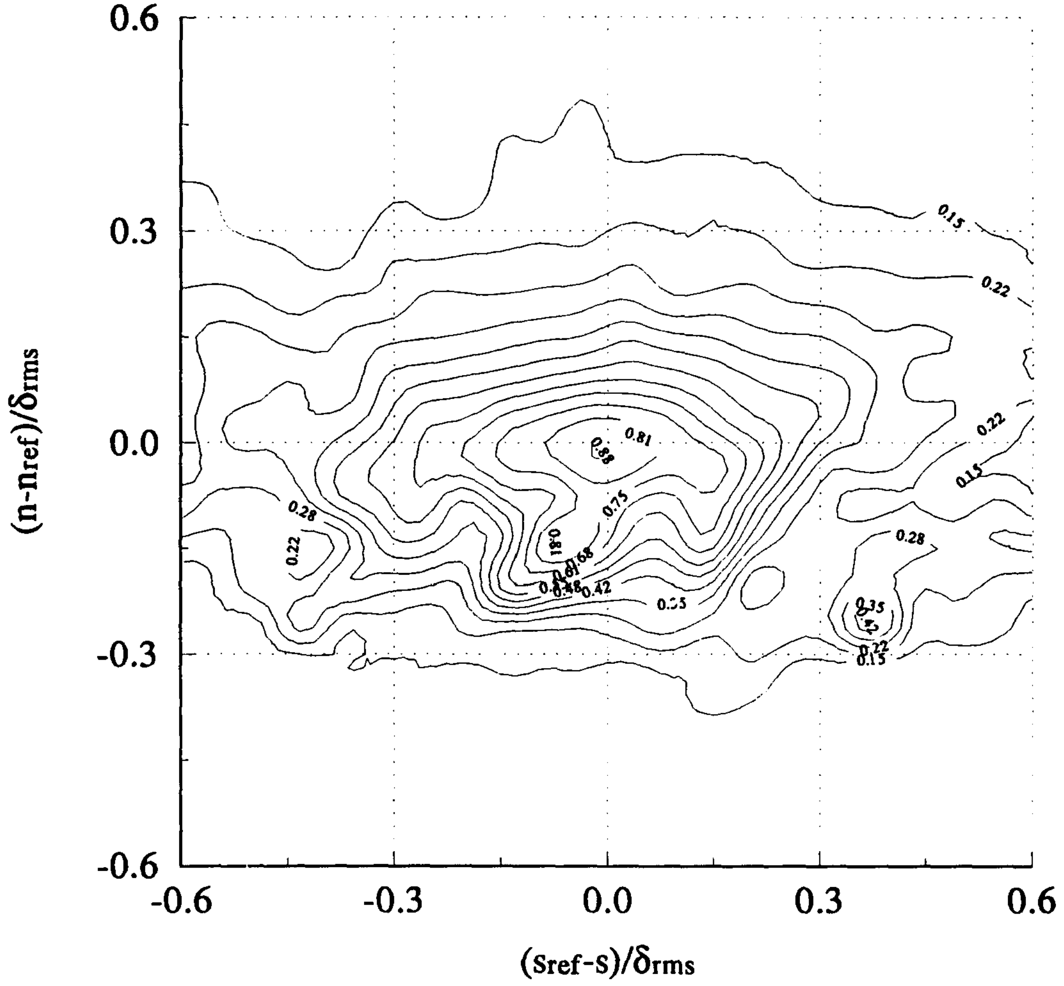

Figure 73. Spatial correlation contours for the ensemble of streamwise visualizations of the boundary layer downstream of the 14° centered expansion. The reference point for the correlation is at a normal distance of $n/\delta_0 = 1.0$ above the surface.

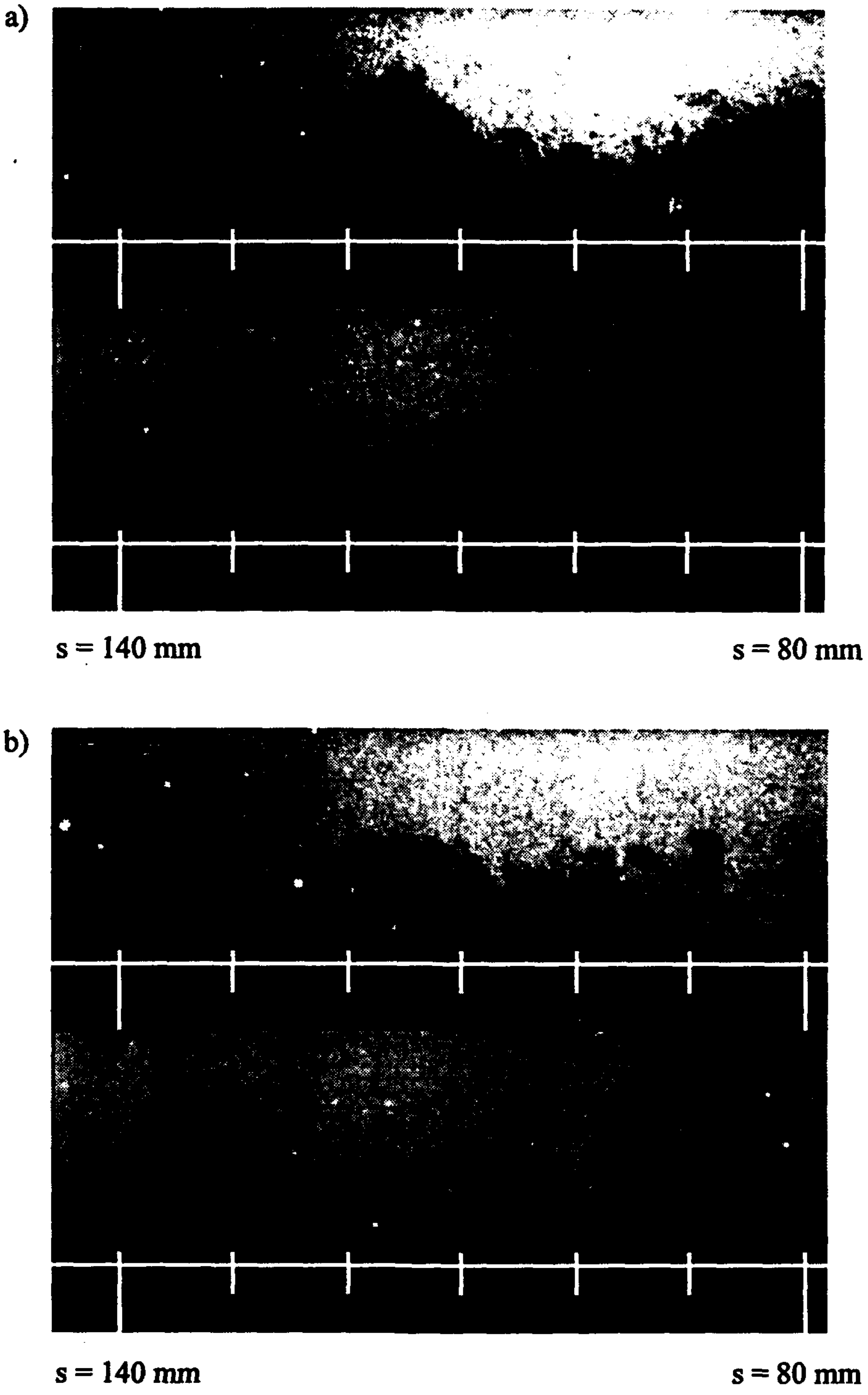

Figure 74. Double-pulse streamwise views of the flat plate boundary layer. The bottom images were acquired 25.0 μs after the top images.

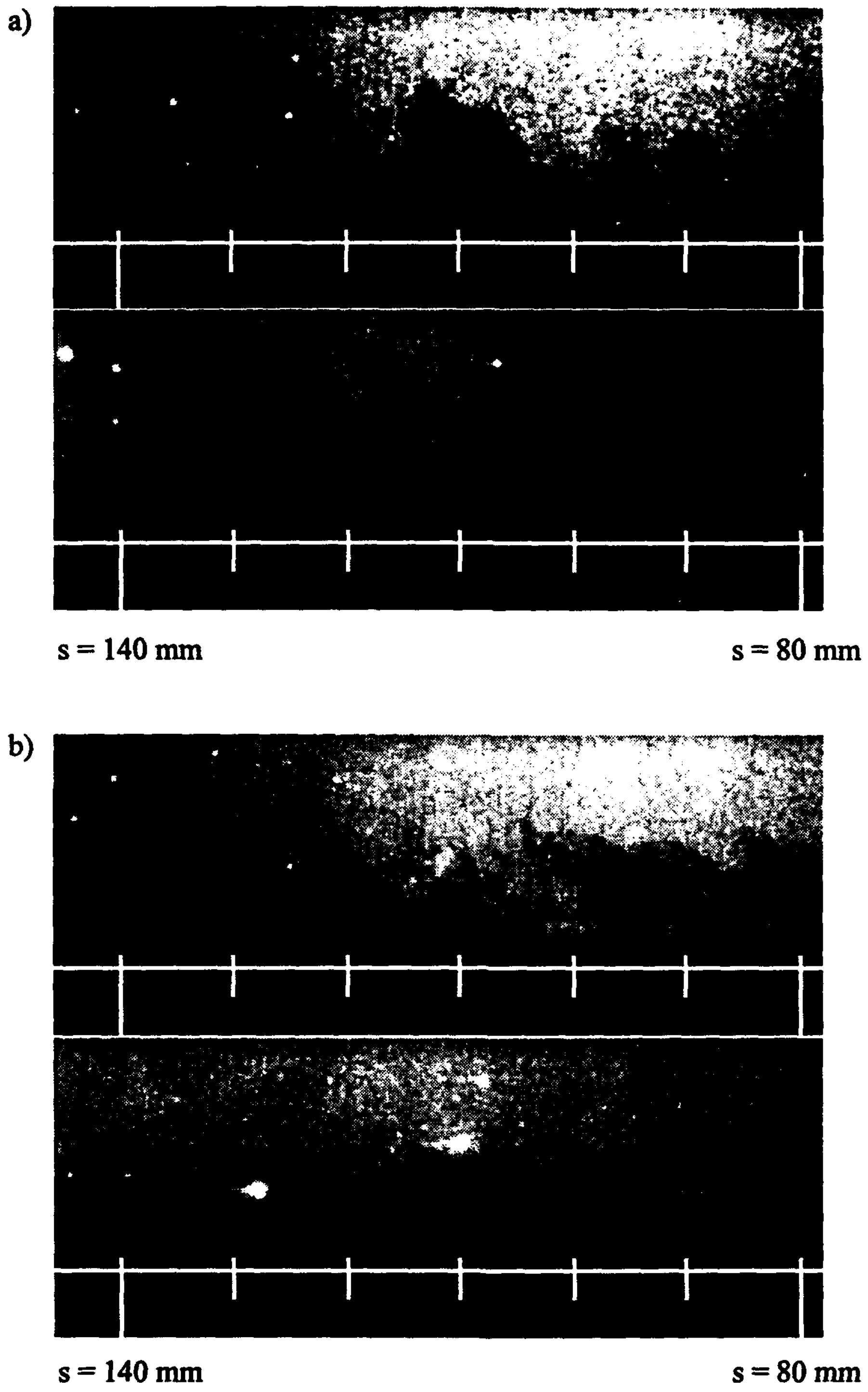

Figure 75. Double-pulse streamwise views of the flat plate boundary layer. The bottom images were acquired 25.0 μs after the top images.

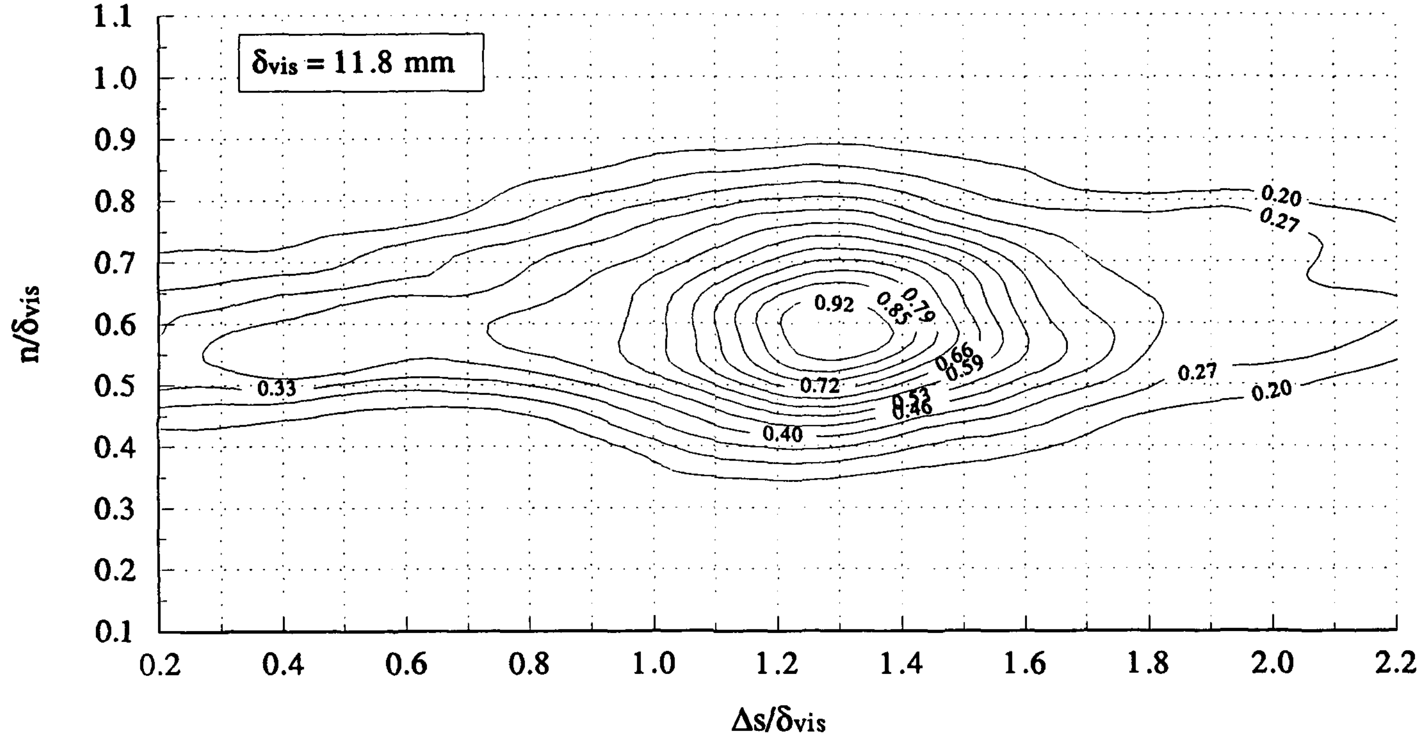

Figure 76. Correlation contours for double-pulse visualizations of the flat plate boundary layer. The time delay between the initial and delayed images is 25.0 μs. The downstream direction is from left to right.

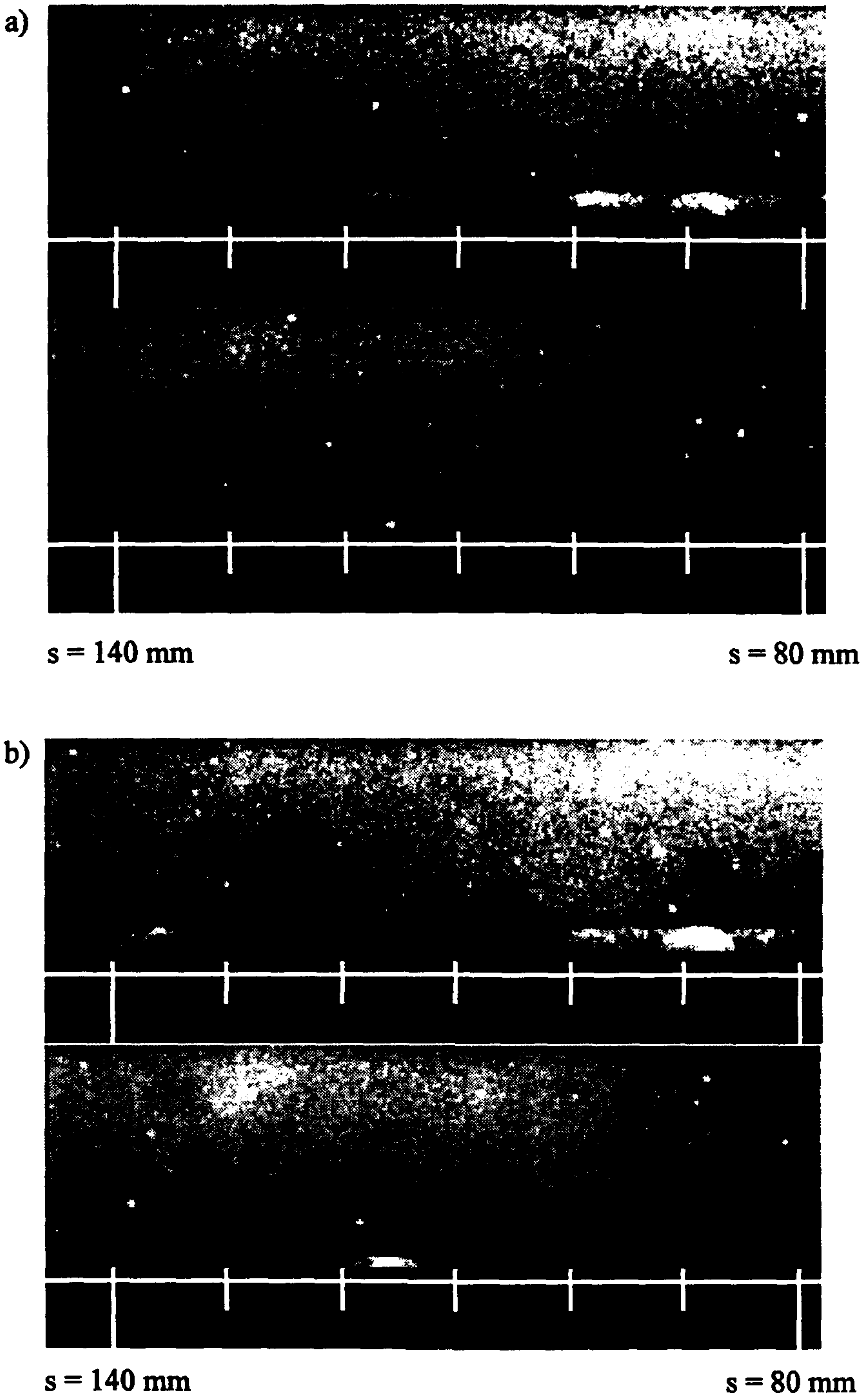

Figure 77. Double-pulse streamwise views of the flat plate boundary layer. The bottom images were acquired 50.0 μs after the top images.

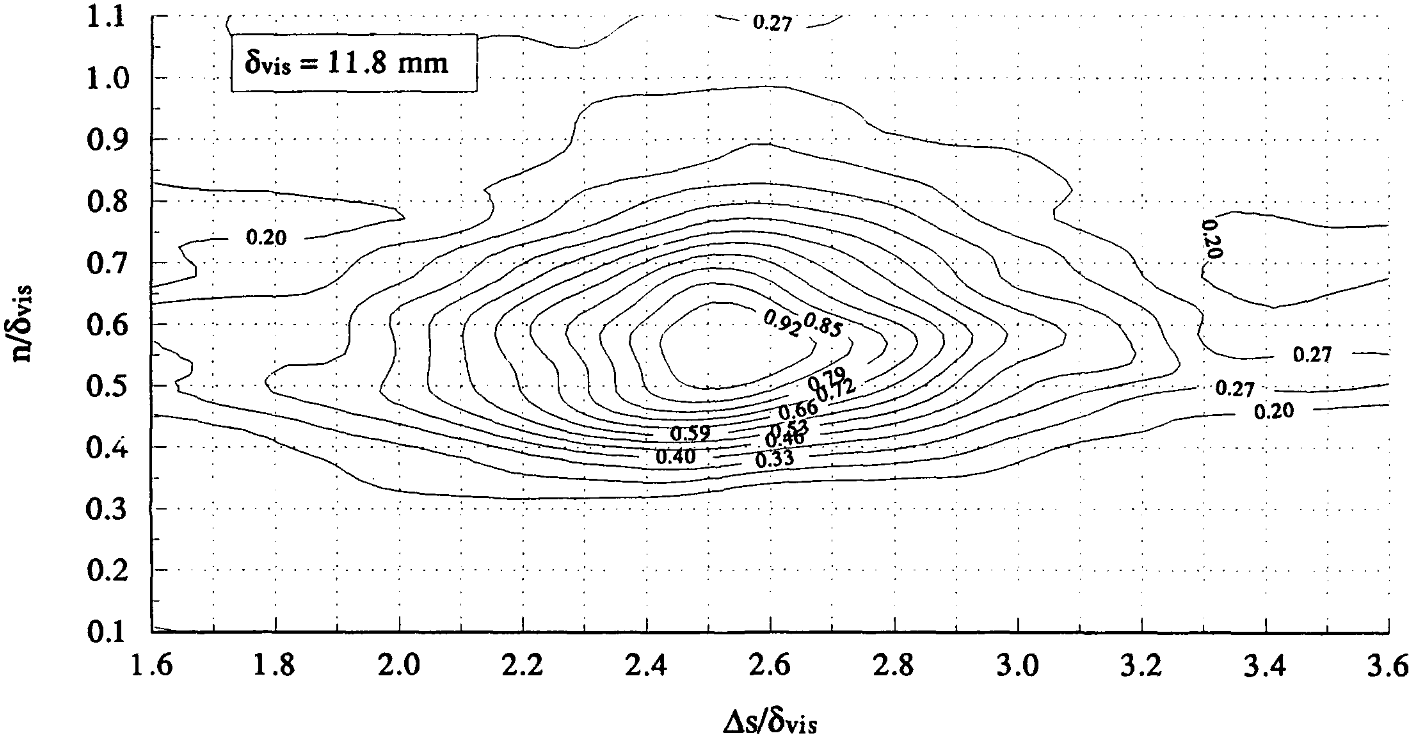

Figure 78. Correlation contours for double-pulse visualizations of the flat plate boundary layer. The time delay between the initial and delayed images is 50.0 μs. The downstream direction is from left to right.

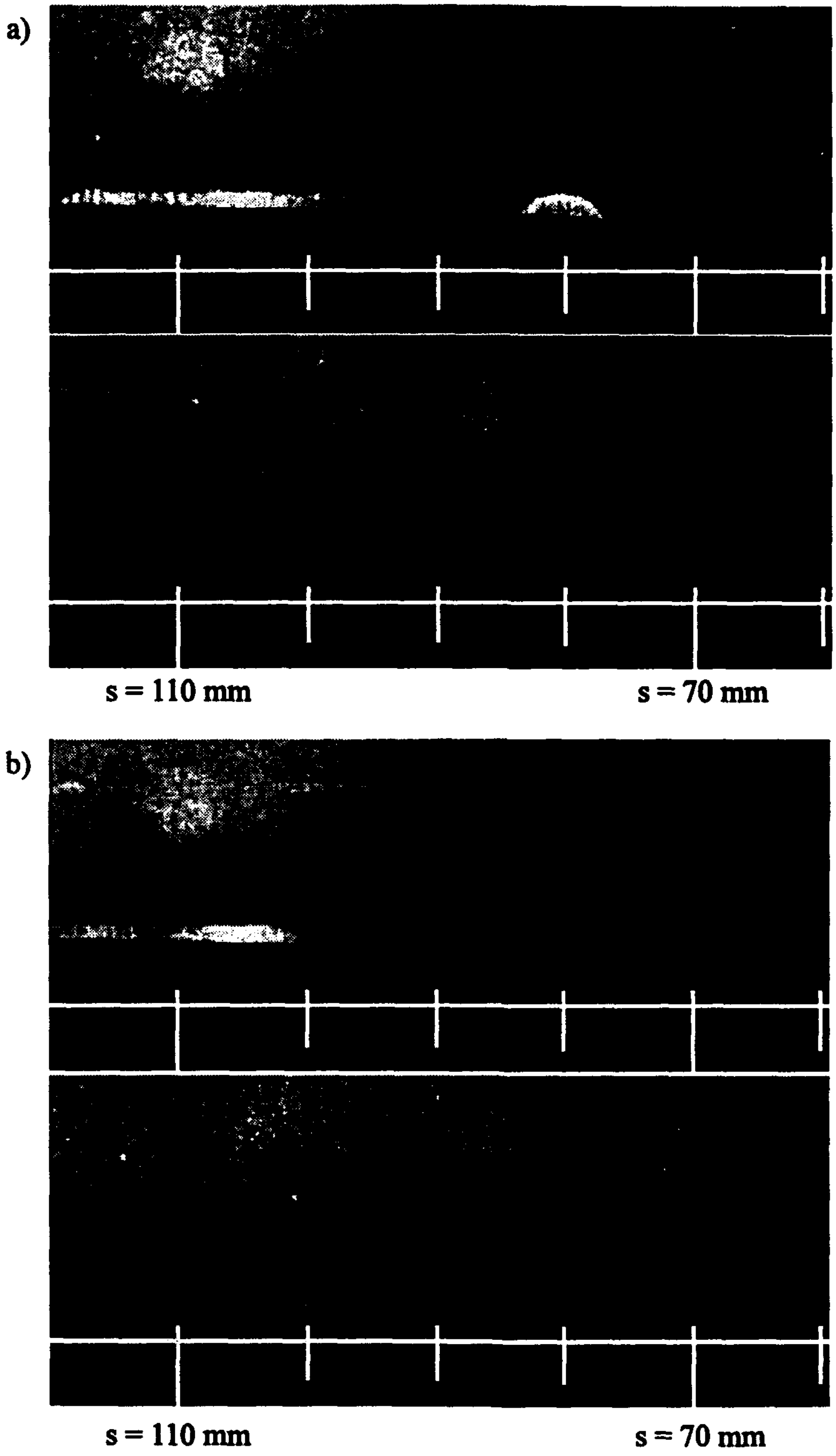

Figure 79. Double-pulse streamwise views of the boundary layer downstream of the 7° centered expansion. The bottom images were acquired 23.9 μs after the top images.

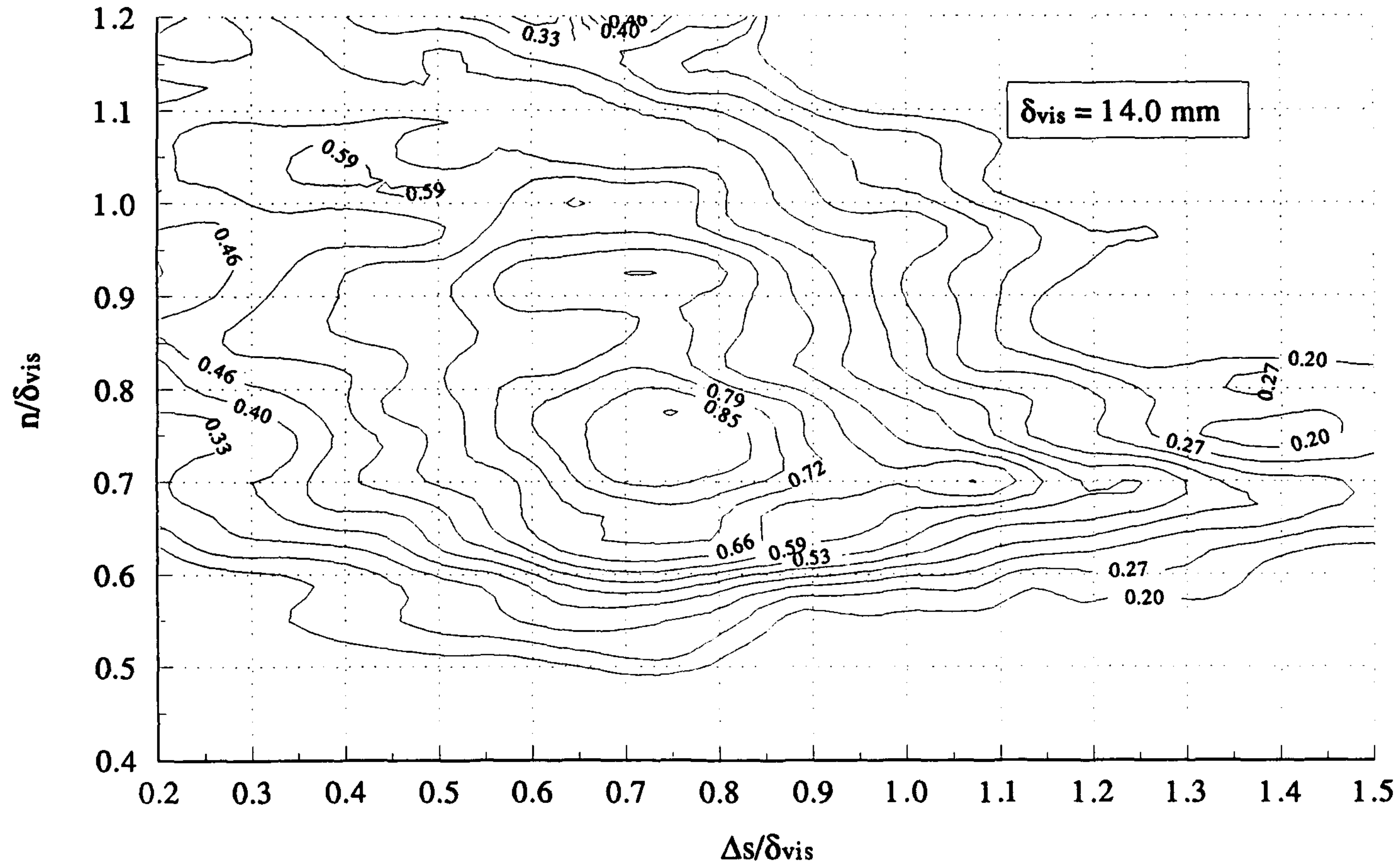

Figure 80. Correlation contours for double-pulse visualizations of the boundary layer downstream of the 7° centered expansion. The time delay between the initial and delayed images is 16.0 μs. The downstream direction is from left to right.

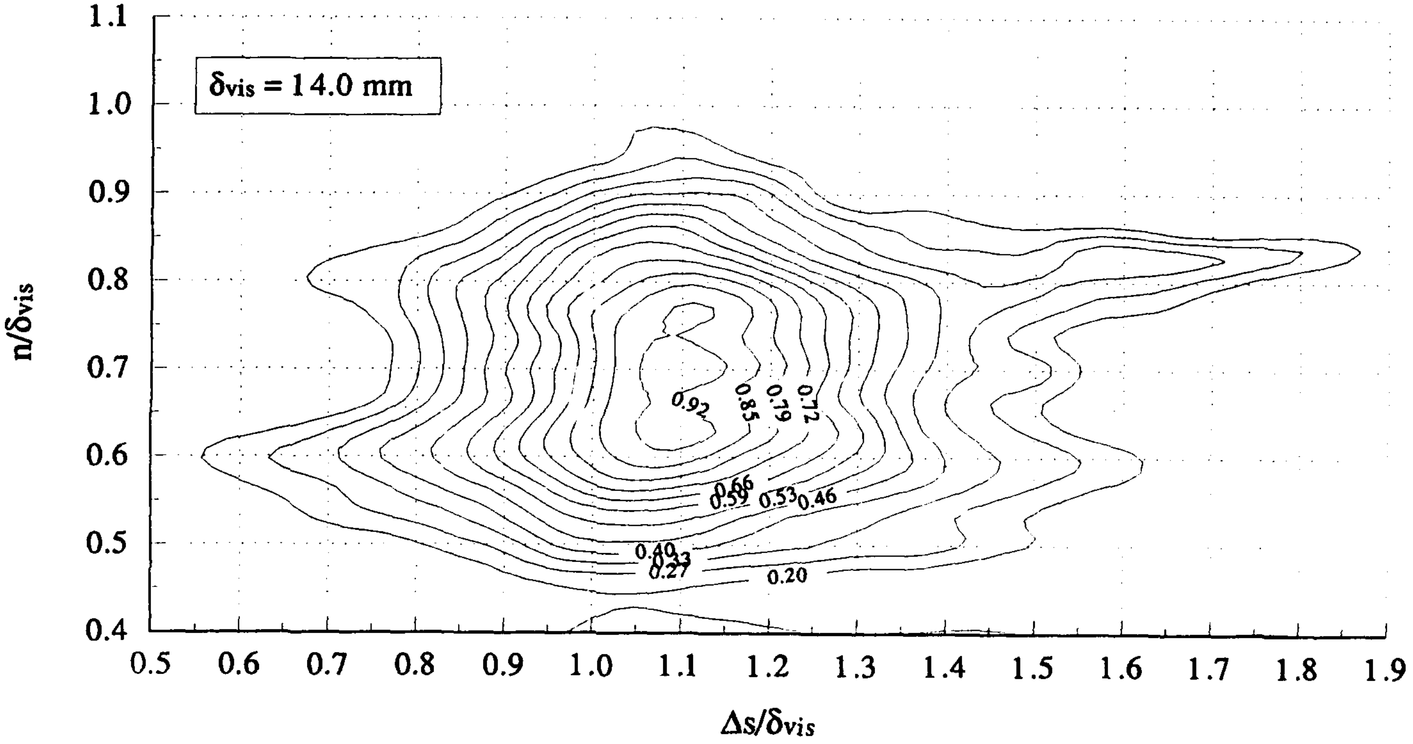

Figure 81. Correlation contours for double-pulse visualizations of the boundary layer downstream of the 7° centered expansion. The time delay between the initial and delayed images is 23.9 μs. The downstream direction is from left to right.

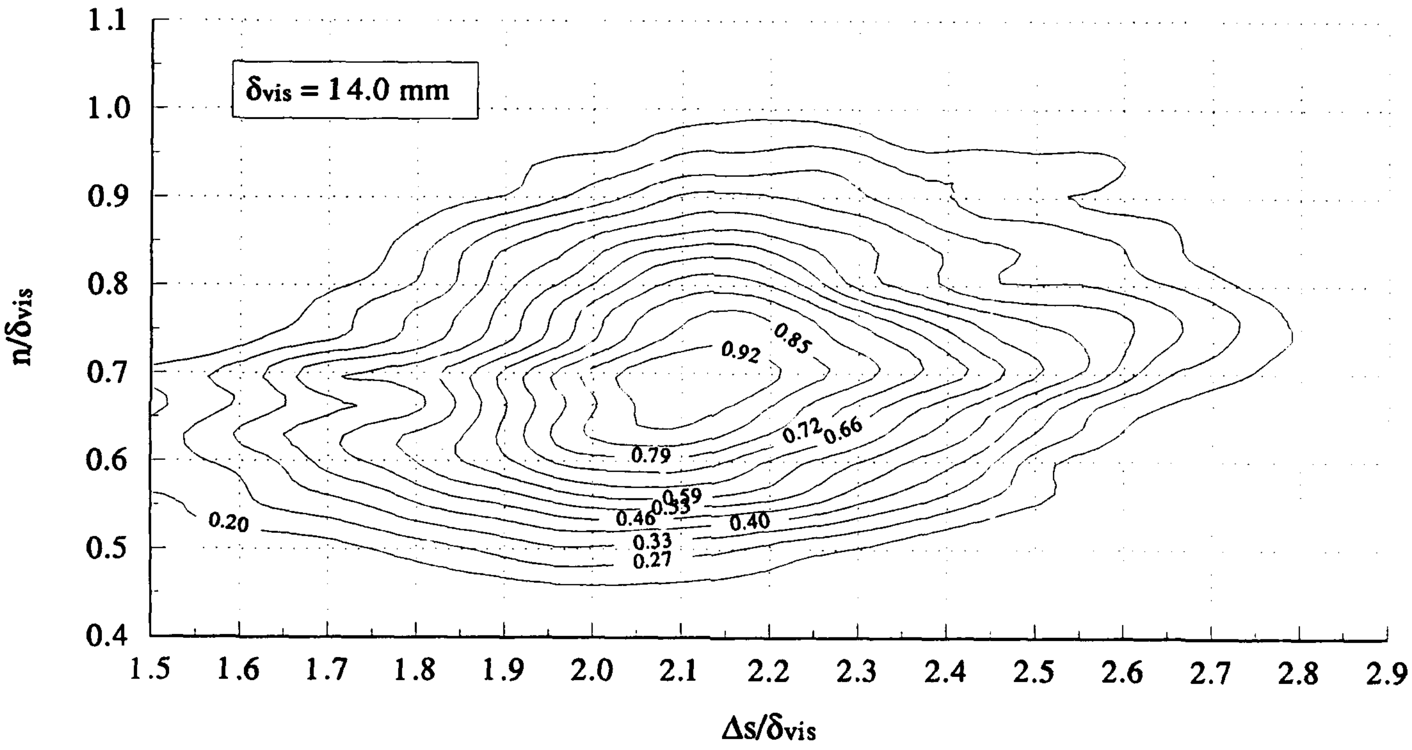

Figure 82. Correlation contours for double-pulse visualizations of the boundary layer downstream of the 7° centered expansion. The time delay between the initial and delayed images is 47.9 μs. The downstream direction is from left to right.

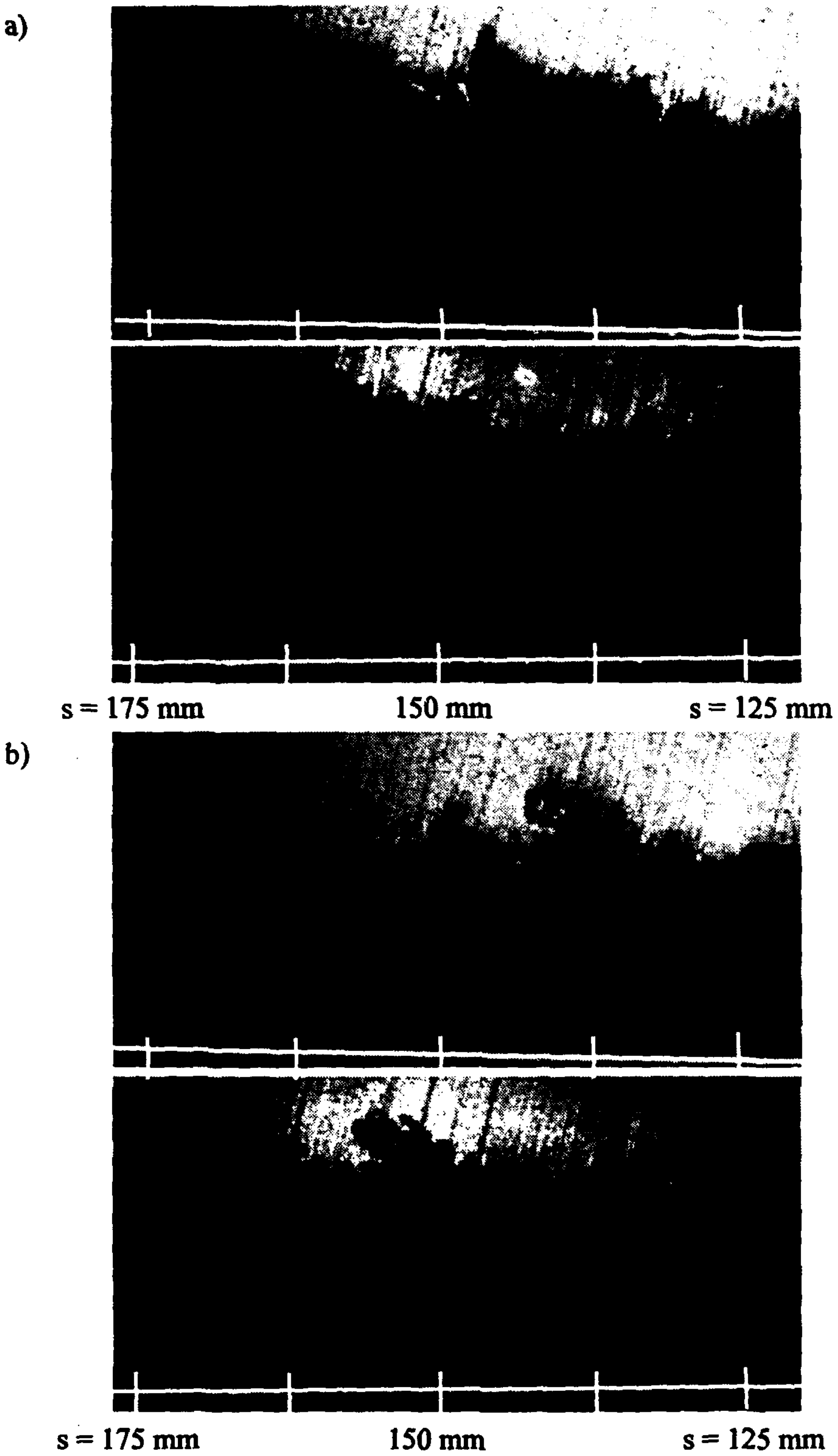

Figure 83. Double-pulse streamwise views of the boundary layer downstream of the 14° centered expansion. The bottom images were acquired 23.0 μs after the top images.

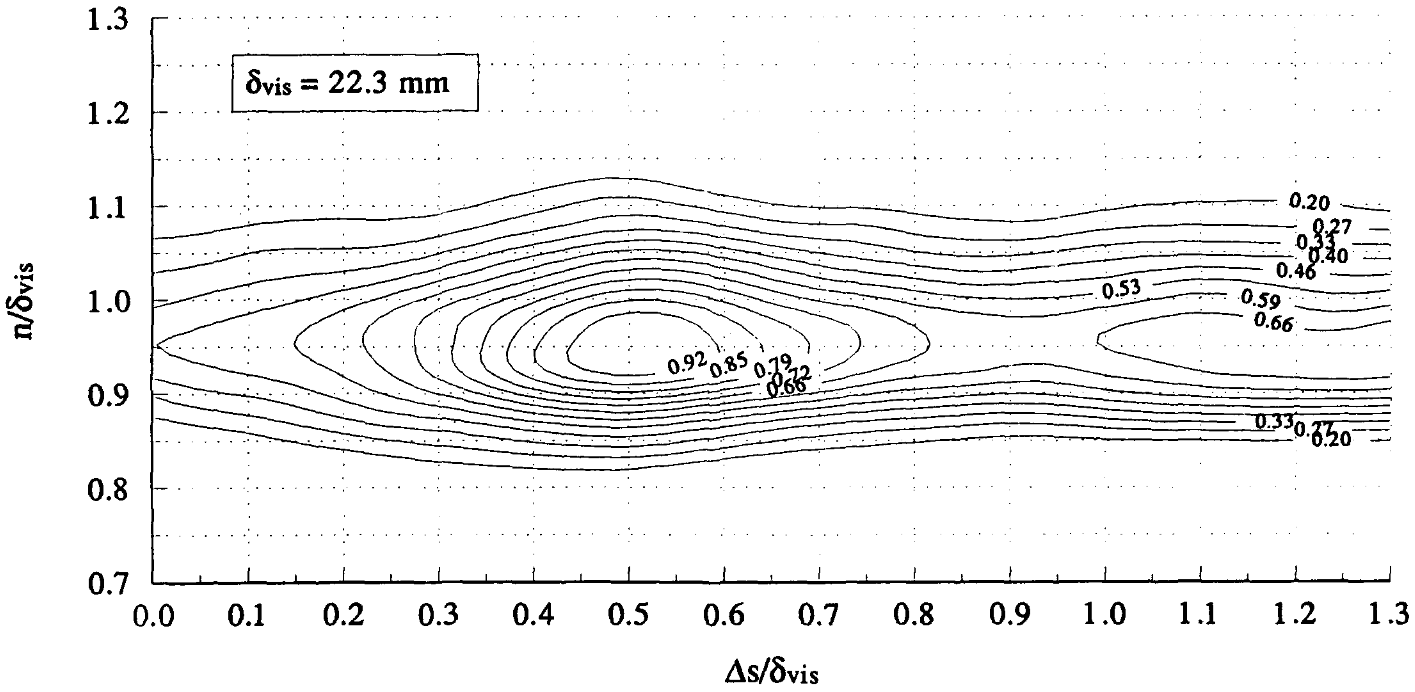

Figure 84. Correlation contours for double-pulse visualizations of the boundary layer downstream of the 14° centered expansion. The time delay between the initial and delayed images is 23.1 μs. The downstream direction is from left to right.

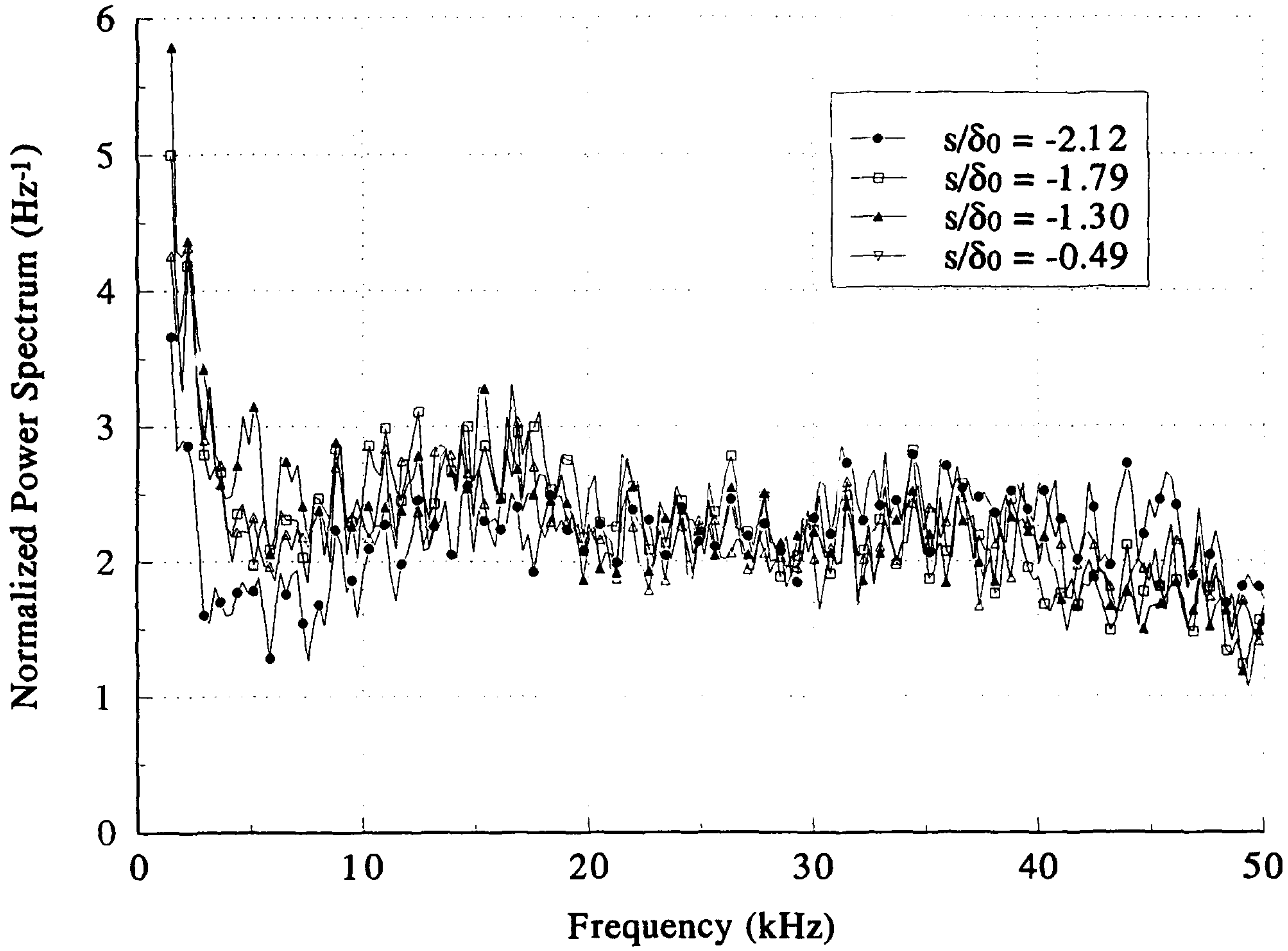

Figure 85. Normalized power spectra in the Mach 3 incoming boundary layer with the transducers oriented in the streamwise direction.

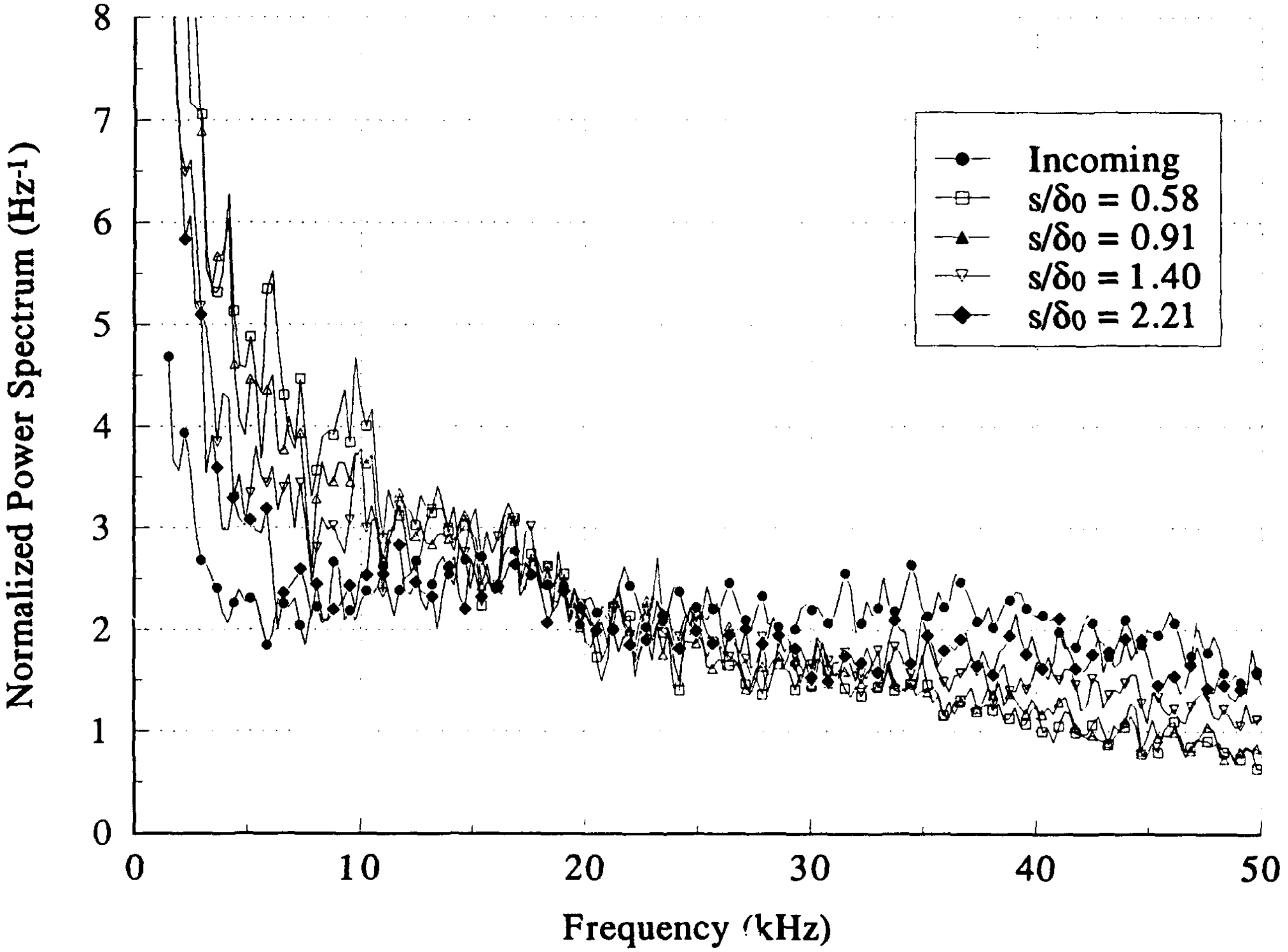

Figure 86. Normalized power spectra at the first plug location downstream of the 7° centered expansion and the average normalized power spectrum at the plug location upstream of the expansion corner.

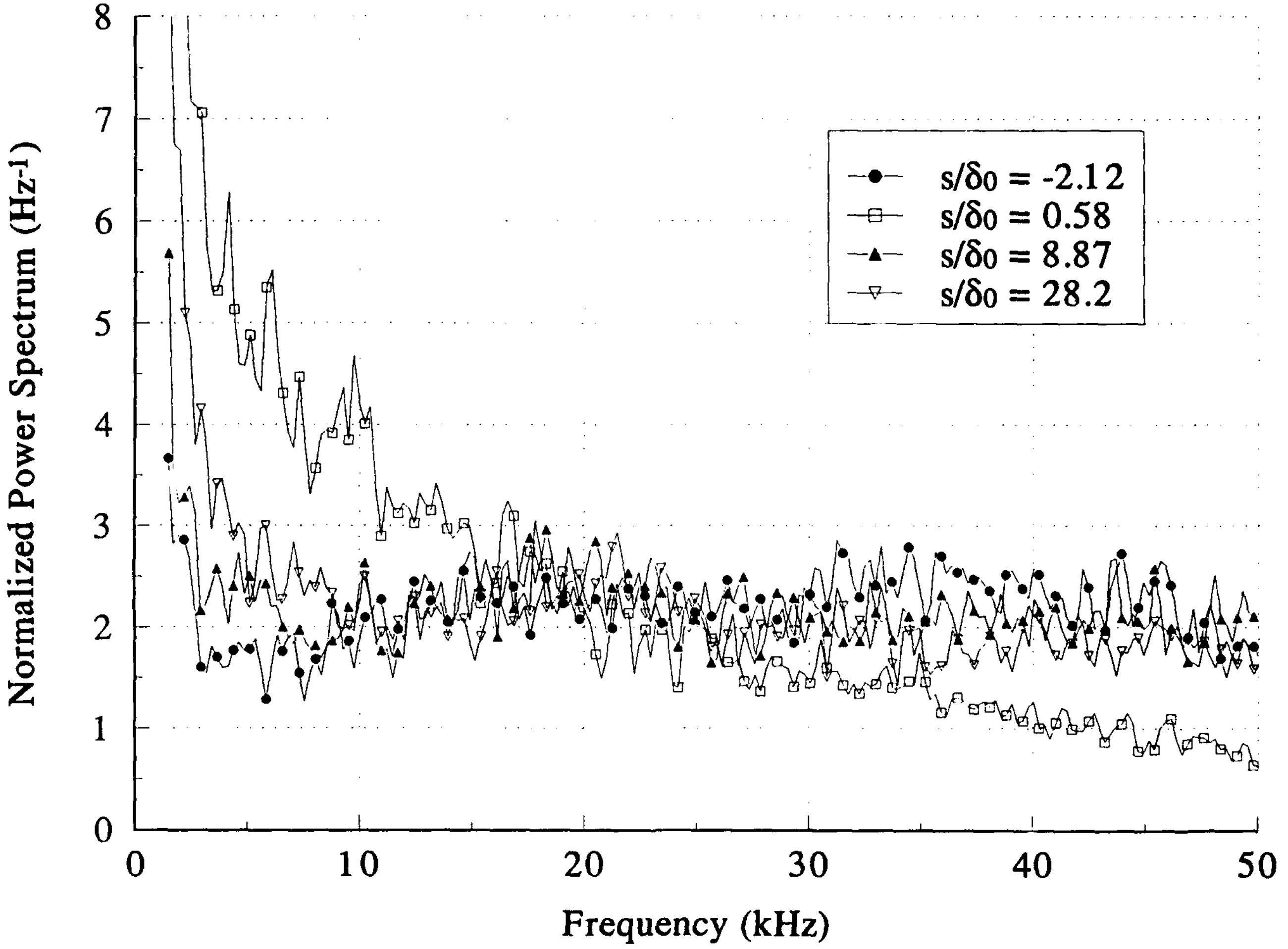

Figure 87. Streamwise evolution of the normalized power spectrum for transducer #1 through the 7° centered expansion.

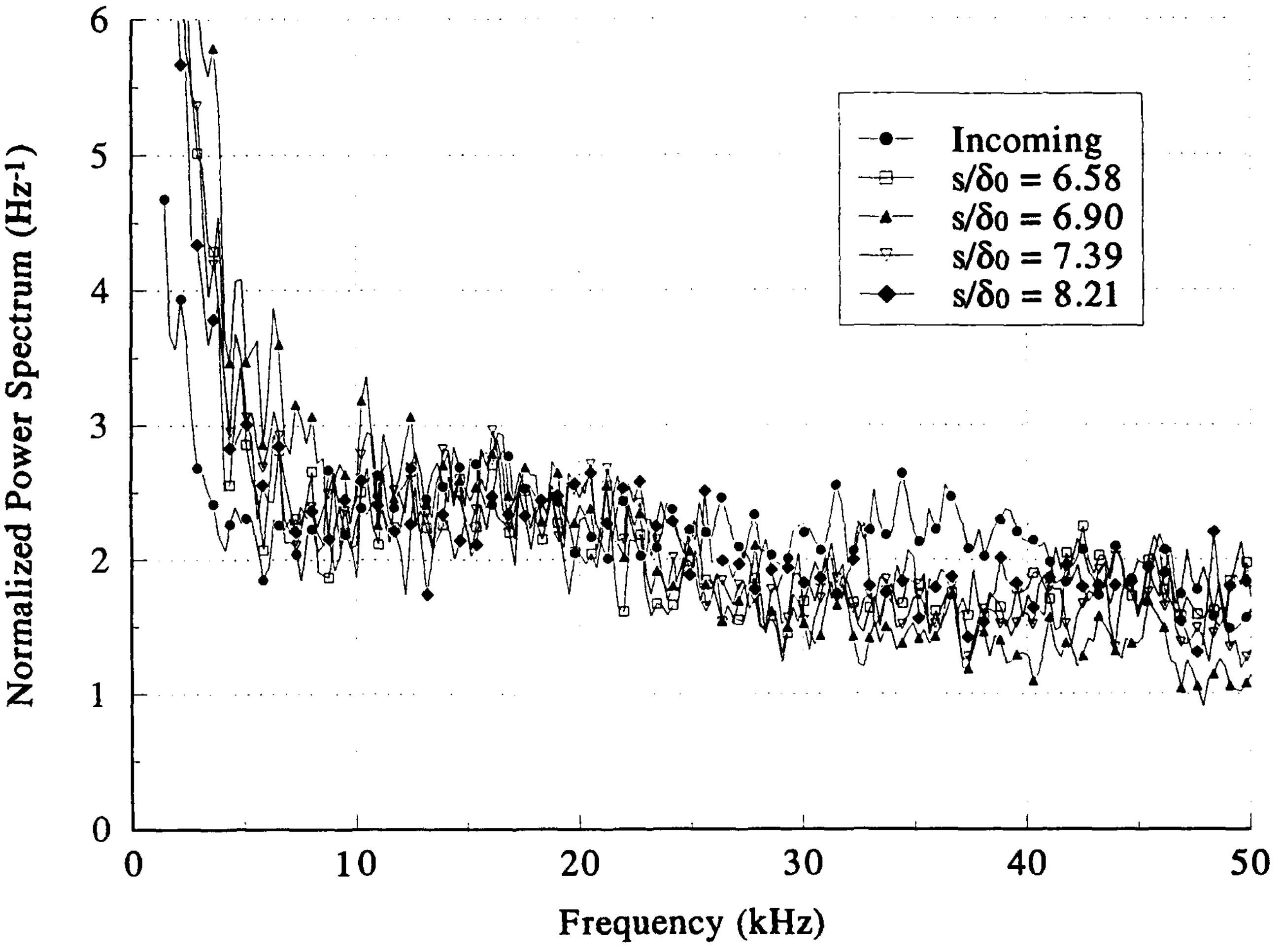

Figure 88. Normalized power spectra at the first plug location downstream of the 7° gradual expansion and the average normalized power spectrum at the plug location upstream of the expansion.

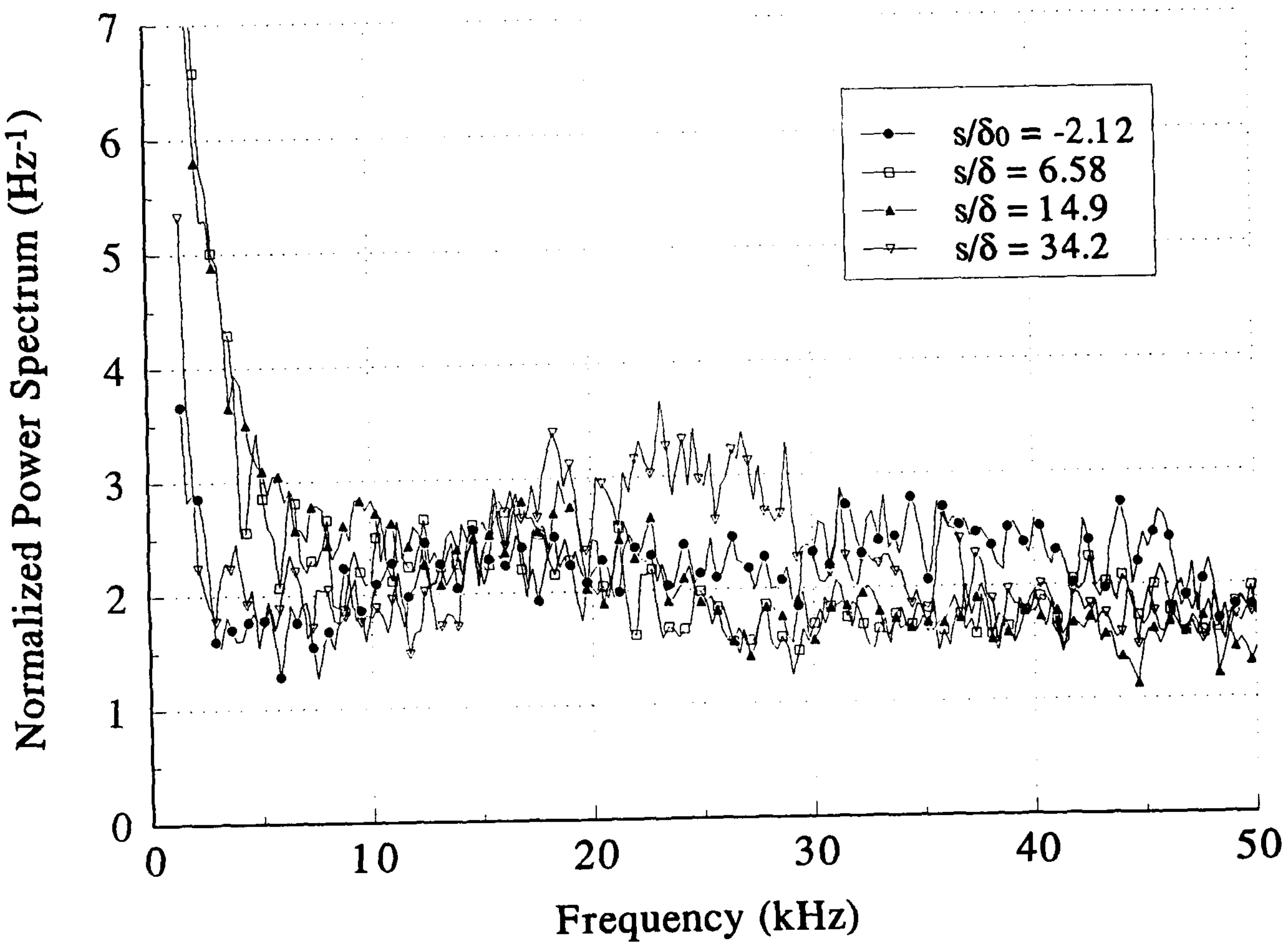

Figure 89. Streamwise evolution of the normalized power spectrum for transducer #1 through the 7° gradual expansion.

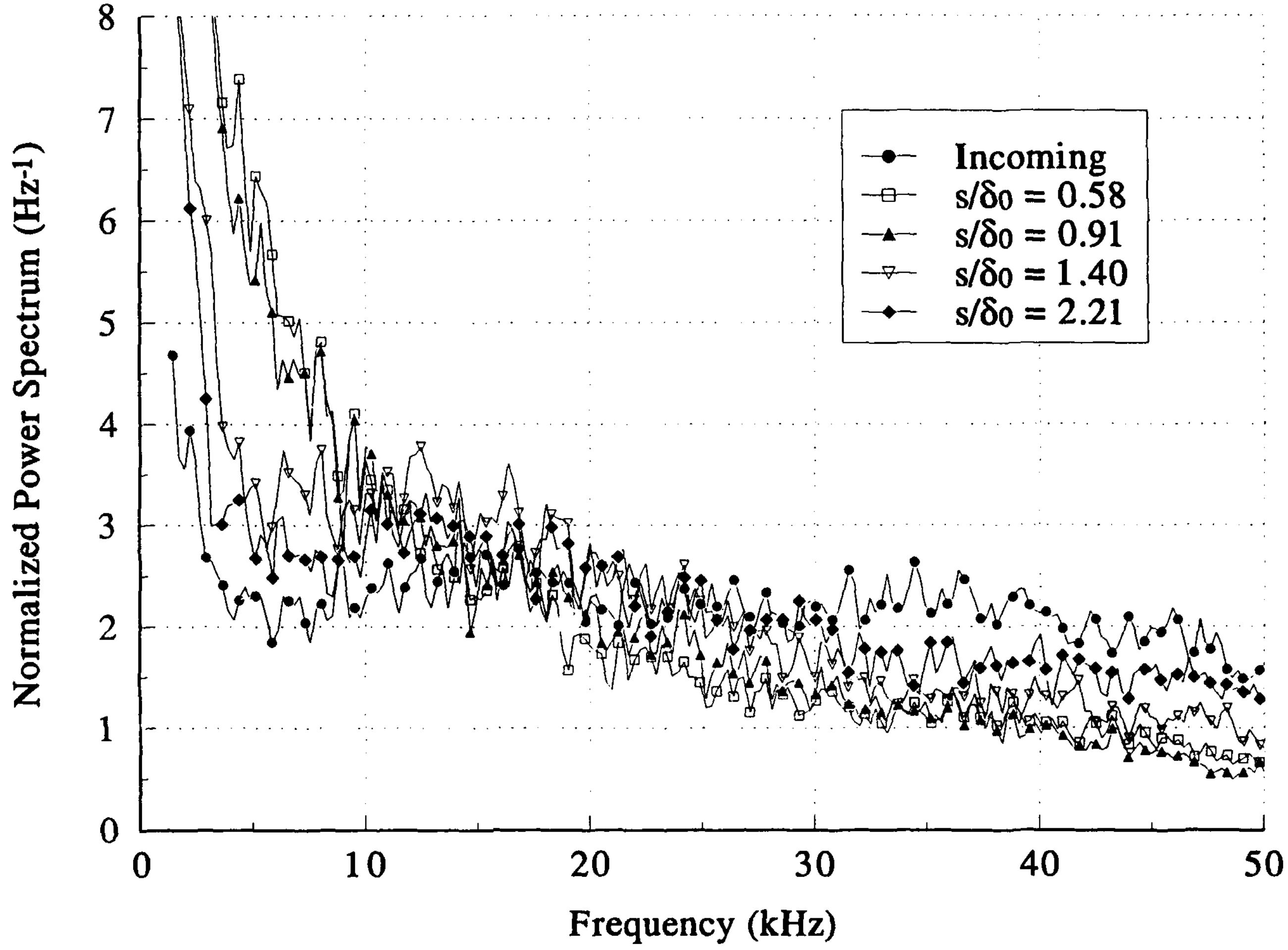

Figure 90. Normalized power spectra at the first plug location downstream of the 14° centered expansion and the average normalized power spectrum at the plug location upstream of the expansion corner.

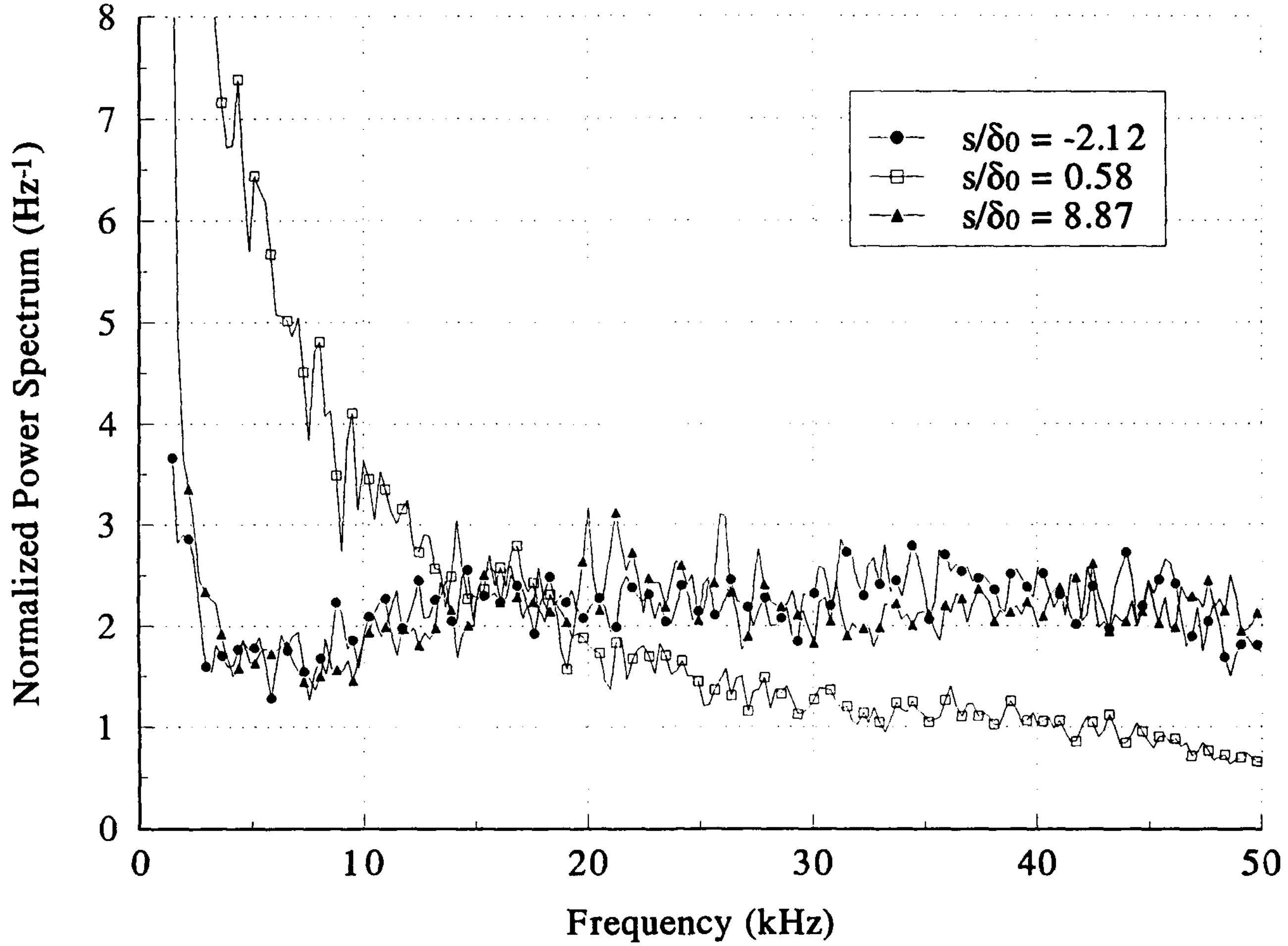

Figure 91. Streamwise evolution of the normalized power spectrum for transducer #1 through the 14° centered expansion.

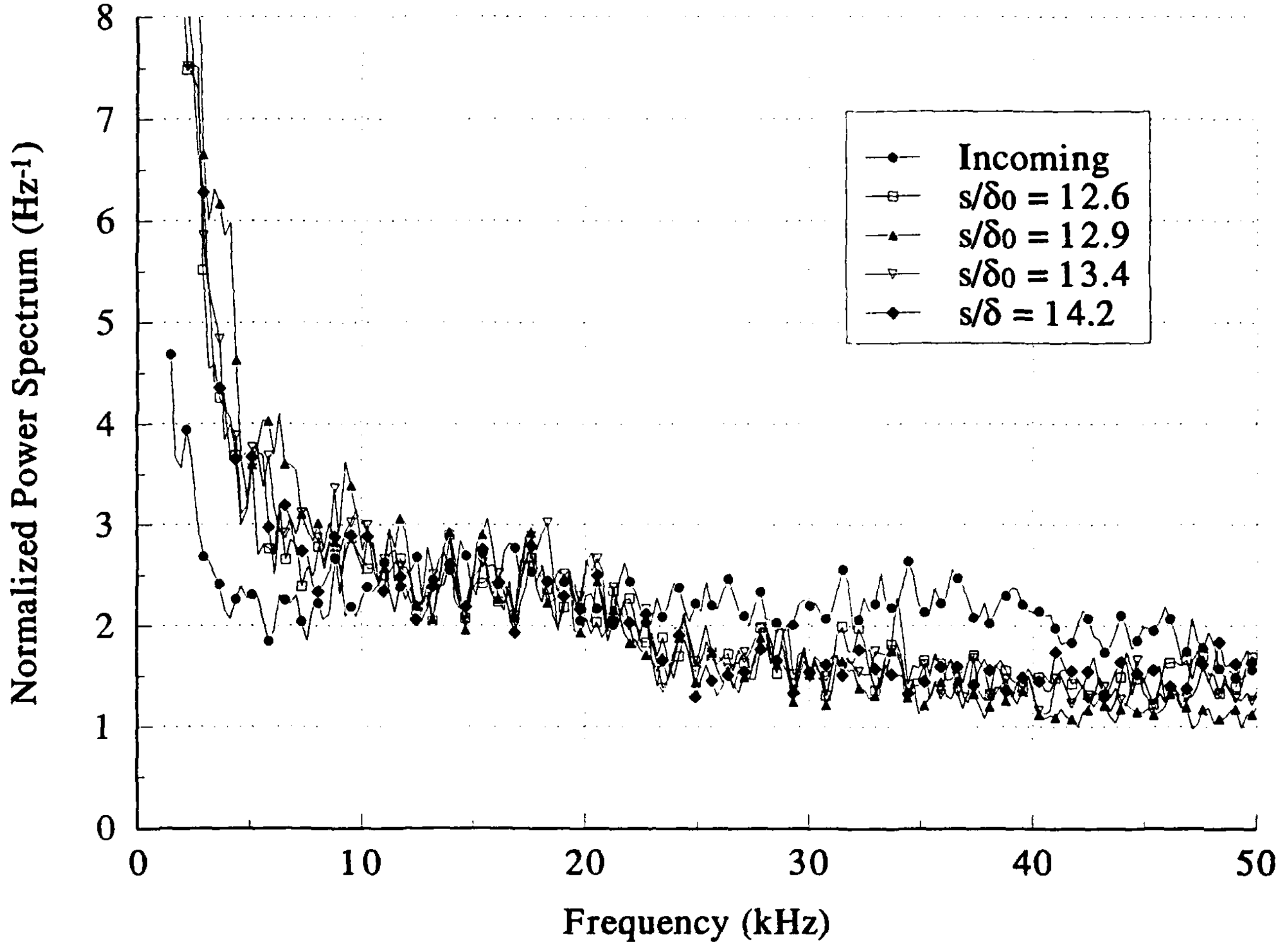

Figure 92. Normalized power spectra at the first plug location downstream of the 14° gradual expansion and the average normalized power spectrum at the plug location upstream of the expansion.

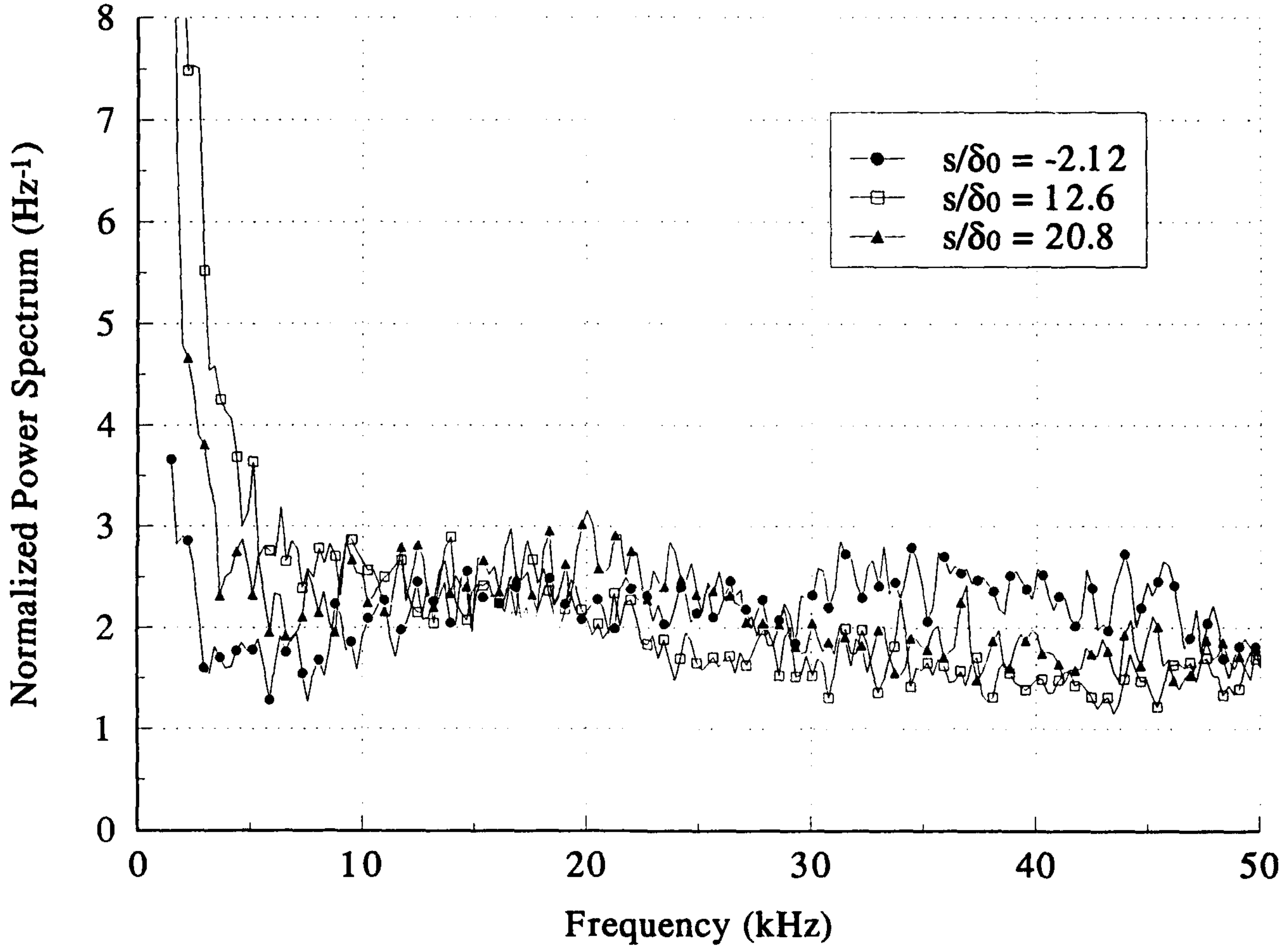

Figure 93. Streamwise evolution of the normalized power spectrum for transducer #1 through the 14° gradual expansion.

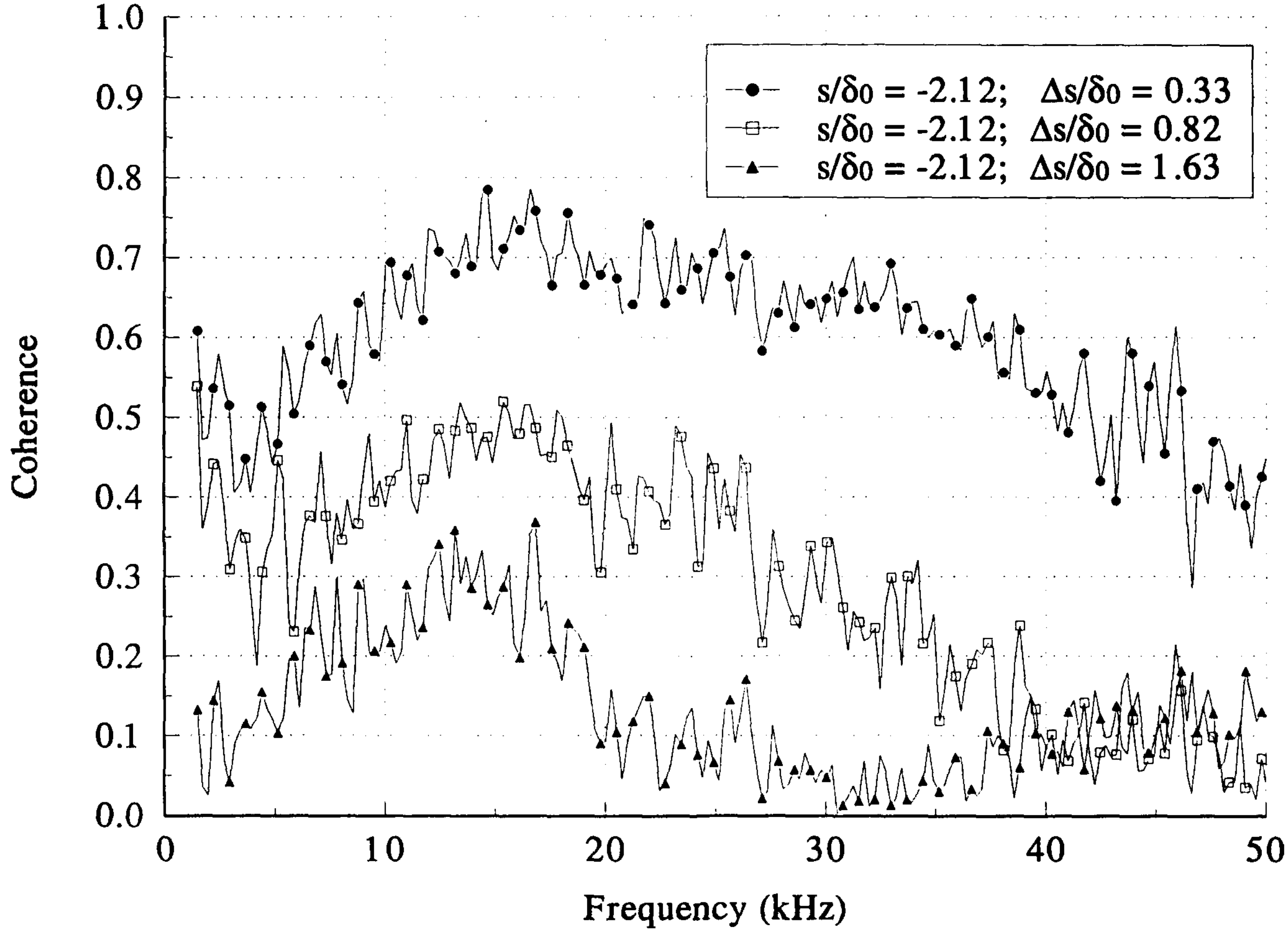

Figure 94. Streamwise choherence for three transducer separations in the incoming Mach 3 boundary layer.

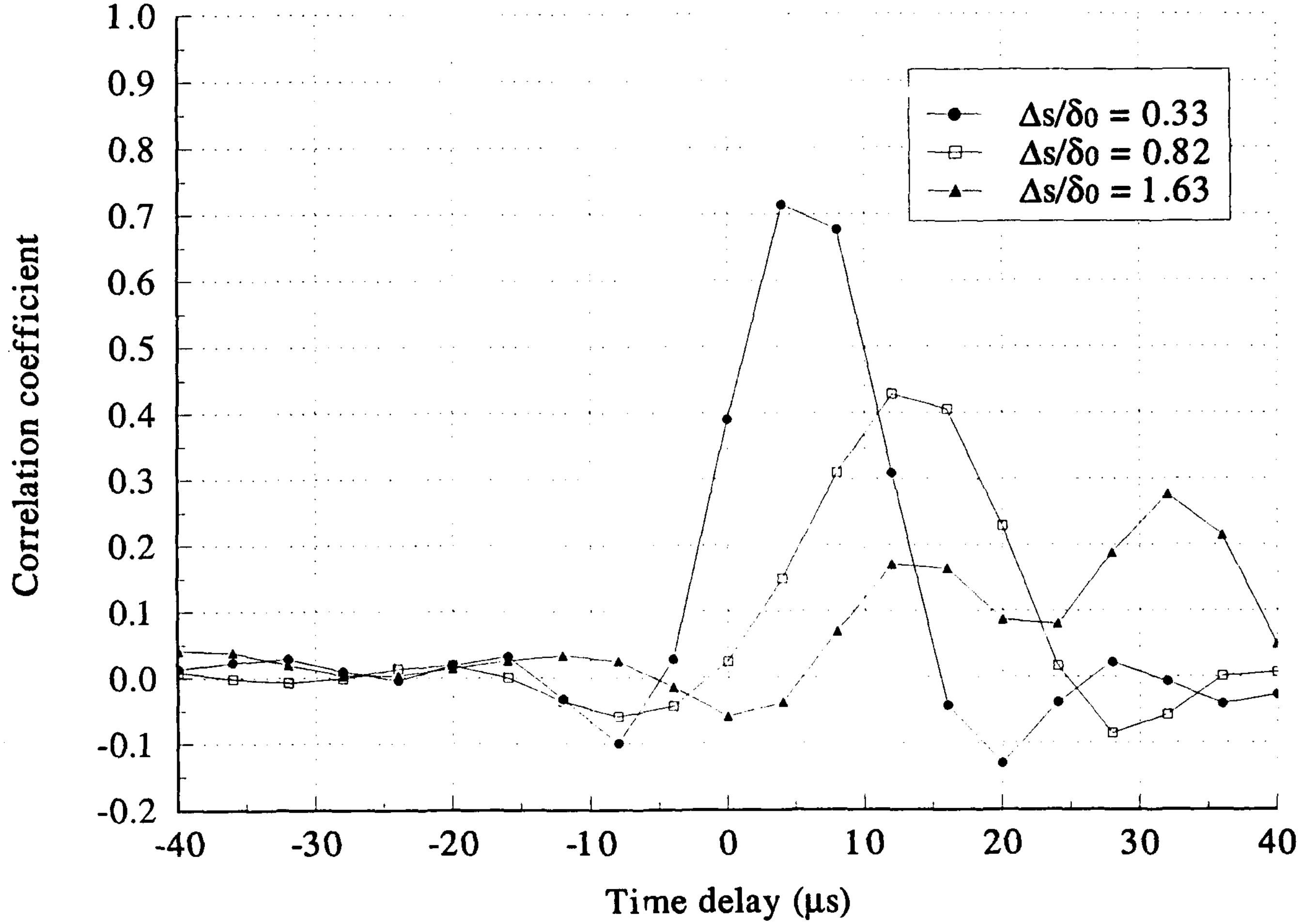

Figure 95. Streamwise space-time correlations at s/δo = -2.12 for three transucer separations in the incoming Mach 3 boundary layer.

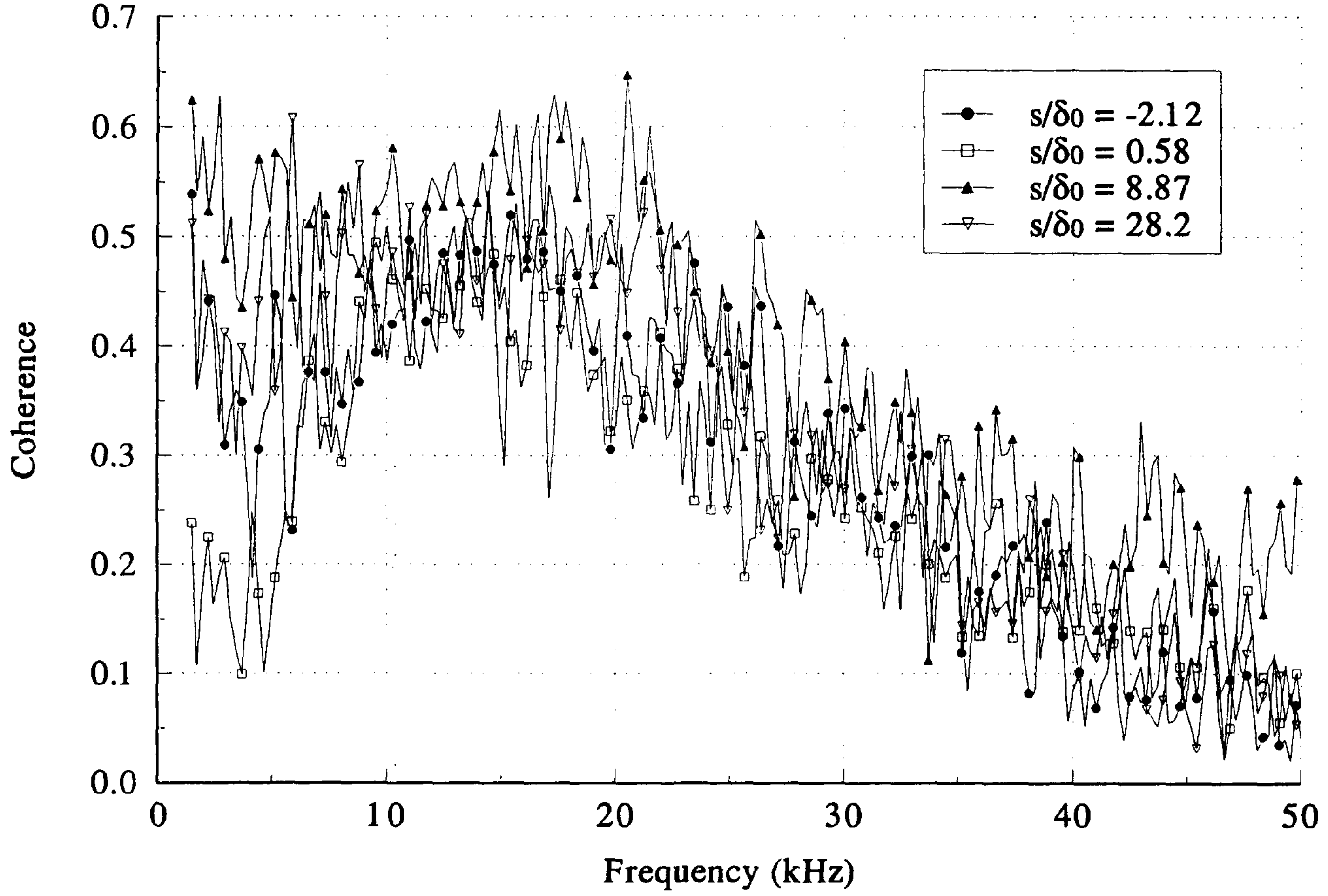

Figure 96. Streamwise evolution of the streamwise coherence for Δs/δo = 0.82 downstream of the 7° centered expansion.

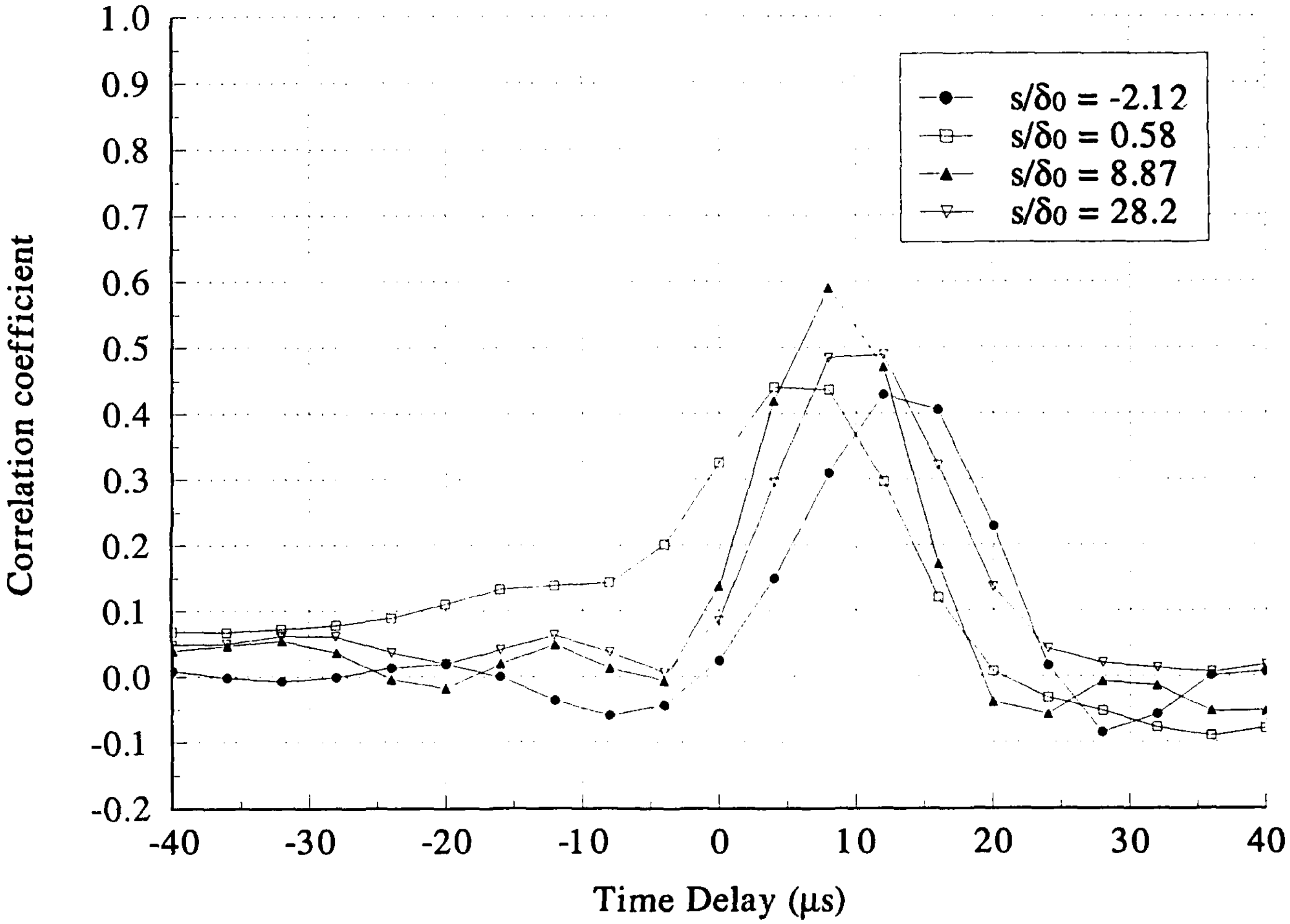

Figure 97. Streamwise space-time correlations for a transducer separation of Δs/δo = 0.82 in the boundary layer before and after the 7° centered expansion.

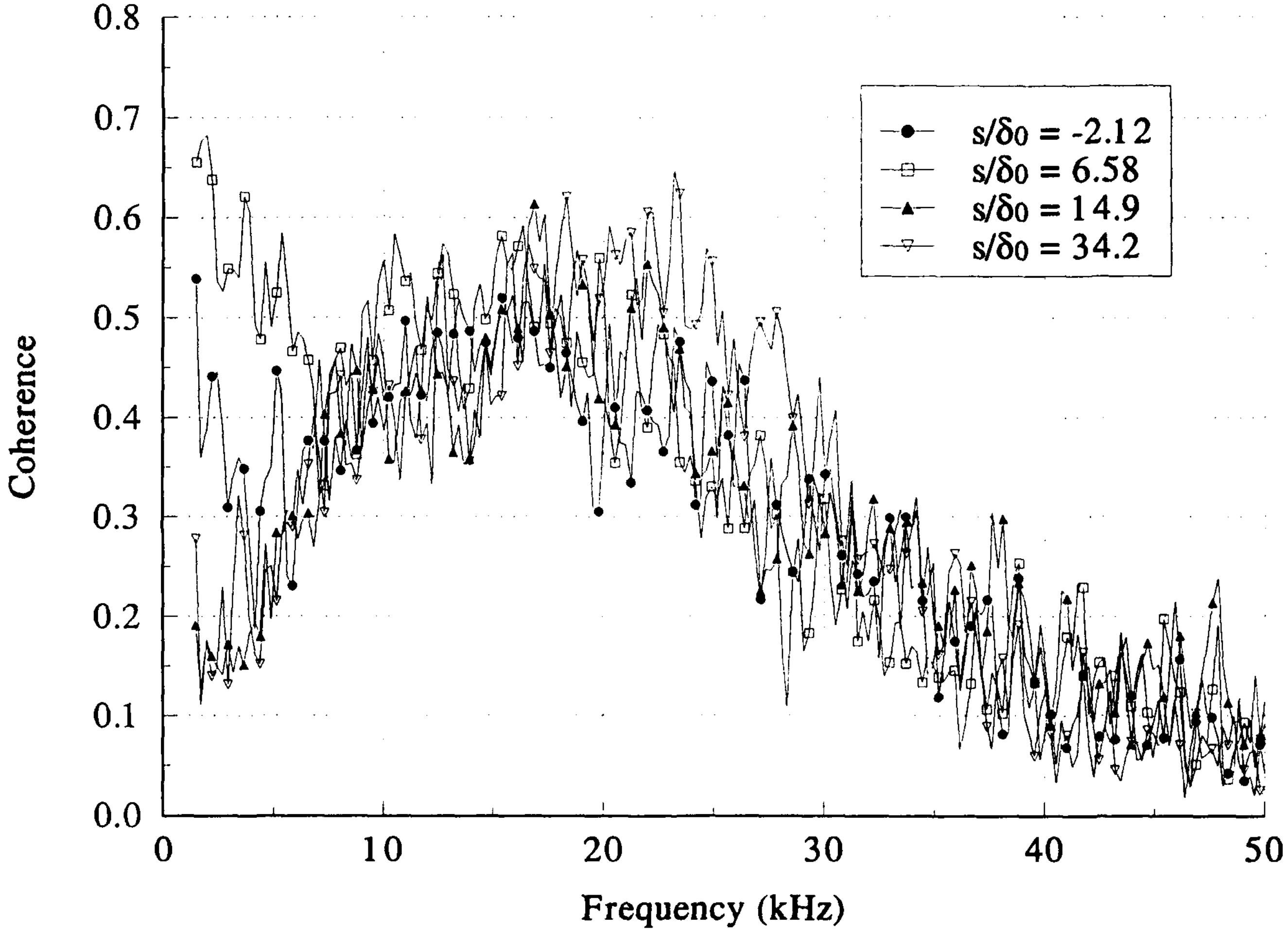

Figure 98. Streamwise evolution of the streamwise coherence for $\Delta s/\delta_0 = 0.82$ downstream of the 7° gradual expansion.

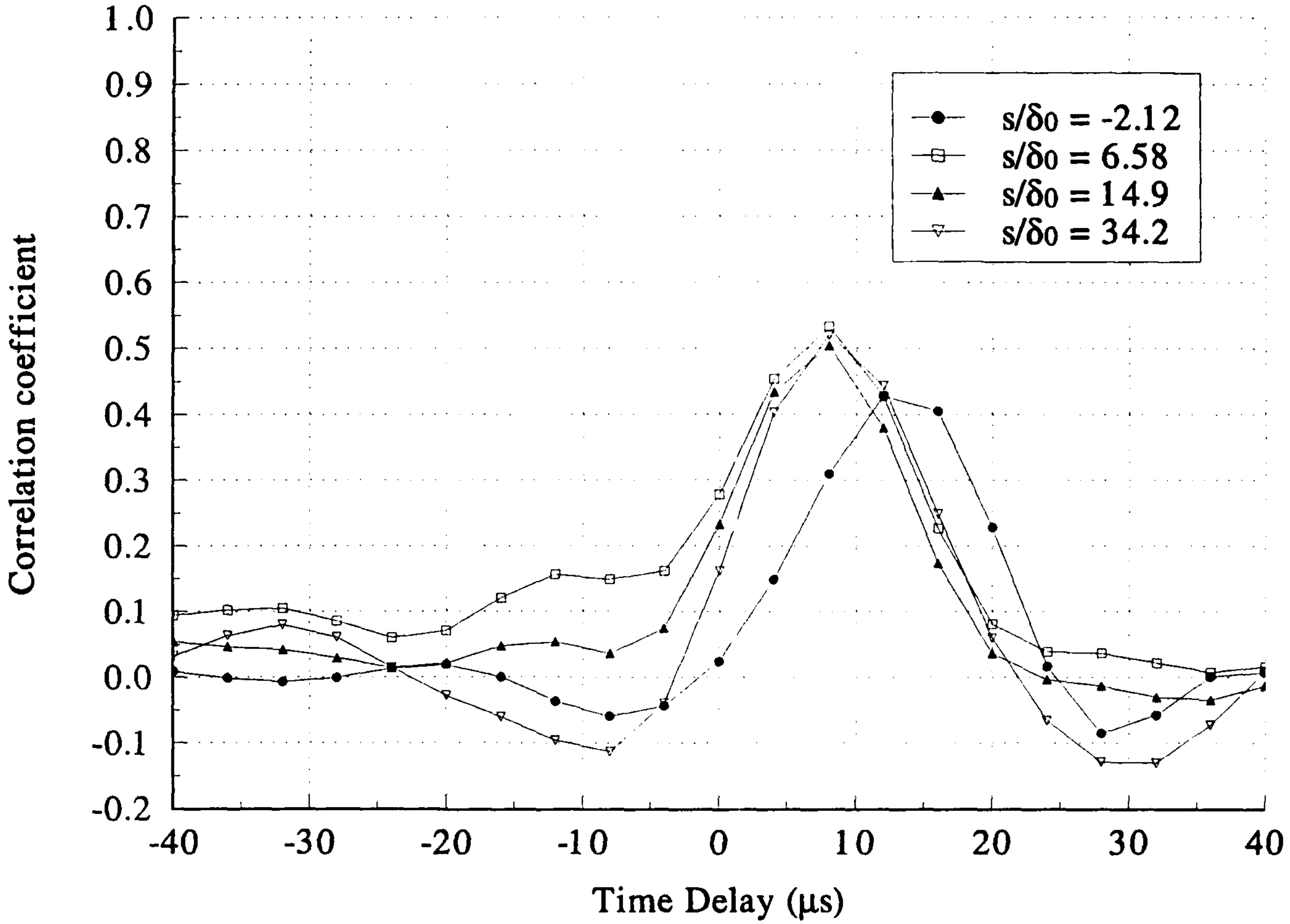

Figure 99. Streamwise space-time correlation for Δs/δo = 0.82 in the boundary layer before and after the 7° gradual expansion.

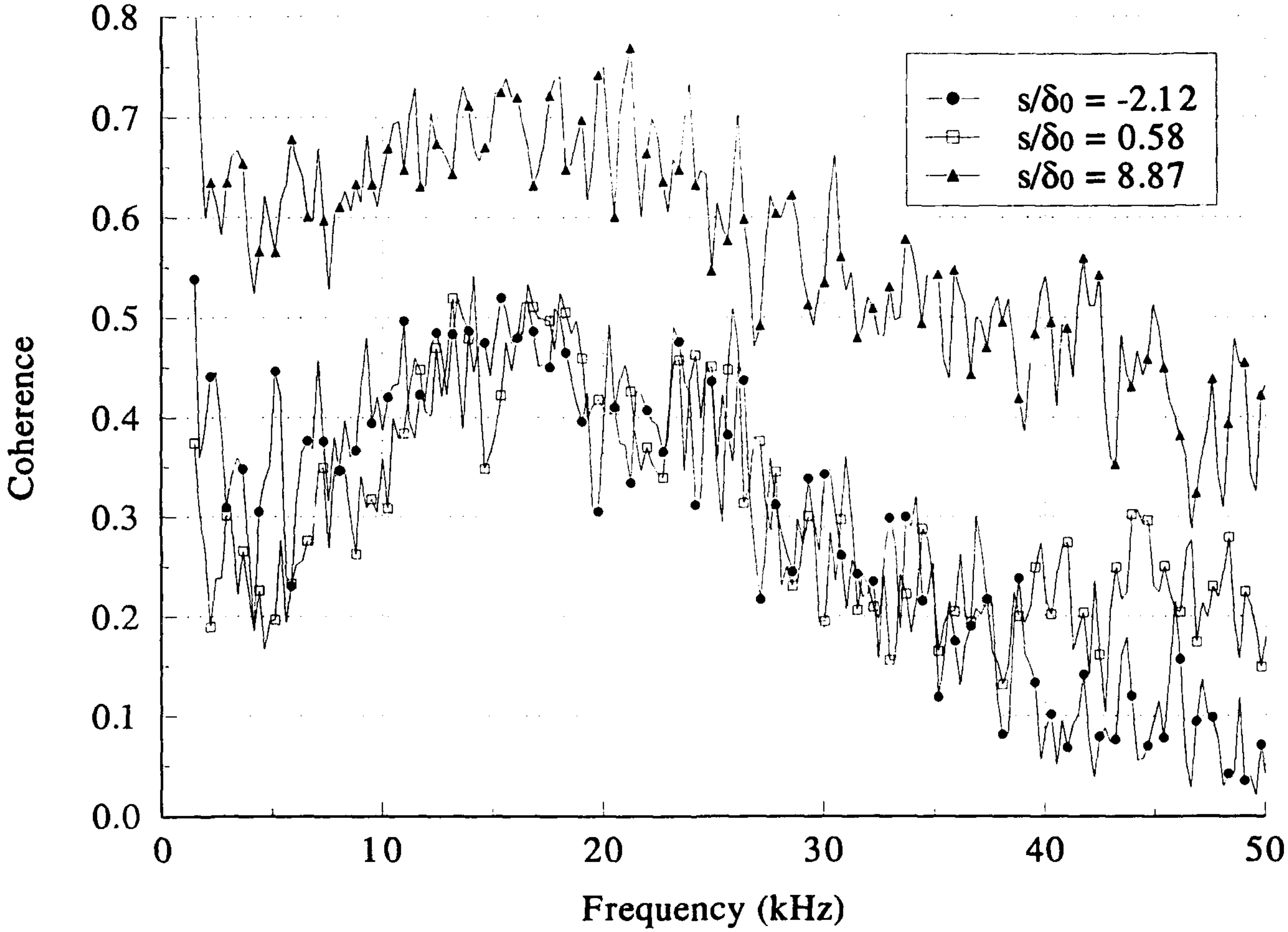

Figure 100. Streamwise evolution of the streamwise coherence for Δs/δ0 = 0.82 downstream of the 14° centered expansion.

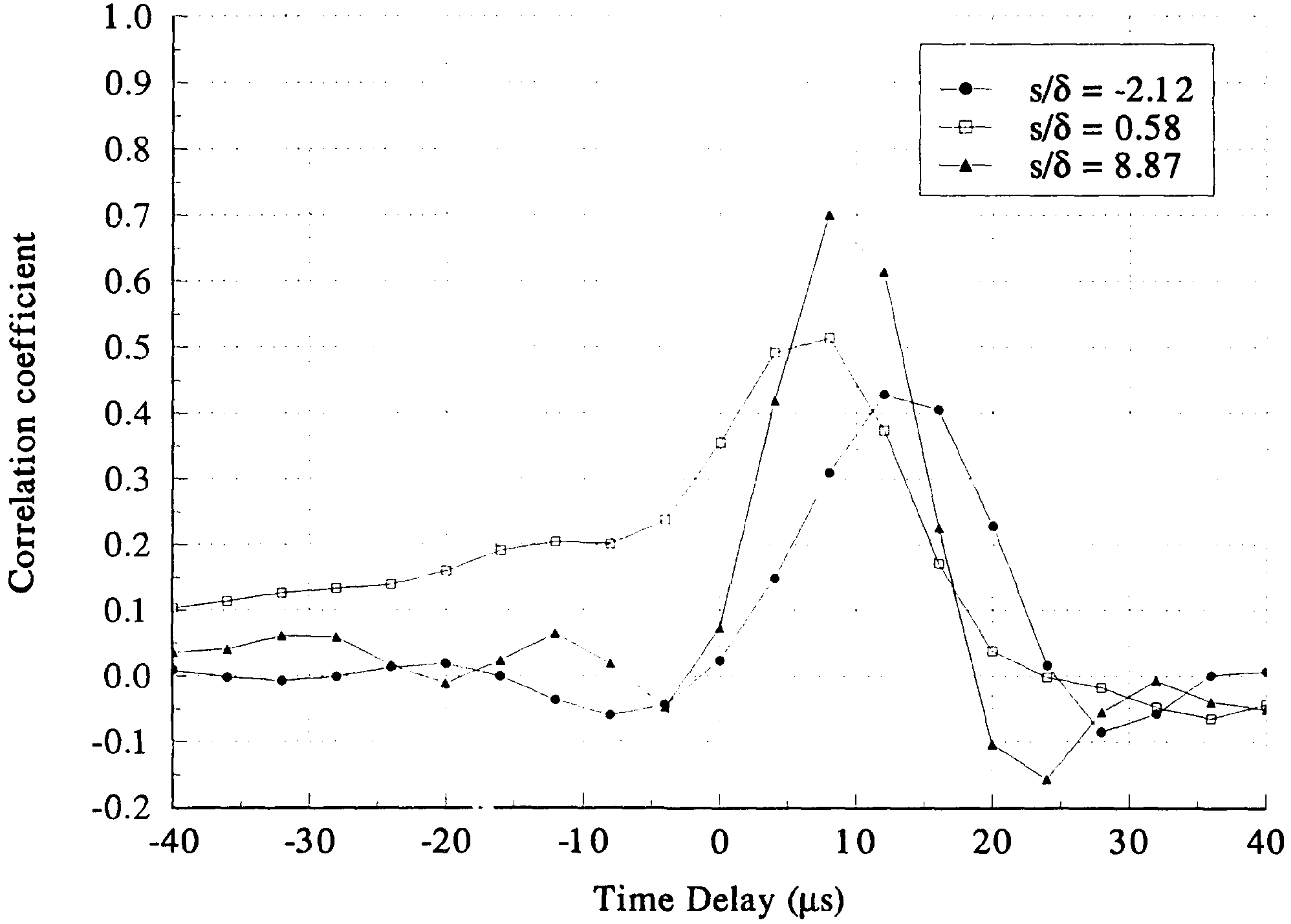

Figure 101. Streamwise space-time correlations for $\Delta s/\delta_0 = 0.82$ in the boundary layer before and after the 14° centered expansion.

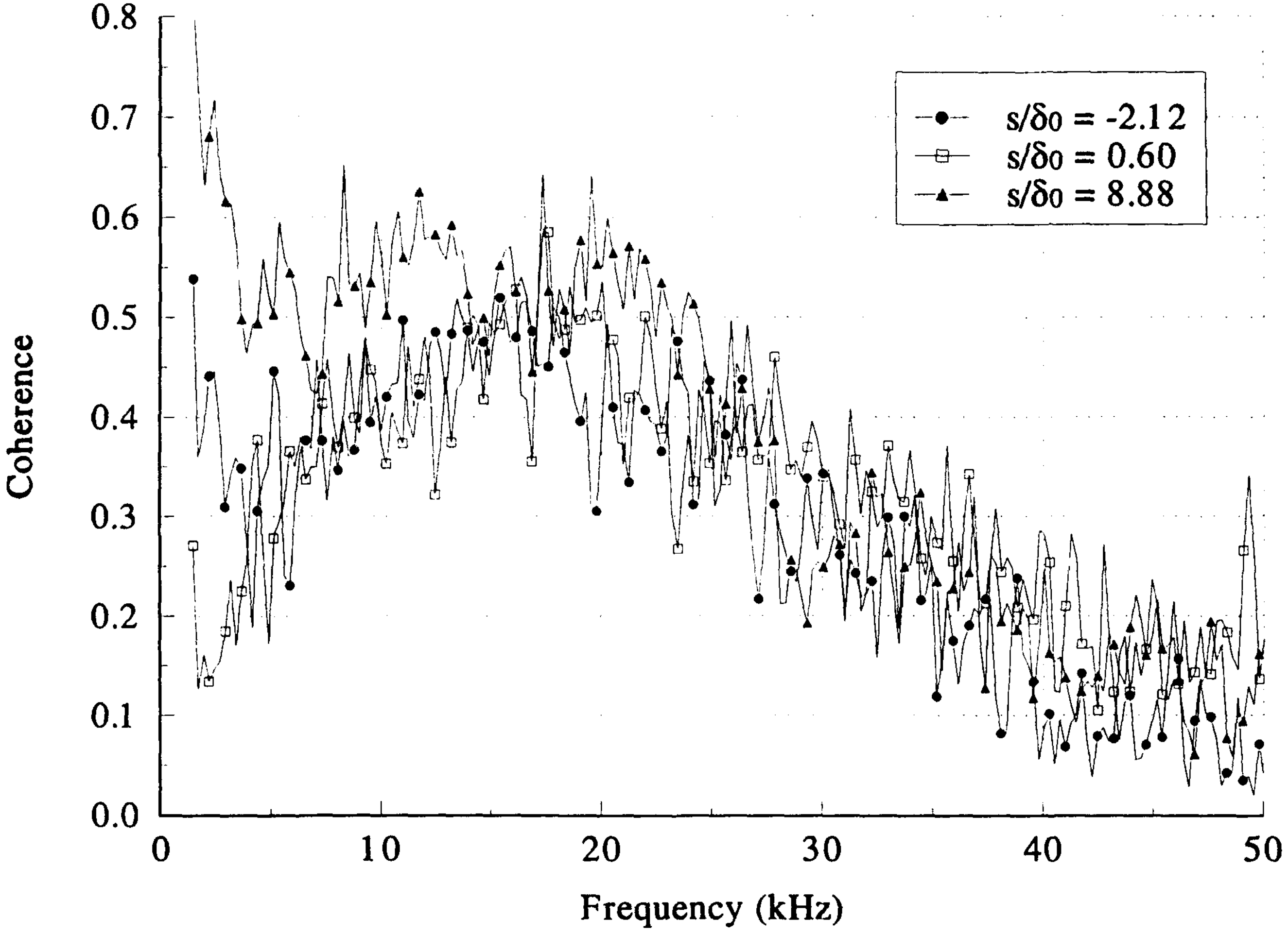

Figure 102. Streamwise evolution of the streamwise coherence for Δs/δo = 0.82 downstream of the 14° gradual expansion.

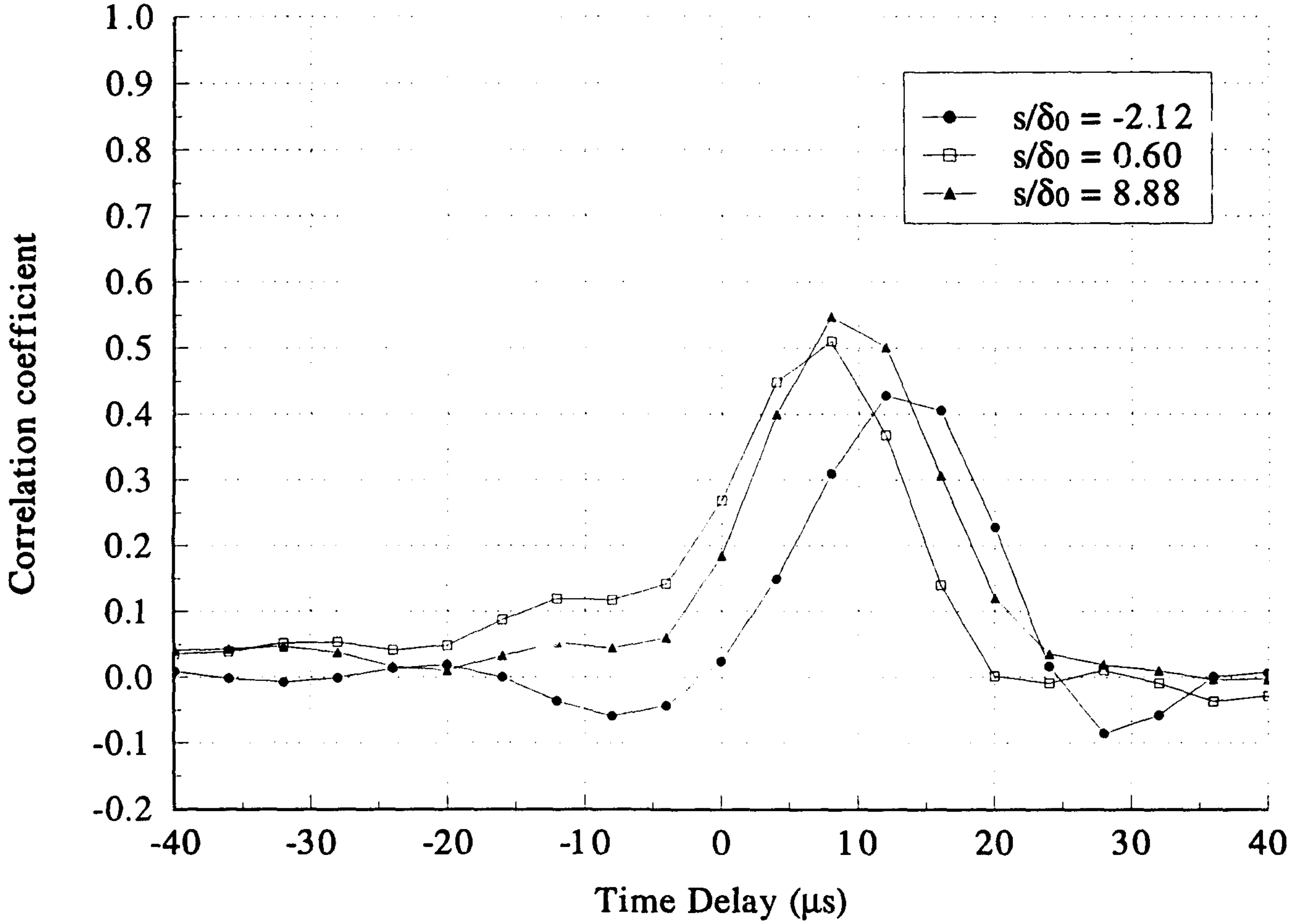

Figure 103. Streamwise space-time correlations for Δs/δo = 0.82 in the boundary layer before and after the 14° gradual expansion.

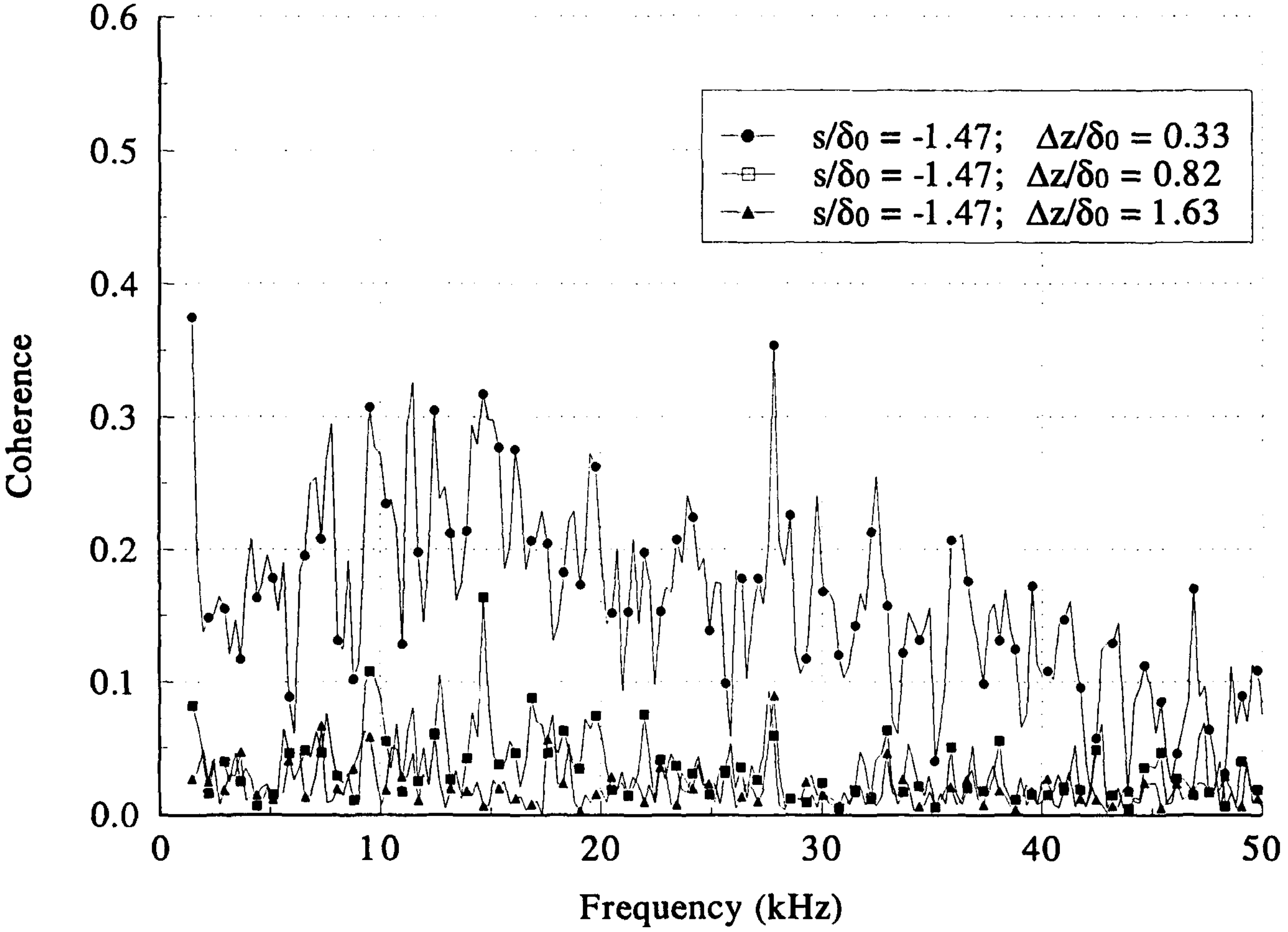

Figure 104. Spanwise coherence for three transducer separations in the incoming Mach 3 boundary layer.

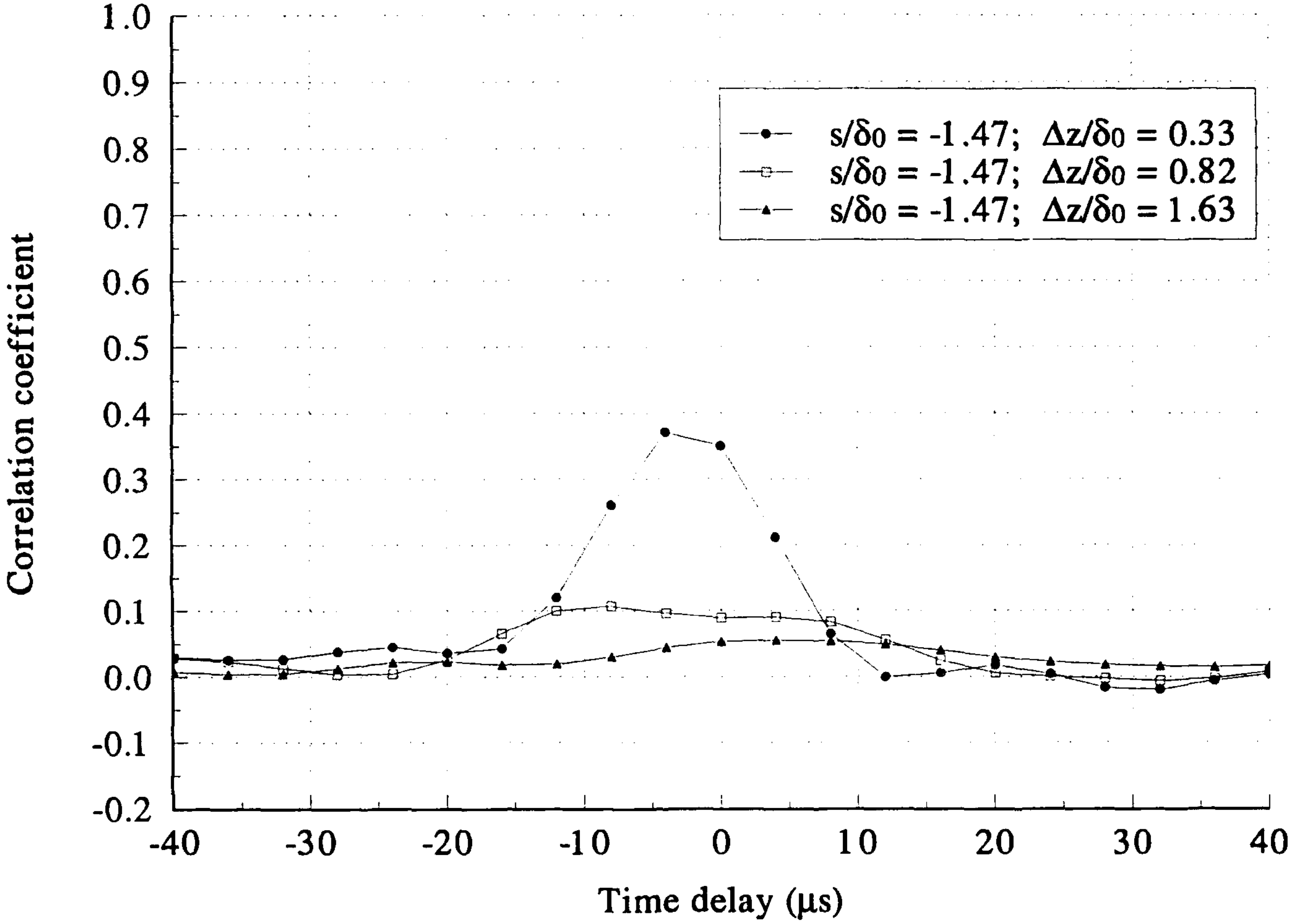

Figure 105. Spanwise space-time correlations for three transducer separations in the incoming Mach 3 boundary layer.

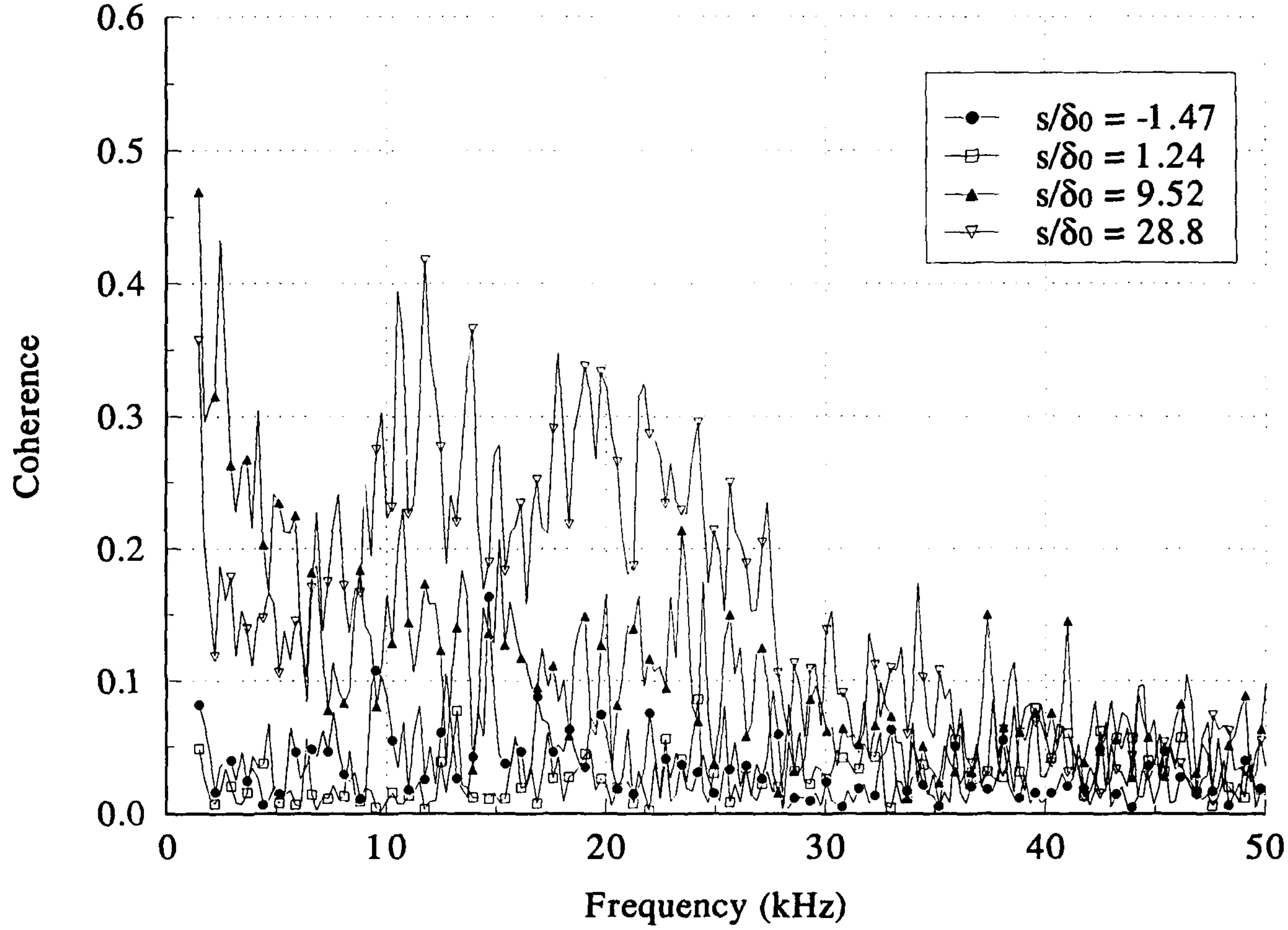

Figure 106. Streamwise evolution of the spanwise coherence for Δz/δo = 0.82 downstream of the 7° centered expansion.

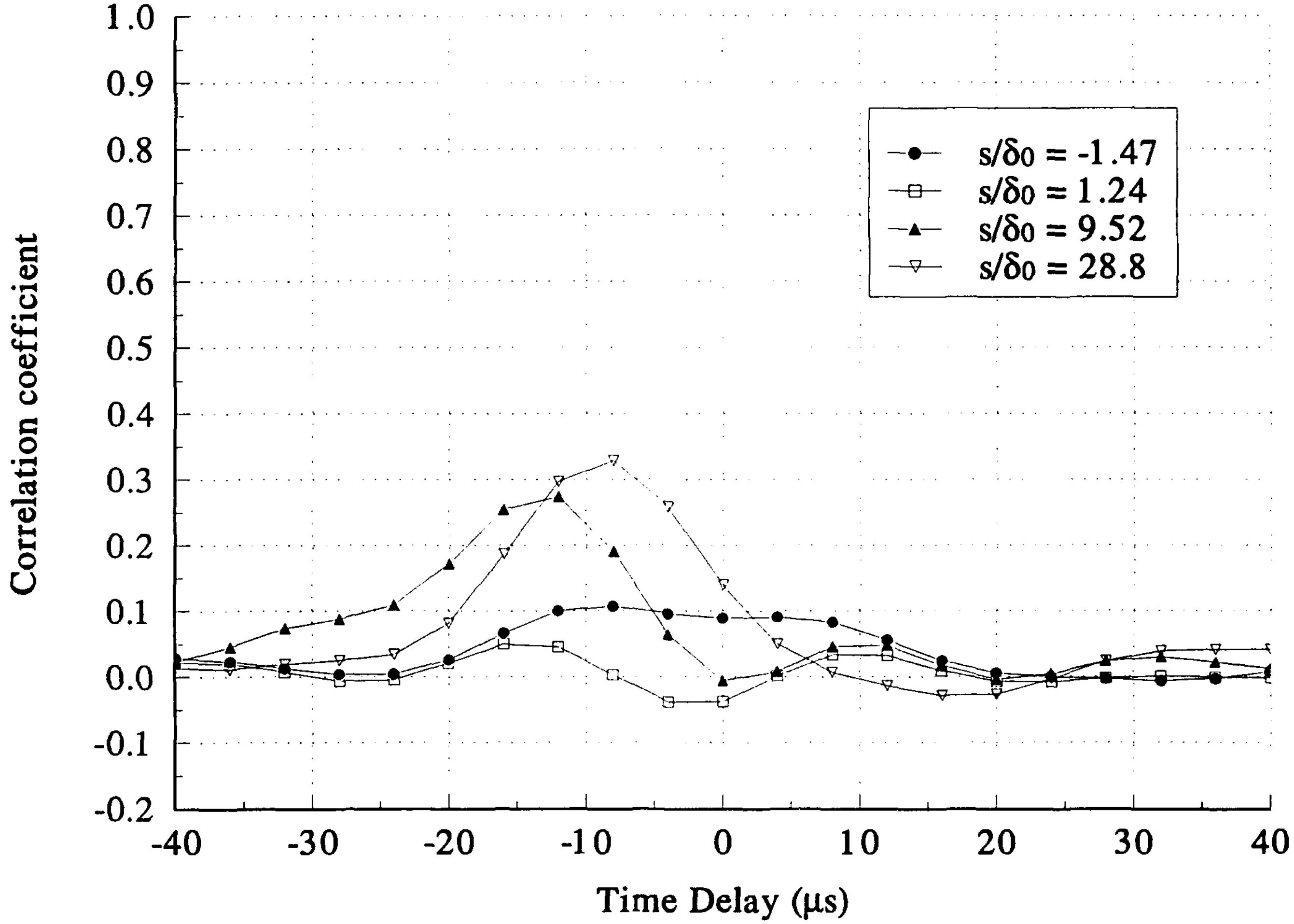

Figure 107. Spanwise space-time correlations for $\Delta z/\delta_0 = 0.82$ in the boundary layer before and after the 7° centered expansion.

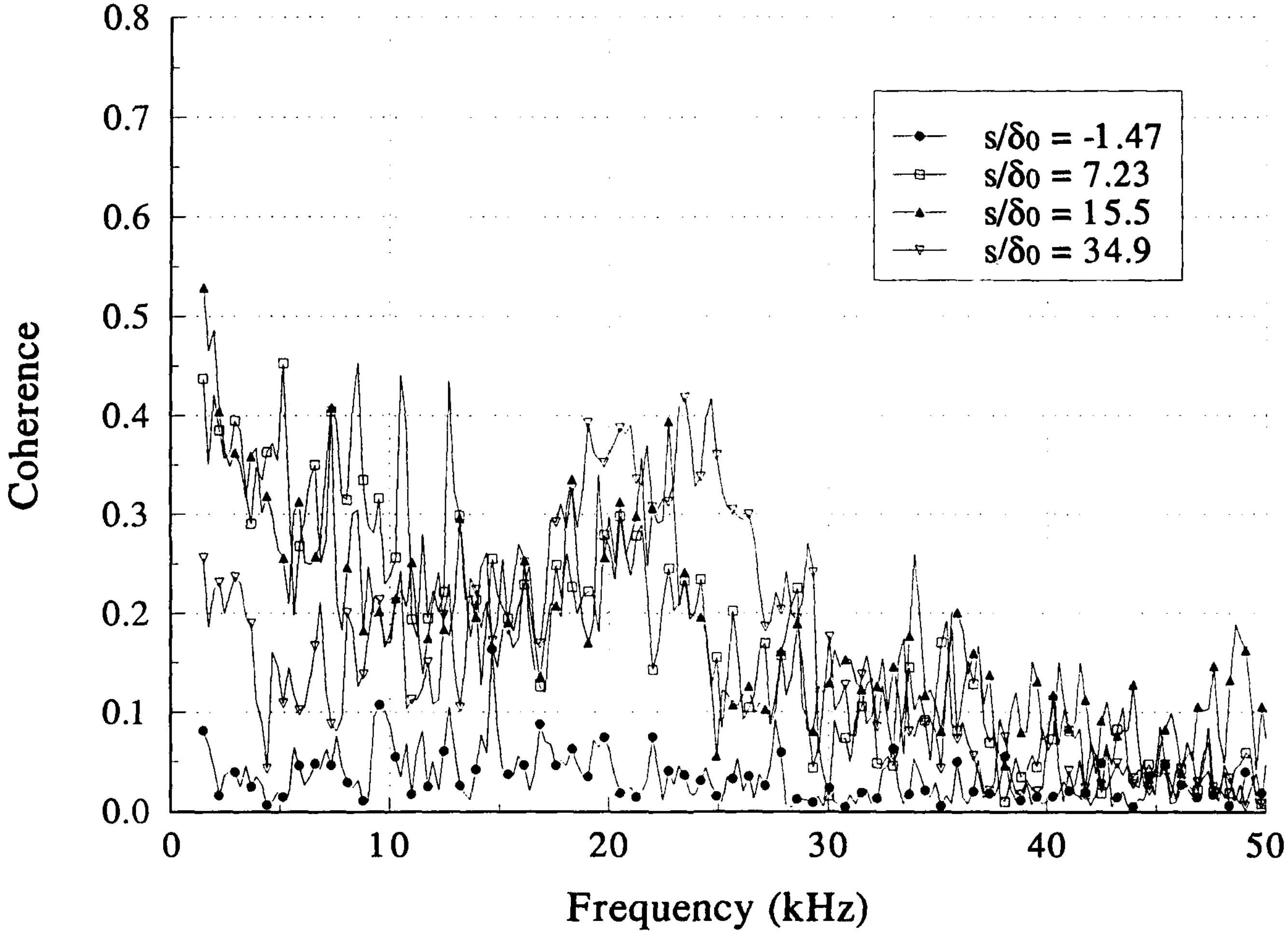

Figure 108. Streamwise evolution of the spanwise coherence for Δz/δo = 0.82 downstream of the 7° gradual expansion.

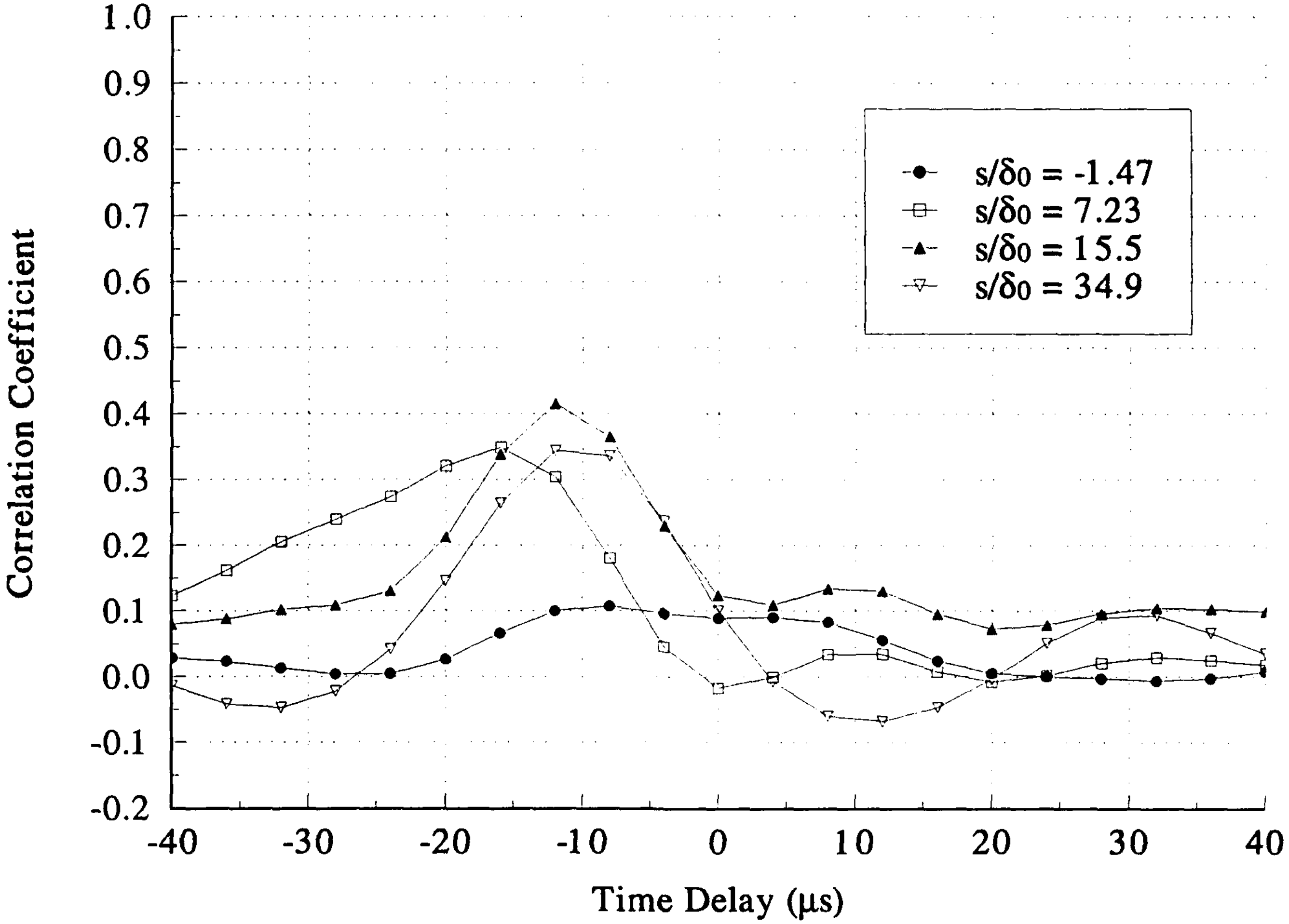

Figure 109. Spanwise space-time correlations for Δz/δo = 0.82 in the boundary layer before and after the 7° gradual expansion.

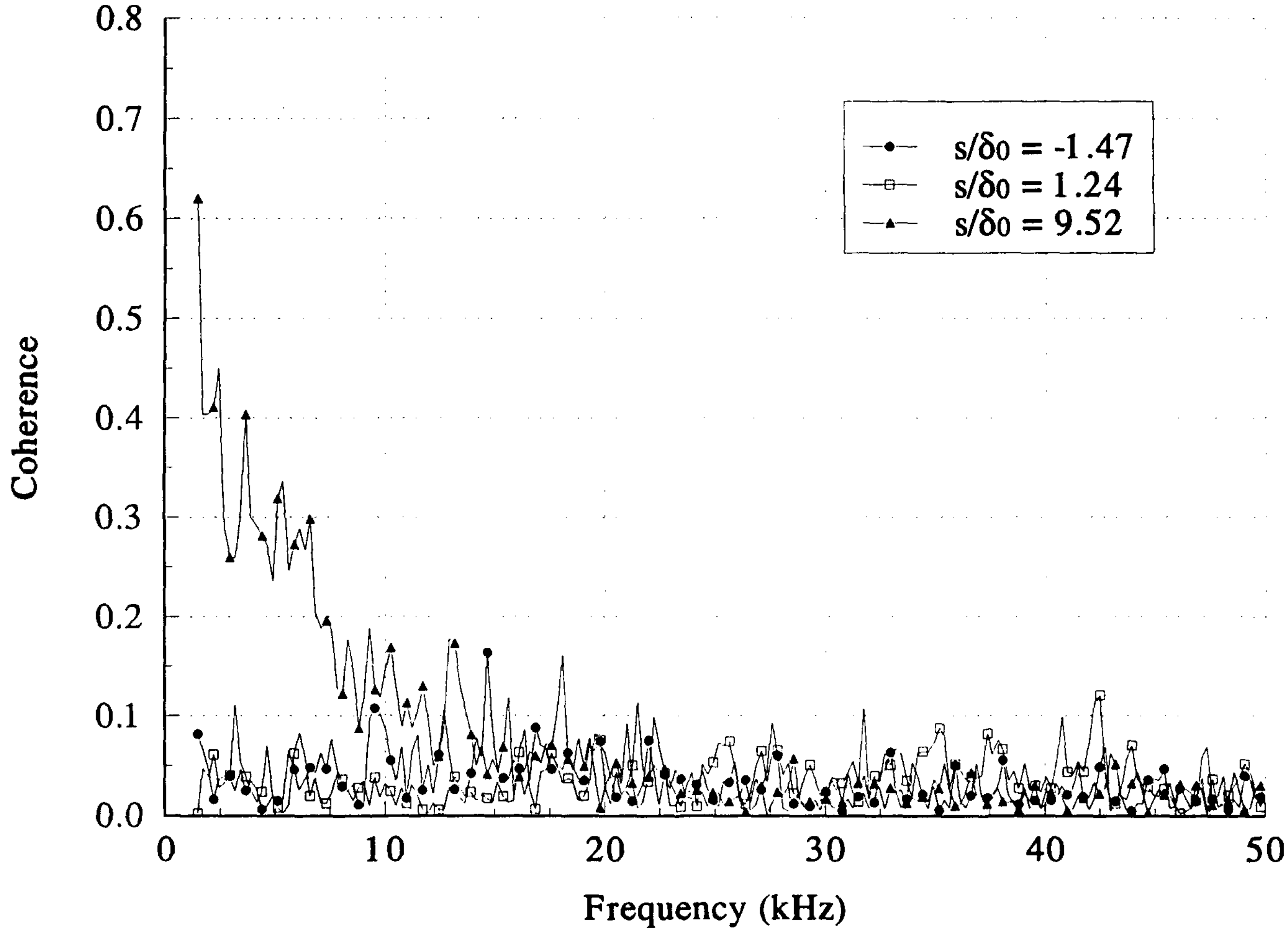

Figure 110. Streamwise evolution of the spanwise coherence for $\Delta z/\delta_0 = 0.82$ downstream of the 14° centered expansion.

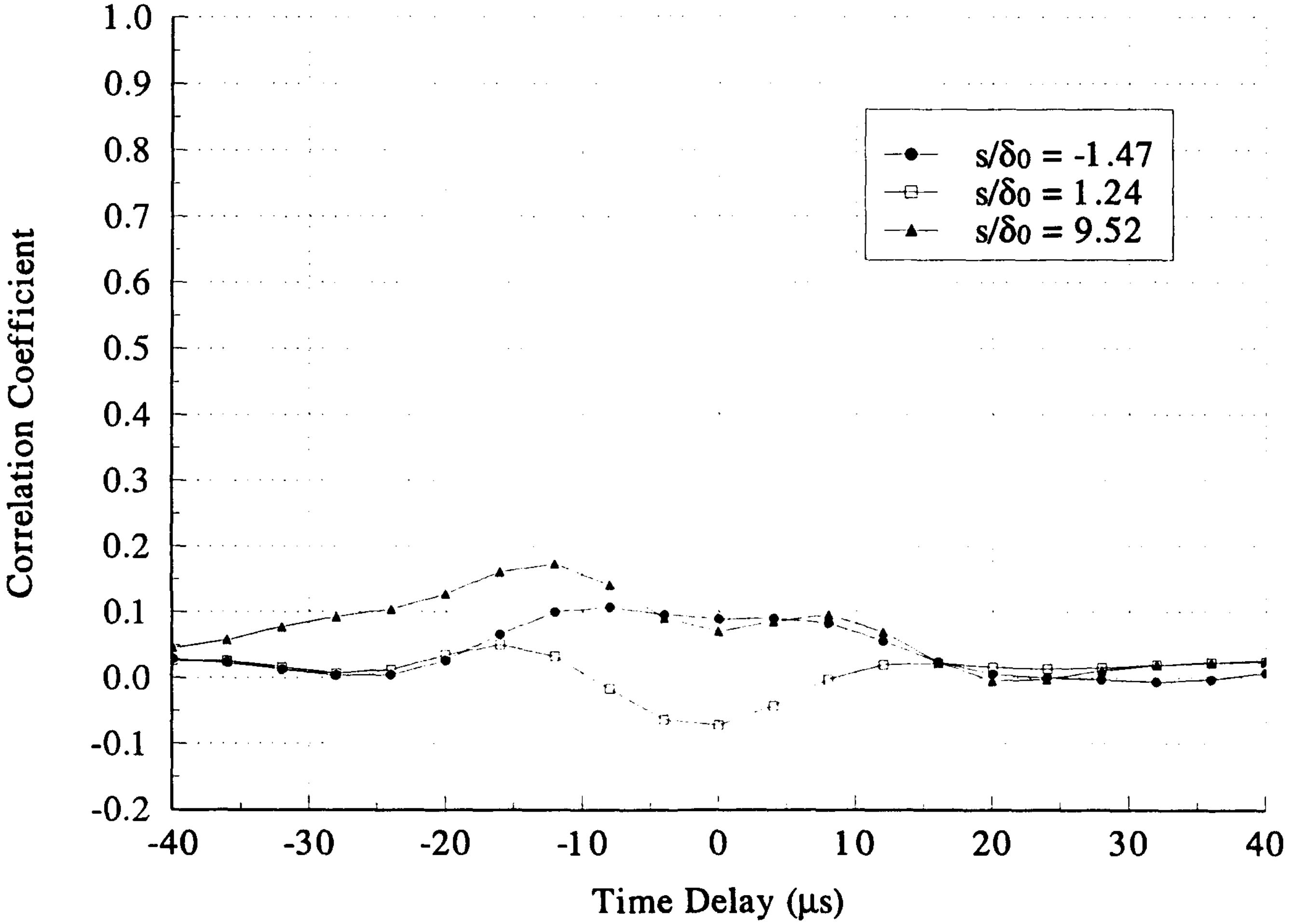

Figure 111. Spanwise space-time correlations for Δz/δo = 0.82 in the boundary layer before and after the 14° centered expansion.

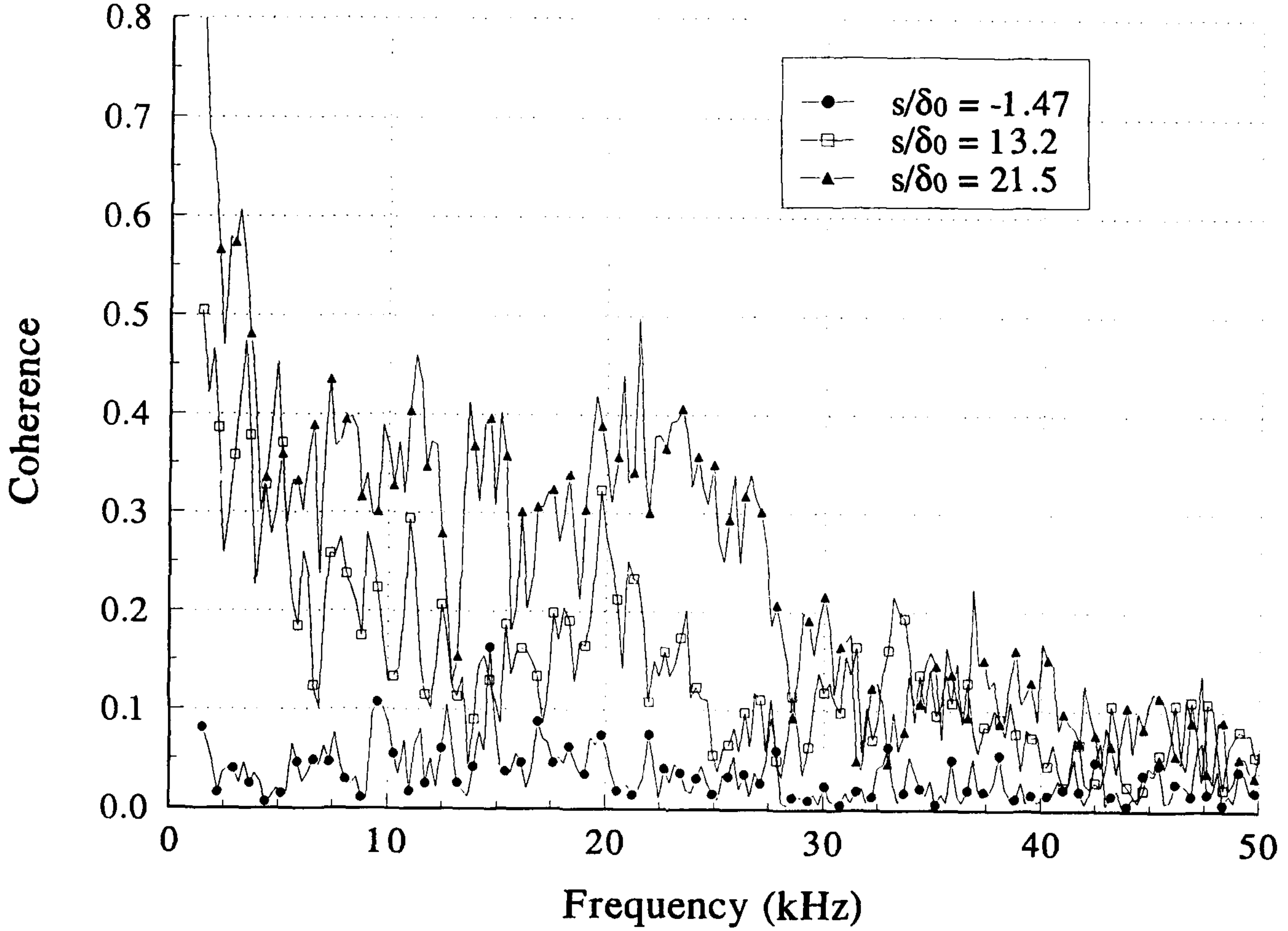

Figure 112. Streamwise evolution of the spanwise coherence for Δz/δ0 = 0.82 downstream of the 14° gradual expansion.

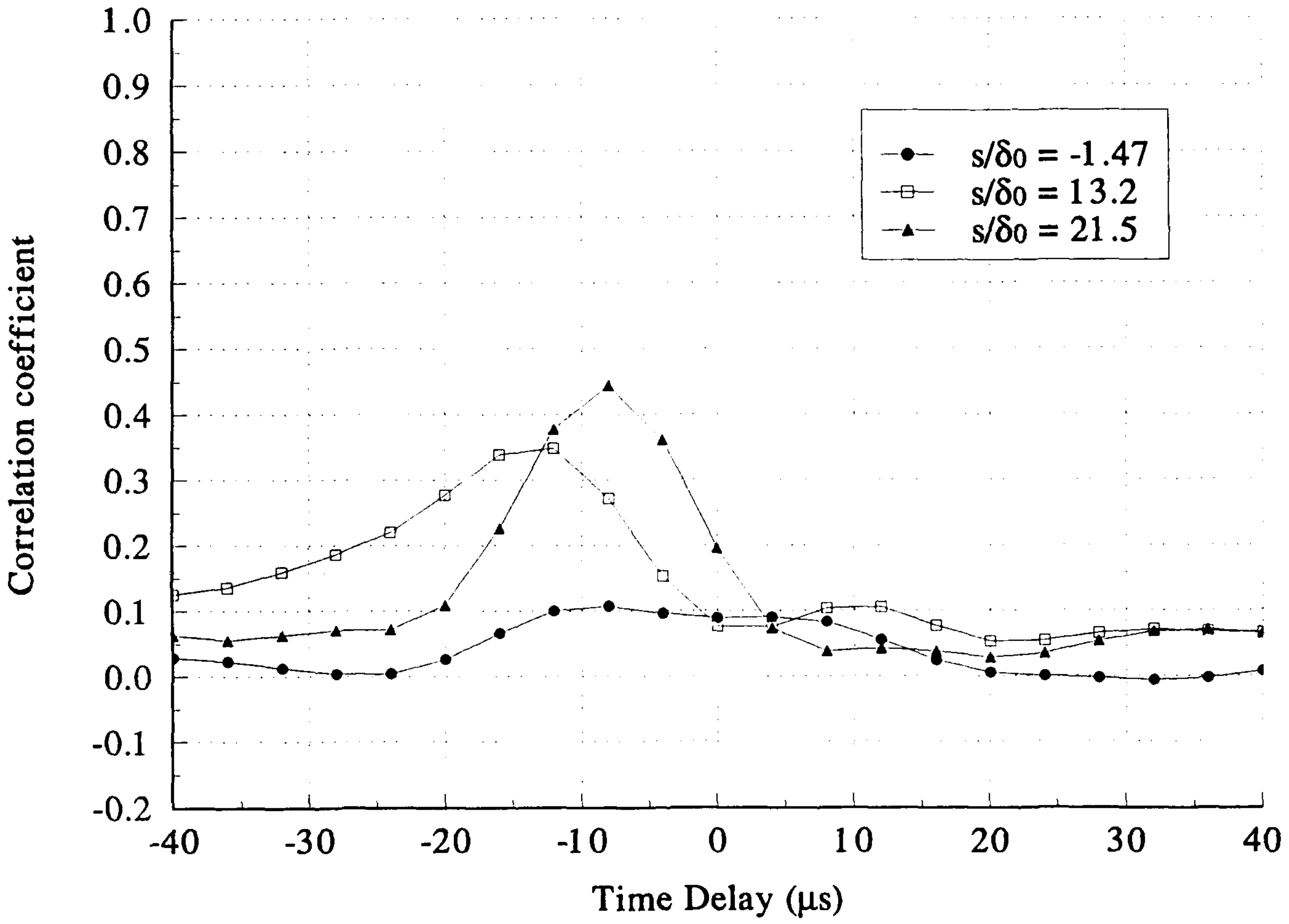

Figure 113. Spanwise space-time correlations for $\Delta z/\delta_0 = 0.82$ in the boundary layer before and after the 14° gradual expansion.